FUNCTIONAL MOLECULAR MAGNETIC MATERIALS BASED ON TRANSITION METAL COMPLEXES, ORGANOCYANIDE RADICALS AND METAL ORGANIC FRAMEWORKS

A Dissertation

by

HAOMIAO XIE

Submitted to the Office of Graduate and Professional Studies of
Texas A&M University
in partial fulfillment of the requirements for the degree of

DOCTOR OF PHILOSOPHY

Chair of Committee,	Kim R. Dunbar
Committee Members,	Timothy R. Hughbanks
	Donald G. Naugle
	Michael Nippe
Head of Department,	Simon North

December 2020

Major Subject: Chemistry

ABSTRACT

Molecule-based functional magnetic materials are of great interest due to their promising potential applications in new generation of electronic devices. Single molecule magnets (SMMs) and spin-crossover (SCO) moieties are two important categories of molecular materials that exhibit magnetic bistability. Solid state assemblies of these molecules combined with other functional moieties, such as tetracyanoquinodimethane (TCNQ) and metal organic frameworks (MOFs) can result in an enhancement of the original properties and/or coexistence/synergistic interactions of more than one functionality. The goal of the research in this dissertation was to explore ways to manipulate solid state structures and physical properties of SMMs and SCO building blocks by (1) manipulating supramolecular interactions between TCNQ and SCO/SMM units and (2) using crystalline MOFs platforms for nanostructuring SMMs for potential applications in electronic devices.

Two types of molecular magnetic bistability, SMM properties (in $[Co^{II}(Fctp)_2](TCNQ)_2$ (**1**)) and SCO (in $[Co^{II}(Fctp)_2](TCNQ)_2 \cdot MeCN$ (**2**) and $[Co^{II}(Fctp)_2](TCNQF)_2 \cdot MeCN$ (**3**)), have been achieved with the same transition metal complex, $[Co^{II}(Fctp)_2]^{2+}$, by using the two TCNQ radicals, $TCNQ^{\cdot -}$ and $TCNQF^{\cdot -}$. Single crystal structures and theoretical computational studies reveal that the supramolecular interactions play important roles in the tuning of the magnetic properties.

A mixed-stacked of partially charged TCNQ (electron acceptor) and the phenothiazinyl (PTZ, electron donor) group on the SCO molecule ($[Co(PTZ\text{-}tpy)_2]^{2+}$)

were achieved in the compound $[Co(PTZ\text{-}tpy)_2]_2(TCNQ)_{4.5}\cdot 2.5MeCN$ (**6**) by introducing charge transfer interactions between conducting and SCO building blocks. The temperature dependent solid state structures as well as the magnetic and conducting properties were compared to the non-SCO Zn analogues, $[Zn(PTZ\text{-}tpy)_2]_2(TCNQ)_{4.5}\cdot 2.5MeCN$ (**7**) which revealed synergistic behavior of SCO and electron transfer between different TCNQ stacks as well as the semiconducting properties. The results demonstrate that introducing supramolecular interactions is a promising way to manipulate solid state structure as well as to realize interesting synergistic effects between different functionalities.

Finally, the installation of octahedral Co^{II} single SMM sites in the mesoporous MOF, UMCM-1, was achieved via post synthetic ion exchange reactions. Detailed studies of magnetization relaxation processes of the installed Co^{II} SMMs moieties were performed. The results indicate that the undesired Raman and direct relaxation processes were suppressed by using the mesoporous MOF as a platform for the SMMs assembly.

DEDICATION

To my father who loved and supported me in my life

ACKNOWLEDGEMENTS

I sincerely thank my advisor Prof. Kim R. Dunbar for her guidance and support throughout my Ph.D. studies. It would not have been possible for me to achieve this stage without her professional direction and patient assistance all along. Learning and performing research in the Dunbar Group helped me to develop my experimental as well as critical thinking and independent problem solving skills. I would also like to thank my committee members, Prof. Timothy R. Hughbanks, Prof. Donald G. Naugle and Prof. Michael Nippe for their guidance and educations in my Ph. D studies.

I would like to thank Prof. Mario Wriedt in Clarkson University and Dr. Darpandeep Aulakh from his group for the collaborative work on the SMM MOF project. I would also like to Prof. Lei Fang in the Chemistry Department at Texas A&M University for his collaboration with our group on aspects of his research and his help with conductivity measurements.

I also want to thank Dr. Yu-Sheng Chen and Dr. Su-Yin Grass Wang in the Advanced Photon Source facility at Argonne National Laboratories for help with single crystal X-ray diffraction experiments using the synchrotron radiation source. Use of the Advanced Photon Source was supported by the U. S. Department of Energy, Office of Science, Office of Basic Energy Sciences, under Contract No. DE-AC02-06CH11357. The data sets were collected on ChemMatCARS at beamline 15-ID-B,C,D. The data that have been collected at the APS have been essential for the success of my research.

I would like to thank Dr. Kuduva R. Vignesh and Dr. Mukesh Singh for their help and contributions to the theoretical calculations in this work.

I would also like to thank Chemistry Department and Texas A&M University for providing the support of essential facilities and instruments for my research.

I offer my sincere thanks to my mentor Dr. Xuan Zhang who introduced me to the organocyanide-based magnetic molecular material project. His mentoring and help in my personal life are very important for me in my career. I would also like to thank Dr. María Fernanda Ballesteros-Rivas for her help and support in research and in my personal life.

I would like to thank my colleagues: Dr. Dimitrios Alexandropoulos, Dr. Maria Ballesteros Rivas, Dr. Brian Dolinar, Dr. Hanhua Zhao, Dr. Yuanzhu Zhang, Dr. Toby Woods, Dr. Sayan Saha, Dr. Jill Frank, Dr. Codi Sanders, Dr. Andrew Brown, Dr. Amanda David, Dr. Mohamed Saber, Dr. Francisco Birk, Dr. David Kempe, Dr. Kelsey Schulte, Dr. Agustin Millet, Dr. Siyoung Sung, Ryan Coll, Ellen Song, An Vu, Zhe Shen, Juan Sun, Junjie Huang, Zhilin Guo, Dr. Yue Ma, Dr. Min-Xia Yao, Dr. Sui-Jun Liu and Dr. Wen-Bin Sun. I will never forget the help they provided and the great moments we had together. I would like to thank all my friends for the friendship and support in my scientific and personal life.

At the end, I would like to thank my father, Junwei Xie and my mother Zhilian Yang and all my family members. I really hope my father could see my achievement of obtaining my Ph.D. My father and mother are the most important people in my life. I could not stand at this point without their love and support.

CONTRABUTORS AND FUNDING SOURCES

Contributors

This work was supervised by a dissertation committee consisting of Professor Kim R. Dunbar, Professor Lei Fang, Professor Timothy R. Hughbanks, Professor Michael Nippe of the Department of Chemistry and Professor Donald G. Naugle of the Department of Physics.

The theoretical calculation results and analysis in Chapter II were provided by Dr. Kuduva R. Vignesh from our group. The samples that were used in Chapter IV were provided by Dr. Darpandeep Aulakh from the Wriedt Group in Clarkson University.

All other work conducted for the dissertation was completed by the student independently.

Funding Sources

This research was supported by the National Science Foundation under CHE-1808779 and the Robert A. Welch Foundation under Grant A-1449 for summer support.

TABLE OF CONTENTS

Page

ABSTRACT ii

DEDICATION iv

ACKNOWLEDGEMENTS v

CONTRIBUTORS AND FUNDING SOURCES vii

TABLE OF CONTENTS viii

LIST OF FIGURES x

LIST OF TABLES xvii

CHAPTER I INTRODUCTION 1

- Molecule-Based Multifunctional Materials: Molecular Magnetic Bistability 1
  - Single Molecule Magnets 2
  - Spin-crossover 7
- Organocyanide-Based Conducting/Semiconducting Materials 13
- Supramolecular Interactions in Multifunctional Materials 23

CHAPTER II TUNING MAGNETIC PROPERTIES OF COBALT (II) BIS-FERROCENYLTERPY CATIONS VIA SUPRAMOLECULAR INTERACTIONS WITH ORGANOCYANIDE RADICAL ANIONS 27

- Introduction 27
- Experimental Section 29
  - Synthetic Procedures 29
  - Single Crystal X-ray Crystallography 33
  - Powder X-ray Diffraction 33
  - Magnetic Measurements 33
  - Computational Details 34
- Results and Discussion 35
  - X-ray Crystallographic Studies 35
  - Magnetic Properties 42
  - Theoretical Calculations 60
  - Discussion 67

Conclusions 71

CHAPTER III CONDUCTING SPIN-CROSSOVER CHARGE-TRANSFER COMPLEXES BASED ON THE COBALT(II) BIS-(NMETHYLPHENOTHIAZINETERPY) MOIETY WITH PARTIALLY CHARGED 7,7,8,8-TETRACYANOQUINODIMETHANE 72

Introduction 72
Experimental Section 73
Synthetic Procedures 73
Single Crystal X-ray Crystallography 75
Powder X-ray Diffraction 76
Magnetic Measurements 76
X-ray Photoelectron Spectroscopy 76
Conductivity Measurements 76
Results and Discussion 97
Structural Characterizations 97
Electron Paramagnetic Resonance (EPR) Studies 106
Magnetic Properties 117
Cyclic Voltammetry Measurements 125
UV-vis Spectra 130
X-ray Photoelectron Spectroscopy (XPS) 139
Conducting Properties 140
Conclusions 142

CHAPTER IV MAGNETIC CHARACTERIZATION OF METAL-ORGANIC FRAMEWORKS FUNCTIONALIZED WITH SINGLE MOLECULE MAGNETS 143

Introduction 143
Experimental Section 146
Sample Preparation 146
Neutron Activation Analysis(NAA) 147
Solid State UV-vis Spectra 148
Magnetic Measurements 148
Results and Discussion 149
Elemental Analysis and Solid State UV-vis Spectra 149
Magnetic Properties 150
Conclusions 168

CHAPTER V SUMMARY AND FUTURE OUTLOOK 170

REFERENCES 175

LIST OF FIGURES

Page

Figure I-1 Energy-m_s diagram for an SMM with $S = 10$ ground state and negative axial zero field splitting parameter D. 3

Figure I-2 The d orbital splitting diagrams of d^7 electron configurations in an octahedral geometry. 9

Figure I-3 Tanabe-Sugano diagram for a d^7 octahedral configuration and the crossover point. 10

Figure I-4 χT vs T plots of (a) typical SCO behavior and (b) SCO behavior with thermal hysteresis 12

Figure I-5 Structure of TCNQ, possible interactions and reduced anion and di-anionic species. 14

Figure I-6 Conducting mechanisms in solid state: (a) band conducting via orbital overlaps, (b) charge hopping and (c) proton-conductivity. 16

Figure I-7 Conducting pathway in $Tl(TCNQCl_2)$[46] through (a) π…π stacking and (b) chemical bonds. Adapted from Ref. 46 with permission of John Wiley and Sons. 17

Figure I-8 Carbon-carbon bonds of TCNQ used for charge state evaluation with the Kistenmacher formula. 18

Figure I-9 Energy scales of supramolecular interactions.[119] Adapted from Ref. 119. with permission of The Royal Society of Chemistry. 24

Figure I-10 Solid-state structural modifications of SCO – TCNQ multifunctional materials 26

Figure II-1 The asymmetric units in the crystal structures of (a) $[Co^{II}(Fctp)_2](TCNQ)_2$ (1), (b) $[Co^{II}(Fctp)_2](TCNQ)_2 \cdot MeCN$ (2) and (c) $[Co^{II}(Fctp)_2](TCNQF)_2 \cdot MeCN$ (3) with thermal ellipsoids drawn at the 70% probability level. The fluorine atoms are disordered in TCNQF and the hydrogen atoms are omitted for the sake of clarity. Color code: carbon: grey; nitrogen: blue; cobalt: purple; iron: orange; fluorine: yellow. 38

Figure II-2 Views along the *a* crystal axis of (a) 2 and (b) 3. The crystal origins of 3 were reset to the same position as 2 by a (1/2, 1/2, 1/2) translation.

Hydrogen atoms were omitted for the sake of clarity. Color code: carbon: grey; nitrogen: blue; cobalt: purple; iron: orange; fluorine: yellow. 39

Figure II-3 a) Short contacts of TCNQ, pyridyl and ferrocenyl groups involved in intermolecular interactions in 1. (b) The packing assemblies of 1 along the *a* axis of the unit cell with intermolecular interactions. Hydrogen atoms were omitted for the sake of clarity. Color code: carbon: grey; nitrogen: blue; cobalt: purple; iron: orange. 40

Figure II-4 Powder X-ray diffraction for (a) 1, (b) 2, (c) 3 and (d) 1' The red lines represent the experimental data; the black lines represent the simulated diffraction patterns based on the single crystal structure data. 47

Figure II-5 (a) χT vs T plot, the circles represent the experimental data and the read line represents the linear fit; (b) magnetization plot for 1'. 49

Figure II-6 (a) χT vs T plot and (b) field-dependent magnetization curve at 1.8 K for compound 1. (c) Reduced magnetization plots from 1-7 T. The solid lines are the best fit from the Hamiltonian in Equation 1.3. 50

Figure II-7 Frequency dependence of (a) in-phase and (b) out-of-phase ac susceptibility data from 1 Hz to 1000 Hz under HDC = 500 Oe from 1.8 K to 5.8 K and (c) Cole-Cole plots with best fits (solid lines) for 1 from 1.8 to 5.8 K..... 51

Figure II-8 Frequency dependence of (a) in-phase and (b) out-of-phase ac susceptibility from 1 Hz to 1000 Hz under H_{DC} = 1750 Oe from 1.8 K to 5.8 K and (c) Cole-Cole plots with best fits (solid lines) for 1..... 52

Figure II-9 Frequency dependence of (a) in-phase and (b) out-of-phase ac susceptibility from 1 Hz to 1000 Hz at T = 1.8 K under H_{dc} fields from 0 Oe to 6000 Oe and (c) Cole-Cole plots with best fits (solid lines) for 1..... 53

Figure II-10 (a) Magnetic field dependence, (b) and (c) temperature dependence of 1 with the best fits by using Equation 1.12 and Equation 1.11. The solid lines are the total fit (red lines) and contributions of different relaxation processes (orange, yellow, green and blue represent the contribution from Orbach, Raman, Direct and QTM processes respectively) for the inverse relaxation time τ^{-1}..... 54

Figure II-11 χT vs T plots of 2 and 3. The open circles represent the experimental data and the solid lines represent the fitting by using Equation 1.14. 55

Figure II-12 $\mathbf{ln1} - \boldsymbol{nHSnHS}$ vs 1/*T* plots of (a) 2 and (b) 3 for fitting the SCO thermodynamic parameter. 56

Figure II-13. CASSCF computed d-orbital ordering for the Co(II) ion in 1. Spin-up (black) and spin-down (red) arrows represent α and β electrons. The pink and blue regions indicate the positive and negative signs of wave functions respectively. 62

Figure II-14. DFT computed frontier molecular orbitals energy diagram of {[Co(Fctp)$_2$](TCNQ)$_2$} and {[Co(Fctp)$_2$](TCNQF)$_2$} complexes. The orbital surfaces were plotted with 0.02 isovalues. The yellow and blue regions indicate the positive and negative signs of wave functions respectively. 63

Figure II-15. Plots of frontier molecular orbital surfaces of (a) HOMO (b) LUMO (c) LUMO+1 for {[Co(Fctp)$_2$](TCNQ)$_2$} with isovalues = 0.02 from DFT calculations. The yellow and blue regions indicate the positive and negative signs of the wavefunctions respectively. 64

Figure II-16. Plots of frontier molecular orbital surfaces of (a) HOMO (b) LUMO (c) LUMO+1 for {[Co(Fctp)$_2$](TCNQF)$_2$} with isovalues = 0.02 from DFT calculations. The yellow and blue regions indicate the positive and negative signs of the wavefunctions respectively. 65

Figure II-17 Asymmetric disordered fluorine substituent on $TCNQF^{-\cdot}$ in 3. The refined occupancies for F1a, F1b, and F1c are 0.566, 0.099 and 0.335 respectively. Hydrogen atoms were omitted for the sake of clarity. 70

Figure II-18 Dipole moments of (a) low-spin (0.7688 Debye) and (b) high-spin (4.0338 Debye) $[Co(Fctp)_2]^{2+}$ cations from the DFT calculations. 70

Figure III-1 Asymmetric units of (a) 6 and (b) 7. Hydrogen atoms and solvent molecules were omitted for the sake of clarity. Colour code: carbon: grey; nitrogen: blue; cobalt: purple; sulfur: orange. 86

Figure III-2 There different TCNQ packing patterns that exist in the solid state structures of 6 and 7. 87

Figure III-3 Interlayer stacking patterns of 6 and 7 in (a) (002) and (b) (001) plane. 88

Figure III-4 Temperature dependence of M-N coordination bond lengths in (a) and (b): compound 6 (M = Co); (c) and (d): compound 7 (M = Zn). 89

Figure III-5 Temperature dependence of charges on TCNQ units in (a) compound 6 and (b) compound 7. 91

Figure III-6 Temperature dependence of charges on TCNQ stacking modes in (a) compound 6 and (b) compound 7. 92

Figure III-7 Intermolecular distances between TCNQ and PTZ groups in compound (a) 6 (b) 7. 93

Figure III-8 Temperature-dependent TCNQ-TCNQ interplanar spacing between (a) A-B, (b) B-C, (c) D-D and (d) E-E in compound 6 and 7. 94

Figure III-9 Temperature-dependent TCNQ-PTZ interplanar spacing between (a) PTZ-A, (b) PTZ-D and (c) PTZ-E in compound 6 and 7. 96

Figure III-10 Temperature-dependent X-band EPR spectra of (a) 4, (b) 5 and (c) 6. The black solid lines represent the best fit with the parameters in table III-12, III-13 and III-14. The resonance intensities were all scaled by the maximum intensity. 105

Figure III-11 The χT vs T plots, (a), (c), (e), and the Magnetization vs H plots, (b), (d), (e), for compound 4, 6 and 7 respectively. The open circles represent the experimental data points. The solid lines indicate the theoretical fittings. 109

Figure III-12 (a) $\mathbf{ln}\boldsymbol{nrad2}(\mathbf{1}-\boldsymbol{nrad})$ vs 1/*T* plot and (b) the localized radical contribution to χT. 112

Figure III-13 $\mathbf{ln1}-\boldsymbol{nHSnHS}$ vs 1/*T* plots of (a) 4 and (b) 6 for fitting the SCO thermodynamic parameters. 113

Figure III-14 Magnetization vs magnetic field (H) at 1.8 K of 1 (open circle) and simulation (solid lines) with (a) L.S. Co^{II} (S = 1/2, g_{aver} = 2.14) and (b) 93% L.S. Co^{II} (S = 1/2, g_{aver} = 2.14) and 7% H.S. Co^{II} (S = 3/2, g_{iso} = 2.62 and D = + 44.9 cm^{-1}). 114

Figure III-15 . Magnetization vs magnetic field (H) at 1.8 K of 6 (open circle) and simulation (solid lines) with L.S. Co^{II} (S = 1/2, g_{aver} = 2.14) and H.S. Co^{II} (S = 3/2, g_{iso} = 2.62 and D = + 44.9 cm^{-1}) at (a) 2 K, (b) 3 K, (c) 5 K and (d) 7 K. 115

Figure III-16 cyclic voltammetry diagram of compound 4, 5 and TCNQ in acetonitrile (vs Fc/Fc+) with 2 M NBu_4PF_6 as electrolyte. 123

Figure III-17 Differential pulse voltammetry plots of (a) 4 and (b) 5 and the fitting of peaks with Gaussian function. 124

Figure III-18 (a) Solid state UV-vis absorption spectra of 6 and 7. The intensities were scaled by the absorption of maximum peaks. (b) UV-vis spectra of compound 4-7, TBA(TCNQ) and $TEA(TCNQ)_2$ in acetone solution. 126

Figure III-19 (a) UV-vis absorption spectra of 4 and 5. (b) Gaussian decomposition of 1 with two different components. 127

Figure III-20 (a) UV-vis absorption spectra of 6 and 7. (b) UV-vis absorption spectra of TCNQ starting material TBA(TCNQ) and $TEA(TCNQ)_2$..... 128

Figure III-21 . UV-vis absorption spectra of (a) 6; and (b) 7 and the contributions from deferent components. 129

Figure III-22 XPS spectra for S2p of compound (a) 4, (b) 5, (c) 6 and (d) 7. The blue, green and red lines represent the experimental data, fits of $S2p_{3/2}$ and $S2p_{1/2}$ respectively. The short dots represents for the sum of total fits. 132

Figure III-23 . XPS spectra for C1s of compound (a) 4, (b) 5, (c) 6 and (d) 7. The blue represents the experimental data. The short dots represent the full fitting. The red and green lines represent for the different C1s components in compound 6 and 7. 134

Figure III-24 XPS spectra for N1s of compound (a) 4, (b) 5, (c) 6 and (d) 7. The blue represents the experimental data. The short dots represent the full fitting..... 136

Figure III-25 XPS spectra for Co2p of compound (a) 4 and (b) 7. The blue represents the experimental data. The short dots represent the full fitting. The red and purple lines represent the fitting for $Co2p_{3/2}$ and $Co2p_{1/2}$ while green and azure lines represent for the fitting of their satellite peaks. 138

Figure III-26 Ln of relative resistance vs inverse temperature plots of 6 (blue open circle) and 7 (red open circle) with the linear fits (dash lines) in the range of 100-300 K. 140

Figure IV-1 Structural positions of MOFs that can be used to install SMMs..... 146

Figure IV-2 Exchange mechanism of the Co^{2+} metal ion with the Zn_4O nodes. 148

Figure IV-3. Solid state UV-visible spectra of 8 (pink) and 9 (blue)..... 150

Figure IV-4 . Temperature-dependent magnetic susceptibility data for 8 (open circles) measured under a field of H = 1000 Oe. The solid line represents the best fit with the Hamiltonian shown in Equation 4.1. 152

Figure IV-5 Temperature dependence of (a) χT (black circles) and (b) $1/\chi$ (open circle) of 9 with Curie-Weiss law: $1/\chi = T/C - \theta$, where C is Curie constant and θ is Weiss constant. The best fit yield C = 2.90 emu K mol^{-1} and θ = -164 K. 153

Figure IV-6 Frequency dependence of (a) in-phase and (b) out-of-phase ac susceptibility data from 1 Hz to 1000 Hz under a dc field ranging from 0 Oe to 6000 Oe at T = 2.5 K and (c) Cole-Cole plots with best fit (solid lines) for 8. 154

Figure IV-7 Frequency dependence of (a) in-phase and (b) out-of-phase ac susceptibility data from 1 Hz to 1000 Hz under dc fields ranging from 0 Oe to 6000 Oe at T = 3.0 K and (c) Cole-Cole plots with best fit (solid lines) for 8 155

Figure IV-8 Field dependence of the inverse of relaxation time τ^{-1} of 8 at 2.5 K (red circle) and 3.0 K (black square). The solid lines show the best fit to the data with Equation 1.12. 157

Figure IV-9 Field dependence of the inverse relaxation time τ^{-1} at (a) 2.5 K and (b) 3.0 K. Red lines show best fits to data with Equation 1.12. The red and blue lines show relative contributions from QTM and direct spin-phonon relaxation processes. 158

Figure IV-10 Frequency dependence of (a) in-phase and (b) out-of-phase ac susceptibility data from 1 Hz to 1000 Hz under H_{DC} = 500 Oe and (c) Cole-Cole plots with best fits (solid lines) for 8. 159

Figure IV-11 Frequency dependence of (a) in-phase and (b) out-of-phase ac susceptibility data from 1 Hz to 1000 Hz under H_{DC} = 1500 Oe and (c) Cole-Cole plots with best fits (solid lines) for 8. 160

Figure IV-12 Frequency dependence of (a) in-phase and (b) out-of-phase ac susceptibility data from 1 Hz to 1000 Hz under H_{DC} = 4000 Oe and (c) Cole-Cole plots with best fits (solid lines) for 8. 161

Figure IV-13 Temperature dependence of the inverse of relaxation time τ-1 of 1 under H_{DC} = 500 (black squares), 1500 (red circle) and 4000 Oe (blue triangles). The solid lines show the best fits to the data with Equation 1.11. 164

Figure IV-14 Temperature dependence of the inverse relaxation time τ^{-1} under (a) 500 Oe and (b) 1500 Oe and (c) 4000 Oe. Black lines show fits to data with Equation 1.11. The red, blue, green and teal lines show relative contributions from Orbach, direct, Raman relaxation and QTM processes. 165

LIST OF TABLES

Page

Table I-1 Spin configurations and related parameters for d^4-d^7 3*d* transition metals in an octahedral geometry 11

Table I-2 Redox potentials of select TCNQ derivatives in MeCN (vs Fc/Fc^+) with 0.1 M TBA(PF_6) electrolyte at room temperature. 14

Table I-3 Summary of conductivity (σ_{300K}), activation gap (ΔE_{gap}) and SCO transition temperature ($T_{1/2}$) of published SCO-semiconducting compounds with TCNQ building blocks. 23

Table II-1 Crystallographic and refinement parameters for $[Co(FcTp)](TCNQ)_2$ compounds. 41

Table II-2 Co-N bond distances in 1 (100 K), 2 (120 K) and 3 (120 K). 42

Table II-3 Continuous shape measure analysis results from SHAPE v2.10 42

Table II-4 Fitting parameters of the Cole-Cole plots for variable-field AC magnetic susceptibilities data for 1 at T = 1.8 K. 57

Table II-5 Fitting parameters of the Cole-Cole plots for variable-field AC magnetic susceptibilities of 1 under H_{DC} = 500 Oe. 58

Table II-6 Fitting parameters of the Cole-Cole plots for variable-field AC magnetic susceptibilities of 1 under H_{DC} = 1750 Oe. 59

Table II-7 Fitting parameters of χT vs T plots for 2 and 3 obtained from the least squares method 59

Table II-8. CASSCF computed D, E/D and g_x, g_y and g_z values, transition energies (cm^{-1}) and contributions to D value from the first four excited states for 1. 66

Table II-9. Selected structural parameters of 2 computed using TPSSh functionals (see Figure II-1 for labels). 66

Table II-10. Energy of the spin states produced by the TPSSh/DFT calculations. 66

Table III-1 Crystallographic and refinement parameters for 4-7 77

Table III-2 Temperature dependent M-N bond lengths in 6 (Co) and 7 (Zn) 78

Table III-3 Temperature-dependent interplanar distance between TCNQ units and phenothiazinyl groups in compound 6 (Co). 80

Table III-4 Temperature-dependent interplanar distance between TCNQ units and phenothiazinyl groups in compound 7 (Zn)..... 80

Table III-5 Formal charges that estimated by Kistenmatcher's formula on TCNQ in compound 6 at 110K..... 81

Table III-6 Formal charges that estimated by Kistenmatcher's formula on TCNQ in compound at 110K..... 81

Table III-7 Temperature-dependent M-N distances (Å) of 6 and 7. 82

Table III-8 Temperature dependent formal charges that estimated by Kistenmatcher's formula on TCNQ in compound 6..... 84

Table III-9 Temperature-dependent formal charges that estimated by Kistenmatcher's formula on TCNQ in compound 7..... 84

Table III-10 Temperature dependent formal charges that estimated by Kistenmatcher's formula on TCNQ triads in compound 6..... 85

Table III-11 Temperature dependent formal charges that estimated by Kistenmatcher's formula on TCNQ triads in compound 7..... 85

Table III-12 EPR fitting parameters: g values, ^{59}Co hyperfine coupling parameters (A) and line width (lw) of compound 4 in solid state..... 104

Table III-13 EPR fitting parameters: g values, ^{59}Co hyperfine coupling parameters (A) and line width (lw) of compound 6 in solid state..... 104

Table III-14 EPR fitting parameters: g values and line width of compound 7 in solid state. 104

Table III-15 Fitting parameters of χT vs T plots for 4 and 6 found via the least-squares method..... 107

Table III-16 Evaluated temperature-dependent $(TCNQ)_2^{\cdot -}$ radical fraction from charges on type E TCNQ and the reaction constants K..... 108

Table III-17 Redox potential and current intensities of cyclic voltammetry measurements of 4, 5 and TCNQ. 122

Table III-18 Potential, current intensities and full width of half maximum (FWHM) of differential pulse voltammetry peaks of compound 4 and 6..... 122

Table IV-1Elemental analysis results from NAA experiment 149

Table IV-2 . Fitting parameters of the Cole-Cole plots of variable-field AC magnetic susceptibilities of 8 at T = 2.5 K 156

Table IV-3 Fitting parameters of the Cole-Cole plots of variable-field AC magnetic susceptibilities of 8 at T = 3.0 K. 156

Table IV-4 Fitting parameters of the Cole-Cole plots of variable-temperature AC magnetic susceptibilities for 8 under H_{DC} = 500 Oe..... 162

Table IV-5 Fitting parameters of the Cole-Cole plots of variable-temperature AC magnetic susceptibilities for 8 under H_{DC} = 1500 Oe..... 162

Table IV-6 Fitting parameters of the Cole-Cole plots of variable-temperature AC magnetic susceptibilities for 8 under H_{DC} = 4000 Oe..... 163

Table IV-7. Fitting parameters of relaxation processes of 8 and reported example of $\{[(Co(NCS)_2)_3(k^3\text{-}TPT)_4]\cdot a(H2O)\cdot b(MeOH)\}_n$ 168

CHAPTER I

INTRODUCTION

Molecule-Based Multifunctional Materials: Molecular Magnetic Bistability

Molecular materials with different properties such as magnetic bistability, electrical conductivity and optical properties, are categories of materials for new generations of electronic devices due to their intrinsic quantum nature and structural diversity thanks to powerful organic and/or inorganic synthetic methodologies.

Molecular bistability has gained enormous attention in the field of molecular functional materials over the past three decades. Traditional bulk magnets such as metals, metallic alloys, and metal oxides are not able to preserve their magnetic bistability at the nanoscale level when the size of the ferromagnetic/ferromagnetic particles reach their single-domain limit and exhibit superparamagnetic behavior. In order to pursue high-density data storage and processing applications, achieving magnetic bistability at the molecular level is an important goal for producing future generations of electronic devices. Apart from a few examples of molecular magnetic stability in purely organic molecules, such as π-stacked 1,3,2-dithiazolyl radicals[1-2], the majority of molecular materials that exhibit magnetic bistability contain transition metal and lanthanide spin centers. Two major categories of compounds with magnetic bistability are single molecule magnets (SMMs) and spin-crossover (SCO) compounds. Both of these types of materials have been extensively investigated; key concepts and findings are described in the following sections.

Single Molecule Magnets

Single molecule magnets (SMMs) are molecular compounds that are able to retain their magnetization orientation in a zero external magnetic field below a certain temperature known as the blocking temperature, T_B. Two signature behaviors of SMMs are slow relaxation of the magnetization under an alternating current (AC) magnetic field and magnetic hysteresis below T_B. The first example of an SMM, $[Mn_{12}O_{12}(O_2CCH_3)_{16}\cdot 4H_2O]$, also known as "$Mn_{12}$", is a dodecanuclear manganese compound bridged by twelve μ_3-oxo and twelve acetate bridges reported by Gatteschi and coworkers as well as Christou and Hendrickson in the 1990s.[3-5] An $S = 10$ spin ground state is achieved for Mn_{12} by antiferromagnetic coupling between four Mn^{IV} ($S = 3/2$) and eight Mn^{III} ($S = 2$) units bridged by μ_3-oxo ligands. The effective energy barrier was found to be 61 K with a blocking temperature of ~ 3 K.[5] In this type of SMM, the energy barriers (U) and blocking temperatures are dependent on the spin ground states (S) and magnetic anisotropy (negative axial anisotropy parameter D_z) induced by the splitting of magnetic sublevels (Figure I-1). For an SMM with quenched first-order orbital angular momentum such as Mn_{12}, the relationship between energy barriers, S and D are:

$$U = |D|S^2 \text{ for integer } S \qquad \textbf{Equation 1.1}$$

$$U = |D|(S^2 - 1/4) \text{ for half integer } S \qquad \textbf{Equation 1.2}$$

In the first decade, research focused almost exclusively on the synthesis of SMMs with high nuclearities in order to achieve a huge spin ground state, S, to increase the energy barrier. Although compounds with gigantic spin ground states have been

synthesized, for example, Mn_{19} (S = 83/2)[6], Mn_{25} (S = 61/2)[7] and Mo_8Mn_{14} (S = 31)[8] compounds, it was found that the lack of proper local symmetries of the single ion spin centers in these compounds results in a decrease in anisotropy, and a general lack of SMM behavior was found.

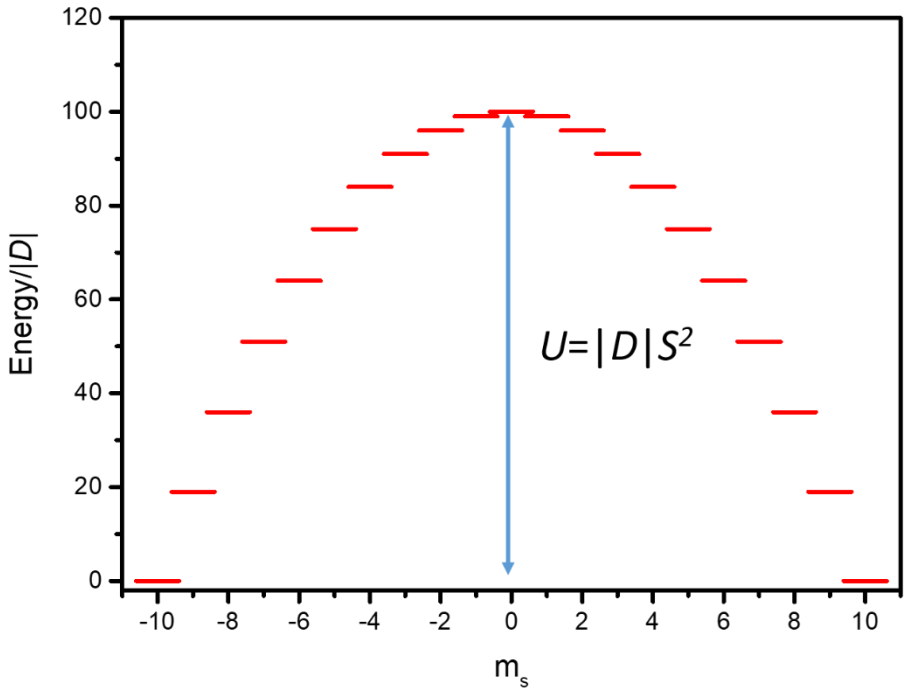

Figure I-1 Energy-m_s diagram for an SMM with S = 10 ground state and negative axial zero field splitting parameter D.

Another important strategy for increasing the energy barrier is improving the axial anisotropy for single-ion transition metal and lanthanide complexes by manipulating the symmetry and ligand field strength of the coordination sphere. Recently, a breakthrough was reported by Layfield and the coworkers[9] who prepared the dysprosium metallocene single-molecule magnet, $[(\eta^5\text{-Cp*})Dy(\eta^5\text{-Cp}^{iPr5})][B(C_6F_5)_4]$

which exhibits magnetic hysteresis above the boiling point of liquid nitrogen (77 K) up to 80 K. It is noted that the highest energy barrier record for transition metal based SMMs is [(sIPr)Co^{II}NDmp] with an effective energy barrier of 413 cm^{-1}.[10]

For compounds with quenched orbital angular momentum, the spin state *S* is a good quantum number and the single-ion anisotropy is caused by second order spin-orbit coupling. The Hamiltonian of such a system can be described as:

$$\widehat{H} = D[\hat{S}_z^2 - S(S+1)/3] + E(\hat{S}_x^2 - \hat{S}_y^2) \qquad \textbf{Equation 1.3}$$

where *D* and *E* are the axial and rhombic (transverse) zero field splitting parameters; $\hat{S}_x$, $\hat{S}_y$ and $\hat{S}_z$ are spin operators along x, y and z directions. A large and negative *D* value creates an energy barrier for magnetization relaxation. The transverse parameter *E* is also critical, as a large magnitude of *E* causes mixing between the $m_s = \pm S$ microstates and other m_s states by the $\hat{S}_x^2$ and $\hat{S}_y^2$ operators as the $\hat{S}_z$ operator does not commute with the total Hamiltonian $\widehat{H}$. Significant quantum tunneling of magnetization is observed under these conditions and results in an under-barrier spin relaxation.[11-12] Thus, realizing the $|E/D| \sim 0$ condition via controlling the coordination environment around the metal ion is essential for designing high-performance SMMs.

For the spin systems that involve unquenched orbital angular momentum or having spin-orbit coupling effects stronger than the ligand field, such as lanthanide ions with well-shielded 4f electrons, the spin quantum number *S* is no longer a valid parameter for the system. The total angular momentum, $\boldsymbol{J} = \boldsymbol{L} + \boldsymbol{S}$, instead of $\boldsymbol{S}$, is used to describe the magnetic states. The anisotropy induced by the crystal field can be described with the Stevens operators $\hat{O}_k^q(\boldsymbol{J})$ as:

$$\widehat{H}_{CF} = \sum_{k,q} \theta_k B_k^q \hat{O}_k^q(\hat{\boldsymbol{J}}) \qquad \textbf{Equation 1.4}$$

where B_k^q is the crystal field parameters and θ_k is the operator equivalent factors, k = 2, 4, 6,…, 2J and $-k \leq q \leq +k$.[13-14] The B_k^q parameters with q = 0 terms are related to the axial anisotropy while other terms are related to the transverse anisotropy. Enhancing the axial anisotropy and minimizing the transverse ones are key strategies to increase the energy barrier for SMMs and, indeed, much research effort over the past decade has been directed at developing strategies for enhancing the SMM properties by manipulation of the ligand field around the single ions.[15-20]

For the experimental aspects, alternating current (ac) magnetization measurements are used to probe the relaxation time and energy barrier. The ac magnetic susceptibility $\chi(\omega)$consists of in-phase ($\chi'(\omega)$) and out-of-phase ($\chi''(\omega)$) components:

$$\chi(\omega) = \chi'(\omega) - i\chi''(\omega) \qquad \textbf{Equation 1.5}$$

where ω is the angular frequency and $\omega = 2\pi f$. The Cole-Cole equation can be used to extract the relaxation time (τ):

$$\chi(\omega) = \chi_s + \frac{\chi_T - \chi_s}{1+(i\omega\tau)^{1-\alpha}} \qquad \textbf{Equation 1.6}$$

where χ_s, χ_T are susceptibility at static and infinite frequency; τ and α are the characteristic relaxation time and the factor that relates to the distribution of relaxation times.[21-22] (α is in the range of 0-1 and α = 0 corresponds to the Debye model with a single relaxation time τ). The possible processes that contribute to relaxation are Orbach, Raman, Direct, and Quantum tunneling processes.[14] The Orbach thermal mechanism involves the spin relaxation over the energy barrier, U, which is through the excited

states of magnetic sublevels. The temperature dependence of the relaxation time for an Orbach process is described by the Arrhenius equation:

$$\tau_{Orbach}^{-1} = \tau_0^{-1} e^{-\frac{U_{\text{eff}}}{k_B T}} \qquad \textbf{Equation 1.7}$$

where τ_0, U_{eff}, k_B and T are the pre-exponential factor, effective energy barrier, Boltzmann constant and temperature, respectively. Besides the Orbach process, quantum tunneling is also critical in certain systems with non-negligible transverse anisotropy. The typical form of the QTM contribution is:

$$\tau_{QTM}^{-1} = \frac{B_1}{1+B_2 H^2} \qquad \textbf{Equation 1.8}$$

where B_1 and B_2 are the parameters that relate to the tunneling splitting and inter-level transition time and H is the external static magnetic field.[23] The quantum tunneling rate decreases by ~ H^{-2} under a large magnetic field at low temperatures. Although the expression does not explicitly include the temperature dependence, studies by Zheng and coworkers indicate that the temperature dependence of QTM correlates with the temperature promoted phonon that originates from the dynamic crystal field.[24]

The two phonon-assisted relaxation processes are direct spin-lattice relaxation and Raman processes.[25] The former one involves one-phonon absorption/emission with the resonance energy ($\hbar\omega$) to flip the spin. It is both temperature and magnetic field dependent:

$$\tau_{direct}^{-1} = AH^{n_1}T \qquad \textbf{Equation 1.9}$$

where *A* is a constant; *H* and *T* are the external magnetic field and temperature. The power n_1 = 2 for a non-Kramers doublet and 4 for a Kramers doublet. The relaxation times for Raman relaxation are merely temperature dependent and follow the power law:

$$\tau_{Raman}^{-1} = CT^{n_2} \qquad \textbf{Equation 1.10}$$

where C is a constant, *T* is the temperature; n_2 = 7 for non-Kramers doublet and 9 for Kramers doublet, although n_2 with other values between 1 and 6 are possible when both optical and acoustic phonons are involved.[14, 26]

If one considers the contributions from all four relaxation processes, the expression of relaxation times can be expressed as:

$$\tau_{total}^{-1} = \tau_0^{-1} e^{-\frac{U_{\text{eff}}}{k_B T}} + \frac{B_1}{1+B_2 H^2} + AH^{n_1}T + CT^{n_2} \qquad \textbf{Equation 1.11}$$

The direct fit of relaxation times with Equation 1.11 can result in an over-parameterization issue. In order to prevent such problems, parameters B_1, B_2 and *A* can be obtained by fitting the field dependence of relaxation time with the magnetic field-dependent relaxation time data sets at fixed temperatures with Equation 1.12:

$$\tau^{-1}(H) = \frac{B_1}{1+B_2 H^2} + AH^{n_1}T + constant \qquad \textbf{Equation 1.12}$$

Then, the parameters U_{eff}, *C* and n_2 can be obtained by fitting the temperature dependent relaxation time data sets at a fixed static magnetic field with Equation 1.11.

Spin-crossover

Spin-crossover (SCO) compounds are another category of molecules with magnetic bistablity which involves spin transitions between high-spin (H.S.) and low-spin (L.S.) states in *d*-block metal complexes triggered by external stimuli such as

temperature, irradiation, and pressure. The SCO phenomenon was first identified in Fe^{III} complexes with thiocabamate ligands by Cambi and coworkers in 1931.[27] This phenomenon was also observed in the important biological Fe^{II}-heme coenzyme for oxygenation.[28] The topic of SCO behavior have been extensively developed over the last several decades including the structural and functional varieties, theoretical aspects and practical applications.[29] The most typical SCO compounds are 3*d* transition metal complexes with d^4-d^7 electronic configurations; these systems include Mn^{III} (d^4), Fe^{III} (d^5), Fe^{II} (d^6), Co^{II} (d^7) in octahedral/pseudo-octahedral geometries. (Table I-1) Rare SCO examples of Ni^{II} with the d^8 configuration have been observed in square planar[30] and square prismatic[31] geometries. The process of SCO involves the reconfiguration of electron populations in different *d* orbitals and induces a change in the number of unpaired electrons as well as the overall metal-ligand bonding (Figure I-2). The phenomenon requires comparable ligand field stabilization energy of the L.S. and H.S. states, which is determined by the energy of the ligand field splitting, Δ, and the repulsion of paired electrons, *P*. For example for $3d^n$ configuration ions in an octahedral geometry, appropriate ligand field strengths for SCO can be found around the crossover point of ground states in the Tanabe-Sugano diagrams. (Table I-1) The example of d^7 is shown in Figure I-3.[32] The SCO behavior changes the magnetic properties of transition metal centers due to the difference in spin states and also changes the geometry of the coordination sphere as a result of population of bonding, antibonding and non-bonding orbitals. Here we take Co^{II} (d^7) ion as an example (Figure I-2). The electron configuration changes from $t_{2g}^5e_g^2$ to $t_{2g}^6e_g^1$ as it goes from a H.S. (S = 3/2) state to a

L.S. (S = 1/2) state. The ligand field splitting, Δ_{oct}, becomes larger for the L.S. state to compensate for the additional electron pairing energy in the t_{2g} orbitals. As the electron population of the e_g orbitals (σ-antibonding orbitals) decreases from the H.S. state to the L.S. state, a decrease in the metal-ligand bond distances is expected, in the range of 0.1-0.2 Å.[33] Significant Jahn-Teller effects are also observed in cases that involve states with degeneracies in σ-antibonding orbitals which causes changes in the coordination sphere as well as electric dipole moments.[34] The optical properties that relate the transitions involving *d* orbitals also change during the SCO process. [35-36]

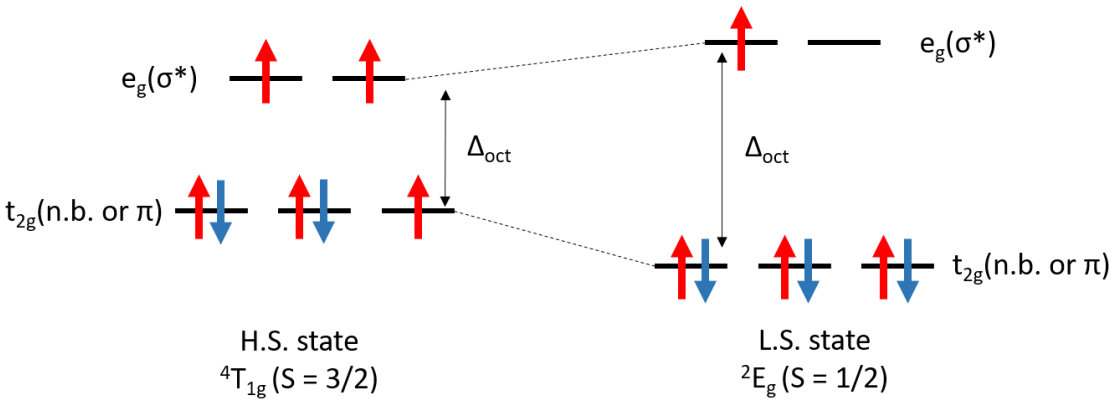

Figure I-2 The d orbital splitting diagrams of d^7 electron configurations in an octahedral geometry.

The signature magnetic behavior of thermal spin-crossover is an "S" shaped curve (Figure I-4 (a)) of the χT vs T plot due to the changes in H.S. and L.S. state populations at different temperatures. The curve is described by equation[37]:

$$\ln\left[\frac{1-n_{HS}}{n_{HS}}\right] = \frac{[\Delta H + \Gamma(1-2n_{HS})]}{RT} - \frac{\Delta S}{R} \qquad \textbf{Equation 1.13}$$

where n_{HS} is the mole fraction of high-spin species, ΔH, ΔS and Γ are the molar enthalpy, molar entropy and SCO cooperativity parameters respectively and R is the gas constant. For the non-cooperative case, such as in the gradual SCO system, the SCO cooperativity parameters $\Gamma = 0$ and the equation are described by the equation:

$$\ln\left[\frac{1-n_{HS}}{n_{HS}}\right] = \frac{\Delta H}{RT} - \frac{\Delta S}{R} \qquad \textbf{Equation 1.14}$$

and the $\ln\left[\frac{1-n_{HS}}{n_{HS}}\right]$ vs 1/T plot has a linear relationship with $\frac{\Delta H}{R}$ as slope and $-\frac{\Delta S}{R}$ as the intersection with the y-axis. The transition temperature, $T_{1/2}$, at which the population of H.S. state and L.S. states are equal, is expressed as:

$$T_{1/2} = \frac{\Delta H}{\Delta S} \qquad \textbf{Equation 1.15}$$

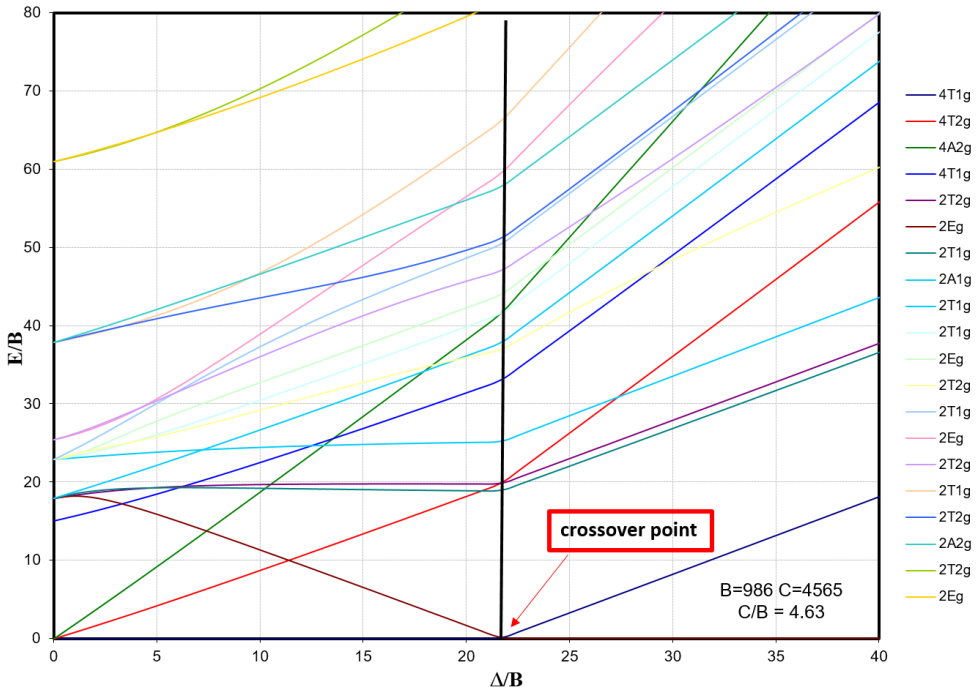

Figure I-3 Tanabe-Sugano diagram for a d^7 octahedral configuration and the crossover point.

Table I-1 Spin configurations and related parameters for d^4-d^7 3*d* transition metals in an octahedral geometry

Electronic configurations	ions	L.S. states	H.S. states	Crossover point ligand field (Δ_{oct}/B)*	ΔS_{el} (J K^{-1} mol^{-1})**
d^4	Mn^{III}	$^3T_1$ (S = 1)	^5E (S = 2)	27.1	4.2
d^5	Fe^{III}	$^2T_2$ (S = 1/2)	$^6A_1$ (S = 5/2)	28.6	9.1
d^6	Fe^{II}	$^1A_1$ (S = 0)	$^5T_2$ (S = 2)	18.9	13.4
d^7	Co^{II}	^2E (S = 1/2)	$^4T_1$ (S = 3/2)	21.9	5.8

* The values correspond to the Δ_{oct}, the ligand field splitting in an octahedral geometry, at which the energy levels of H.S. state and L.S. state exhibit crossover on Tanabe-Sugano diagrams. *B* is the Racah interelectronic repulsion parameter.[38]
** $\Delta S_{el} = R\ln[(2S_{H.S.}+1)/(2S_{L.S.}+1)]$ is the molar entropy change contribution from the change of spin multiplicity.

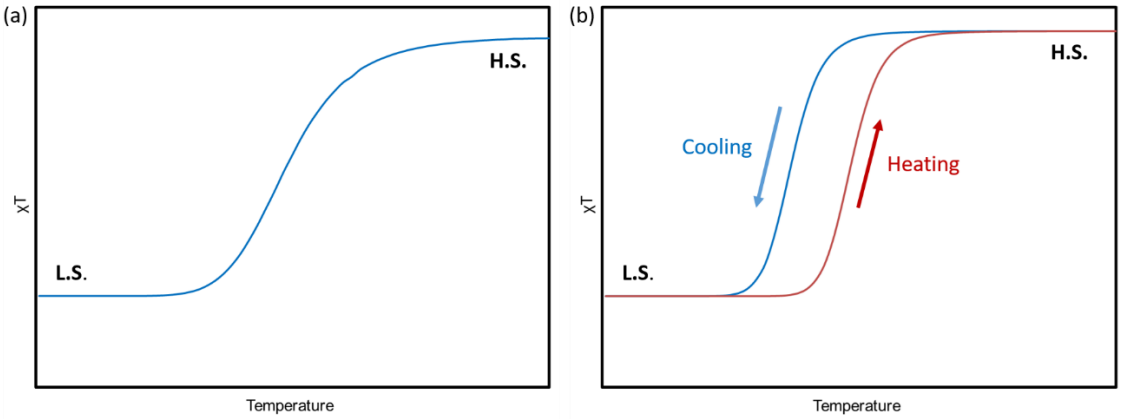

Figure I-4 χT vs T plots of (a) typical SCO behavior and (b) SCO behavior with thermal hysteresis

Certain compounds, particularly [Fe(pz)[Pt(CN)$_4$]]·solvates,[39] exhibit thermal hysteresis behaviors wherein the χT vs T curves of heating and cooling processes do not overlap. Such behavior originates from cooperative effects in the solid state and has potential applications in the memory storage application.[40] Recently, devices with single SCO molecules as molecular junctions have been fashioned by sandwiching a single SCO molecule between gold electrodes at the nanoscale level. The conductivity switching induced by a transition between the L.S. and H.S. states with external stimuli, such as light irradiation[41-42] and electric field[43] was achieved at the single-molecule level. Recently, merging conducting properties with the SCO phenomenon has become a forefront topic by combining organic conducting moieties such as organocyanide compounds with SCO complexes. A detailed discussion of this subject is provided in the following sections.

Organocyanide-Based Conducting/Semiconducting Materials

Polydentate organocyanide compounds, such as 7,7,8,8-tetracyanoquinodimethane (TCNQ) and its derivatives, are well-known redox active molecules used in the design of multifunctional materials. The electron withdrawing effect of the four cyano groups on TCNQ renders it an excellent electron acceptor that can undergo two reversible reductions to $TCNQ^{\cdot-}$ radical and $TCNQ^{2-}$ dianion (Figure I-5). Given the structural characteristics of TCNQ, there are four important features that enable interactions between TCNQ and magnetic coordination complexes: (1) The π-conjugation system on TCNQ for the π…π interactions (2) The negative charge of $TCNQ^{\cdot-}$ radical/ partially charged TCNQ for electrostatic interactions (3) The electron acceptor characteristic for charge transfer interactions and (4)The coordination ability of four cyano groups of TCNQ. Moreover, the four hydrogen atoms on the aromatic ring can be substituted with other functional groups such as halides, alkyl groups and alkoxy groups and others to tune the dipole moments and redox potentials of the TCNQ derivatives. Select reduction potentials of TCNQ derivatives are summarized in Table I-2. These characteristics of TCNQ derivatives make them ideal building blocks for the synthesis of functional organic and inorganic-organic hybrid materials.

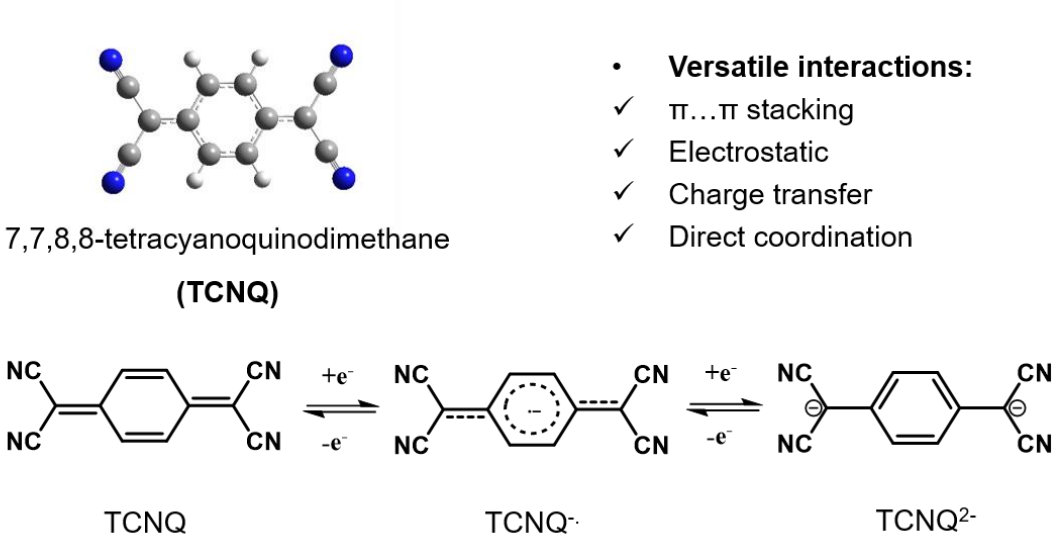

Figure I-5 Structure of TCNQ, possible interactions and reduced anion and di-anionic species.

Table I-2 Redox potentials of select TCNQ derivatives in MeCN (vs Fc/Fc^+) with 0.1 M TBA(PF_6) electrolyte at room temperature.

Derivatives	$E_{1/2}(Q/Q^{\cdot-})$/V	$E_{1/2}(Q^{\cdot-}/Q^{2-})$/V
$TCNQMe_2$	-0.28	-0.76
TCNQ	-0.18	-0.72
TCNQF	-0.09	-0.62
$TCNQI_2$	+0.03	-0.42
$TCNQCl_2$	+0.05	-0.46
$TCNQBr_2$	+0.06	-0.43

Semiconducting behavior is one of the most important signature properties of TCNQ and its derivatives. The origins of conductivity in the solid state are organized into three different charge transport mechanisms: (a) charge transport through band structure, (b) charge hopping and (c) proton-conductivity (Figure I-6).[44-45] In the case of TCNQ-based conducting/semiconducting materials, the major mechanism of charge

transport is through the band structure formed by the one-dimensional π…π stacking of TCNQ moieties. In metal-TCNQ binary compounds, such as $Tl(TCNQCl_2)$[46] (Figure I-7), the band structure formed by the coordination bonding between metal centers and TCNQ moieties also has critical contributions to the solid state conductivity. Theoretical studies of metal-TCNQ compounds[47] indicate that the transfer integral between π-orbitals between TCNQ derivatives are significantly larger than the ones between TCNQ derivatives coordinated to metal centers and causes larger delocalization of conducting electrons along the π…π stacking direction. Although the metal-based bands are more localized, the contribution to conductivity can still be significant if the energy is close to the empty TCNQ antibonding-π orbital based bands. The temperature-dependent semiconducting behavior in such a system is described by the Arrhenius equation:

$$\sigma(T) = \sigma_0 e^{-\frac{E_a}{k_B T}} \qquad \textbf{Equation 1.16}$$

where σ, σ_0, E_a, $k_B$and T are conductivity, pre-exponential factor, thermal activation band gap, Boltzmann constant and temperature.

Apart from the band conducting mechanisms, charge hopping is another important mechanism that enables high conductivities in materials with significant donor-acceptor charge transfer interactions such as TTF-TCNQ thin films.[48] In contrast to the band conducting mechanism, the charge hopping mechanism involves the electron/hole transfer between the donor and acceptor without direct orbital overlap.

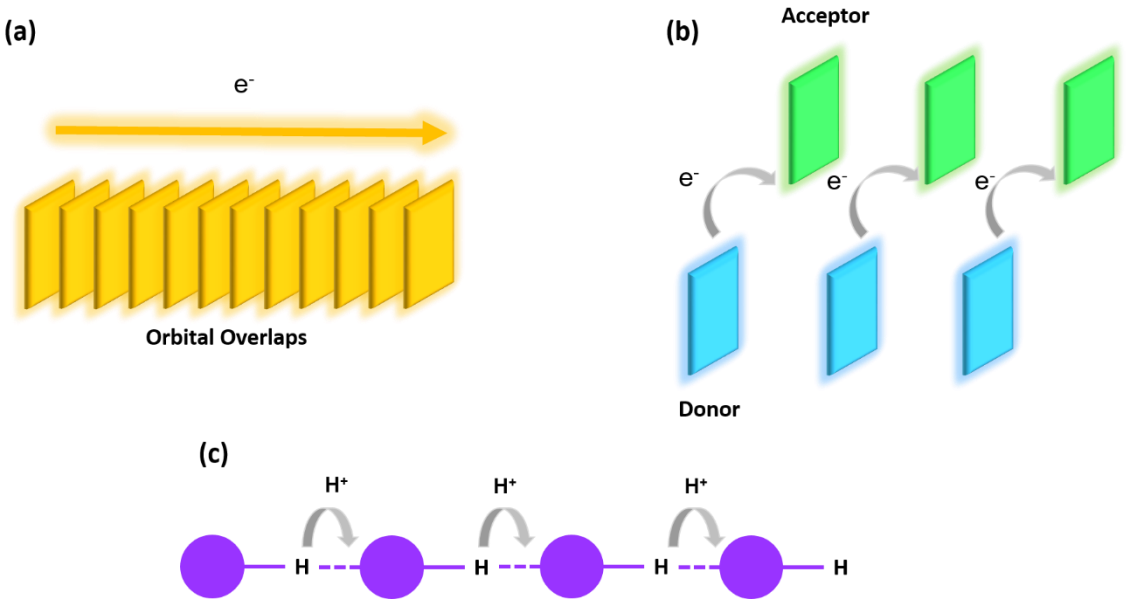

Figure I-6 Conducting mechanisms in solid state: (a) band conducting via orbital overlaps, (b) charge hopping and (c) proton-conductivity.

Interesting TCNQ-protonated heterocyclic materials with` coupled protonic and electronic conduction have been synthesized.[49-54] The protonic conductivity in such compounds is facilitated by the hydrogen bonding between co-crystallized protonated heterocyclic compounds such as benzimidazolium, 4,4'-biimidazolium and protonated 1,4-diazabicyclo[2.2.2]octane.

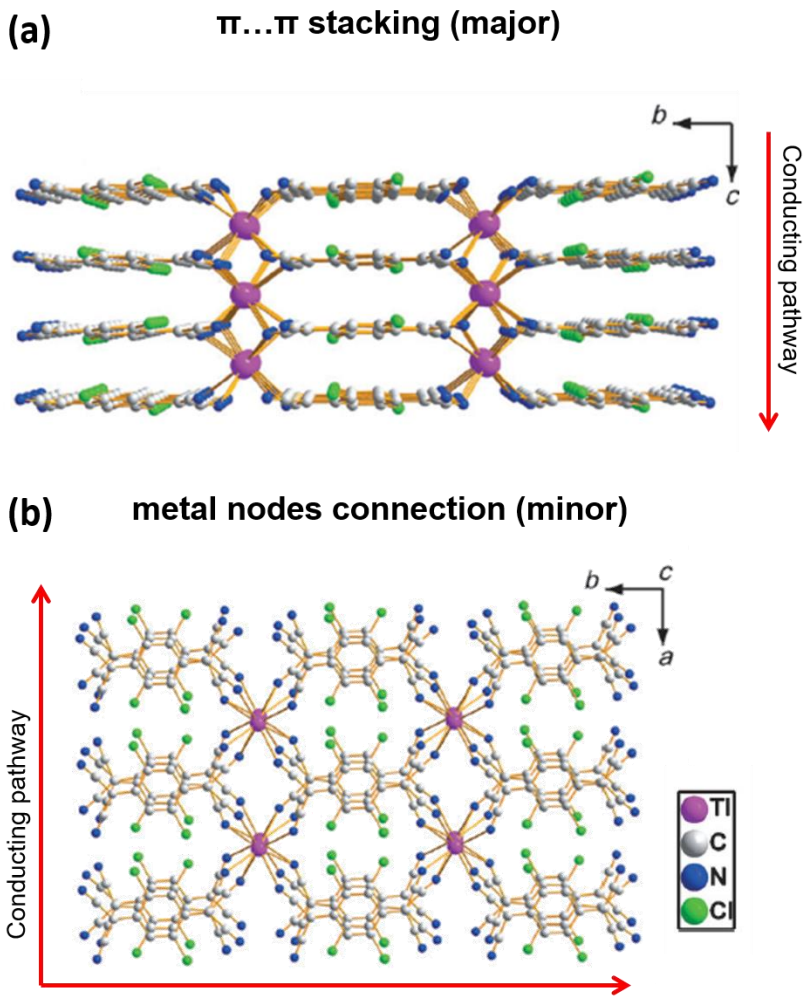

Figure I-7 Conducting pathway in $Tl(TCNQCl_2)$[46] through (a) $\pi\ldots\pi$ stacking and (b) chemical bonds. Adapted from Figure 2 in Ref. 46 with permission of John Wiley and Sons.

In addition to the protonic conducting mechanism, the other two mechanisms are highly related to the charge state of the TCNQ moieties. Single crystal X-ray diffraction and spectroscopic studies are powerful tools for charge state analysis. Since the negative charge on reduced TCNQ species, such as $TCNQ^{\cdot-}$ and $TCNQ^{2-}$, is fully delocalized on the antibonding π* orbital, the C-C bond lengths and the C-C/C-N vibration frequencies

are highly dependent on the charge state of TCNQ moieties. From the information of solid state structures, an empirical formula, developed by Kistenmacher and coworkers[55], can be used to evaluate the charge state on TCNQ molecules:

$$\rho = A\left[\frac{c}{b+d}\right] + B \qquad \textbf{Equation 1.17}$$

where ρ is the charge density on TCNQ moiety, *A* and *B* are empirical parameters which equal to -41.667 and 19.833 respectively. Variables, b, c and d, are the C-C bond lengths as indicated in Figure I-8.

Infrared spectroscopy is another powerful tool to probe the oxidation state changes of TCNQ molecules. Redshifts of C≡N stretching frequencies (ν_{CN}) and C-H bending frequencies (δ_{CH}) in the IR spectra are expected when the negative charge on TCNQ increases.[56] The ν_{CN} and δ_{CH} modes are located at 2222 and 860 cm^{-1} for neutral TCNQ and 2207, 2196, 2179 and 826 cm^{-1} for $TCNQ^{\cdot -}$ in LiTCNQ.

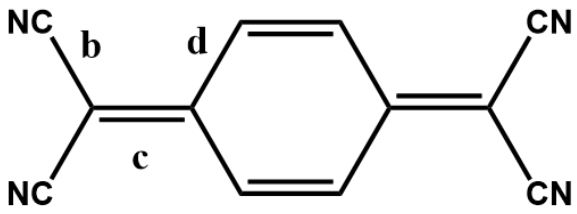

Figure I-8 Carbon-carbon bonds of TCNQ used for charge state evaluation with the Kistenmacher formula.

In the history of the development of TCNQ-based functional materials, the most well-known compound is the organic binary charge transfer compound, TTF-TCNQ which exhibits metallic conducting behavior.[57] Given this spectacular finding, a great

deal of research effort by organic and material scientists has focused on designing functional materials with TCNQ and various electron donor organic molecules such as polythiophene, pyrene and coronene.[58-59] In addition to the purely organic phases, metal-TCNQ binary compounds are also another important category of functional materials. The first example of such a material with notable electric properties is Cu^{I}(TCNQ) which was reported by Acker and Hertler in 1962.[60] In spite of the fact that this discovery occurred over a half century ago, studies of Cu(TCNQ) and other metal-TCNQ materials is still a hot topic in the field of inorganic chemistry and materials science for their numerous applications in gas sensors,[61-63] high-performance batteries,[64-67] catalysis[68-72] and conducting devices.[73-75] Compounds with higher structural complexities, such as TCNQ-based redox active metal-organic frameworks (MOFs), have also been reported over last decade. TCNQ-dianion-based porous MOFs were first developed by Kitagawa and other researchers with interesting guest-host interactions between $TCNQ^{2-}$ skeletons and encapsulated guest molecules.[76-82] Miyasaka and coworkers have carried out extensive work on classes of carboxylate-bridged diruthenium transition metal-TCNQ charge transfer compounds that exhibit interesting conducting and magnetic properties.[83-97]

The Dunbar group also has a rich tradition of research in this field. One of the benchmarks in our research is the discovery of polymorphism in Cu^{I}(TCNQ) which resolved the irreproducibility of the voltage-controlled switching behavior of Cu^{I}(TCNQ) based electronic devices.[98] Another landmark result was the discovery of a crystal-to-crystal phase transition between poorly and highly semiconducting phases in

Tl(TCNQ) metal-organic frameworks by Dr. Carolina Avendano from our group.[99] A family of transition metal-TCNQ binary compounds, $M^{II}(TCNQ)_2$ (M = Mn, Fe, Co, Ni), with magnetic ordering and semi-conductivity were prepared by Dr. Hanhua Zhao from our group during his search for cooperative magnetism and conductivity.[100] By introducing the organic bridging ligand 4,4'-bipyridine, a highly conducting coordination polymer, $\{[Mn(4,4'\text{-bpy})(^1\eta\text{-TCNQ})_2(MeOH)_2]TCNQ\}\cdot 0.5MeOH$, with a 3.8 $S\cdot cm^{-1}$ room temperature conductivity was prepared by Dr. Maria Ballesteros Rivas in the Dunbar group. This compound was the first such highly conducting metal-organic polymer of its kind and it remains a unique example of the combination of a metal-ligand backbone flanked by partially charged stacks of TCNQ radicals.[101]

More recently, our group demonstrated that, by assembling 3d-4f moieties $[(valpn)CuTb(H_2O)_4]^{2+}$ with $TCNQF^{-\cdot}$ radical anions, one can introduce conducting properties into the material and also achieve a higher energy barrier for single chain magnet (SCM) behavior compared to its $[Fe(CN)_6]^{3-}$ bridged counterpart.[102] As compared to the bulk magnetic behavior mentioned above, single molecule magnet and spin-crossover (SCO) properties which can be realized in finite molecular systems do not require long-range magnetic ordering to operate and are more promising for the miniaturization of electronic devices.[29, 103-104]

For TCNQ based conducting SMM hybrid materials, it was recently reported by our group that [Dy(TPMA)(μ-TCNQ)(μ-OH)](TCNQ)$_2$·CH$_3$CN, in which the Dy(III) is capped with the tetradentate ligand tris(2-pyridylmethyl)amine (TPMA), assembles by direct coordination of the TCNQ radical anion.[105] This compound exhibits slow relaxation of the magnetization over the temperature range of 5.0-8.0 K and semiconductivity from 180-350 K. Efforts have also been made to combine the spin-crossover moieties with TCNQ derivatives as the conducting part. The compound, [Co(terpy)$_2$](TCNQ)$_3$·MeCN, which is composed of the SCO moiety [Co(terpy)$_2$]$^{2+}$ and partially charged TCNQ layers, was crystallized and studied by Dr. Xuan Zhang in our group.[106] Synergistic effects between the SCO units and semiconducting behavior were observed which are triggered by SCO induced structural changes in the coordination sphere which perturb the solid-state packing of the TCNQ stacks. To date, there are only seven examples of semiconducting TCNQ complexes with SCO behavior reported in the literature.[107-113] Most of these compounds are based on Fe^{II} or Fe^{III} SCO moieties with the exception of one with a Mn^{III} SCO moiety[112] and two based on Co^{II} SCO moieties.[108, 110] The conductivities (σ_{300K}), activation gaps (ΔE_{gap}) and SCO transition temperatures ($T_{1/2}$) for these materials are summarized in Table I-3.

Compounds [Fe^{II}(tpma)(xbim)](ClO$_4$)(TCNQ)$_{1.5}$·DMF,[107] [Co^{II}(terpy)$_2$](TCNQ)$_3$·CH$_3$CN,[108] [Fe^{II}(HC(pz)$_3$)$_2$](TCNQ)$_3$,[109] [Co^{II}(terpy)$_2$](TCNQ)$_4$·3DMF·0.5H$_2$O[110] and [Fe^{III}sal$_2$-trien)](TCNQ)$_2$·CH$_3$OH[111] exhibit gradual SCO behavior along with semiconducting properties over the same temperature ranges. Compounds [Mn^{III}(5-Cl-sal-N-1,5,8,12)]TCNQ$_{1.5}$·2CH$_3$CN[112] and

$[Fe^{II}_2(bpypz)_2(TCNQ)_2](TCNQ)_2$ [113] exhibit SCO behavior with thermal hysteresis. The SCO temperature of the Mn^{III} compound is lower than the semiconducting region and an abrupt SCO transition in the case of $[Fe^{II}_2(bpypz)_2(TCNQ)_2](TCNQ)_2$ led to fractures in the crystals. TCNQ units in all seven compounds form segregated stacking in the solid state and the SCO moieties are not directly involved in the conducting pathway except for some TCNQ units that are directly coordinated to the SCO Fe^{II} centers in compound $[Fe^{II}_2(bpypz)_2(TCNQ)_2](TCNQ)_2$.

As the aforementioned discussion attests, results thus far have demonstrated bi-functionality of molecular magnetism and conductivity in TCNQ-coordination complexes but systematic studies of functionalities via ligand design to introduce and enhance synergistic interactions between different functionalities has not been comprehensively investigated. Given that the underlying basis for synergistic effects between different functionalities in molecular multi-functional materials is intermolecular interactions, the introduction of weak forces is key to successful realization of true multi-functionality.

Table I-3 Summary of conductivity (σ_{300K}), activation gap (ΔE_{gap}) and SCO transition temperature ($T_{1/2}$) of published SCO-semiconducting compounds with TCNQ building blocks.

Compound	σ_{300K} (S cm^{-1})	ΔE_{gap} (meV)	$T_{1/2}$ (K)
$[Fe^{II}(tpma)(xbim)](ClO_4)(TCNQ)_{1.5}\cdot DMF$[107]	0.2	110	145
$[Co^{II}(terpy)_2](TCNQ)_3\cdot CH_3CN$[108]	0.13	470	~390
$[Fe^{II}(HC(pz)_3)_2](TCNQ)_3$[109]	1.5×10^{-2}	170	445
$[Co^{II}(terpy)_2](TCNQ)_4\cdot 3DMF\cdot 0.5H_2O$[110]	3.3×10^{-4}	175	>300
$[Fe^{III}sal_2\text{-trien})](TCNQ)_2\cdot CH_3OH$[111]	1.5	50	410
$[Mn^{III}$(5-Cl-sal-N-1,5,8,12)]$TCNQ_{1.5}\cdot 2CH_3CN$[112]	1×10^{-4}	200	73/123
$[Fe^{II}_2(bpypz)_2(TCNQ)_2](TCNQ)_2$ [113]	7.4×10^{-2}	57	337/339

Supramolecular Interactions in Multifunctional Materials

Supramolecular interactions are a category of non-covalent interactions such as van de Waals force, hydrogen bonding, π···π interactions, electrostatic interactions and charge transfer interactions.[114-115] Although they are not as strong as covalent bonding, these secondary interactions are critical in determining the structural and functional diversities in biological systems such as secondary/tertiary/quaternary proteins[116] and nucleic acid structures.[117] Apart from the natural existing molecules, supramolecular interactions are also essential in artificial molecular machines.[118] The Nobel Prize in Chemistry for 2016 was awarded to Jean-Pierre Sauvage, Sir J. Fraser Stoddart and

Bernard L. Feringa for "their design and production of molecular machines." The supramolecular interactions not only enable the self-assembly of these molecular machines but also control of nanoscale dynamics.

In the quest for multifunctional materials with synergistic interactions between different properties, it is crucial to understand that supramolecular interactions are key elements for enhancing interactions between different functional moieties. As discussed in prior sections, TCNQ and its derivatives have the potential to engage in a wide range of supramolecular interactions including π···π stacking, electrostatic interactions, charge transfer and coordination bonding (Figure I-9). [119] As such, the main goal of the research in this dissertation is to design magnetic moieties whose properties are engaged in an interplay with TCNQ radicals through these supramolecular interactions. The compound $[Co^{II}(terpy)_2](TCNQ)_3 \cdot CH_3CN$[108] studied by our group is a good starting point for modification of the SCO moiety, $[Co^{II}(terpy)_2]^{2+}$, in order to engender stronger interactions with TCNQ moieties which is the main strategy for the work described in this dissertation.

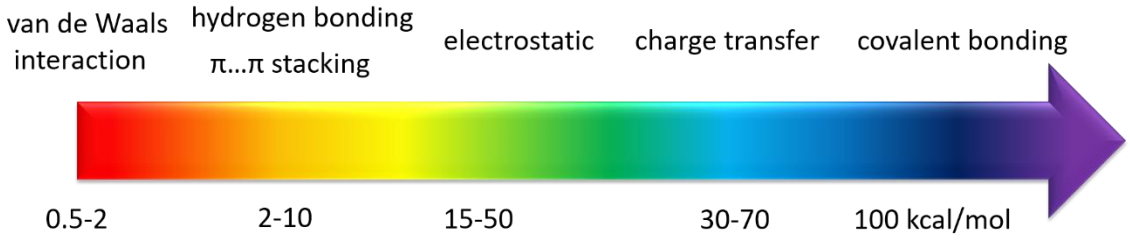

Figure I-9 Energy scales of supramolecular interactions. Adapted from Fig. 8 in Ref. 119. with permission of The Royal Society of Chemistry.

By modifying the substituents on the terpyridine ligand, the solid state structure of SCO-TCNQ assemblies can be tuned such that one can obtain segregated stacking of TCNQ units as well as mixed-stacking between TCNQ moieties and pendant groups on SCO moieties if the supramolecular interactions between TCNQ and the pendant groups are stronger than the inter-TCNQ interactions. The possible structural modifications of SCO – TCNQ multifunctional materials are depicted in Figure I-10. Although the mixed-stacking structure may lower the conductivity of the material to some extent, the direct involvement of the SCO moieties in the conducting pathway is expected to introduce a stronger synergistic interaction between different functionalities and result in novel physical properties.

With these objectives in mind, research presented in this dissertation describes the syntheses and structure-function studies of new materials that explore how intermolecular interactions can be used to tune magnetic properties and lead to synergistic interactions between functionalities. In Chapter II, mechanisms of how two different molecular bistabilities, SMM and SCO properties, can be achieved with the same cationic moiety by introducing supramolecular interactions between the pendant groups on magnetic cationic moieties and organocyanide anions are presented. Chapter III describes the synthesis of a novel charge transfer complex with an SCO induced electron transfer phenomenon in the solid state. Detailed structure-function relationships revealed a synergistic effect between SCO and switching of semiconducting behavior. The results in Chapter IV describe the effect of installing SMM molecules in a mesoporous metal-organic framework as a promising method for suppressing magnetic

relaxation by minimizing magnetic interactions between magnetic centers. The overall conclusions and future outlooks are discussed in Chapter V.

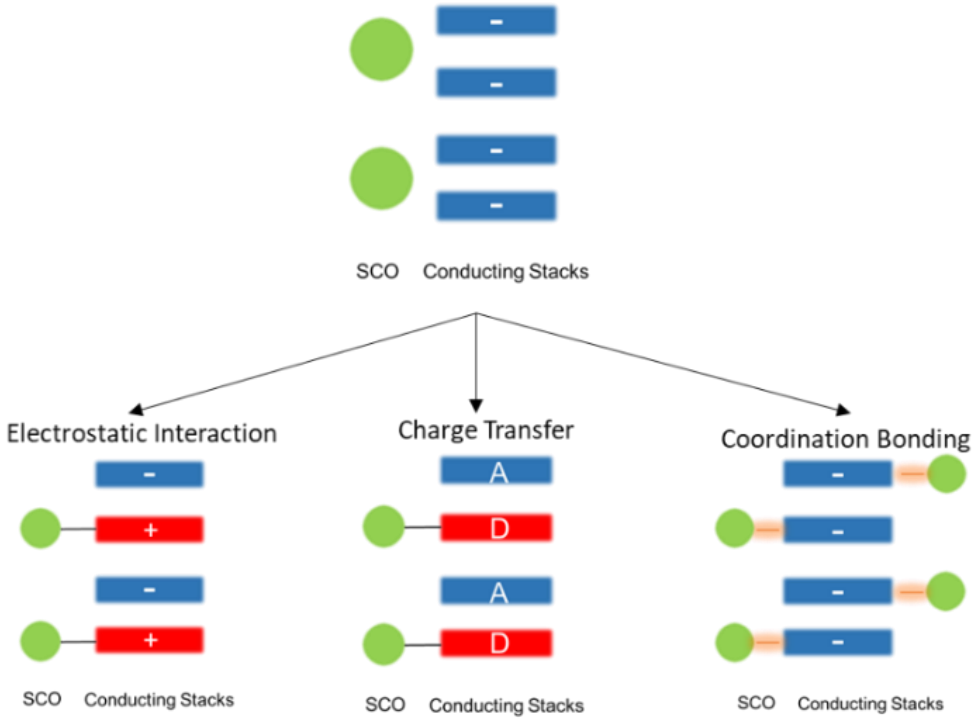

Figure I-10 Solid-state structural modifications of SCO – TCNQ multifunctional materials

CHAPTER II

TUNING MAGNETIC PROPERTIES OF COBALT (II) BIS-FERROCENYLTERPY CATIONS VIA SUPRAMOLECULAR INTERACTIONS WITH ORGANOCYANIDE RADICAL ANIONS*

Introduction

Molecule-based materials that exhibit magnetic bistability are promising candidates for the design of new generations of electronic and magnetic devices, two important categories of which are spin-crossover (SCO) compounds[120-122] and single-molecule magnets (SMM).[123-126] The up/down spin states or the differences in magnetic moments between high-spin states and low-spin states provide the basic units for data storage and/or quantum computing.

Supramolecular interactions are well known for their capacity to tune SCO[127-129] and SMM[130-135] behavior. Our particular interest is the study of supramolecular interactions of Co(II) SCO moieties with anions and solvent molecules.[17, 136] In general, the low-spin (L.S.) Co^{II} state is favored as the ground state in bis(terpy) derivatives due to the strong ligand field of the terpyridine ligand.[137-139] The SCO phenomenon in $[Co^{II}(terpy)_2]^{2+}$ cations can be mediated by geometric restrictions and supramolecular interactions, the effects of which lower the energy gap between H.S. and L.S. states. In addition to these intrinsic effects in the solid state, there are several rare examples of

* "From spin-crossover to single molecule magnetism: tuning magnetic properties of Co(II) bis-ferrocenylterpy cations *via* supramolecular interactions with organocyanide radical anions" H. Xie, K. R. Vignesh, X. Zhang and K. R. Dunbar, *J. Mater. Chem. C*, 2020, **8**, 8135 **DOI:** 10.1039/D0TC00830C- Reproduced by permission of The Royal Society of Chemistry.

compounds with either SCO or SMM properties whose properties can be inter-converted via ligand or crystal field modifications or light irradiation.[139-146] Recently, Wang and co-workers reported that the presence or absence of water molecules in the interstices of a crystal triggers a single-crystal to single-crystal transition that induces a switching between SCO and SMM behavior.[147] These interesting findings notwithstanding, difficulties in predicting the position and intermolecular interactions of solvents in a crystal renders this approach untenable for the rational design of materials with tunable properties.

The introduction of supramolecular interactions between magnetic cations and counter anions constitutes a more promising strategy than random packing of solvent molecules for tuning solid-state structures and magnetic functionalities. Recently, Hayami and coworkers[129] achieved tuning of the SCO behavior of the $[Fe^{II}(qnal)_2]^+$ cation by introducing aromatic counterions, but structure-function relationships were not possible given that larger conjugated aromatic anions altered not only the π···π interactions between the anion and the SCO metal cation but also the overall geometric parameters.

In the current study, the co-crystallization of $[Co^{II}(Fctp)_2]^{2+}$ cations (Fctp = 4'-ferrocenyl-2,2':6',2''-terpyridine) that contain redox-active pendant ferrocenyl groups with $TCNQ^-$ and $TCNQF^-$ radical anions (TCNQ = 7,7,8,8-tetracyanoquinodimethane, TCπNQF = 2-fluoro-7,7,8,8-tetracyanoquinodimethane) led to the isolation of supramolecular assemblies of the magnetic cations and the tunable organocyanide anions. The introduction of the ferrocenyl pendant group changes the solid state

architecture, with respect to the geometry of the cation moiety and introduces π···π interactions between the ferrocenyl and TCNQ/TCNQF moieties. The advantages of introducing $TCNQ^{\cdot-}$ or $TCNQF^{\cdot-}$ are (1) π-conjugation enables π···π interactions with cationic moieties that contain aromatic groups; (2) the fluorine substituent on $TCNQF^{\cdot-}$ tunes the frontier orbital energies as well as its electron accepting ability and introduces a dipole moment which engenders dipole-dipole interactions and (3) similar van der Waals radii of fluorine (1.47 Å) and hydrogen atoms (1.20 Å)[148-150] allows for the preservation of the solid state structure with minimum perturbations form steric effects. The three compounds $[Co^{II}(Fctp)_2](TCNQ)_2$ (**1**), $[Co^{II}(Fctp)_2](TCNQ)_2 \cdot MeCN$, (**2**), and $[Co^{II}(Fctp)_2](TCNQF)_2 \cdot MeCN$, (**3**), were obtained as crystals from co-crystallization of $[Co^{II}(Fctp)_2]^{2+}$ cations with $TCNQ^{\cdot-}$ and $TCNQF^{\cdot-}$ radical anions. The paramagnetic moiety, $[Co^{II}(Fctp)_2]^{2+}$, in **1** exhibits SMM behavior under an applied field whereas the isomorphs **2** and **3** exhibit non-identical SCO behavior. Structural, magnetic and computational studies were performed to probe the structure-property relationships in the solid state.

Experimental Section

Synthetic Procedures

LiTCNQ[151] and LiTCNQF[152-153] salts were prepared according to reported methods. All experiments were performed under a N_2 atmosphere. Solvents were purified by distillation under N_2.

Synthesis of the Fctp Ligand

The synthesis of Fctp has been reported in the literature.[154] A modified one-pot synthesis was used for the ligand synthesis.[155] A quantity of NaOH (0.8 g, 20 mmol) was suspended in 15 mL of Polyethylene Glycol 300 at 0 ℃ and 2-acetylpyridine (2.42 g, 20 mmol) was added at 0 ℃ with stirring for 10 minutes after which time 10-methyl-3-formylphenothiazine (2.41 g, 10mmol) was added to form a dark red solution. Stirring at 0 ℃ was continued for an additional 2 hours after which time the temperature was gradually increased to room temperature. An aliquot of $NH_3 \cdot H_2O$ (30%, 30 mL) was added and the mixture was refluxed for 12 hours. After the solution had cooled to room temperature, 50 mL of water was added and the resulting yellow-brown precipitate was collected by filtration, washed with 50 mL of hot ethanol and dried in air. The yield was 1.27 g (2.8 mmol, 28%) of orange powder. ^{1}H-NMR (300 MHz, $CDCl_3$): δ (in ppm) 8.75 (d, 2H), 8.66 (dt, 2H), 8.52 (d, 2H), 7.88 (td, 2H), 7.36 (ddd, 2H), 5.02 (t, 2H), 4.47 (t, 2H), 4.10 (s, 5H). IR (KBr, cm^{-1}): 1602.9 (s), 1581.6 (s), 1566.2 (m), 1548.8 (m), 1465.9(s), 1408.0 (s), 1386.8 (m), 1103.3 (m), 819.7 (s), 800.5 (s), 787.0 (s), 731.0 (s), 669.3 (s), 657.7 (m), 621.1 (m).

Synthesis of $[Co^{II}(Fctp)_2](PF_6)_2$

The salt $[Co^{II}(Fctp)_2](PF_6)_2$ was prepared by a modified literature method.[154] A sample of $Co(OAc)_2 \cdot 4H_2O$ (0.5 mmol, 125 mg) was dissolved in 5 mL of methanol and Fctp (1 mmol, 419 mg) in 4 mL $CHCl_3$ was added gradually which led to the formation of a dark purple solution. The mixture was stirred at room temperature for 30 minutes and 508 mg of a dark purple powder was obtained by adding an aqueous solution of

KPF_6 (278 mg in 10 mL H_2O). The product was collected and dried in air; 85.3% yield. IR (KBr, cm^{-1}): 1610.6(m), 1543.0 (m), 1496.8 (m), 1471.7 (m), 1433.1 (m), 1251.8 (m), 1107.1 (m), 1031.9 (m), 829.4 (vs), 790.8 (s), 746.5 (m), 671.2 (m), 655.8 (m).

Synthesis of $[Co^{II}(Fctp)_2](TCNQ)_2 \cdot MeCN$

The salts $[Co^{II}(Fctp)_2](PF_6)_2$(0.05 mmol, 59 mg) and LiTCNQ(0.1 mmol, 21 mg) were separately dissolved in 5 mL of MeCN/MeOH (1:1, v/v). The two solutions were layered in a 20 mL test tube for one week. During this time, two distinct phases of crystals formed with different colors and morphologies. A manual separation of the two phases gave 23 mg of purple block crystals (**1**, $[Co^{II}(Fctp)_2](TCNQ)_2$) and 8 mg of intensely coloured blue platelets (**2**, $[Co^{II}(Fctp)_2](TCNQ)_2 \cdot MeCN$). IR of **1** (KBr, cm^{-1}): 3097.7 (w), 2169.9 (s), 2148.7 (s), 1583.6 (s), 1543.0 (m), 1504.5 (s), 1471.7 (m), 1433.1 (s), 1350.2 (s), 1176.6 (s), 1012.6 (m), 825.5 (s), 787.0 (s). Elemental analysis of **1**: calculated (%): C (68.27), H (3.56), N (15.06); found: C (67.99), H (3.55), N (15.15). IR of **2** (KBr, cm^{-1}): 3076.5 (w), 2173.8 (s), 2150.6 (s), 1602.8 (m), 1568.1 (s), 1504.5 (s), 1433.1 (m), 1361.7 (s), 1170.8 (s), 1004.9 (m), 825.5 (s), 788.9 (s), 746.4 (m), 669.3 (m), 574.8 (m). Elemental analysis of **2**: calculated (%): C (67.69), H (3.68), N (15.65); found: C (67.71), H (3.74), N (15.53).

Synthesis of $[Co^{II}(Fctp)_2](TCNQF)_2 \cdot MeCN$

Samples of $[Co^{II}(Fctp)_2](PF_6)_2$(0.05 mmol, 59 mg) and LiTCNQF(0.1 mmol, 23 mg) were dissolved in 5 mL of MeCN/MeOH(1:1, v/v) and layered in a 20 mL test tube for one week. A 32 mg quantity of a pure phase in the form of intensely coloured blue platelet crystals (**3**, $[Co^{II}(Fctp)_2](TCNQF)_2 \cdot MeCN$) were obtained. IR (KBr, cm^{-1}):

3078.4 (w), 2179.6 (s), 2160.3 (s), 1599.0 (s), 1570.0 (m), 1543.0 (m), 1494.8 (s), 1433.1 (m), 1381.0 (s), 1357.9 (s), 1253.7 (m), 1188.2 (m), 1016.5 (m), 825.5(m), 788.9 (s), 746.4 (m), 729.1 (m), 669.3 (m), 574.8 (m). Elemental analysis: calculated (%): C (66.20), H (3.44), N (15.24); found: C (66.08), H (3.40), N (15.15).

Synthesis of $[Zn^{II}(Fctp)_2](PF_6)_2$

The salt $[Zn^{II}(Fctp)_2](PF_6)_2$ was prepared by a modified literature method.[154] A sample of $Zn(OAc)_2 \cdot 4H_2O$ (0.25 mmol, 64 mg) was dissolved in 5 mL of methanol and Fctp (0.5 mmol, 209.5 mg) dissolved in 4 mL of $CHCl_3$ was gradually added which led to the formation of a dark purple solution. The mixture was stirred at room temperature for 30 minutes and 250 mg of a dark purple powder was obtained by adding an aqueous solution of KPF_6 (278 mg in 10 mL H_2O) which was collected and dried in air; 80 % yield. IR (KBr, cm^{-1}): 1612.5(m), 1600.9(m), 1572.0(m), 1548.8 (m), 1473.6 (m), 1431.2 (m), 1252.6 (m), 1030.0 (m), 1014.6 (m), 825.2 (vs), 792.7 (s), 767.7 (m), 671.2 (m), 655.8 (m), 555.5(m).

Synthesis of $[Zn^{II}(Fctp)_2](TCNQ)_2$

The salts $[Zn^{II}(Fctp)_2](PF_6)_2$(0.05 mmol, 60 mg) and LiTCNQ (0.1 mmol, 21 mg) were separately dissolved in 5 mL of MeCN/MeOH (1:1, v/v). The two solutions were layered in a 20 mL test tube for one week. A pure phase of dark block purple crystals that had formed during this period were filtered to give 25 mg of purple block crystals (**1'**, $[Zn^{II}(Fctp)_2](TCNQ)_2$) IR of **1'** (KBr, cm^{-1}): 3090.7 (w), 2164.9 (s), 2145.6 (s), 1610.5 (s), 1600.9 (s), 1572.0 (s), 1548.8 (m), 1501.3 (s), 1473.6 (m), 1431.2 (s), 1352.2 (s), 1252.7 (m), 1164.9 (m), 1030.0 (m), 1012.6 (m), 827.5 (s), 790.8 (s), 555.5(s).

Elemental analysis of **1'**: calculated (%): C (67.93), H (3.54), N (14.98); found: C (67.73), H (3.56), N (15.01).

Single Crystal X-ray Crystallography

Single-crystal diffraction data of **1** were collected at 100 K with the synchrotron radiation source (λ=0.41328 Å) at the ChemMatCars beamline 15-ID-B at the Advanced Photon Source (APS), Argonne National Laboratories. Crystals of **2** and **3** were collected at 120 K on a Bruker D8 Quest diffractometer equipped with a microfocus MoKα radiation source (λ=0.71073 Å) with an Iμs CMOS detector. The data sets were recorded by the φ-scan and ω-scan methods and integrated with Bruker APEX 3 software package. Absorption corrections were performed in the SADABS-2016/2 (Bruker, 2016/2) package. Solution and refinement of the crystal structures was carried out using the SHELXT[156] and SHELXL[157] programs and the graphical interface Olex2.[158]

Powder X-ray Diffraction

Powder X-ray diffraction data were collected on a Bruker D8 powder X-ray diffractometer at room temperature with Cu X-ray radiation to verify the phase purity of the bulk products. Powder diffraction patterns were simulated from single-crystal X-ray structural data by using Mercury CSD 2.0.

Magnetic Measurements

A Quantum Design MOMS-XL SQUID instrument was used for magnetic measurements over the temperature range of 1.8-300 K and in the field range of 0-7 T. The ac measurements were performed with a 2 Oe measuring field with frequencies

from 1 to 1000 Hz. The diamagnetic contributions of sample holders and diamagnetic contributions of atoms were corrected by using a calibrated empty sample holder and Pascal's constants.

Computational Details

Ab initio CASSCF (Complete Active Space Self-Consistent Field) calculations were performed to compute the ZFS (*D*) of the Co^{II}, ion for **1** using the ORCA 3.0 suite of programs.[159] The BP86 functionals were employed along with scalar relativistic ZORA Hamiltonians and ZORA-def2-TZVP basis sets for the metal ions and the first coordination sphere and def2-SVP was used for the remainder of the atoms. The RI approximation with secondary TZV/J Columbic fitting basis sets were used along with increased integration grids (Grid 5 in ORCA convention). The tight SCF convergence was used throughout the calculations ($1x10^{-8}$ Eh). The SOC contributions in the *ab initio* framework were obtained using second-order perturbation theory as well as by employing the effective Hamiltonian approach which enables calculations of all matrix elements to be made numerically with the anisotropic spin Hamiltonian from the *ab initio* energies and wave functions. The state average-CASSCF (Complete Active Space Self-Consistent Field) method was used to compute the ZFS. The active space comprises seven active electrons in five active d-orbitals (d^7 system; CAS (7,5)) for the Co^{II} ion. With this active space, 10 quartet and 40 doublet states were computed for the Co^{II} ion by the configuration interaction procedure. [160] In order to understand the SCO behavior of **2**, calculations were performed using the TPSSh functional[161-162] with Alhrich[163-164] triple- ζ basis set as implemented in the Gaussian 09 suite of programs. The d-orbital

ordering was plotted using 'LOEWDIN-energies' from the ORCA output that contains each root contribution and the corresponding electronic arrangement along with their plausible transition energies. The Effective Hamiltonian from the CASSCF calculation provides the calculated D and E parameters with their "Individual contribution to the D-tensor". For each contribution, the program predicts the plausible transition energies between the d-orbitals and those D values compared with the LOEWDIN energies.

DFT calculations were performed to investigate the intermolecular interactions between $[Co^{II}(Fctp)]^{2+}$ and $(TCNQ)_2^{2-}$/$(TCNQF)_2^{2-}$ using the Gaussian 09 program.[165] A long-range corrected functional with dispersion corrections, ωB97x-D,[166] was employed for the single point energy calculation with cc-pVTZ basis sets for metal ions and 6-311++G** basis sets for the other atoms.

Results and Discussion

X-ray Crystallographic Studies

For the reaction between $[Co^{II}(Fctp)_2](PF_6)_2$ and LiTCNQ, two types of pseudo-polymorphic products with different colors and morphologies, **1** and **2**, were obtained. The major product is the purple block phase **1** ($[Co^{II}(Fctp)_2]$ $(TCNQ)_2$, phase-I) and the minor one is the dark blue platelet phase of **2,** ($[Co^{II}(Fctp)_2]$ $(TCNQ)_2 \cdot MeCN$, phase-II). The structures of **1** (at 100 K) and **2** (at 120 K) were elucidated by single-crystal X-ray diffraction methods (Figure II-1 (a) and (b), Table II-1). The Co(II) ions in both phases are six-coordinate with nitrogen atoms from two Fctp ligands, but the Co-N distances are significantly different in **1** and **2** as evidenced by the data compiled in Table II-2. In phase **1**, the cobalt center is in a compressed octahedral geometry and exhibits relatively

long, and nearly equal, axial Co1-N1 (2.045(2) Å) and Co1-N2 (2.054(2) Å) distances which fall into the range of high-spin Co^{II} species.[139] In contrast, the phase-II structure exhibits shorter axial Co-N bond distances of 1.877(2) Å for Co1-N1 and 1.936(2) Å for Co1-N2, an indication that the Co(II) center is in the low-spin state. [136, 139, 167] Continuous shape measure (CShMs) analysis was performed with SHAPE 2.1[168] and the results are summarized in Table II-3. The smallest deviation values for Co(II) centers in **1** (5.283) and **2** (2.771)**,** are found for the octahedral geometry. Compound **1** exhibits a larger deviation from the octahedral geometry than **2**, which is in accord with reported values of high-spin and SCO Co(II)-bis(terpy) compounds.[147]

A single crystal phase, $[Co^{II}(Fctp)_2](TCNQF)_2 \cdot MeCN$ phase-II (**3**), was obtained when the reaction was performed with LiTCNQF. Compounds **2** and **3** are isomorphs as evidenced by the unit cell dimensions and contents (at 120 K, Table II-1, Figure II-2). The Co-N bond distances in **3** slightly deviate from the ones in **2** but all are within the range for L.S. Co(II) compounds. The fluorine substituent on $TCNQF^{\cdot -}$ in **3** disordered and was modeled with partial occupancies that sum to 1 for each $TCNQF^{\cdot -}$ asymmetric unit.

Supramolecular interactions, especially π…π contacts, play an important role in organizing the solid-state structures of the new materials. In the case of **1**, the interplanar distance for the two distinct $TCNQ^{\cdot-}$ radicals is 2.911 Å in **1** (Figure II-3 (a)), much shorter than the sum of the van der Waals radii of two carbon atoms (3.40 Å). This short contact is an indication that the $TCNQ^{\cdot-}$ radical anion pairs exist as antiferromagnetically coupled π-dimers[169] which is also confirmed by the magnetic measurements of the Zinc analog (**1'**) of **1**. The ferrocenyl group also engages in a short contact (3.108 Å) with a $TCNQ^{\cdot-}$ radical anion which serves to constrain the geometry of the $[Co^{II}(Fctp)_2]^{2+}$ cation. Two other short contacts that involve pyridyl groups on the Fctp ligand are also observed with relatively longer distances (3.316 Å for ferrocenyl…pyridyl and 3.402 Å for TCNQ…pyridyl). (Figure II-3 (a)) These short contacts propagate a one-dimensional chain along the **a** axis of the unit cell (Figure II-3 (b)).

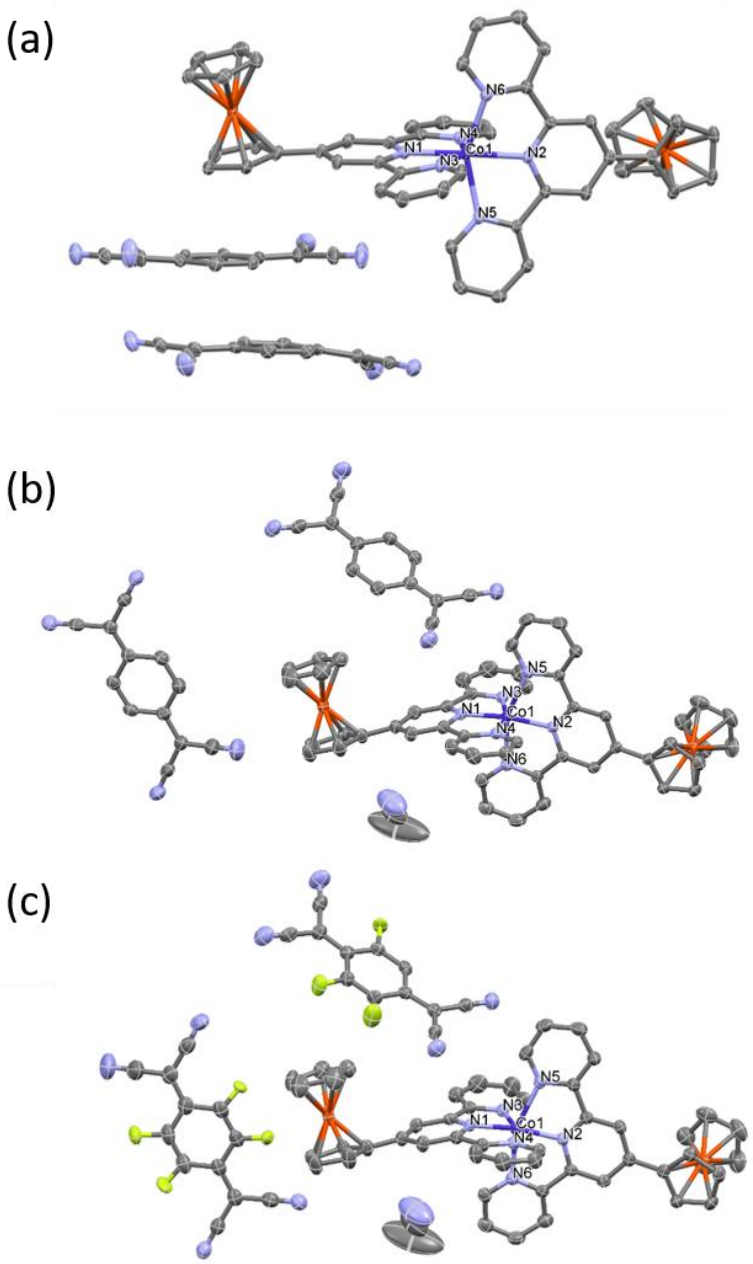

Figure II-1 The asymmetric units in the crystal structures of (a) $[Co^{II}(Fctp)_2](TCNQ)_2$ (1), (b) $[Co^{II}(Fctp)_2](TCNQ)_2 \cdot MeCN$ (2) and (c) $[Co^{II}(Fctp)_2](TCNQF)_2 \cdot MeCN$ (3) with thermal ellipsoids drawn at the 70% probability level. The fluorine atoms are disordered in TCNQF and the hydrogen atoms are omitted for the sake of clarity. Color code: carbon: grey; nitrogen: blue; cobalt: purple; iron: orange; fluorine: yellow.

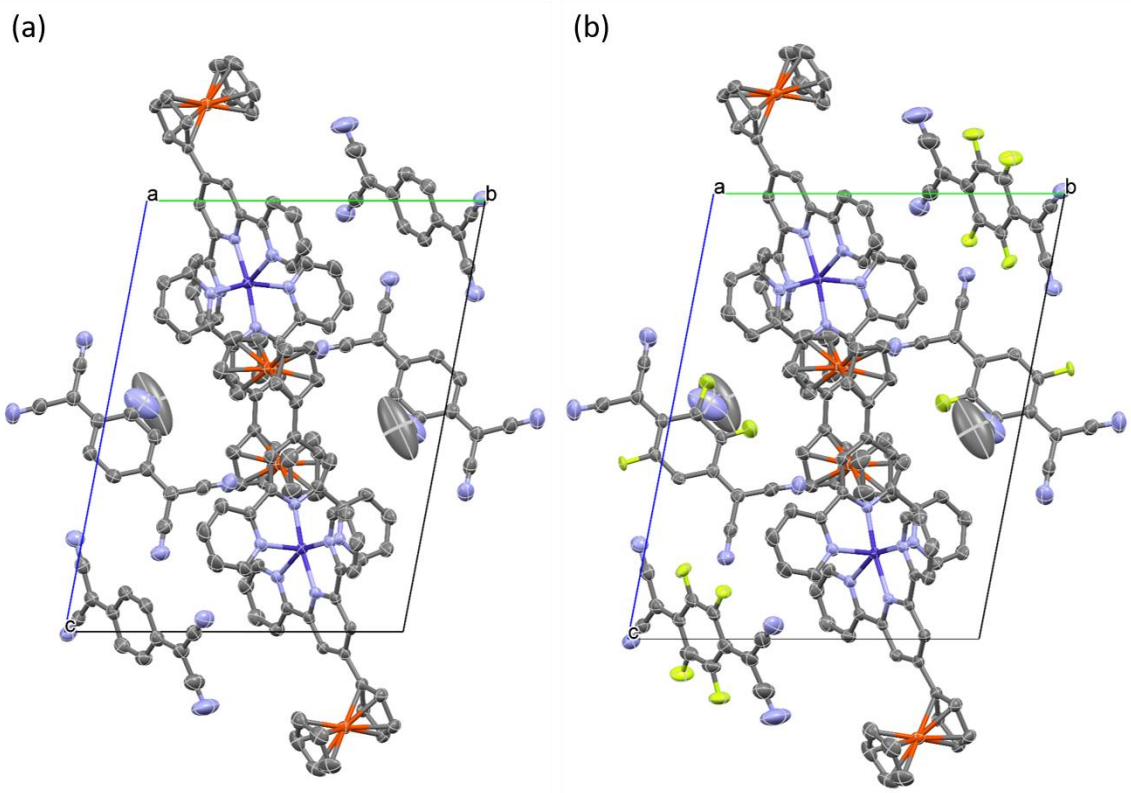

Figure II-2 Views along the *a* crystal axis of (a) 2 and (b) 3. The crystal origins of 3 were reset to the same position as 2 by a (1/2, 1/2, 1/2) translation. Hydrogen atoms were omitted for the sake of clarity. Color code: carbon: grey; nitrogen: blue; cobalt: purple; iron: orange; fluorine: yellow.

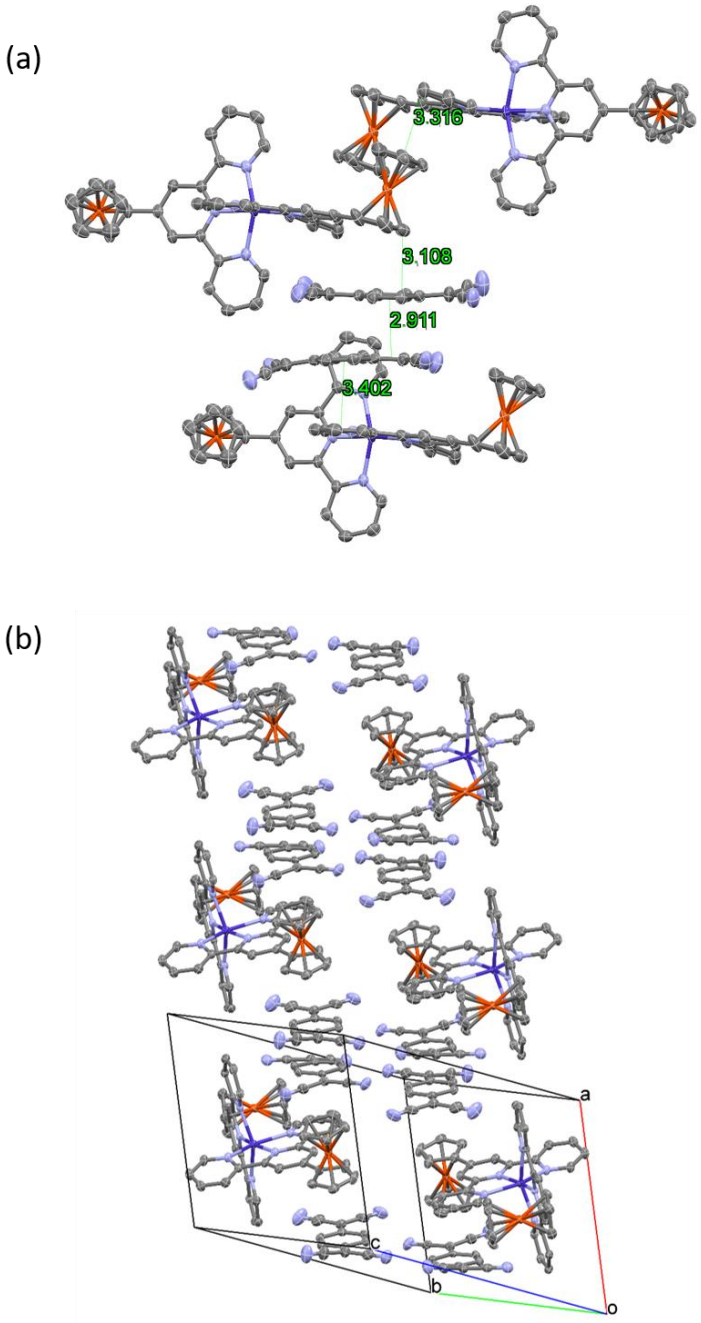

Figure II-3 a) Short contacts of TCNQ, pyridyl and ferrocenyl groups involved in intermolecular interactions in 1. (b) The packing assemblies of 1 along the *a* axis of the unit cell with intermolecular interactions. Hydrogen atoms were omitted for the sake of clarity. Color code: carbon: grey; nitrogen: blue; cobalt: purple; iron: orange.

Table II-1 Crystallographic and refinement parameters for [Co(FcTp)](TCNQ)$_2$ compounds.

Compound	**1**	**1'**	**2**	**3**
Empirical formula	C74H46CoFe2N14	C74H46 ZnFe2N14	C76H49CoFe2N15	C76H47CoF2Fe2N15
Formula weight	1301.88	1308.32	1342.93	1378.91
Temperature/K	100	110	120	120
Crystal system	triclinic	triclinic	triclinic	triclinic
Space group	P-1	P-1	P-1	P-1
a/Å	12.0595(5)	12.0572(3)	12.2917(3)	12.2558(5)
b/Å	12.6422(5)	12.6478(3)	15.1866(4)	15.3186(6)
c/Å	19.9814(8)	20.0264(5)	18.3369(4)	18.3379(7)
α/°	88.0990(10)	88.1340(10)	95.632(2)	96.059(2)
β/°	84.1870(10)	83.998(2)	100.2620(10)	99.428(2)
γ/°	71.5970(10)	71.4820(10)	113.4630(10)	113.636(2)
Volume/Å3	2875.7(2)	2879.97(12)	3035.00(13)	3055.0(2)
Z	2	2	2	2
ρcalcg/cm3	1.504	1.509	1.47	1.499
μ/mm-1	0.192	0.972	0.803	0.805
F(000)	1334	1340.0	1378	1410
Crystal size/mm3	0.053 × 0.045 × 0.04	0.2 × 0.15 × 0.1	0.2 × 0.1 × 0.02	0.15 × 0.14 × 0.06
Radiation	Synchrotron (λ= 0.41328)	MoKα (λ = 0.71073)	MoKα (λ = 0.71073)	MoKα (λ = 0.71073)
2Θ range for data collection/°	2.296 to 34.2820.	3.942 to 55.044	4.132 to 55.042	4.146 to 55.118
Index ranges	-17 ≤ h ≤ 16, -18 ≤ k ≤ 13, -28 ≤ l ≤ 28= 0.06	15 ≤ h ≤ 15, -16 ≤ k ≤ 16, -26 ≤ l ≤ 26	-15 ≤ h ≤ 15, -19 ≤ k ≤ 19, -23 ≤ l ≤ 23	-15 ≤ h ≤ 15, -19 ≤ k ≤ 19, -23 ≤ l ≤ 23
Reflections collected	56557	67792	106824	121984
Independent reflections	16730 [Rint = 0.0648, Rsigma = 0.0676]	13233 [R_{int} = 0.0614, R_{sigma} = 0.0414]	13900 [Rint = 0.0631, Rsigma = 0.0320]	14000 [Rint = 0.1183, Rsigma = 0.0571]
Data/restraints /parameters	16730/0/820	13233/0/820	13900/0/848	14000/0/911
Goodness-of-fit on F2	1.008	1.082	1.1	1.044
Final R indexes [I>=2σ (I)]	R_1 = 0.0398, wR_2 = 0.0889=	R_1 = 0.0344, wR_2 = 0.0729	R_1 = 0.0438, wR2 = 0.1072	R_1 = 0.0453, wR_2 = 0.1055
Final R indexes [all data]	R_1 = 0.0645, wR_2 = 0.0972	R_1 = 0.0344, wR_2 = 0.0729	R_1 = 0.0547, wR2 = 0.1131	R_1 = 0.0598, wR_2 = 0.1135
Largest diff. peak/hole / e Å-3	0.41/-0.51	0.49/-0.53	1.43/-0.80	0.68/-0.74

$R_1 = \Sigma(||F_0| - |F_C||)/\Sigma|F_0|$. $wR_2 = [\Sigma w(|F_0|^2 - |F_C|^2)^2/(\Sigma w|F_0|^2)^2]^{1/2}$. $w = 0.75/(\sigma^2(F_o) + 0.00010\,F_o)$. Goodness-of-fit = $\{\sum [w(F_o^2 - F_c^2)^2]/(n-p)\}^{1/2}$, where n is the number of reflections and p is the total number of parameters refined.

Table II-2 Co-N bond distances in 1 (100 K), 2 (120 K) and 3 (120 K).

Bond length/Å	**1**([Co^{II}(Fctp)$_2$] (TCNQ)$_2$)	**2**([Co^{II}(Fctp)$_2$] (TCNQ)$_2$·MeCN)	**3**([Co^{II}(Fctp)$_2$] (TCNQF)$_2$·MeCN)
Co1-N1	2.045 (2)	1.877(2)	1.873(2)
Co1-N2	2.054 (2)	1.936(2)	1.944(2)
Co1-N3	2.195(2)	1.987(2)	1.978(2)
Co1-N4	2.161 (2)	1.998(2)	1.990(2)
Co1-N5	2.153(2)	2.157(2)	2.162(2)
Co1-N6	2.155(2)	2.136(2)	2.138(2)

Table II-3 Continuous shape measure analysis results from SHAPE v2.10

Symmetry	Shape	Deviation value (CShMs)			
		1	**1'**	**2**	**3**
D6h	Hexagon	33.793	33.603	32.841	32.642
C5v	Pentagonal pyramid	17.461	18.037	21.455	21.16
Oh	**Octahedron**	**5.283**	**5.413**	**2.771**	**2.819**
D3h	Trigonal prism	7.504	7.794	10.037	9.968
C5v	Johnson pentagonal pyramid J2	21.636	22.23	25.221	24.894

Magnetic Properties

Temperature-dependent magnetic susceptibility measurements of **1**, **1'**, **2** and **3** were performed under a 0.1 T DC field over the temperature range of 1.8-300 K. The phase purities of **1**, **1'**, **2** and **3** (Figure II-4) were verified by powder X-ray diffraction. The isomorphic zinc analog (**1'**) of **1** was synthesized and characterized to evaluate the magnetic contribution from $TCNQ^{\cdot-}$. The magnetic susceptibility and magnetization measurements of **1'** (Figure II-5) indicate that the sample is almost diamagnetic. χT vs T plot shows only a small temperature-independent paramagnetism (4.5×10^{-4} emu mol^{-1}). The magnetization at 2K is only ~0.017 μ_B at 7T which demonstrates the diamagnetic nature of the $(TCNQ)_2^{2-}$ dimer in the phase-I structure which corresponds well with results reported in the literature.[170]

The room temperature χT value of **1** is 3.00 emu K mol^{-1} which is higher than the expected value for a spin-only $S = 3/2$ (1.88 emu K mol^{-1}) ion due to spin-orbit coupling. The decrease of χT value at low temperature is attributed to zero-field splitting effects. Magnetization data at 1.8 K and reduced magnetization data from 1.8 to 5 K were also collected (Figure II-6 (b)). The Hamiltonian in Equation 1.3 was used to simultaneously fit the temperature-dependent (Figure II-6 (a)) and field-dependent (Figure II-6 (b) and (c)) static magnetic susceptibility data. The best fit gives D = -57.0 cm^{-1}, E = -17.9 cm^{-1}, g_x = 2.07, g_y = 2.20 and g_z = 3.06. The D value from the fitting was comparable to the reported value for high-spin Co(II) bis-terpyridine compounds.[147] A reasonable unique fit was obtained by using these parameters; the shapes of field-dependent magnetization curves indicate strong dependence on the anisotropy of $\boldsymbol{g}$ tensor at low temperature.

An AC study of compound **1** was performed under 0-6000 Oe external DC fields at 1.8 K. (Figure II-9) No out-of-phase signals were observed under 0 Oe which is due to fast quantum tunneling of the magnetization (QTM). The relaxation times (τ) under different DC fields were extracted from fittings of Cole-Cole plots (Table II-4). The τ value increases as the field increases from 250 Oe to 1750 Oe and then decreases up to 6000 Oe. Two relaxation processes, QTM and direct spin-phonon relaxation, were taken into consideration to fit the field-dependence of τ^{-1} with Equation 1.12. The least-square fitting yielded A = 7.77× 10^3 T^{-4} K^{-1}s^{-1}, $B_1 = 0.97 \times 10^3$ s^{-1} and $B_2 = 3.39 \times 10^2$ T^{-2}. The individual components of the contributions from different relaxation processes are shown in

Figure II-10 (a), from which it can be ascertained that the effect of QTM is suppressed as the field increases. Conversely, the contribution from direct spin-phonon relaxation increases as the field strength increases. The τ^{-1} reaches its minimum at approximately H_{dc} = 1750 Oe.

The temperature dependence of the relaxation time was also investigated under two different DC fields (500 Oe and 1750 Oe). The in-phase, out-of-phase signals and Cole-Cole plots are shown in Figure II-7 and II-8. The relaxation times were extracted with Cole-Cole equation and listed in Table II-5 and II-6. Two additional terms, an Orbach process and a Raman process, were introduced to model the temperature dependence of τ^{-1} with Equation 1.11. The best fit yields: U_{eff} = 19.1 K, $\tau_0 = 9.8 \times 10^{-6}$ s, C = 3.4×10^{-4} K^{-9} s^{-1}, n = 9. (Figure II-10. (b) and (c)) The U_{eff} and τ_0 values are comparable to reported field-induced SMMs with six-coordinate Co^{II} centers.[18] The Raman components C and n are in the range expected for a Kramers ion (n = 6-9 and C < 0.1).[14, 171] The QTM process under 1750 Oe is well suppressed compared to a field of 500 Oe. At low temperatures, the contribution to τ^{-1} is primarily from an Orbach process under a 1750 Oe DC field whereas the contribution from the Raman process is insignificant at low temperature but increases rapidly as the temperature increases.

The χT values for **2** (Figure II-11) increase from 0.748 emu K mol^{-1} at 2 K, which corresponds to two S = 1/2 spin centers (χT = 0.375 for S = 1/2, g = 2.00), to 1.96 emu mol^{-1} K^{-1} at 300 K. The contribution to χT at 2 K is from low-spin Co^{II} and the non-dimerized TCNQ radical which is in good agreement with the

observed crystal structure. The high-spin state of Co^{II} in **2** is not fully populated at 300 K compared to that of **1** for which the χT value is ~ 3 emu mol^{-1} K^{-1} at 300 K. Similar spin-crossover behavior for **3** was observed. The χT value at 2 K is 0.848 emu K mol^{-1}, slightly higher than the value for **2**, and increases more rapidly than **2** to reach a value of 3.20 emu K mol^{-1} at 300 K. These results indicate that the L.S. to H.S. transition of the $[Co^{II}(Fctp)_2]^{2+}$ cation is facilitated in **3** compared to **2**. The incomplete spin-state transition of **3** at low temperature is attributed to the geometric constraints of the crystal lattice and coordination sphere and/or supramolecular interactions.[167, 172-174]

Equation 1.13 was used to fit the spin-crossover behaviors of **2** and **3**. The n_{HS} values at certain temperatures were calculated from the equation as follows:

$$n_{HS}(T) = [\chi T - (\chi T)_{LS} - (\chi T)_{rad} - (\chi T)_{TIP}]/[(\chi T)_{HS} - (\chi T)_{LS}] \quad \textbf{Equation 2.1}$$

where $(\chi T)_{HS}$, $(\chi T)_{LS}$, $(\chi T)_{rad}$ and $(\chi T)_{TIP}$ are the χT values for high-spin Co(II), low-spin Co(II), $TCNQ^{\cdot-}$/ $TCNQF^{\cdot-}$ radical and temperature-independent paramagnetism. The $(\chi T)_{HS}$, $(\chi T)_{LS}$ and $(\chi T)_{rad}$ values were fixed as $(\chi T)_{HS} = 3.00$ emu K mol^{-1} (S = 3/2, g_{iso} = 2.53 from **1**) and $(\chi T)_{LS} = (\chi T)_{rad} = 0.375$ emu K mol^{-1} (S = 1/2, g = 2.00). On the other hand, χT value at certain temperature can be expressed as:

$$\chi T = n_{HS}(\chi T)_{HS} + (1 - n_{HS})(\chi T)_{LS} + (\chi T)_{rad} + \chi_{TIP} T \quad \textbf{Equation 2.2}$$

The approximately linear relationships of the plots Figure II-12 (a) and (b) indicates that the Γ terms are negligible for **2** and **3** and that equation S2 can be rewritten as Equation 1.14. The slope of $\ln\left[\frac{1-n_{HS}}{n_{HS}}\right]$ vs $1/T$ plot is $\frac{\Delta H}{R}$ and the

intersection with the y-axis is $-\frac{\Delta S}{R}$. The parameters from least-squares fitting with Equations 1.14 and 2.2 of χT vs T plots are summarized in Table II-7. The transition temperature, $T_{1/2}$, is defined as the temperature at which $n_{HS} = n_{LS}$ so that the $T_{1/2}$ can be expressed as $T_{1/2} = \frac{\Delta H}{\Delta S}$. The best fits of χT vs T curves are shown in Figure II-11. The fit matches well with experimental data for **2** from 2 - 300 K. Differences between the fitting and experimental data, however, were observed for **3** below 120 K. Similar phenomena have been observed for several SCO systems with geometric constraints of the crystal lattice and coordination sphere and/or supramolecular interactions.[167, 172-174] Since the steric effect of the fluorine substitution on $TCNQF^{\cdot-}$ is insignificant, the incomplete SCO transition is attributed to the electric dipole interaction between the $TCNQF^{\cdot-}$ and $[Co(Fctp)_2]^{2+}$ moieties. The best fit of χT vs T curves led to values of ΔH = 8.69 kJ mol^{-1}, ΔS = 25.8 J K^{-1} mol^{-1} for **2** which exhibits a $T_{1/2}$ of 336 K and ΔH = 3.12 kJ mol^{-1}, ΔS = 13.8 J K^{-1} mol^{-1} for **3** with a $T_{1/2}$ of 226 K. The magnitude of ΔH and ΔS for **2** and **3** are comparable to the reported Co^{II}-bisterpy SCO compounds.[147, 175] Given that **2** and **3** are isostructural, the only variance that can account for the difference in SCO behavior is the presence of $TCNQ^{\cdot-}$ versus the $TCNQF^{\cdot-}$ radical anions. As expected, no out-of-phase signals were observed for **2** and **3** at 1.8 K under external DC fields from 0 to 6000 Oe which is consistent with an S = 1/2 ground state with no energy barrier between Ms = ±1/2 states.

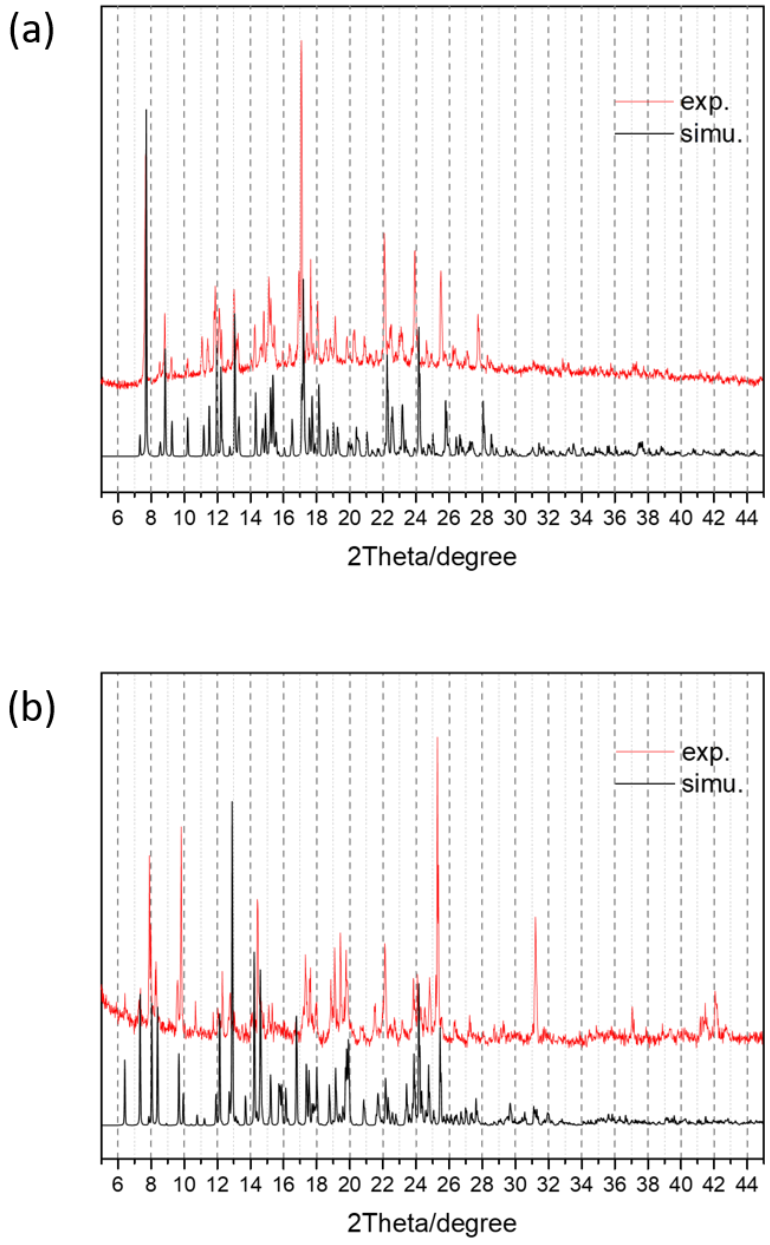

Figure II-4 Powder X-ray diffraction for (a) 1, (b) 2, (c) 3 and (d) 1' The red lines represent the experimental data; the black lines represent the simulated diffraction patterns based on the single crystal structure data.

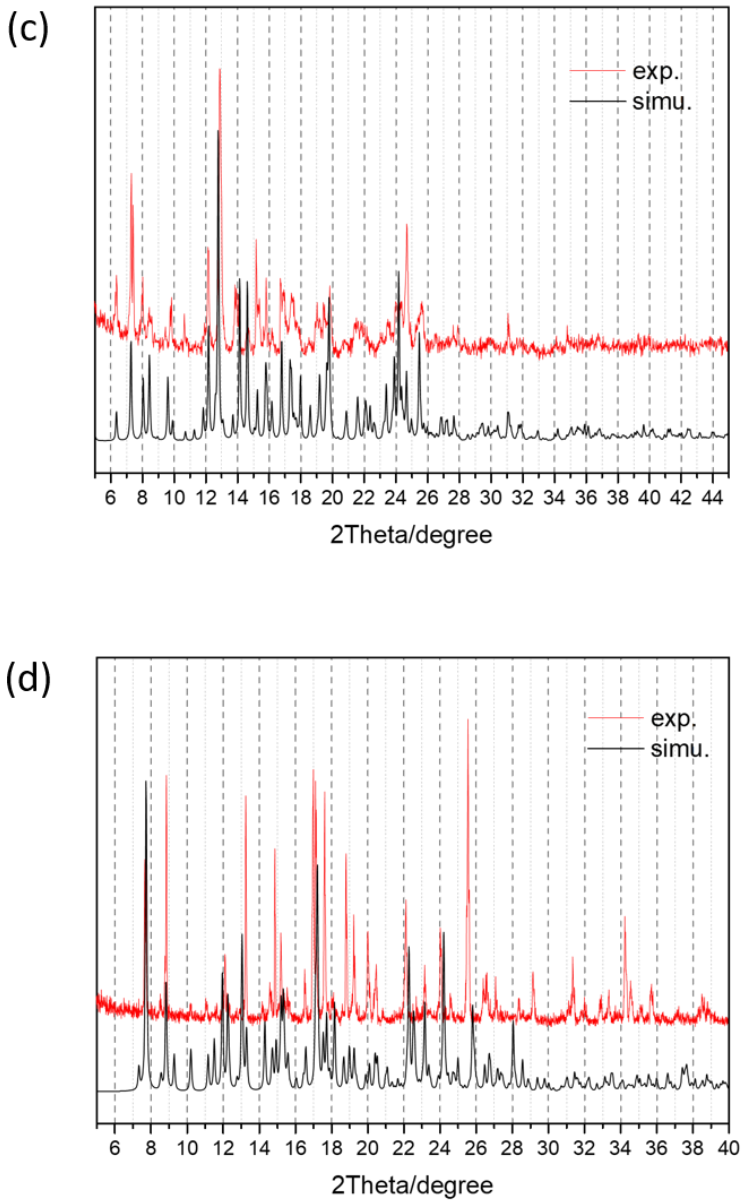

Figure I-4 Continued

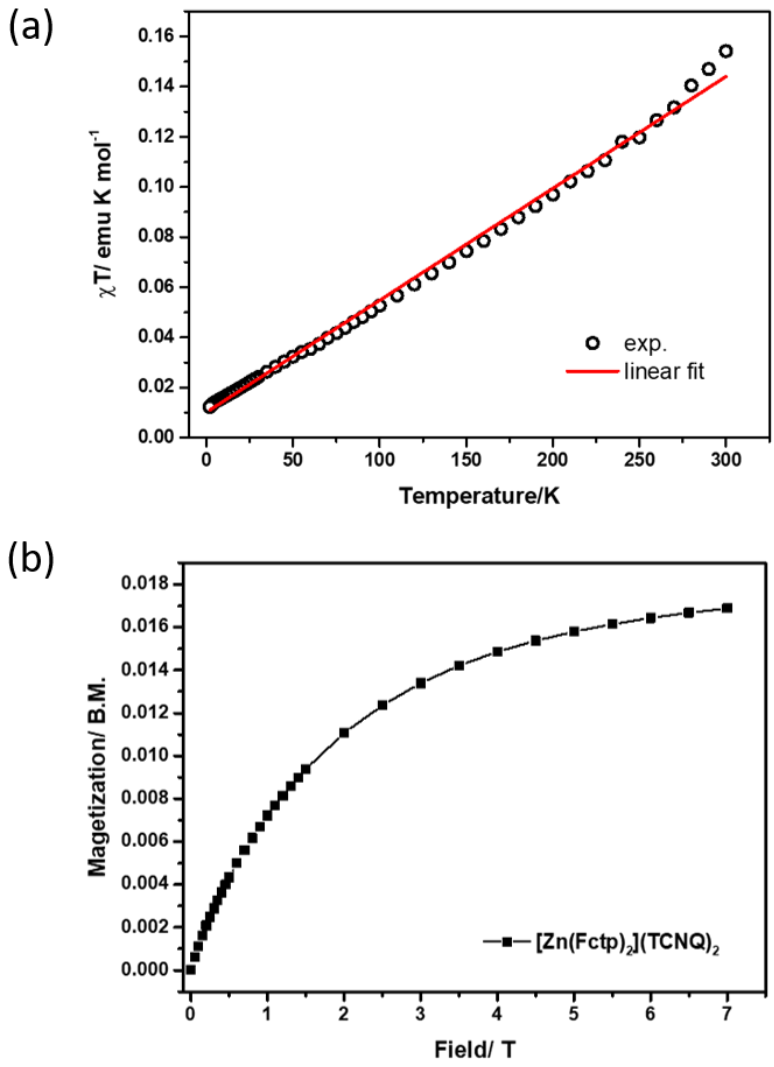

Figure II-5 (a) χT vs T plot, the circles represent the experimental data and the read line represents the linear fit; (b) magnetization plot for 1'.

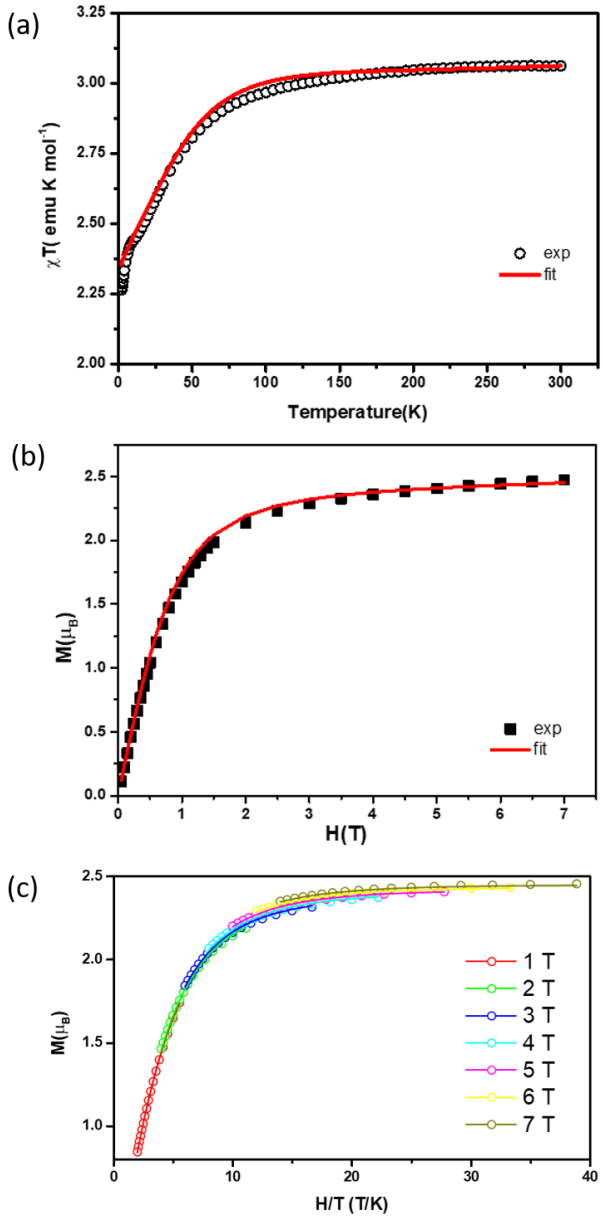

Figure II-6 (a) χT vs T plot and (b) field-dependent magnetization curve at 1.8 K for compound 1. (c) Reduced magnetization plots from 1-7 T. The solid lines are the best fit from the Hamiltonian in Equation 1.3.

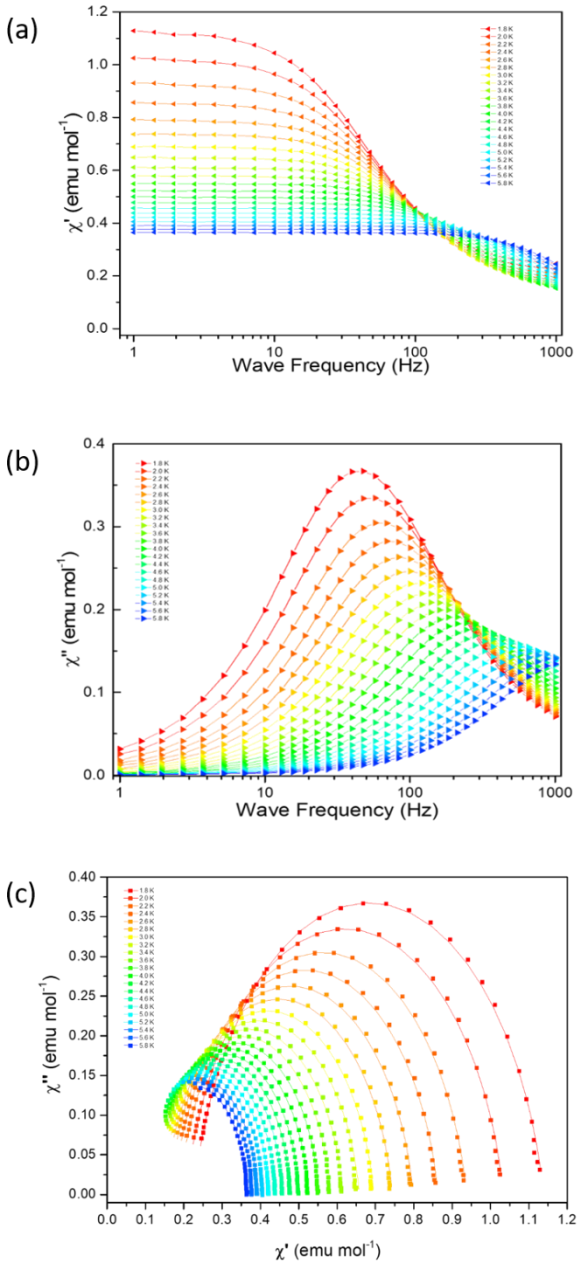

Figure II-7 Frequency dependence of (a) in-phase and (b) out-of-phase ac susceptibility data from 1 Hz to 1000 Hz under HDC = 500 Oe from 1.8 K to 5.8 K and (c) Cole-Cole plots with best fits (solid lines) for 1 from 1.8 to 5.8 K.

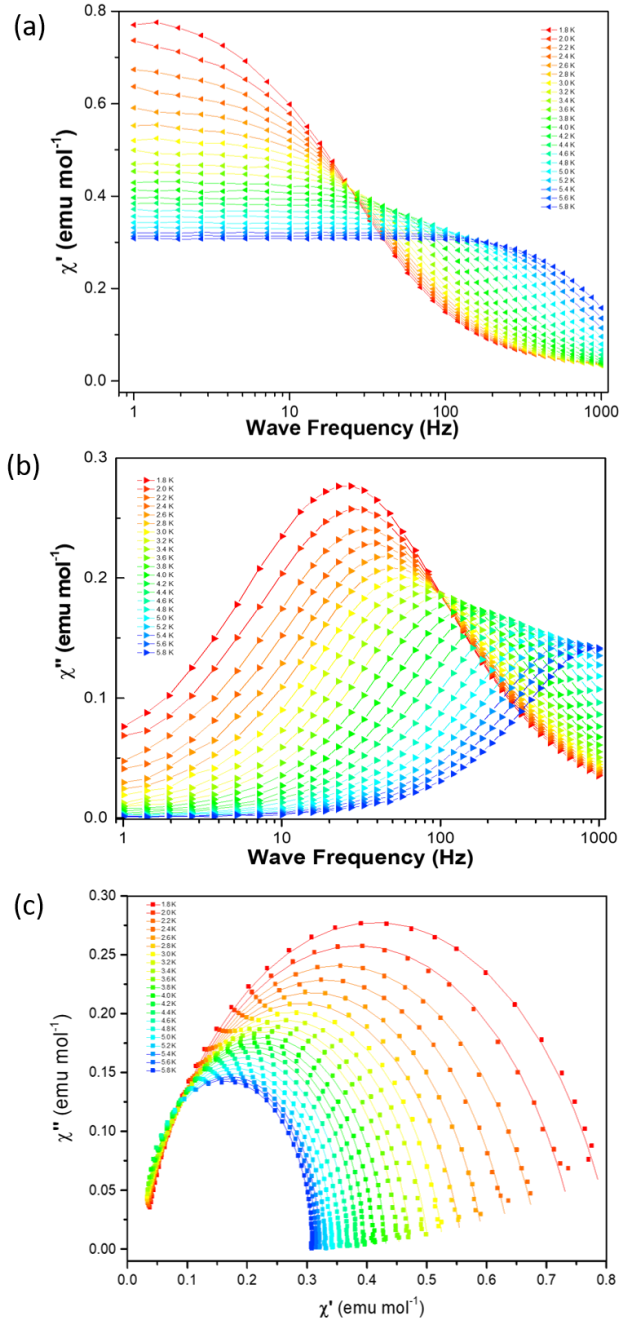

Figure II-8 Frequency dependence of (a) in-phase and (b) out-of-phase ac susceptibility from 1 Hz to 1000 Hz under H_{DC} = 1750 Oe from 1.8 K to 5.8 K and (c) Cole-Cole plots with best fits (solid lines) for 1.

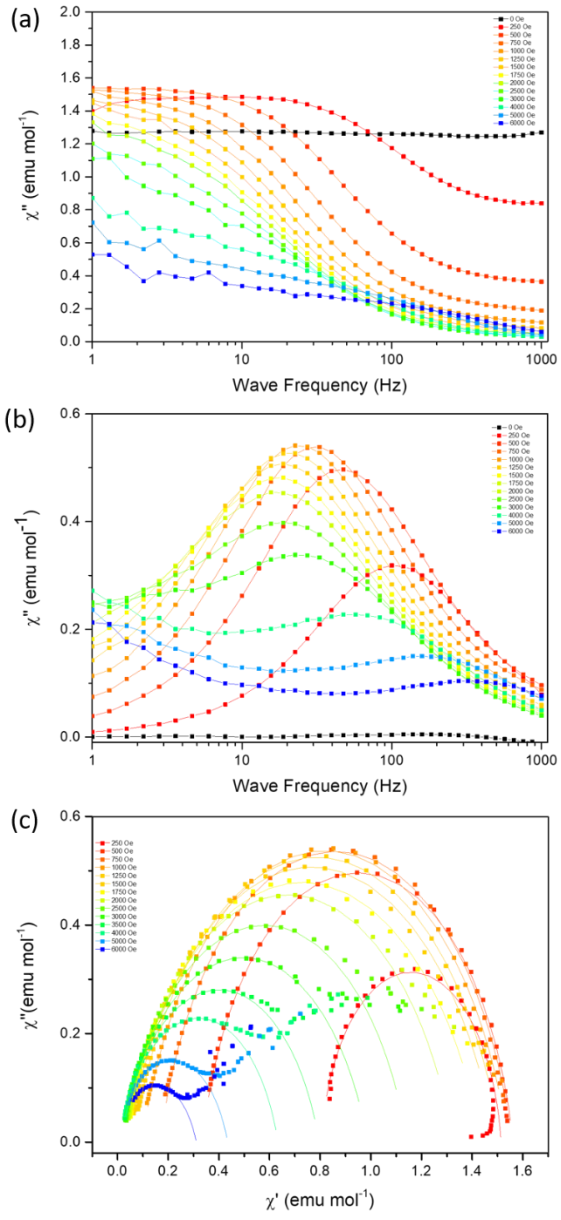

Figure II-9 Frequency dependence of (a) in-phase and (b) out-of-phase ac susceptibility from 1 Hz to 1000 Hz at T = 1.8 K under H_{dc} fields from 0 Oe to 6000 Oe and (c) Cole-Cole plots with best fits (solid lines) for 1.

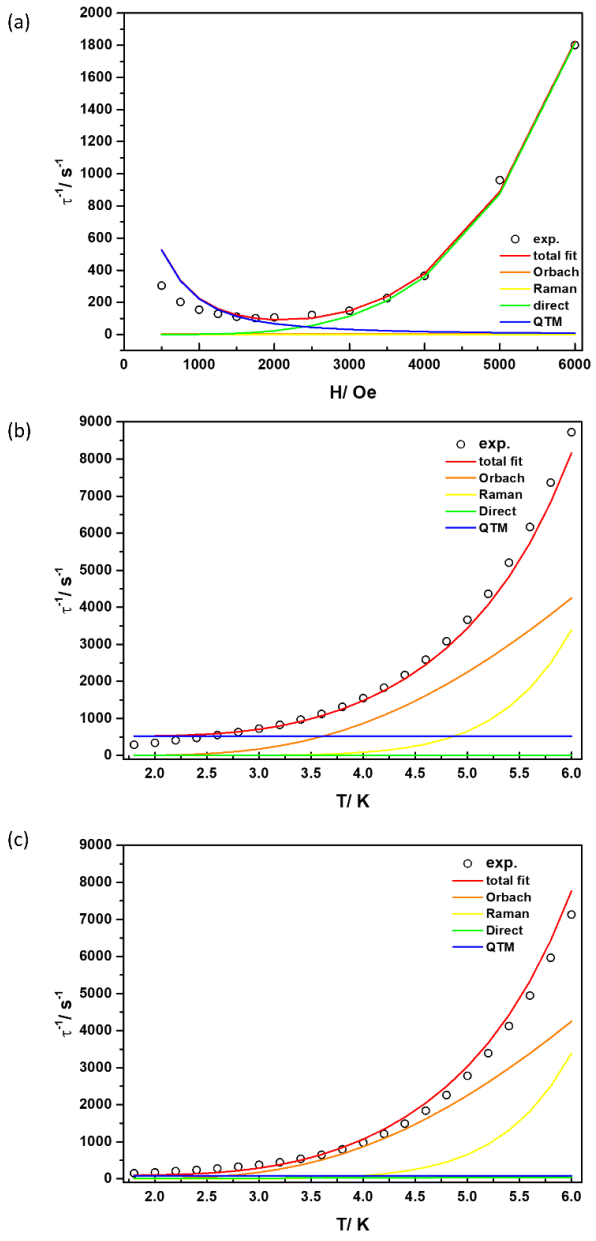

Figure II-10 (a) Magnetic field dependence, (b) and (c) temperature dependence of 1 with the best fits by using Equation 1.12 and Equation 1.11. The solid lines are the total fit (red lines) and contributions of different relaxation processes (orange, yellow, green and blue represent the contribution from Orbach, Raman, Direct and QTM processes respectively) for the inverse relaxation time τ^{-1}.

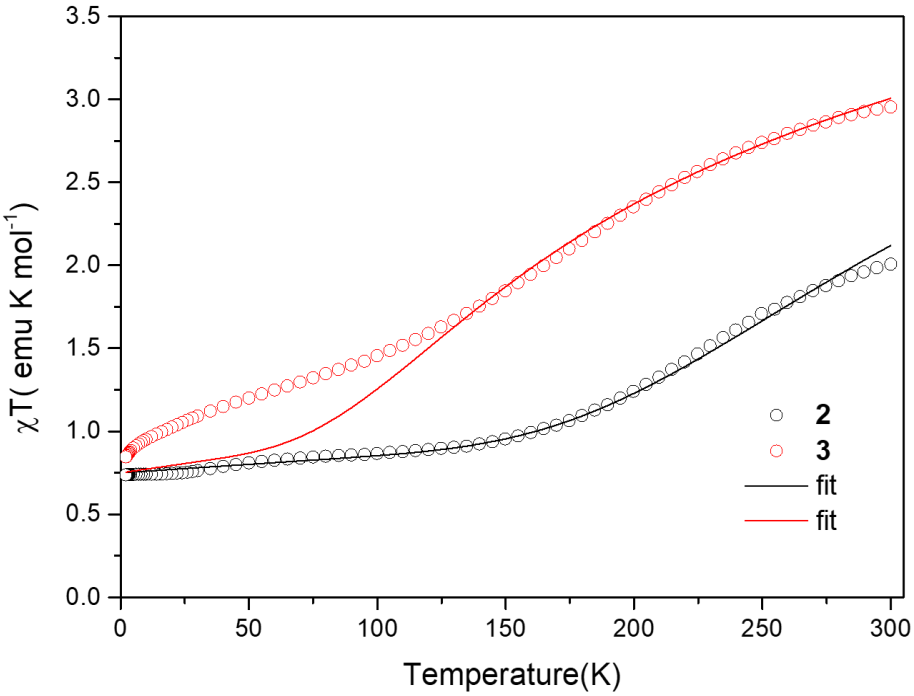

Figure II-11 χT vs T plots of 2 and 3. The open circles represent the experimental data and the solid lines represent the fitting by using Equation 1.14.

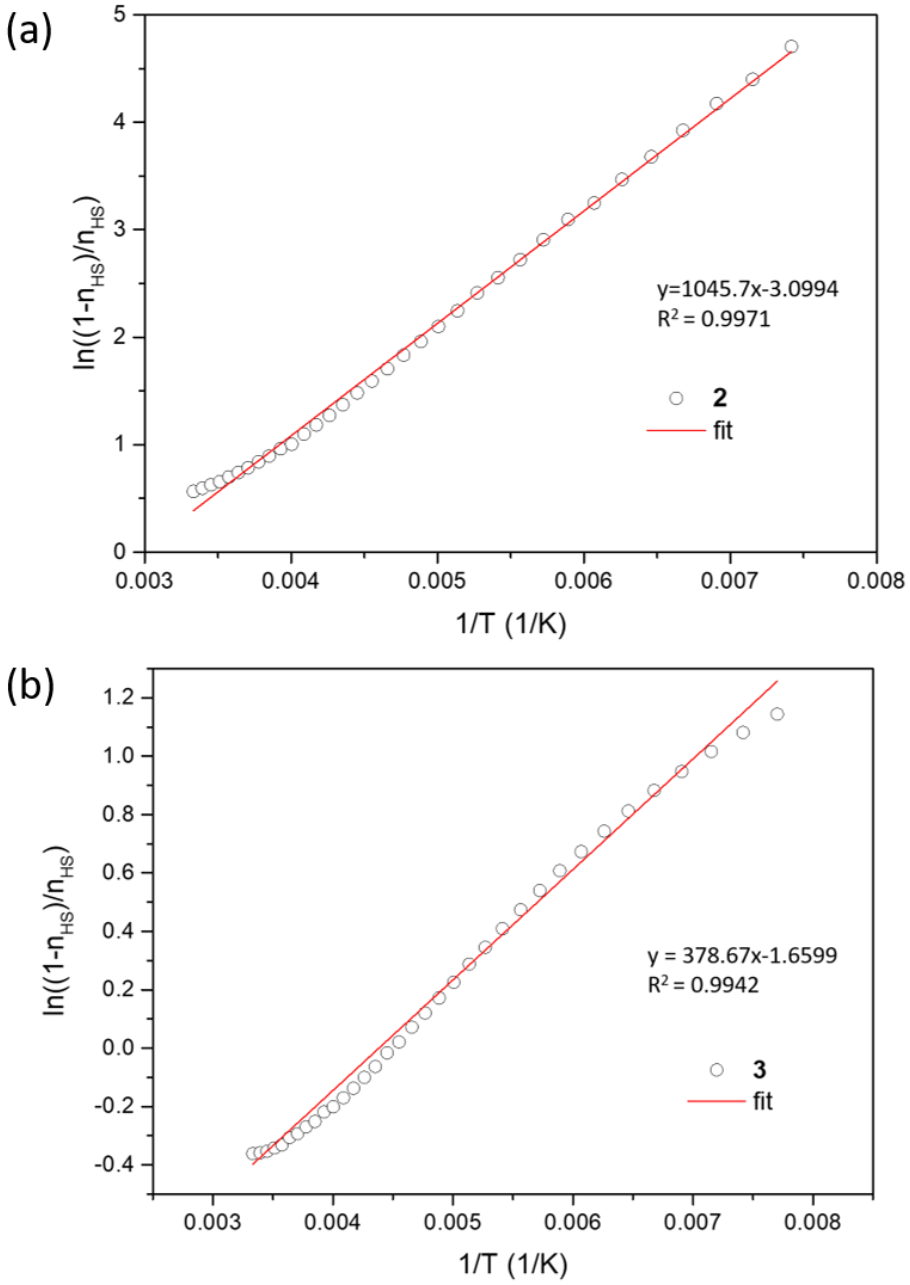

Figure II-12 ln $\left[\frac{1-n_{HS}}{n_{HS}}\right]$ vs 1/*T* plots of (a) 2 and (b) 3 for fitting the SCO thermodynamic parameter.

Table II-4 Fitting parameters of the Cole-Cole plots for variable-field AC magnetic susceptibilities data for 1 at T = 1.8 K.

H/Oe	χ_s / emu mol^{-1}	χ_T / emu mol^{-1}	τ / s	α
250	0.803029	1.513700	0.001505	0.079183
500	0.335141	1.560120	0.003292	0.132153
750	0.168002	1.556210	0.004961	0.162339
1000	0.095445	1.540634	0.006498	0.185753
1250	0.059656	1.512402	0.007815	0.202525
1500	0.036339	1.491969	0.009086	0.224662
1750	0.019631	1.439722	0.009915	0.244189
2000	0.021347	1.324544	0.009453	0.221707
2500	0.014191	1.143987	0.008248	0.215059
3000	0.005019	0.987262	0.006757	0.227973
3500	0.003641	0.795444	0.004431	0.212963
4000	0.002684	0.632542	0.002736	0.199705
5000	0.000000	0.422131	0.001042	0.210715
6000	0.000000	0.310067	0.000555	0.247732

Table II-5 Fitting parameters of the Cole-Cole plots for variable-field AC magnetic susceptibilities of 1 under H_{DC} = 500 Oe.

T/ K	χ_s / emu mol^{-1}	χ_T / emu mol^{-1}	τ / s	α
1.8	0.225751	1.138662	0.003434	0.136459
2.0	0.205087	1.034141	0.002908	0.134518
2.2	0.186434	0.937890	0.002444	0.131322
2.4	0.172673	0.863551	0.002102	0.126461
2.6	0.160589	0.798571	0.001814	0.122552
2.8	0.150670	0.744174	0.001581	0.117771
3.0	0.141917	0.695506	0.001376	0.112655
3.2	0.132523	0.658052	0.001205	0.115585
3.4	0.127941	0.615099	0.001031	0.099231
3.6	0.122480	0.582680	0.000890	0.090950
3.8	0.117484	0.552504	0.000760	0.082234
4.0	0.113100	0.525014	0.000646	0.072830
4.2	0.108839	0.500463	0.000546	0.064389
4.4	0.105106	0.478085	0.000460	0.055670
4.6	0.101473	0.457583	0.000386	0.047800
4.8	0.098021	0.438861	0.000324	0.040724
5.0	0.095132	0.421581	0.000273	0.033889
5.2	0.091647	0.405395	0.000229	0.028894
5.4	0.087712	0.390752	0.000192	0.025647
5.6	0.084745	0.377088	0.000162	0.020391
5.8	0.080182	0.364228	0.000136	0.020008

Table II-6 Fitting parameters of the Cole-Cole plots for variable-field AC magnetic susceptibilities of 1 under H_{DC} = 1750 Oe.

T/ K	χ_s / emu mol^{-1}	χ_T / emu mol^{-1}	τ / s	α
1.8	0.017743	0.812731	0.006616	0.223733
2.0	0.016241	0.752787	0.005724	0.222138
2.2	0.017212	0.688890	0.004811	0.207378
2.4	0.018110	0.641018	0.004144	0.193241
2.6	0.019375	0.596736	0.003547	0.176140
2.8	0.020208	0.559781	0.003051	0.160736
3.0	0.020929	0.528463	0.002616	0.145613
3.2	0.020737	0.503347	0.002232	0.135550
3.4	0.022243	0.473873	0.001844	0.111759
3.6	0.022456	0.454479	0.001537	0.098005
3.8	0.022818	0.432519	0.001255	0.082040
4.0	0.022991	0.413782	0.001021	0.068815
4.2	0.022907	0.397285	0.000825	0.055039
4.4	0.022789	0.384167	0.000671	0.046723
4.6	0.022706	0.369304	0.000544	0.039098
4.8	0.022320	0.355687	0.000442	0.034189
5.0	0.021981	0.342535	0.000359	0.027009
5.2	0.022217	0.331465	0.000295	0.020961
5.4	0.022328	0.321776	0.000243	0.012717
5.6	0.022875	0.315234	0.000202	0.006265
5.8	0.021158	0.308997	0.000168	0.004965

Table II-7 Fitting parameters of χT vs T plots for 2 and 3 obtained from the least squares method

Compound	**2**	**3**
ΔH (kJ mol^{-1})	8.69	3.12
ΔS (J K^{-1} mol^{-1})	25.8	13.8
χ_{TIP} (emu mol^{-1})	0.00102	0.00224
$T_{1/2}$(K)	336	226

Theoretical Calculations

Ab initio CASSCF calculations were carried out to probe the origin and sign of the observed *D* values of Co^{II} ion in **1**. Computed g_x, g_y and g_z values along with the transition energies of the first four excited states and their contributions to the *D* value for **1** are listed in Table II-8. Calculations yielded a g value of 2.36, in good agreement with the experimentally determined g value of 2.44.

The CASSCF computed splitting of the d orbitals for the Co^{II} ion in **1** is depicted in Figure II-13. These results indicate that the first transition of the β spin occurs between the d_{xz} and d_{yz} orbitals with the same $|\pm m_l|$ level which leads to a negative *D* value.[176-177] This low energy transition (~1013 cm^{-1}) contributes a large D value (–70.2 cm^{-1}). The second transition occurs between d_{xy} and d_{yz} orbitals with different $|\pm m_l|$ levels which contributes a positive *D* (+8.4 cm^{-1}) to the total *D* value. Small contributions (–3.9 cm^{-1}) from the third and fourth transition (+1.1 cm^{-1}) do not affect the overall negative *D* value in a significant manner. The CASSCF computed *D* value of -59.9 cm^{-1} is in excellent agreement with the experimental *D* value of -57.2 cm^{-1} for **1**.

DFT calculations using the TPSSh functional (See computational details) were undertaken to unravel details of the spin-crossover features observed for **2**.[178] Computed structural parameters for **2** along with its X-ray structural parameters are summarized in Table II-9. The structural parameters of the optimized structures are generally in good agreement with the X-ray structural parameters. The optimized low-spin (S=1/2) structure in particular closely

resembles the X-ray structure. The computed energies of **2** are provided in Table II-10. For **2**, the Low-Spin (LS) state was found to be the ground state which is consistent with experimental data; the High-Spin (HS) state lies at 13.6 kJ/mol for **2**. Moreover, the small LS-HS energy difference is in the expected range of 0 to 25 kJ/mol for the observation of spin-crossover behavior in **2** which confirms the spin-crossover features.[179-180]

DFT calculations with the ωB97x-D functional were also performed to investigate the intermolecular interactions between the high-spin $[Co^{II}(Fctp)_2]^{2+}$ cation and the $(TCNQ)_2^{2-}/(TCNQF)_2^{2-}$ π-dimers with the phase-I structure. Phase-I is the structure that involves π···π stacking between ferrocenyl group and TCNQ. The comparison was made to address why the TCNQF does not favor the phase-I structure. The energy diagram of the frontier molecular orbitals for {[Co(Fctp)$_2$](TCNQ)$_2$}(**c1**) and {[Co(Fctp)$_2$](TCNQF)$_2$}(**c2**) complexes is depicted in Figure II-14. The HOMO (*E*= - 6.544 eV for **c1** and -6.584 eV for **c2**) and LUMO (*E*= -2.492 eV for **c1** and -2.715 eV for **c2**) levels for both compounds are based on the $(TCNQ)_2^{2-}/(TCNQF)_2^{2-}$ π-dimer bonding and antibonding orbitals. (Figure II-15 and Figure II-16) The HOMO and LUMO energies are slightly lower for **c2** due to the electron withdrawing effect of the fluorine substituent on $TCNQF^{\cdot-}$. The LUMO+1 orbital (*E*= -1.106 eV) of **c1** is mainly based on the π-antibonding orbital on the terpyridine ligand and the d orbital on the ferrocenyl group attached to it. The LUMO+2 orbital of **c2** is nearly identical to the LUMO+1 of **c1** but lies at higher energy (-0.670 eV). In contrast, the

LUMO+1 orbital of **c2** has similar characteristics to the orbital compositions of LUMO+2 but is located on the terpyridine ligand that is distal from the $(TCNQF)_2^{2-}$ π-dimer. The destabilization of the LUMO+1 and LUMO+2 orbitals of **c2** is caused by an increase of Columbic repulsion due to the presence of the fluorine atom on $(TCNQF)_2^{2-}$. Thus, the energy gap of the $(TCNQ)_2^{2-}$/$(TCNQF)_2^{2-}$ charge transfer to $[Co^{II}(Fctp)_2]^{2+}$ which involves the π···π interactions, $\Delta E_{d\rightarrow a}$, increases from 5.438 eV to 5.914 eV when $TCNQ^{\cdot-}$ is replaced by $TCNQF^{\cdot-}$.

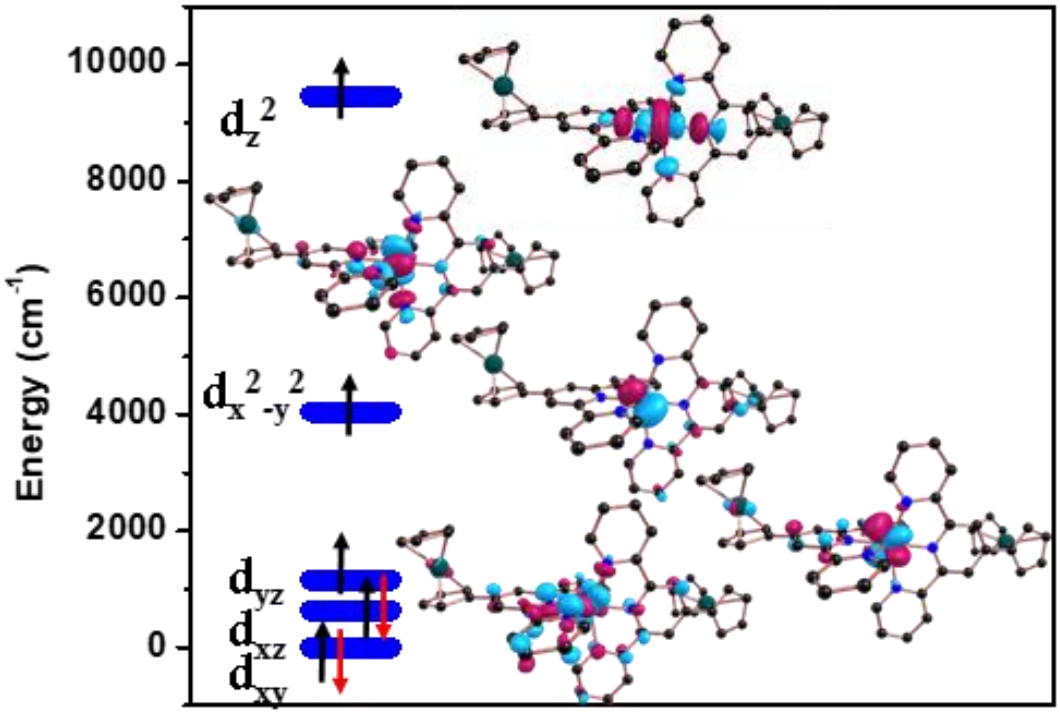

Figure II-13. CASSCF computed d-orbital ordering for the Co(II) ion in 1. Spin-up (black) and spin-down (red) arrows represent α and β electrons. The pink and blue regions indicate the positive and negative signs of wave functions respectively.

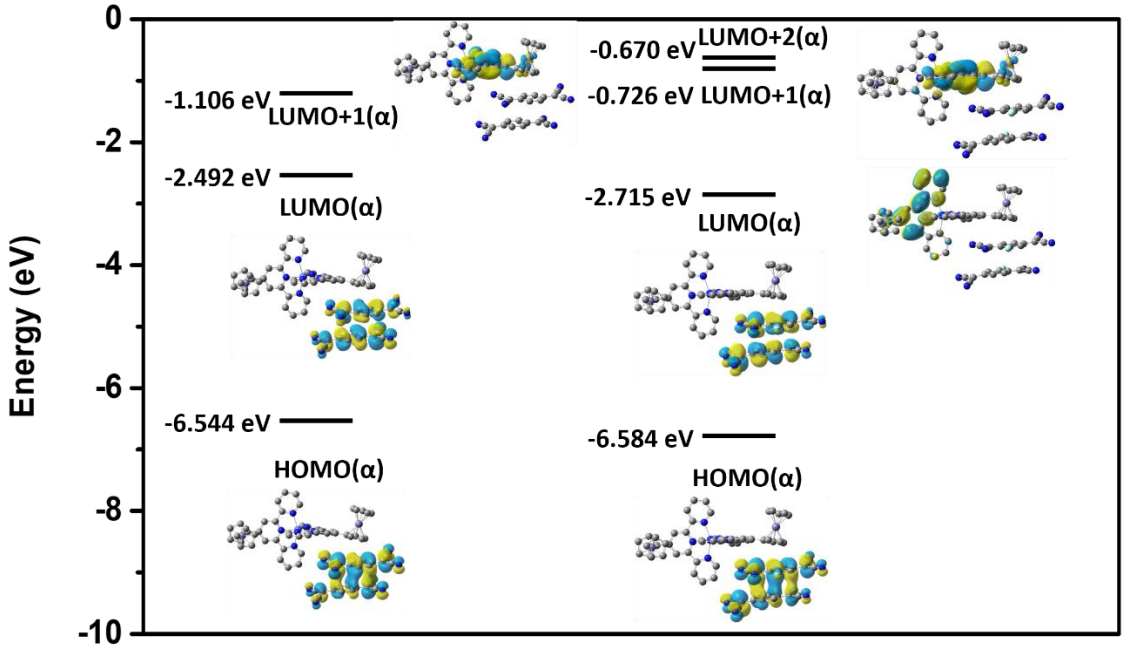

Figure II-14. DFT computed frontier molecular orbitals energy diagram of {[Co(Fctp)$_2$](TCNQ)$_2$} and {[Co(Fctp)$_2$](TCNQF)$_2$} complexes. The orbital surfaces were plotted with 0.02 isovalues. The yellow and blue regions indicate the positive and negative signs of wave functions respectively.

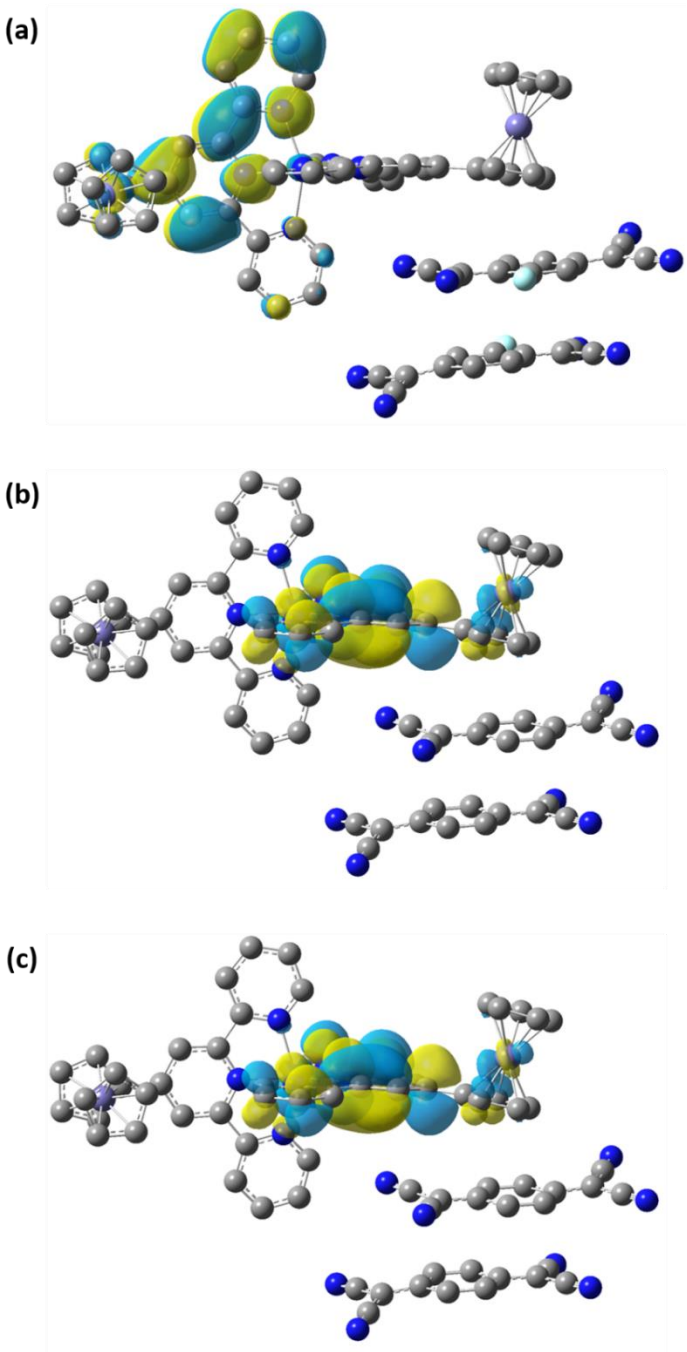

Figure II-15. Plots of frontier molecular orbital surfaces of (a) HOMO (b) LUMO (c) LUMO+1 for {[Co(Fctp)$_2$](TCNQ)$_2$} with isovalues = 0.02 from DFT calculations. The yellow and blue regions indicate the positive and negative signs of the wavefunctions respectively.

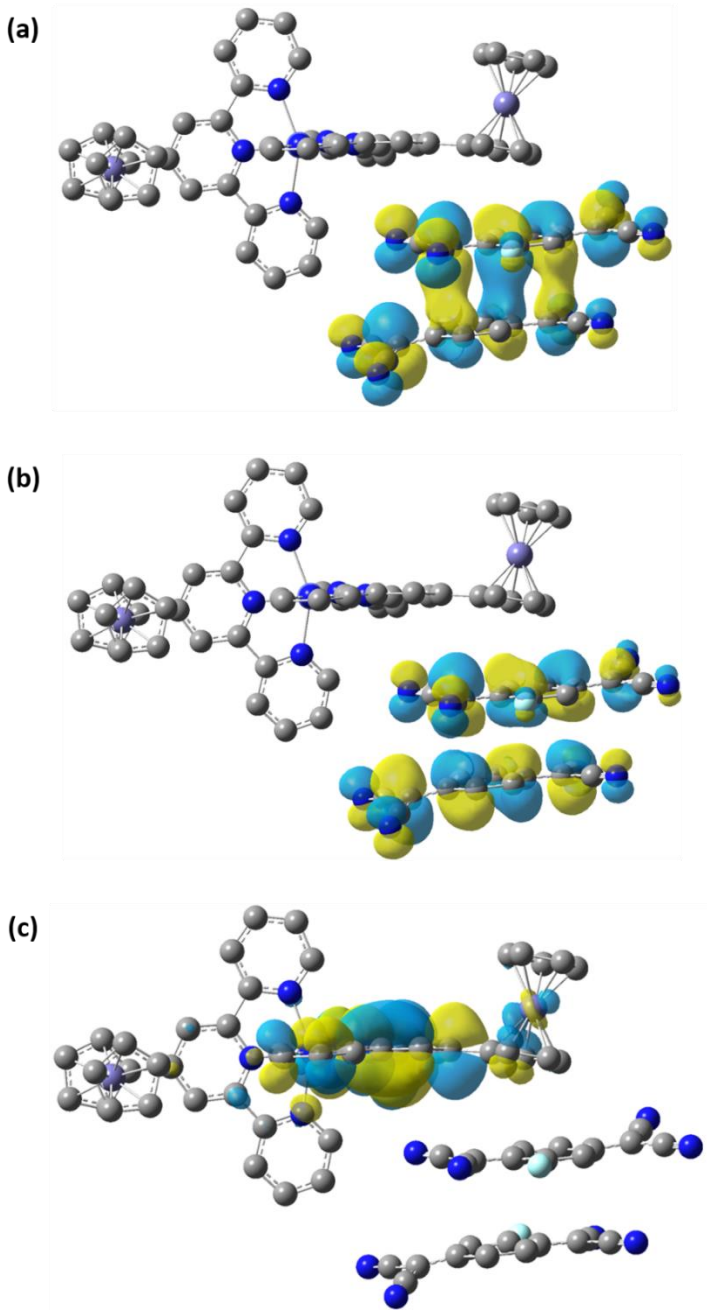

Figure II-16. Plots of frontier molecular orbital surfaces of (a) HOMO (b) LUMO (c) LUMO+1 for {[Co(Fctp)$_2$](TCNQF)$_2$} with isovalues = 0.02 from DFT calculations. The yellow and blue regions indicate the positive and negative signs of the wavefunctions respectively.

Table II-8. CASSCF computed *D*, *E*/*D* and g_x, g_y and g_z values, transition energies (cm^{-1}) and contributions to *D* value from the first four excited states for 1.

D (in cm^{-1}) and *E*/*D*	g_x, g_y, g_z	Excited state	Energy	*D* Contribution
-59.9 and 0.15	2.07, 2.22, 2.80	First	1013.0	-70.2
		Second	2624.4	8.4
		Third	7075.8	-3.9
		Fourth	7805.4	1.1

Table II-9. Selected structural parameters of 2 computed using TPSSh functionals (see Figure II-1 for labels).

2	Bond distances (Å) and angles(°)		
	X-ray	HS	LS
Co-N1	1.877	2.056	1.874
Co-N2	1.936	2.056	1.936
Co-N3	1.987	2.155	2.005
Co-N4	1.998	2.194	2.007
Co-N5	2.157	2.155	2.183
Co-N6	2.136	2.194	2.182
N1-Co-N2	171.1	173.0	179.5
N3-Co-N4	161.6	151.4	162.2
N5-Co-N6	156.8	151.3	157.2

Table II-10. Energy of the spin states produced by the TPSSh/DFT calculations.

Spin State, S	E_s (Hartree)	$\Delta E = E_{3/2} - E_{1/2}$ (kJ/mol)
3/2	-6166.810104	13.55
1/2	-6166.815266	

Discussion

The fact that reactions between $[Co^{II}(Fctp)_2]^{2+}$ and $TCNQ^{\cdot-}$/ $TCNQF^{\cdot-}$ produce compounds with different magnetic properties presents an ideal case for probing the role of supramolecular interactions. For the $TCNQ^{\cdot-}$ case, two phases were obtained, namely a major product, **1** (phase-I), with SMM properties and a minor product, **2** (phase-II) with SCO behavior. In contrast, only one compound, **3** (phase-II), was isolated under the same experimental conditions. These findings indicate that phase-I is more favored when $TCNQ^{\cdot-}$ is used as a counterion and phase-II is more favored for the $TCNQF^{\cdot-}$ derivative.

An important finding in this work is the isolation of compound **1** which exists in the H.S. state. Typically, Co^{II} complexes with terpyridine ligands exist in the L.S. ground state with the H.S. state as excited state[137-139] and, in fact, there are only a few examples of Co(II)-bis(terpyridine)-type compounds that exist in the H.S. state and which exhibit SMM behavior.[147, 181-182] Thus phase-II products should be favored in all cases. The increase in energy required to stabilize $[Co^{II}(Fctp)_2]^{2+}$ in the high-spin state in compound **1** (phase-I) is provided by the supramolecular interactions between the ferrocenyl groups and $TCNQ^{\cdot-}$. As mentioned above, a significant difference in the structures of phase-I and phase-II is the presence of short contacts between the ferrocenyl group on $[Co^{II}(Fctp)_2]^{2+}$ with the $TCNQ^{\cdot-}$ π-dimer (~3.108 Å, Figure II-3) in the former material, which is quite short and falls into the category of π···π interactions.[183]

The energy contributions from the π···π interactions can be decomposed into the sum of electrostatic ($\Delta E_{electrostat}$), Pauli (ΔE_{Pauli}), and orbital interaction (ΔE_{orb}) terms.[184]

Given the evidence of destabilization of the LUMO+1 and LUMO+2 orbitals of **c2** from the DFT calculations, the $\Delta E_{\text{electrostat}}$ and ΔE_{Pauli} terms are augmented by the increase in electron density on $(TCNQF)_2^{2-}$ as compared to $(TCNQ)_2^{2-}$ which renders the π···π interaction unfavorable**.** The ΔE_{orb} term, the absolute value of which is inversely related to $\Delta E_{d\rightarrow a}$ of the donor-acceptor pair involved in the π···π stacking[184-185], also plays an important role in stabilizing the high-spin Co(II) ion in the phase-I structure. The energy diagram obtained from the calculations (Figure II-14), indicates that the $\Delta E_{d\rightarrow a}$ value increases from 5.438 eV to 5.914 eV due to the fluorine substituent. The energy of the donor HOMO is lowered by the electron-withdrawing effect of the fluorine and the LUMO+1 on the acceptor is raised in energy by Columbic repulsion from the electron density on the fluorine substituent; therefore the ΔE_{orb} term is more negative for the $TCNQ^{\cdot-}$ case. Given these findings, the π···π interactions are weaker for the $\{[Co(Fctp)_2](TCNQF)_2\}$ material than for $\{[Co(Fctp)_2](TCNQ)_2\}$. As a result, the phase-I structure is more favored with $TCNQ^{\cdot-}$ and less favored for $TCNQF^{\cdot-}$ owing to the differences in π···π interaction strength between the $[Co^{II}(Fctp)_2]^{2+}$ cations and $TCNQ^{\cdot-}$/TCNQF anions.

Compounds **2** and **3** are isomorphs with the only difference being the fluorine substituent on the $TCNQ^{\cdot-}$ radical anion. The disparity in SCO behavior between **2** and **3** is attributed to the differences in polarities of $TCNQ^{\cdot-}$ and $TCNQF^{\cdot-}$. The asymmetrically substituted $TCNQF^{\cdot-}$ radical anion in **3** (Figure II-17) is disordered in the structure with uneven site occupancies which indicates that the interaction of dipole moments between $[Co^{II}(Fctp)_2]^{2+}$ and $TCNQF^{\cdot-}$ are significant at the crystallization temperature of ~298 K.

The enthalpy change, ΔH, decreases from 8.69 kJ mol^{-1} for **2** to 3.12 kJ mol^{-1} for **3**. The changes in ΔH may be caused by the electric dipolar interactions in the solid-state which reduce the energy difference between the high-spin state and low-spin state in phase-II structures.

The entropy changes, ΔS, are also critical for determining the $T_{1/2}$ values for the SCO phases in this study. The ΔS decreases from 25.8 J K^{-1} mol^{-1} for **2** to 13.8 J K^{-1} mol^{-1} for **3**. Similar trends for Fe(II) SCO complexes have been observed in solution phases with different solvent polarities.[186] The contributions to ΔS are mainly from two sources, the electronic contribution, ΔS_{el}, and vibrational contribution, ΔS_{vib}. The major variation in ΔS for **2** and **3** is ascribed to the differences in ΔS_{vib} since ΔS_{el} (~5.76 J K^{-1} mol^{-1})[187] is the same for Co(II) in **2** and **3**. Experimental and theoretical calculations support the conclusion that the major contribution to ΔS_{vib} in SCO systems is due to metal-ligand vibrations that corresponding to Jahn-Teller distortions associated with the spin-state transition,[188-194] which also induce dipole moment changes of the six-coordinate Co^{II} ion in **2** and **3** (Figure II-18). Thus, considering the non-zero dipole moment of $TCNQF^{\cdot -}$, the electric dipole interactions between $[Co^{II}(Fctp)_2]^{2+}$ and $TCNQF^{\cdot -}$ are responsible for the differences in ΔS for **2** and **3** which leads to the distinct SCO behaviour of these materials.

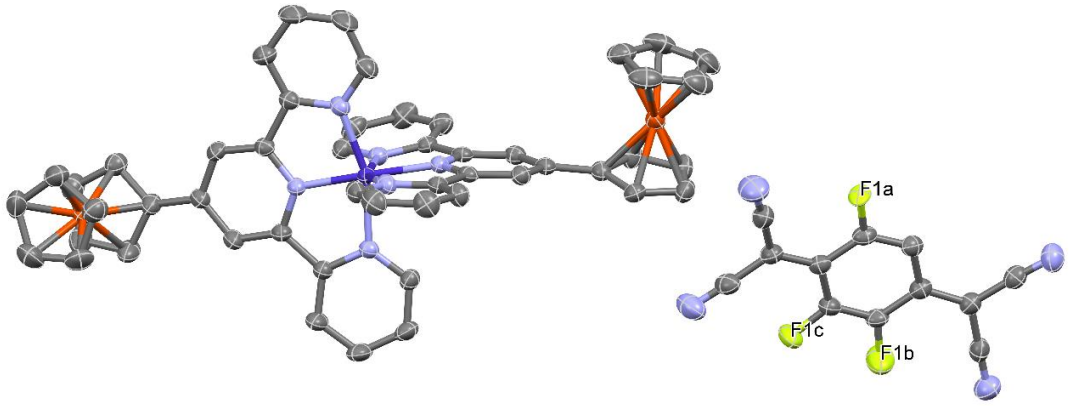

Figure II-17 Asymmetric disordered fluorine substituent on $TCNQF^{-\cdot}$ in 3. The refined occupancies for F1a, F1b, and F1c are 0.566, 0.099 and 0.335 respectively. Hydrogen atoms were omitted for the sake of clarity.

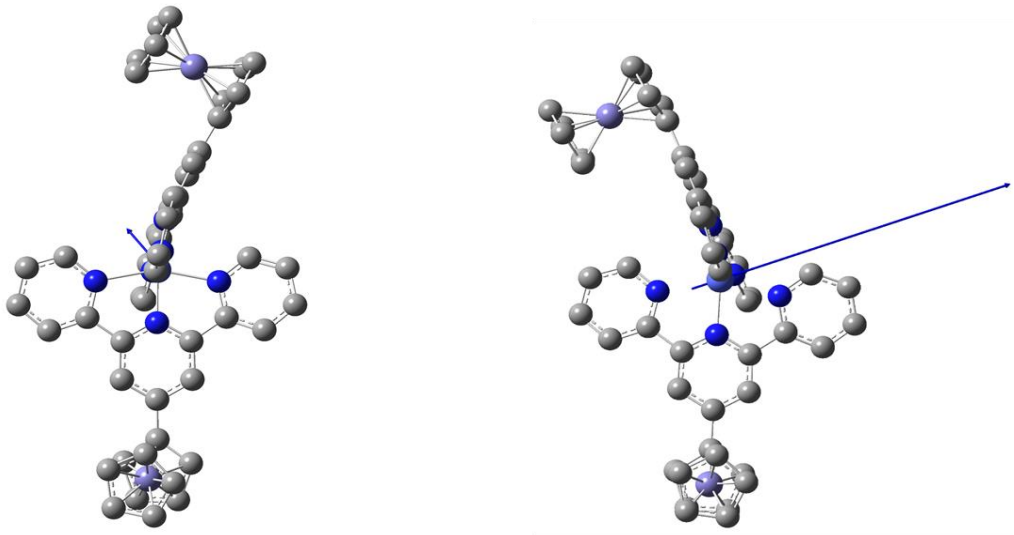

Figure II-18 Dipole moments of (a) low-spin (0.7688 Debye) and (b) high-spin (4.0338 Debye) $[Co(Fctp)_2]^{2+}$ cations from the DFT calculations.

Conclusions

Three new compounds $[Co^{II}(Fctp)_2]$ $(TCNQ)_2$ (**1**), $[Co^{II}(Fctp)_2]$ $(TCNQ)_2 \cdot MeCN$ (**2**) and $[Co^{II}(Fctp)_2]$ $(TCNQF)_2 \cdot MeCN$, (**3**), were prepared and found to exhibit diverse magnetic properties owing to the presence of the radical anion $TCNQ^{\cdot -}$ versus $TCNQF^{\cdot -}$. Two pseudopolymophic products, **1** as the major product and **2** as the minor product, were obtained from the same reaction. Compound **1** exhibits SMM behavior under applied DC fields with an effective energy barrier U_{eff} of 19.1 K and a pre-exponential factor of $\tau_0 = 9.8 \times 10^{-6}$ s, whereas **2** exhibits SCO behavior. The use of $TCNQF^{\cdot -}$ instead of $TCNQ^{\cdot -}$ exclusively leads to the isolation of **3** which is isostructural with **2**. Both **2** and **3** exhibit SCO behavior but with different transition temperatures, $T_{1/2}$ = 336 K for **2** and $T_{1/2}$ = 226 K for **3**. The collective results of single-crystal X-ray studies, theoretical calculations, and thermodynamic parameters indicate that the preference for different phases and SCO behavior is related to supramolecular interactions between $[Co^{II}(Fctp)_2]^{2+}$, and the assemblies of the radical anions $TCNQ^{\cdot -}$ and $TCNQF^{\cdot -}$. These results demonstrate that redox-active organic anions are useful tools for introducing supramolecular interactions and for fine-tuning the magnetic properties of open-shell metal cations by taking advantage of conjugation for π···π interactions, the presence of tunable frontier orbital energies, and the polarity of the organic moieties.

CHAPTER III

CONDUCTING SPIN-CROSSOVER CHARGE-TRANSFER COMPLEXES BASED ON THE COBALT(II) BIS-(NMETHYLPHENOTHIAZINETERPY) MOIETY WITH PARTIALLY CHARGED 7,7,8,8-TETRACYANOQUINODIMETHANE

Introduction

The design of multifunctional molecular magnetic materials exhibiting a cooperative effect of magnetic behavior and other functionalities (*e.g.*, conducting properties and spin-crossover), in addition to control of synergistic effects between different chemical sub-lattices are important challenges in the development of new generations of electronic devices. Extensive studies of such materials have been ongoing for several decades.[195] In this vein, polydentate organocyanide compounds such as 7,7,8,8-tetracyanoquinodimethane (TCNQ) and its derivatives that exhibit tunable redox potentials are excellent choices for multifunctional materials that exhibit both magnetic ordering and conductivity due to their versatility to form coordination bonds as well as to engage in extended π-conjugated stacking. Applications of these concepts to the field of molecular magnetism, single molecule magnet and spin crossover (SCO) behavior in finite molecular systems that do not require long-range magnetic ordering are promising for the miniaturization of electronic devices.

Recently, examples of partially charged TCNQ based conducting SCO compounds have been reported by us and other researchers.[107-113] Results thus far have demonstrated bi-functionality of molecular magnetism and conductivity in TCNQ-

coordination complexes, but systematic tuning of functionalities via ligand design in order to introduce and enhance synergistic interactions between different functionalities has not been yet extensively investigated. The basis of synergistic effects between different functionalities in molecular multi-functional materials is intermolecular interactions. Thus, introducing different intermolecular interactions is key to successful realization of true multi-functionality.

Charge transfer complexes are remarkable compounds that have applications in the elaboration of molecular devices.[196-199] Intermolecular charge transfer can lead to conducting properties and also aid in the coupling of spin centers. Therefore, combining electron donor groups with partially charged TCNQ as an acceptor in the solid state could enhance and/or introduce new functionalities into the molecular system.[96] In this case we chose the phenothiazine (PTZ) moiety as the electron donor because it is known to form strong charge-transfer interactions with neutral TCNQ.[200-201]

Experimental Section

Synthetic Procedures

Synthesis of N-methylphenothiazineterpydine (PTZ-tpy)

The synthesis of the PTZ-tpy molecule has been reported in the literature.[202] In the present work, a modified one-pot synthesis was used for the ligand synthesis. A quantity of NaOH (0.8 g, 20 mmol) was suspended in 15 mL of PEG-300 at 0 ℃, 2-acetylpyridine (2.42 g, 20 mmol) was added with stirring at 0 ℃ for 10 min and then 10-methyl-3-formylphenothiazine (2.41 g, 10mmol) was added to give a dark red solution. The stirring was continued and for an additional 2 h with the temperature gradually

being increased to room temperature and $NH_3 \cdot H_2O$ (30%, 30 mL) was added. The mixture was refluxed for 12 h, cooled to room temperature and treated with 50 mL of water. The resulting yellow-brown precipitate was collected by filtration, washed with 50 mL of hot ethanol and dried in air. Yield is 1.27 g (2.8 mmol, 28%) pale yellow product.

Synthesis of $[Co(PTZ\text{-}tpy)_2]_2(BF_4)_2$ (4)

A sample of PTZ-tpy (444mg, 1.0 mmol) was added to a solution of $Co(BF_4)_2 \cdot 6H_2O$ (0.17g, 0.5 mmol) in 10 mL of acetonitrile to give a dark red solution which was stirred for 2 h. After this time, 100 mL of H_2O was added, the solution was filtered to obtain a dark brown precipitate which was washed with dichloromethane and dried in air. Yield is 522 mg (0.46 mmol, 93%). Single crystals of $[Co(PTZ\text{-}tpy)_2](BF_4)_2 \cdot 2MeCN \cdot Et_2O$ were grown by slow diffusion of EtO_2 into an acetonitrile solution of product.

Synthesis of $[Zn(PTZ\text{-}tpy)_2]_2(BF_4)_2$ (5)

A quantity of PTZ-tpy (222mg, 0.5mmol) was added to a solution of $Zn(BF_4)_2 \cdot 6H_2O$ (0.087g, 0.25 mmol) in 10 mL of acetonitrile. The resulting dark red solution was stirred for 2 h, treated with 100 mL of H_2O and filtered. An orange precipitate was collected, washed with dichloromethane and dried in air. Yield is 260 mg (0.23 mmol, 92%). Single crystals of $[Zn(PTZ\text{-}tpy)_2](BF_4)_2 \cdot 2MeCN$ were grown by slow diffusion of diethyl ether into an acetonitrile solution of the product.

Synthesis of $[Co(PTZ\text{-}tpy)_2]_2(TCNQ)_{4.5} \cdot 2.5MeCN$ (6)

Samples of (n-Bu_4N)(TCNQ) (31 mg, 0.075 mmol) and (Et_3NH)$(TCNQ)_2$ (12.5 mg, 0.025 mmol) were dissolved in 6 mL of acetonitrile and layered with $[Co(PTZtp)_2]_2(BF_4)_2$ (56 mg, 0.05 mmol) dissolved in 6 mL of acetonitrile. Thin dark green platelet crystals were collected by filtration, washed with acetonitrile and dried in air. Yield is 48 mg (0.017 mmol, 67%).

Synthesis of $[Zn(PTZ\text{-}tpy)_2]_2(TCNQ)_{4.5}$·2.5MeCN (7)

Samples of (n-Bu_4N)(TCNQ) (31 mg, 0.075 mmol) and (Et_3NH)$(TCNQ)_2$ (12.5 mg, 0.025 mmol) were dissolved in 6 mL of acetonitrile and layered with a solution of $[Zn(PTZtp)_2]_2(BF_4)_2$ (57 mg, 0.05 mmol) in 6 mL of acetonitrile. Thin dark green platelet crystals were collected by filtration. Washed with acetonitrile. Dried in air and gave 36 mg product (0.013 mmol, 50%).

Single Crystal X-ray Crystallography

Single-crystal diffraction data for **4-7** were collected at 110 K on a Bruker D8 Quest diffractometer equipped with a microfocus MoKα radiation source (λ=0.71073 Å) with an Iμs CMOS detector. The temperature-dependent data of **6** and **7** were collected from 100 K to 300 K with the synchrotron radiation source (λ = 0.41328 Å) at the ChemMatCars beamline 15-ID-B at the Advanced Photon Source (APS), Argonne National Laboratories. The data sets were recorded by φ-scan and ω-scan methods and integrated in the Bruker APEX 3 software package. Absorption corrections were performed in the SADABS-2016/2 (Bruker, 2016/2) package. Solutions and refinements of the crystal structures were carried out using the SHELXT[156] and SHELXL[157] programs and the graphical interface Olex2.[158]

Powder X-ray Diffraction

Powder X-ray diffraction data were collected on a Bruker D8 powder X-ray diffractometer at room temperature with Cu X-ray radiation to verify the phase purity of the bulk products. Powder diffraction patterns were simulated from single-crystal X-ray structural data by using Mercury CSD 2.0.

Magnetic Measurements

A Quantum Design MPMS-XL SQUID instrument was used for magnetic measurements over the temperature range of 1.8-300 K and in the field range of 0-7 T. The diamagnetic contributions of sample holders and diamagnetic contributions of atoms were corrected by using an empty calibrated sample holder and Pascal's constants.

X-ray Photoelectron Spectroscopy

X-ray photoelectron spectroscopy measurements were conducted on the Omicron XPS system with an Argus detector using Omicrons DAR 400 dual Mg/Al X-ray source at room temperature. The voltage was set as 15 kV with current equals 20 mA.

Conductivity Measurements

Conductivities of **6** and **7** were measured by a two-point probe method under vacuum. Pellet samples were prepared by compressing the crystalline powder in a mold with an inner diameter of 25 mm at a pressure of 20 kPa in air. The electrical resistance was measured with a Keithley 2450 SourceMeter.

Table III-1 Crystallographic and refinement parameters for 4-7

Compound	**4**	**5**	**6**	**7**
Empirical formula	$C_{64}H_{56}B_2CoF_8N_{10}OS_2$	$C_{60}H_{46}B_2F_8N_{10}S_2Zn$	$C_{171}H_{105.5}Co_2N_{36.5}S_4$	$C_{171}H_{105.5}N_{36.5}S_4Zn_2$
Formula weight	1277.85	1210.18	2917.51	2930.39
Temperature/K	110.02	110.02	110.01	110.01
Crystal system	monoclinic	monoclinic	triclinic	triclinic
Space group	$P2_1/c$	$P2_1/c$	P-1	P-1
a/Å	16.9942(7)	16.0758(10)	14.136(2)	14.077(3)
b/Å	19.7937(9)	18.4621(12)	15.999(3)	15.925(4)
c/Å	18.4254(8)	18.7046(12)	30.719(4)	30.760(7)
α/°	90	90	96.986(5)	96.345(8)
β/°	110.678(2)	99.274(3)	95.077(4)	94.676(7)
γ/°	90	90	91.989(5)	93.364(8)
Volume/Å^3	5798.6(4)	5478.8(6)	6861.8(18)	6814(3)
Z	4	4	2	2
ρ_{calc}g/cm^3	1.464	1.467	1.412	1.428
μ/mm^{-1}	0.448	0.603	0.376	0.487
F(000)	2636	2480	3010	3022
Crystal size/mm^3	0.23 × 0.21 × 0.14	0.2 × 0.15 × 0.08	0.22 × 0.14 × 0.03	0.022 × 0.013 × 0.004
Radiation	MoKα (λ = 0.71073)	MoKα (λ = 0.71073)	MoKα (λ = 0.71073)	MoKα (λ = 0.71073)
2Θ range for data collection/°	4.51 to 50.754	4.934 to 50.722	4.364 to 50.77	4.408 to 50.7
Index ranges	$-20 \le h \le 20$, $-23 \le k \le 21$, $-22 \le l \le 22$	$-19 \le h \le 19$, $-22 \le k \le 21$, $-22 \le l \le 22$	$-17 \le h \le 17$, $-19 \le k \le 19$, $-37 \le l \le 37$	$-16 \le h \le 16$, $-19 \le k \le 19$, $-37 \le l \le 36$
Reflections collected	40957	36202	99500	182753
Independent reflections	10604 [R_{int} = 0.0956, R_{sigma} = 0.0779]	10012 [R_{int} = 0.1040, R_{sigma} = 0.0923]	25020 [R_{int} = 0.0972, R_{sigma} = 0.1022]	24879 [R_{int} = 0.1393, R_{sigma} = 0.1064]
Data/restraints/ parameters	10604/0/799	10012/0/752	25020/478/2091	24879/608/2091
Goodness-of-fit on F^2	1.072	1.038	1.277	1.06
Final R indexes [I>=2σ (I)]	R_1 = 0.0720, wR_2 = 0.1887	R_1 = 0.0579, wR_2 = 0.1358	R_1 = 0.1140, wR_2 = 0.3068	R_1 = 0.1267, wR_2 = 0.3108
Final R indexes [all data]	R_1 = 0.1008, wR_2 = 0.2069	R_1 = 0.1104, wR_2 = 0.1590	R_1 = 0.1426, wR_2 = 0.3332	R_1 = 0.1601, wR_2 = 0.3376
Largest diff. peak/hole / e Å^{-3}	1.73/-1.06	0.77/-0.79	1.47/-1.04	0.88/-0.94

Table III-2 Temperature dependent M-N bond lengths in 6 (Co) and 7 (Zn)

Temperature/K	Co1-N1	Co1-N2	Co1-N3	Co1-N4	Co1-N5	Co1-N6
100	2.052(5)	2.147(6)	2.141(6)	2.040(4)	2.165(5)	2.150(5)
110	2.052(4)	2.146(6)	2.143(4)	2.042(4)	2.166(5)	2.152(5)
120	2.051(5)	2.149(6)	2.144(6)	2.042(4)	2.168(5)	2.152(5)
140	2.055(5)	2.148(6)	2.148(6)	2.042(4)	2.167(5)	2.151(5)
160	2.056(4)	2.151(6)	2.148(6)	2.046(4)	2.167(5)	2.153(5)
180	2.059(4)	2.149(6)	2.150(6)	2.048(4)	2.170(5)	2.152(5)
200	2.061(5)	2.148(6)	2.150(6)	2.046(4)	2.169(5)	2.149(5)
220	2.059(4)	2.151(6)	2.153(6)	2.046(4)	2.175(5)	2.151(5)
240	2.056(5)	2.151(6)	2.155(6)	2.041(4)	2.174(5)	2.149(5)
260	2.058(5)	2.157(6)	2.154(6)	2.041(4)	2.175(5)	2.150(5)
280	2.064(5)	2.160(6)	2.162(6)	2.045(5)	2.179(5)	2.154(7)
300	2.050(4)	2.133(4)	2.126(4)	2.044(3)	2.166(3)	2.154(3)

Temperature/K	Co2-N7	Co2-N8	Co2-N9	Co2-N10	Co2-N11	Co2-N12
100	1.930(5)	2.047(4)	2.046(4)	1.979(5)	2.163(5)	2.164(5)
110	1.935(5)	2.055(4)	2.053(4)	1.982(4)	2.163(5)	2.162(5)
120	1.941(5)	2.058(4)	2.059(4)	1.985(5)	2.160(5)	2.159(5)
140	1.952(5)	2.069(4)	2.071(4)	1.992(5)	2.156(5)	2.159(5)
160	1.967(5)	2.082(4)	2.085(4)	1.999(5)	2.157(5)	2.157(5)
180	1.982(5)	2.093(4)	2.098(4)	2.005(4)	2.151(5)	2.160(5)
200	1.993(5)	2.098(4)	2.107(4)	2.008(5)	2.149(5)	2.160(5)
220	2.003(5)	2.109(6)	2.115(4)	2.016(5)	2.149(5)	2.163(5)
240	2.011(5)	2.106(6)	2.120(4)	2.017(5)	2.145(5)	2.167(5)
260	2.018(5)	2.114(6)	2.125(6)	2.021(5)	2.144(5)	2.166(5)
280	2.030(5)	2.110(6)	2.134(6)	2.025(5)	2.149(5)	2.172(5)
300	2.018(4)	2.097(4)	2.127(4)	2.026(4)	2.144(3)	2.159(3)

Table III-2 Continued:

Temperature/K	Zn1-N1	Zn1-N2	Zn1-N3	Zn1-N4	Zn1-N5	Zn1-N6
100	2.130(9)	2.17(1)	2.23(1)	2.093(9)	2.223(8)	2.18(1)
110	2.084(9)	2.18(1)	2.19(1)	2.063(9)	2.196(8)	2.161(8)
120	2.093(9)	2.17(1)	2.187(8)	2.095(6)	2.190(8)	2.14(1)
140	2.110(9)	2.17(1)	2.18(1)	2.090(6)	2.206(8)	2.14(1)
160	2.105(9)	2.17(1)	2.18(1)	2.094(6)	2.192(8)	2.14(1)
180	2.115(9)	2.18(1)	2.19(1)	2.099(9)	2.195(8)	2.14(1)
200	2.096(6)	2.173(9)	2.190(8)	2.083(6)	2.209(8)	2.13(1)
220	2.103(9)	2.188(9)	2.192(8)	2.085(6)	2.197(8)	2.18(1)
240	2.103(9)	2.198(9)	2.187(8)	2.090(6)	2.196(8)	2.19(1)
260	2.099(6)	2.208(9)	2.189(8)	2.091(6)	2.198(6)	2.21(1)
280	2.096(6)	2.209(9)	2.205(8)	2.090(6)	2.193(6)	2.207(9)
300	2.075(9)	2.184(9)	2.187(8)	2.079(6)	2.205(8)	2.182(9)

Temperature/K	Zn2-N7	Zn2-N8	Zn2-N9	Zn2-N10	Zn2-N11	Zn2-N12
100	2.089(9)	2.192(8)	2.215(9)	2.101(9)	2.200(9)	2.181(8)
110	2.054(9)	2.144(8)	2.186(9)	2.075(9)	2.187(8)	2.188(9)
120	2.101(6)	2.173(8)	2.198(8)	2.113(6)	2.179(8)	2.181(8)
140	2.100(9)	2.171(8)	2.20(1)	2.112(9)	2.17(1)	2.185(9)
160	2.097(9)	2.169(8)	2.206(9)	2.117(6)	2.176(8)	2.187(8)
180	2.106(9)	2.177(8)	2.219(9)	2.136(9)	2.193(8)	2.207(8)
200	2.094(6)	2.175(7)	2.209(7)	2.107(6)	2.182(8)	2.194(8)
220	2.095(6)	2.176(8)	2.203(7)	2.104(6)	2.183(8)	2.202(8)
240	2.091(6)	2.182(8)	2.207(7)	2.112(6)	2.187(8)	2.206(8)
260	2.094(6)	2.183(8)	2.208(7)	2.107(6)	2.187(8)	2.214(8)
280	2.090(6)	2.196(8)	2.208(7)	2.106(6)	2.187(8)	2.212(8)
300	2.085(6)	2.163(8)	2.199(7)	2.085(6)	2.182(8)	2.212(8)

Table III-3 Temperature-dependent interplanar distance between TCNQ units and phenothiazinyl groups in compound 6 (Co).

Temperature/K	A-B/Å	B-C/Å	D-D/Å	E-E/Å	PTZ-A/Å	PTZ-D/Å	PTZ-E/Å
100	3.111	3.315	2.838	3.221	3.482	3.388	3.280
120	3.122	3.32	2.856	3.235	3.483	3.389	3.282
140	3.133	3.319	2.884	3.247	3.497	3.392	3.286
160	3.137	3.316	2.898	3.257	3.504	3.396	3.291
180	3.150	3.325	2.927	3.270	3.516	3.401	3.298
200	3.176	3.317	2.937	3.282	3.519	3.409	3.301
220	3.176	3.324	2.949	3.292	3.520	3.415	3.308
240	3.197	3.323	2.962	3.303	3.529	3.420	3.308
260	3.217	3.320	2.967	3.312	3.533	3.431	3.318
280	3.252	3.320	2.991	3.328	3.547	3.446	3.332
300	3.214	3.311	3.053	3.361	3.561	3.442	3.325

Table III-4 Temperature-dependent interplanar distance between TCNQ units and phenothiazinyl groups in compound 7 (Zn).

Temperature/K	A-B/Å	B-C/Å	D-D/Å	E-E/Å	PTZ-A/Å	PTZ-D/Å	PTZ-E/Å
100	3.074	3.391	2.928	3.105	3.548	3.418	3.394
120	3.111	3.323	2.800	3.123	3.535	3.447	3.412
140	3.095	3.309	2.837	3.148	3.554	3.450	3.399
160	3.097	3.297	2.809	3.162	3.562	3.452	3.389
180	3.132	3.367	2.856	3.191	3.580	3.482	3.441
200	3.118	3.350	2.842	3.175	3.562	3.471	3.424
220	3.144	3.309	2.865	3.206	3.558	3.480	3.418
240	3.161	3.340	2.904	3.225	3.567	3.475	3.413
260	3.170	3.301	2.917	3.239	3.561	3.485	3.414
280	3.196	3.357	2.925	3.263	3.559	3.502	3.401
300	3.156	3.301	2.951	3.264	3.542	3.472	3.400

Table III-5 Formal charges that estimated by Kistenmatcher's formula on TCNQ in compound 6 at 110K.

Co 110K	b	c	d	ρ	occupancy	charge	Total charge
A	1.424	1.406	1.423	-0.75	1	-0.75	-3.72
B	1.427	1.421	1.410	-1.04	1	-1.04	
C	1.442	1.352	1.414	0.11	0.5	0.06	
D	1.412	1.422	1.425	-1.05	1	-1.05	
E	1.436	1.420	1.414	-0.93	1	-0.93	

Table III-6 Formal charges that estimated by Kistenmatcher's formula on TCNQ in compound at 110K.

Zn 110K	b	c	d	ρ	occupancy	charge	Total charge
A	1.407	1.410	1.419	-0.96	1	-0.96	-4.04
B	1.427	1.433	1.403	-1.27	1	-1.27	
C	1.413	1.375	1.420	-0.40	0.5	-0.20	
D	1.422	1.423	1.416	-1.06	1	-1.06	
E	1.440	1.398	1.418	-0.55	1	-0.55	

Table III-7 Temperature-dependent M-N distances (Å) of 6 and 7.

Temperature/K	Co1-N1	Co1-N2	Co1-N3	Co1-N4	Co1-N5	Co1-N6
100	2.052(5)	2.147(6)	2.141(6)	2.040(4)	2.165(5)	2.150(5)
110	2.052(4)	2.146(6)	2.143(4)	2.042(4)	2.166(5)	2.152(5)
120	2.051(5)	2.149(6)	2.144(6)	2.042(4)	2.168(5)	2.152(5)
140	2.055(5)	2.148(6)	2.148(6)	2.042(4)	2.167(5)	2.151(5)
160	2.056(4)	2.151(6)	2.148(6)	2.046(4)	2.167(5)	2.153(5)
180	2.059(4)	2.149(6)	2.150(6)	2.048(4)	2.170(5)	2.152(5)
200	2.061(5)	2.148(6)	2.150(6)	2.046(4)	2.169(5)	2.149(5)
220	2.059(4)	2.151(6)	2.153(6)	2.046(4)	2.175(5)	2.151(5)
240	2.056(5)	2.151(6)	2.155(6)	2.041(4)	2.174(5)	2.149(5)
260	2.058(5)	2.157(6)	2.154(6)	2.041(4)	2.175(5)	2.150(5)
280	2.064(5)	2.160(6)	2.162(6)	2.045(5)	2.179(5)	2.154(7)
300	2.050(4)	2.133(4)	2.126(4)	2.044(3)	2.166(3)	2.154(3)

Temperature/K	Co2-N7	Co2-N8	Co2-N9	Co2-N10	Co2-N11	Co2-N12
100	1.930(5)	2.047(4)	2.046(4)	1.979(5)	2.163(5)	2.164(5)
110	1.935(5)	2.055(4)	2.053(4)	1.982(4)	2.163(5)	2.162(5)
120	1.941(5)	2.058(4)	2.059(4)	1.985(5)	2.160(5)	2.159(5)
140	1.952(5)	2.069(4)	2.071(4)	1.992(5)	2.156(5)	2.159(5)
160	1.967(5)	2.082(4)	2.085(4)	1.999(5)	2.157(5)	2.157(5)
180	1.982(5)	2.093(4)	2.098(4)	2.005(4)	2.151(5)	2.160(5)
200	1.993(5)	2.098(4)	2.107(4)	2.008(5)	2.149(5)	2.160(5)
220	2.003(5)	2.109(6)	2.115(4)	2.016(5)	2.149(5)	2.163(5)
240	2.011(5)	2.106(6)	2.120(4)	2.017(5)	2.145(5)	2.167(5)
260	2.018(5)	2.114(6)	2.125(6)	2.021(5)	2.144(5)	2.166(5)
280	2.030(5)	2.110(6)	2.134(6)	2.025(5)	2.149(5)	2.172(5)
300	2.018(4)	2.097(4)	2.127(4)	2.026(4)	2.144(3)	2.159(3)

Table III-7 Continued:

Temperature/K	Zn1-N1	Zn1-N2	Zn1-N3	Zn1-N4	Zn1-N5	Zn1-N6
100	2.130(9)	2.17(1)	2.23(1)	2.093(9)	2.223(8)	2.18(1)
110	2.084(9)	2.18(1)	2.19(1)	2.063(9)	2.196(8)	2.161(8)
120	2.093(9)	2.17(1)	2.187(8)	2.095(6)	2.190(8)	2.14(1)
140	2.110(9)	2.17(1)	2.18(1)	2.090(6)	2.206(8)	2.14(1)
160	2.105(9)	2.17(1)	2.18(1)	2.094(6)	2.192(8)	2.14(1)
180	2.115(9)	2.18(1)	2.19(1)	2.099(9)	2.195(8)	2.14(1)
200	2.096(6)	2.173(9)	2.190(8)	2.083(6)	2.209(8)	2.13(1)
220	2.103(9)	2.188(9)	2.192(8)	2.085(6)	2.197(8)	2.18(1)
240	2.103(9)	2.198(9)	2.187(8)	2.090(6)	2.196(8)	2.19(1)
260	2.099(6)	2.208(9)	2.189(8)	2.091(6)	2.198(6)	2.21(1)
280	2.096(6)	2.209(9)	2.205(8)	2.090(6)	2.193(6)	2.207(9)
300	2.075(9)	2.184(9)	2.187(8)	2.079(6)	2.205(8)	2.182(9)

Temperature/K	Zn2-N7	Zn2-N8	Zn2-N9	Zn2-N10	Zn2-N11	Zn2-N12
100	2.089(9)	2.192(8)	2.215(9)	2.101(9)	2.200(9)	2.181(8)
110	2.054(9)	2.144(8)	2.186(9)	2.075(9)	2.187(8)	2.188(9)
120	2.101(6)	2.173(8)	2.198(8)	2.113(6)	2.179(8)	2.181(8)
140	2.100(9)	2.171(8)	2.20(1)	2.112(9)	2.17(1)	2.185(9)
160	2.097(9)	2.169(8)	2.206(9)	2.117(6)	2.176(8)	2.187(8)
180	2.106(9)	2.177(8)	2.219(9)	2.136(9)	2.193(8)	2.207(8)
200	2.094(6)	2.175(7)	2.209(7)	2.107(6)	2.182(8)	2.194(8)
220	2.095(6)	2.176(8)	2.203(7)	2.104(6)	2.183(8)	2.202(8)
240	2.091(6)	2.182(8)	2.207(7)	2.112(6)	2.187(8)	2.206(8)
260	2.094(6)	2.183(8)	2.208(7)	2.107(6)	2.187(8)	2.214(8)
280	2.090(6)	2.196(8)	2.208(7)	2.106(6)	2.187(8)	2.212(8)
300	2.085(6)	2.163(8)	2.199(7)	2.085(6)	2.182(8)	2.212(8)

Table III-8 Temperature dependent formal charges that estimated by Kistenmatcher's formula on TCNQ in compound 6.

Temperature/K	A	B	C	D	E	Total	Total w/o C
100	-0.80	-1.22	-0.58	-1.02	-0.95	-4.28	-3.99
110	-0.91	-1.19	-1.44	-1.05	-0.89	-4.76	-4.04
120	-0.82	-1.07	-0.05	-1.02	-0.90	-3.84	-3.81
140	-0.88	-1.24	-0.20	-1.07	-0.85	-4.14	-4.04
160	-0.93	-1.29	-0.09	-1.09	-0.82	-4.18	-4.13
180	-0.99	-1.20	-0.22	-1.05	-0.85	-4.20	-4.09
200	-0.99	-1.05	-0.03	-1.06	-0.85	-3.97	-3.95
220	-1.08	-1.14	-0.54	-1.09	-0.83	-4.41	-4.14
240	-1.05	-1.18	-0.25	-1.18	-0.71	-4.25	-4.12
260	-1.02	-1.09	-0.79	-1.11	-0.73	-4.35	-3.95
280	-1.15	-1.30	-0.72	-1.16	-0.69	-4.66	-4.30
300	-1.30	-1.18	-2.44	-1.11	-0.60	-5.41	-4.19

Table III-9 Temperature-dependent formal charges that estimated by Kistenmatcher's formula on TCNQ in compound 7.

Temperature/K	A	B	C	D	E	total charge	total charge/C
100	-0.93	-1.15	0.15	-1.07	-0.64	-3.72	-3.79
110	-1.07	-1.22	-0.34	-1.00	-0.56	-4.02	-3.85
120	-1.07	-1.3	-1.37	-1.29	-0.78	-5.13	-4.44
140	-1.07	-1.37	-1.79	-1.15	-0.64	-5.13	-4.23
160	-1.07	-1.37	-3.59	-1.22	-0.57	-6.03	-4.23
180	-1.00	-1.15	-2.48	-1.44	-0.5	-5.33	-4.09
200	-1.15	-1.3	-1.07	-1.07	-0.85	-4.91	-4.37
220	-1.22	-1.45	-0.63	-1.15	-0.57	-4.71	-4.39
240	-1.15	-1.3	-1.45	-1.22	-0.57	-4.97	-4.24
260	-1.07	-1.37	-1.53	-1.15	-0.50	-4.86	-4.09
280	-1.15	-1.3	-1.46	-1.00	-0.57	-4.75	-4.02
300	-1.22	-1.22	-0.71	-1.00	-0.56	-4.36	-4.00

Table III-10 Temperature dependent formal charges that estimated by Kistenmatcher's formula on TCNQ triads in compound 6.

Temperature/K	{ABCBA}	$\{D_2\}$	$\{E_2\}$
100	-4.04	-2.04	-1.90
110	-4.20	-2.10	-1.78
120	-3.78	-2.04	-1.80
140	-4.24	-2.14	-1.70
160	-4.44	-2.18	-1.64
180	-4.38	-2.10	-1.70
200	-4.08	-2.12	-1.70
220	-4.44	-2.18	-1.66
240	-4.46	-2.36	-1.42
260	-4.22	-2.22	-1.46
280	-4.90	-2.32	-1.38
300	-4.96	-2.22	-1.20

Table III-11 Temperature dependent formal charges that estimated by Kistenmatcher's formula on TCNQ triads in compound 7.

Temperature/K	{ABCBA}	$\{D_2\}$	$\{E_2\}$
100	-4.16	-2.14	-1.28
110	-4.58	-2.00	-1.12
120	-4.74	-2.58	-1.56
140	-4.88	-2.30	-1.28
160	-4.88	-2.44	-1.14
180	-4.30	-2.88	-1.00
200	-4.90	-2.14	-1.70
220	-5.34	-2.30	-1.14
240	-4.90	-2.44	-1.14
260	-4.88	-2.30	-1.00
280	-4.90	-2.00	-1.14
300	-4.88	-2.00	-1.12

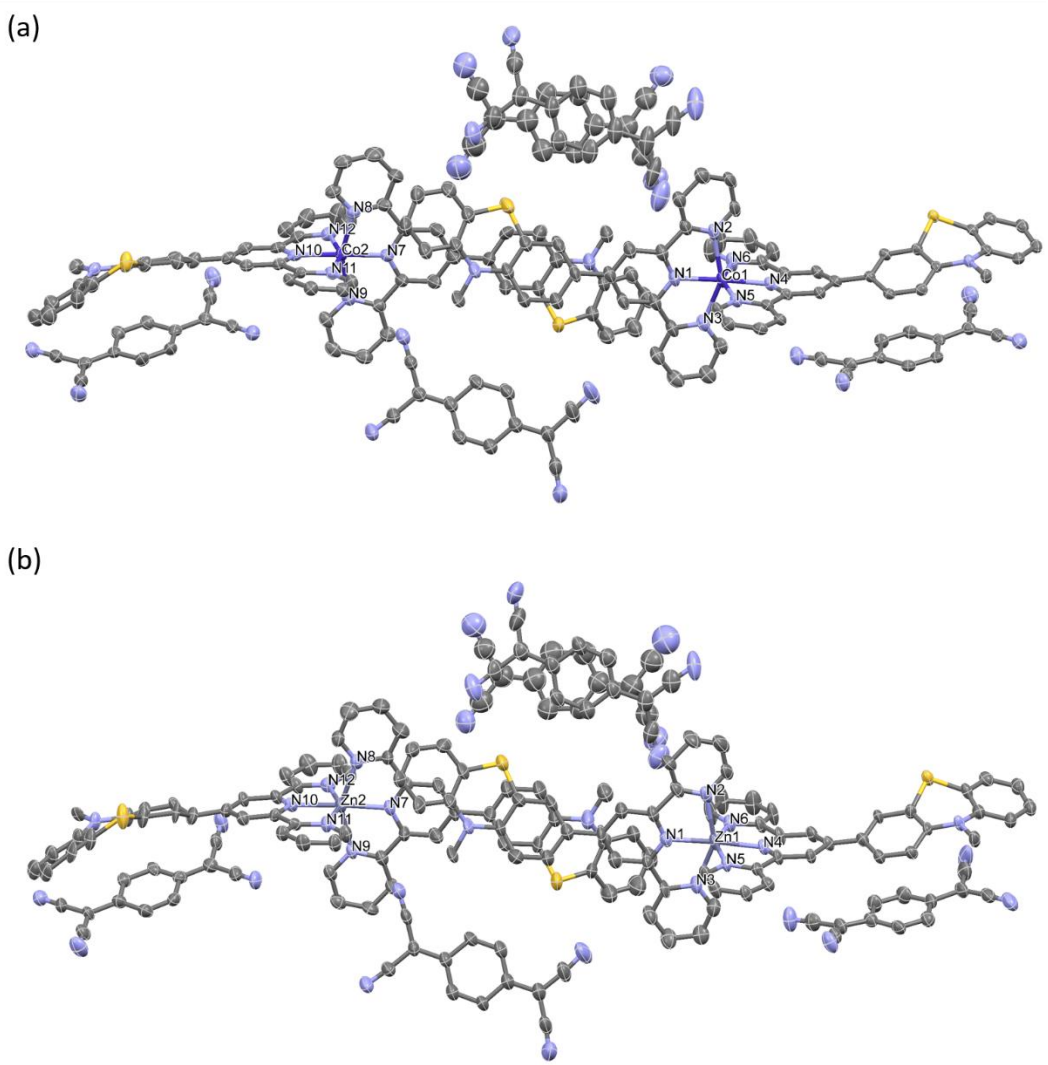

Figure III-1 Asymmetric units of (a) 6 and (b) 7. Hydrogen atoms and solvent molecules were omitted for the sake of clarity. Colour code: carbon: grey; nitrogen: blue; cobalt: purple; sulfur: orange.

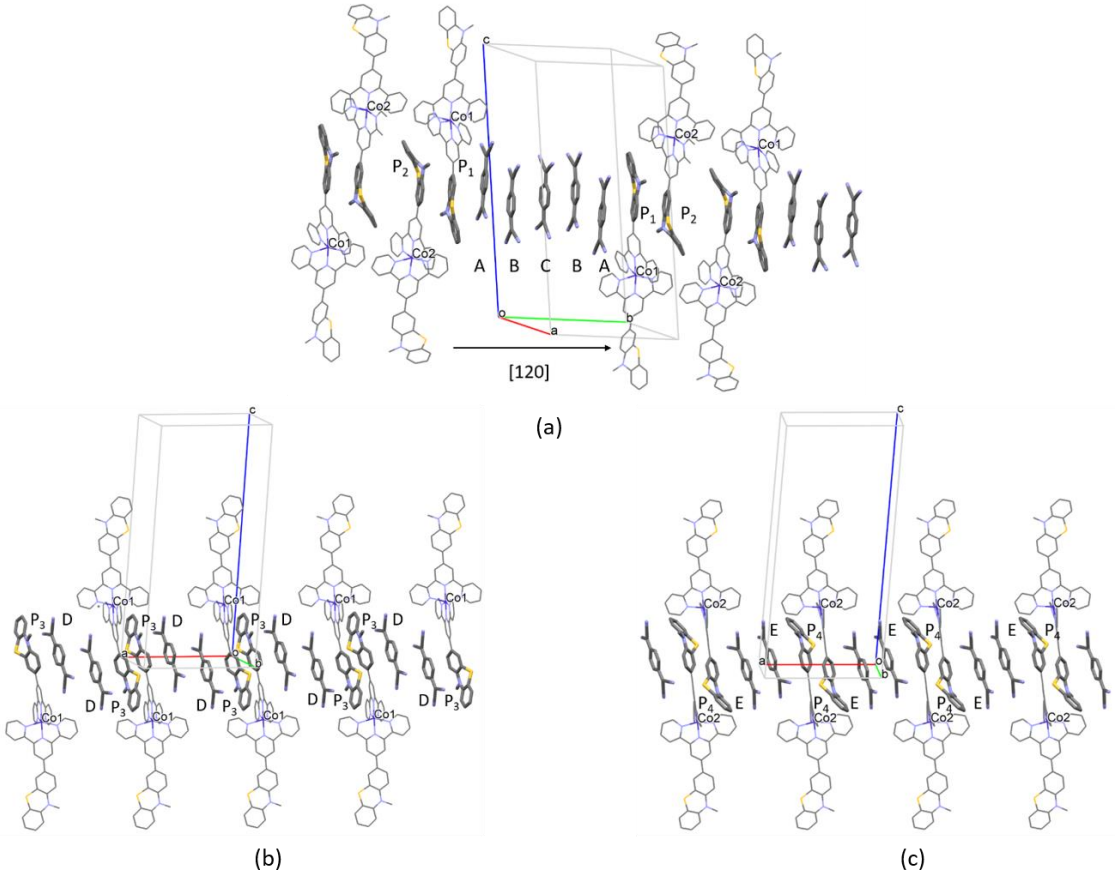

Figure III-2 There different TCNQ packing patterns that exist in the solid state structures of 6 and 7.

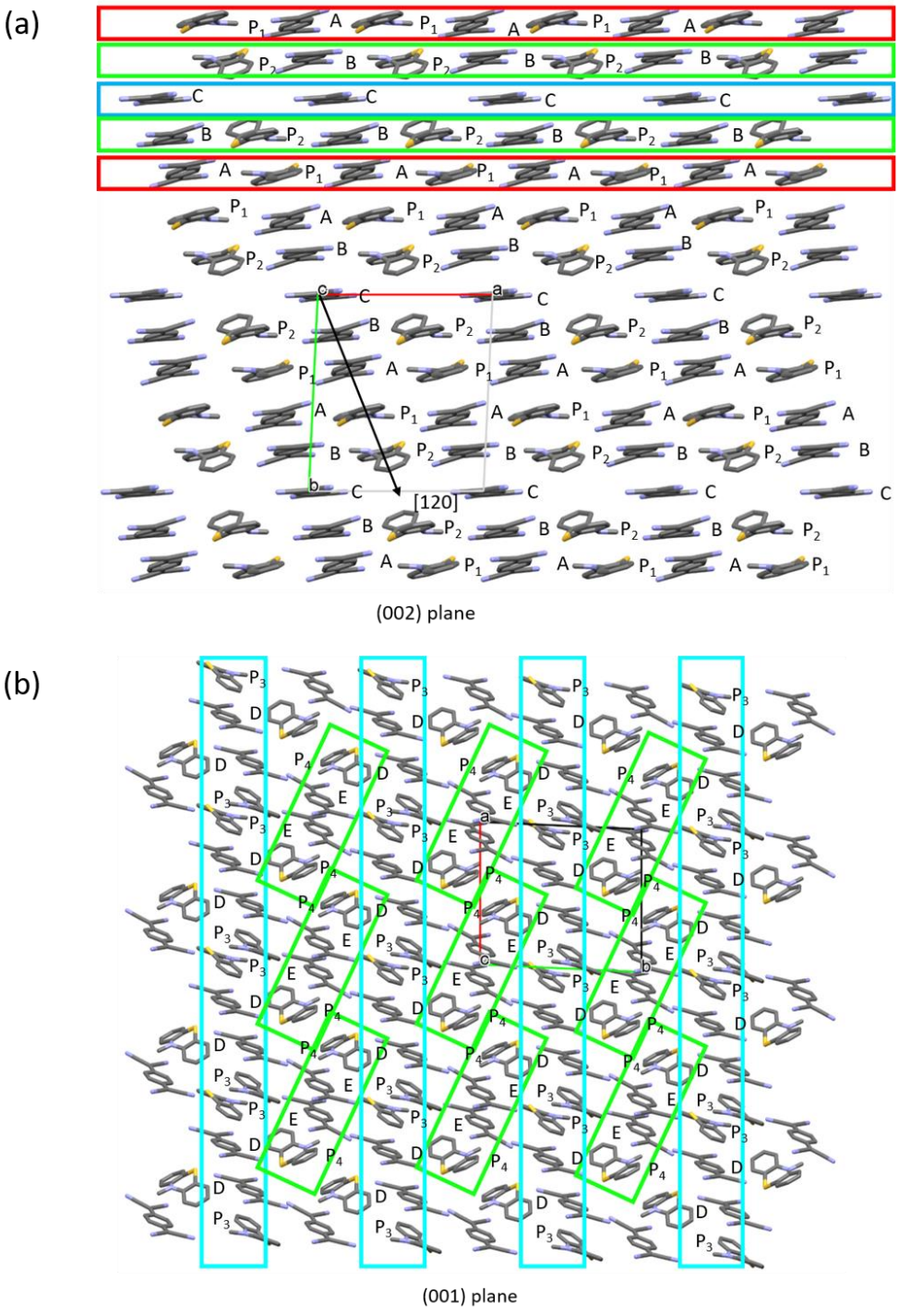

Figure III-3 Interlayer stacking patterns of 6 and 7 in (a) (002) and (b) (001) plane.

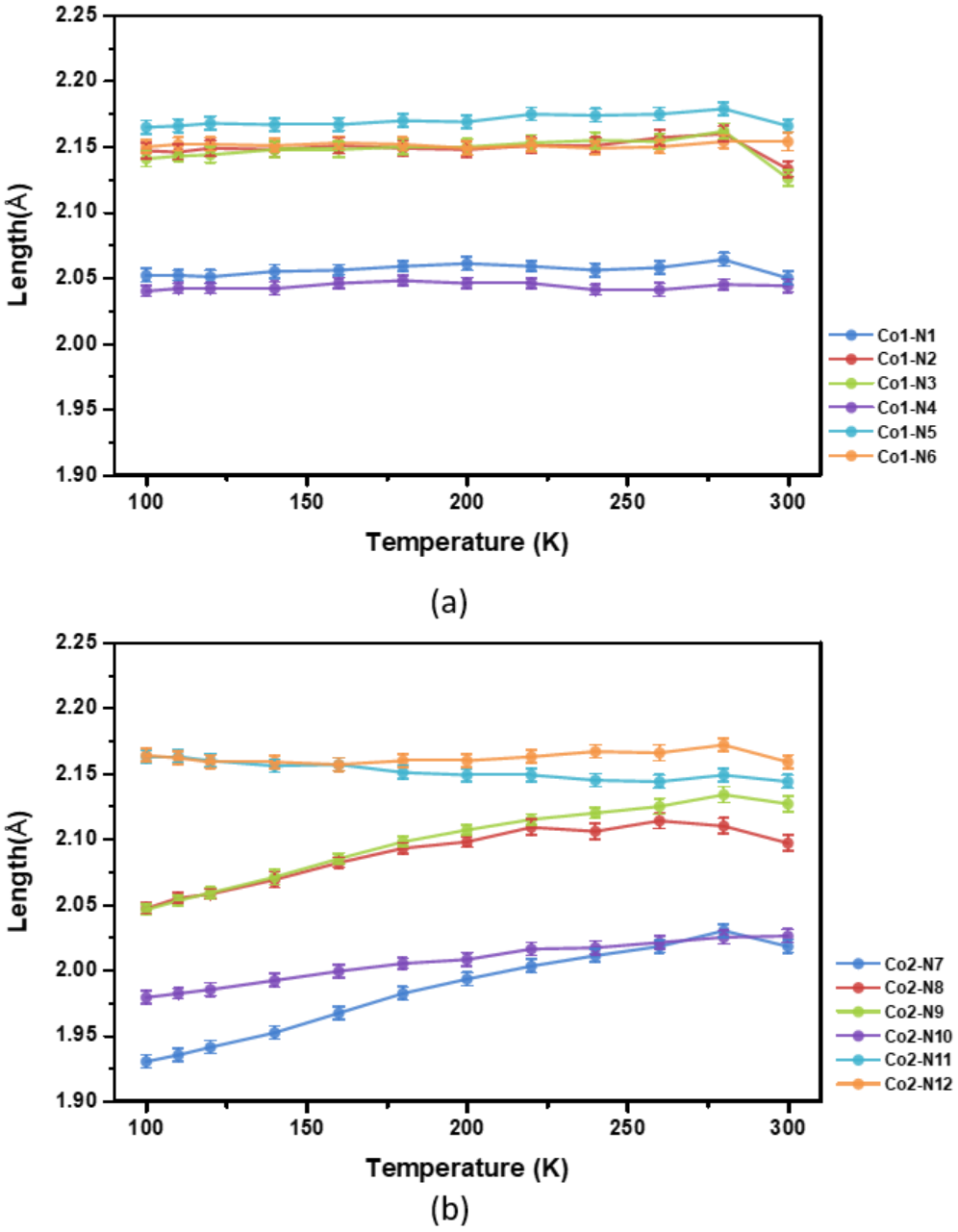

Figure III-4 Temperature dependence of M-N coordination bond lengths in (a) and (b): compound 6 (M = Co); (c) and (d): compound 7 (M = Zn).

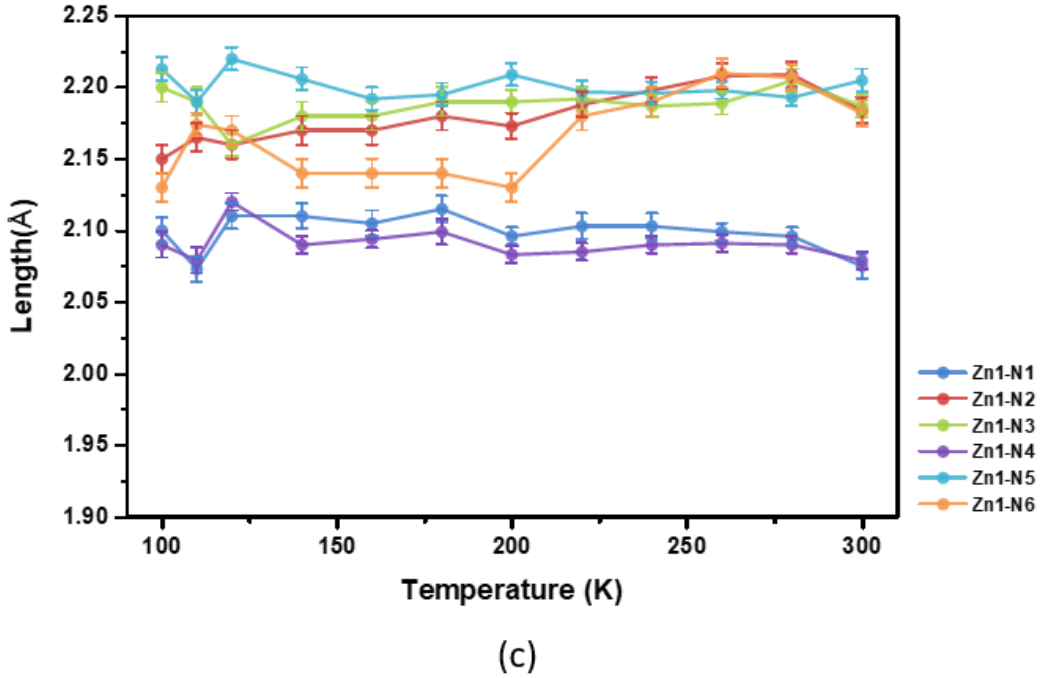

(c)

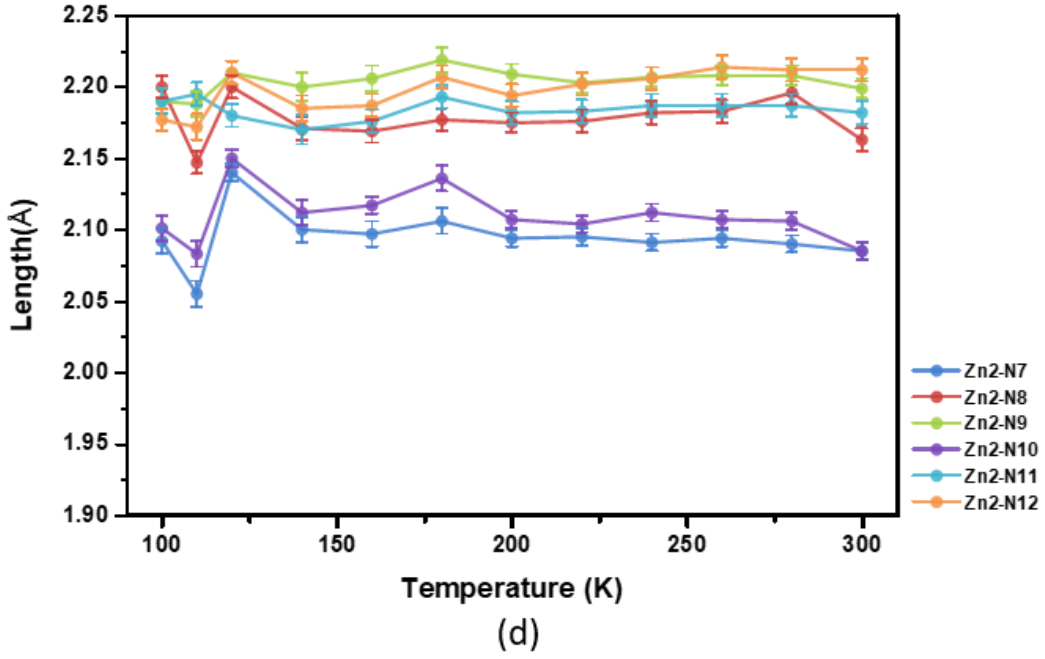

(d)

Figure III-4 Continued

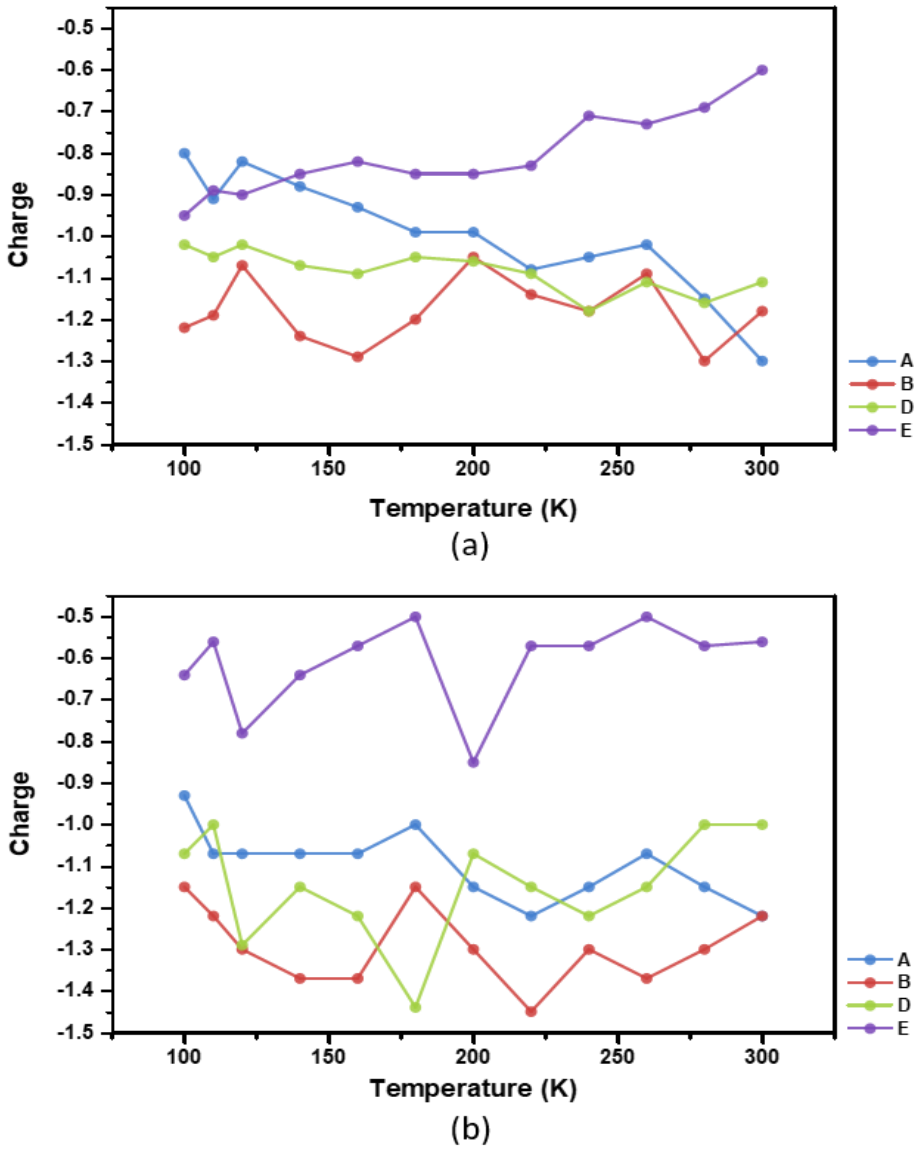

Figure III-5 Temperature dependence of charges on TCNQ units in (a) compound 6 and (b) compound 7.

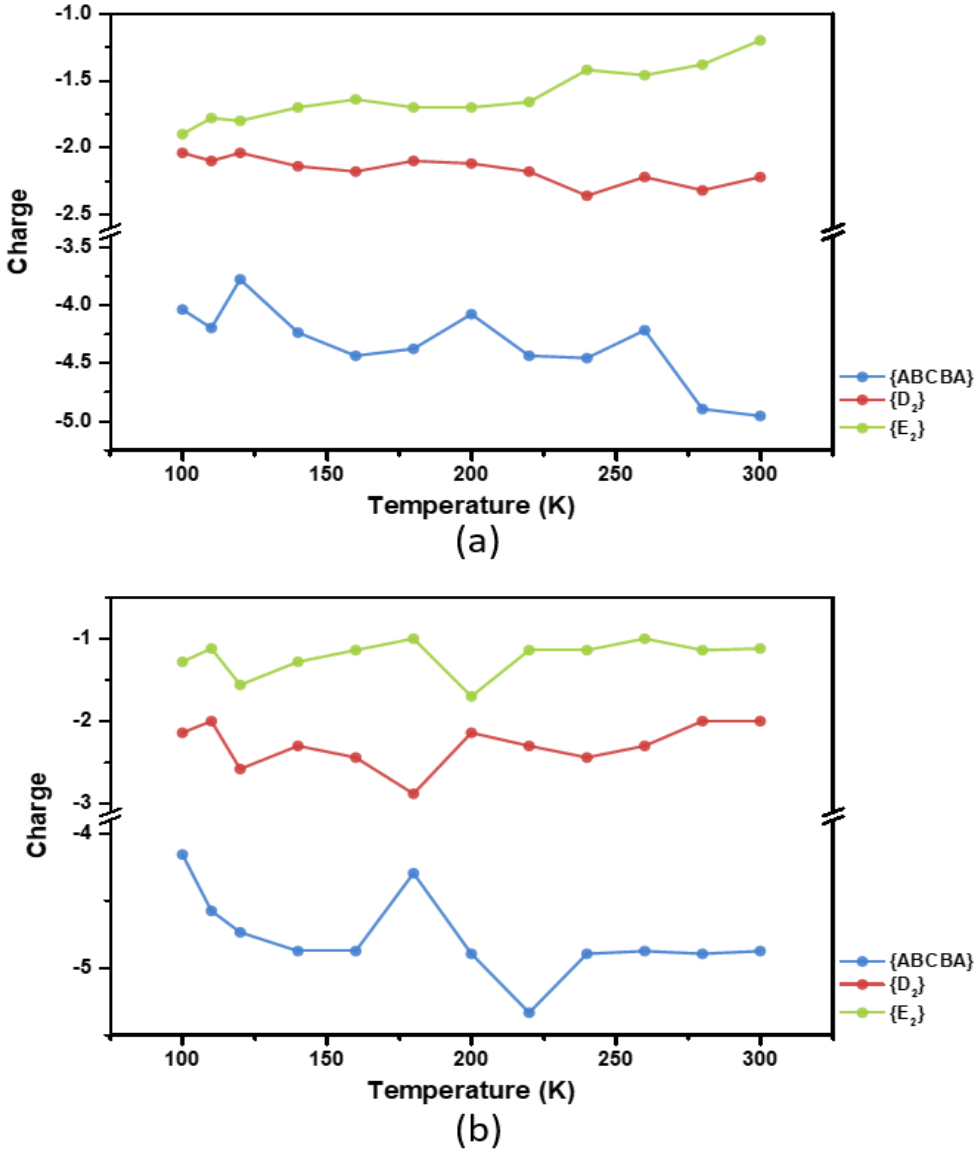

Figure III-6 Temperature dependence of charges on TCNQ stacking modes in (a) compound 6 and (b) compound 7.

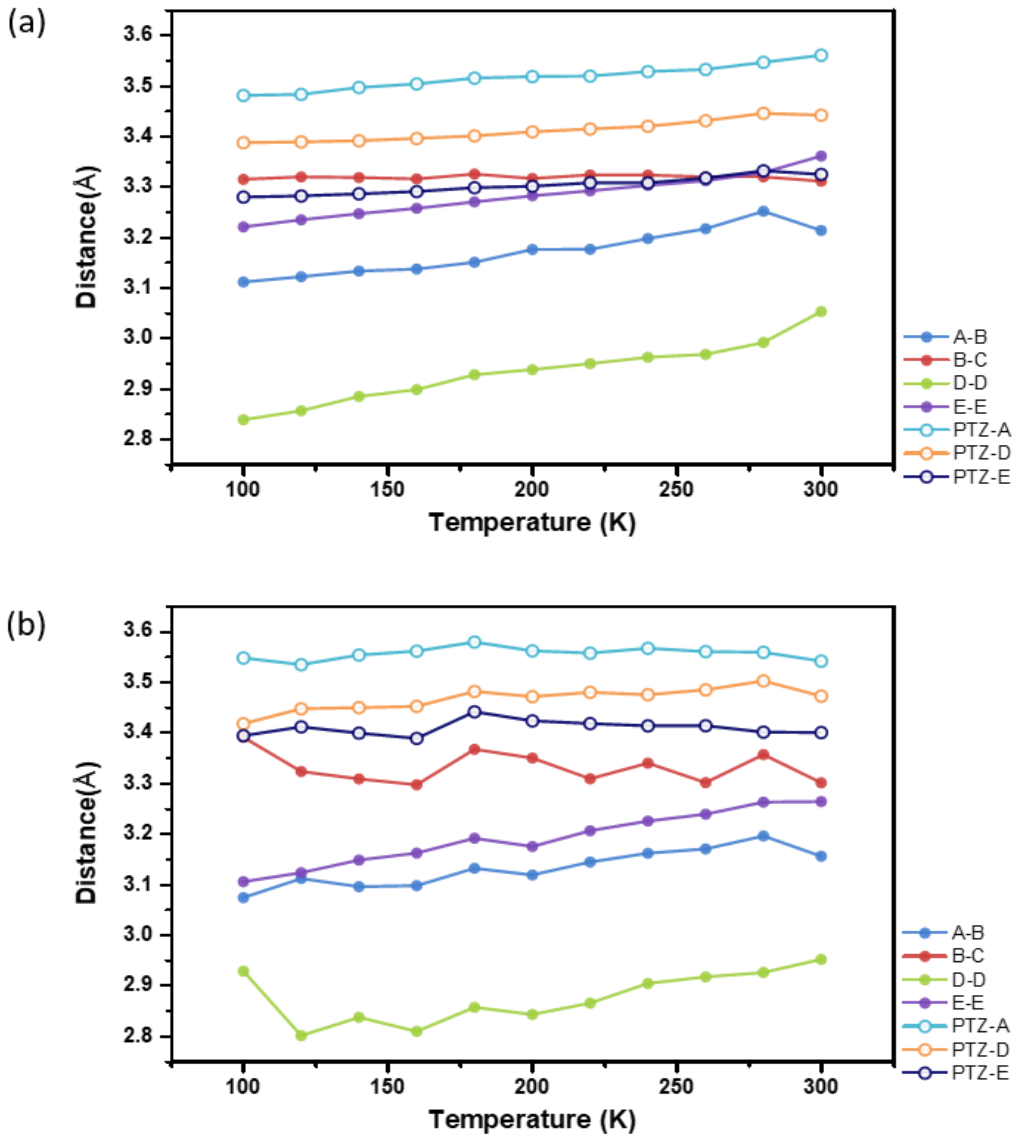

Figure III-7 Intermolecular distances between TCNQ and PTZ groups in compound (a) 6 (b) 7.

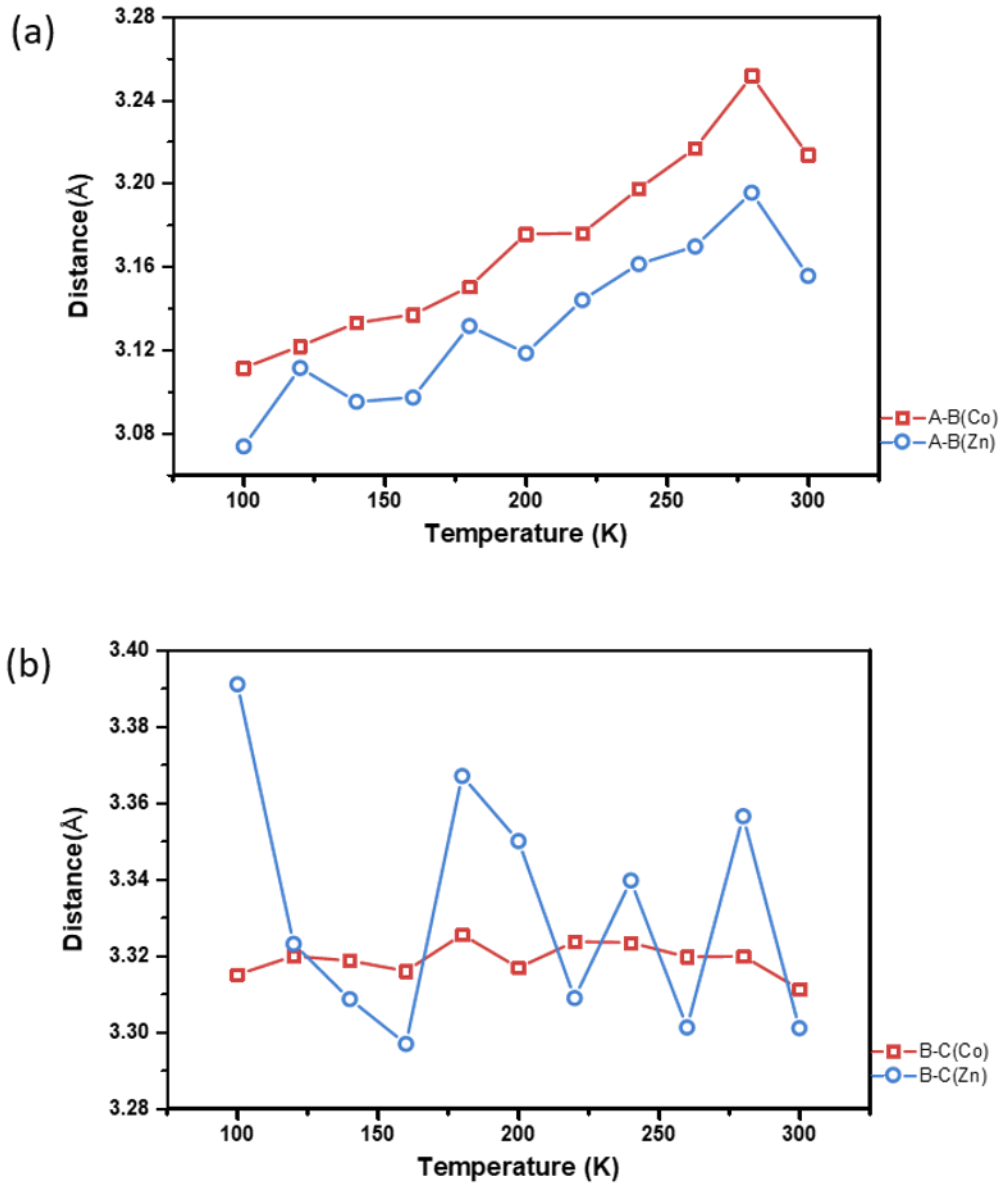

Figure III-8 Temperature-dependent TCNQ-TCNQ interplanar spacing between (a) A-B, (b) B-C, (c) D-D and (d) E-E in compound 6 and 7.

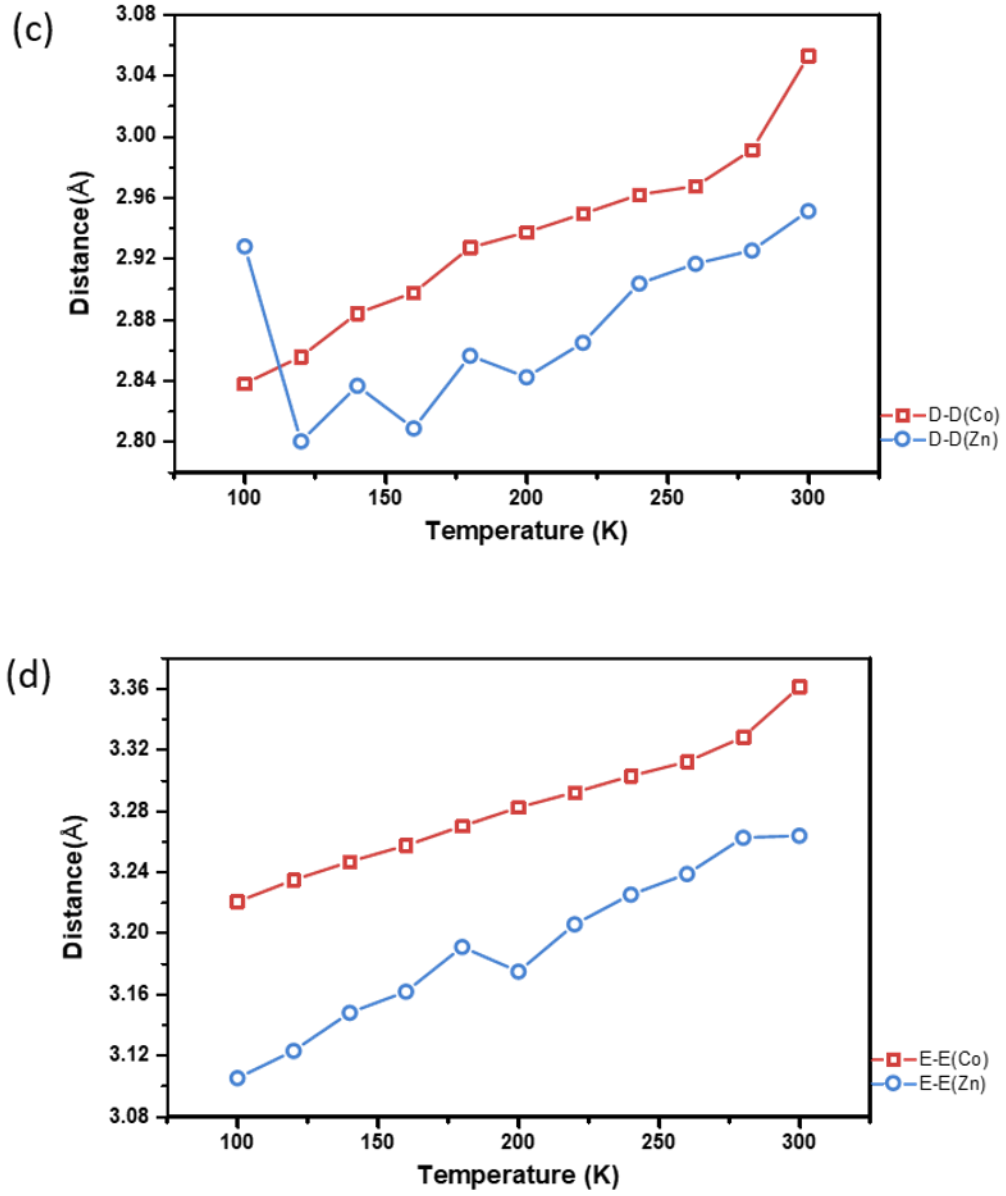

Figure III-8 Continued

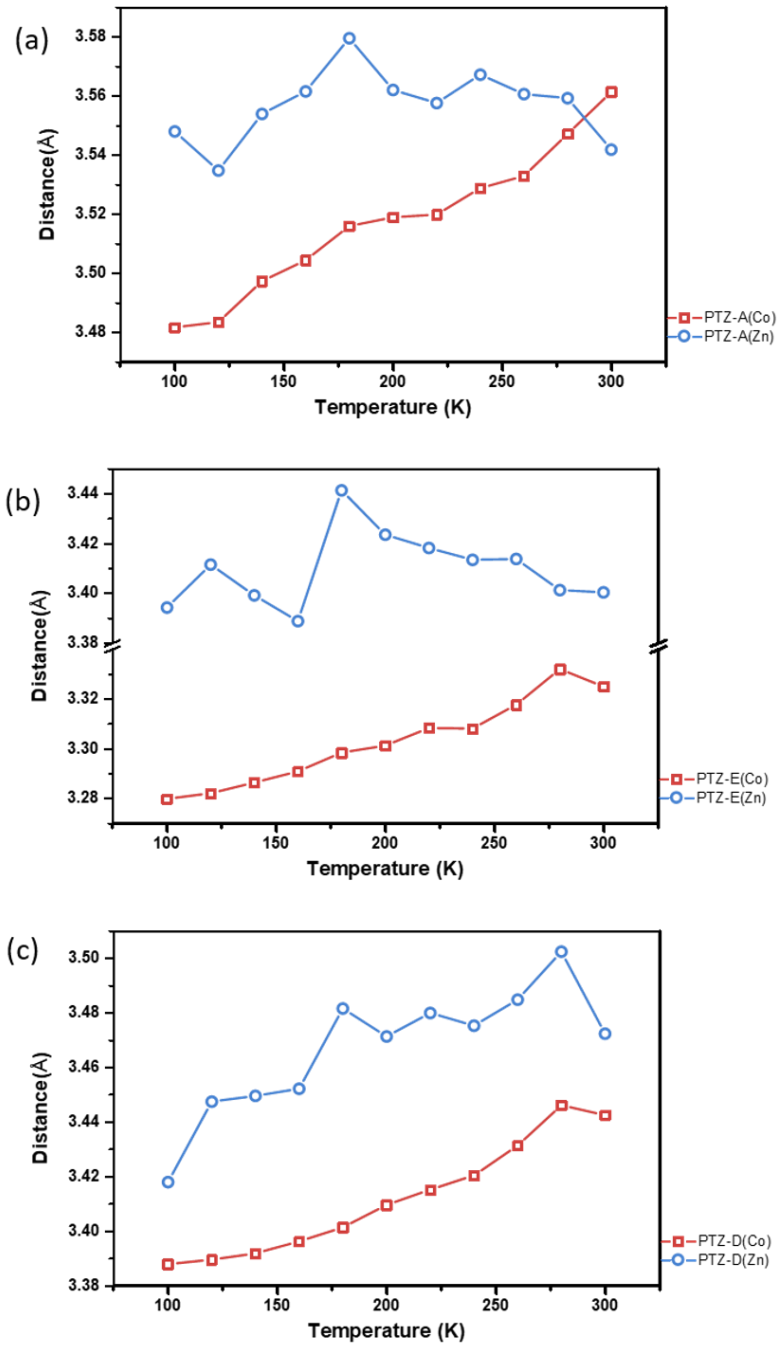

Figure III-9 Temperature-dependent TCNQ-PTZ interplanar spacing between (a) PTZ-A, (b) PTZ-D and (c) PTZ-E in compound 6 and 7.

Results and Discussion

Structural Characterizations

Crystals of $[Co^{II}(PTZ\text{-}tpy)_2](BF_4)_2\cdot 2MeCN\cdot Et_2O$(**4**) and $[Zn^{II}(PTZ\text{-}tpy)_2](BF_4)_2\cdot 2MeCN$(**5**) adopt the monoclinic space group $P2_1/c$ with similar unit cell parameters. (Table III-1) The metal centers are in compressed pseudo-octahedral coordination environments. The axial Co-N distances (1.867(3) Å and 1.914(3) Å) fall into the range between high-spin Co^{II} and low-spin Co^{II} compounds which indicates spin-crossover behavior is occurring for the $[Co^{II}(PTZ\text{-}tpy)_2]^{2+}$ moiety. The axial Zn-N distances (2.070(3) Å and 2.084(3) Å) are longer which is not unusual given that the Zn^{II} ion has a d^{10} closed shell electronic configuration which fills all of the e_g antibonding orbitals. Crystals of $[Co(PTZ\text{-}tpy)_2]_2(TCNQ)_{4.5}\cdot 2.5MeCN$ (**6**) and $[Zn(PTZ\text{-}tpy)_2]_2(TCNQ)_{4.5}\cdot 2.5MeCN$ (**7**) adopt the P-1 space group and are isostructural with similar unit cell parameters at 110 K. Pseudo-merohedral twinning was resolved in order to solve both structures. The twin laws for **6** and **7** were calculated by PLATON software as [-1 0 0 0 -1 0 0.403 0.479 1] and [-1 0 0 0 -1 0 0.386 0.447 1] with BASF values as 0.222 and 0.325 respectively. There are two different $[M(PTZ\text{-}tpy)_2]^{2+}$ moieties in each asymmetric unit. (Figure III-1) The M-N bond lengths of the coordination spheres are listed in Table III-2. For the Zn^{II} analog, **7**, the Zn-N bond lengths range from 2.06 to 2.19 Å for the two different moieties are very similar to each other and are nearly identical to the ones in **5**. In contrast, the Co-N bond distances for Co1 and Co2 are significantly different from each other. For Co1, the axial Co-N bond distances are 2.028(6) Å (Co1-N1) and 2.027(6) Å (Co1-N4) which are close to the Zn-N bond

distances in **5** and **7** and fall into the category of high-spin Co^{II}. On the other hand, Co2-N7 (1.875(6) Å) and Co2-N10 (1.937(6) Å) are shorter and are compatible with low-spin Co^{II} which is similar to the values in **4**.

Similar packing modes of TCNQ moieties are observed for the $[M(PTZ\text{-}tpy)_2]_2(TCNQ)_{4.5}\cdot 2.5MeCN$ compounds (M = Co for **6** and M = Zn for **7**). Four (denoted as A, B, D and E) and one-half (denoted as C with 0.5 occupancies) TCNQ molecules are in the asymmetric unit with three different packing styles. (Figure III-2) Unlike most of the reported stacking modes, TCNQ moieties in **6** and **7** exhibit a mixed-stacking pattern with phenothiazinyl(PTZ) groups. The TCNQ moieties of type A, B and C stack with the PTZ group P_1(on M1) and P_2(on M2) and form columns in the (002) plane which propagate along the [120] crystal direction with a $\{\ldots P_2P_1ABCBAP_1P_2\ldots\}$ repeat pattern. The interplanar distances between different TCNQ moieties and phenothiazinyl (PTZ) groups are compiled in Table III-3 and III-4. The short distances between TCNQ, range from ~2.8 to 3.3 Å, are an indication of $\pi\cdots\pi$ interactions between TCNQ units. The molecular plane of TCNQ-C passes through the inversion center at (0,0,1/2) which is at half-occupancy in the asymmetric unit which leads to a positional disorder of TCNQ-C. Apart from this face-to-face stacking feature, side-by-side packing along the ***a*** axis is also observed. (Figure III-3 (a)) The repeat unit consists of three layers (L_1: $\{\ldots P_1AP_1AP_1A\ldots\}$; L_2: $\{\ldots P_2BP_2BP_2B\ldots\}$ and L_3: {…SolvCSolvCSolvC…}) and propagate as $\{\ldots L_1\ L_2\ L_3\ L_2\ L_1\ldots\}$. The L_1 and L_2 layers consist of an alternating repeat unit of phenothiazinyl groups and TCNQ whereas in L_3 the acetonitrile solvent is present instead of the phenothiazinyl group.

The packing fashion of D and E in (001) planes are different from the ones in the (002) planes. The phenothiazinyl group, P_3, on M1, stacks with D along the ***a*** axis as {…P_3DDP_3…}. (Figure III-3 (b)) Two type-D TCNQ units are correlated by the inversion center as a π-dimers. Short contacts between D and P_3 are observed. In contrast, instead of packing as columns, TCNQ-E forms discrete {P_4EEP_4} moieties with a $(TCNQ)_2$ π-dimer sandwiched between two P_4 (on M2) phenothiazinyl groups. No face-to-face packing between two P_4 groups is observed.

As dictated by the stoichiometry of $[M^{II}(PTZ\text{-}tpy)_2]_2(TCNQ)_{4.5}$ (**6** and **7**), the TCNQ moieties are in partially charged states: 4.5 TCNQ moieties share four negative charges. The well-known empirical Kistenmatcher's formula was used to estimate the charges on different TCNQ species (Table III-5 and III-6). For **6** (M = Co) at 110K; the negative charges on A (-0.75), B (-1.04), D (-1.05) and E (-0.93) are close to -1 whereas C (+0.11) is essentially in its neutral form. The total charges in **6** add up to -3.72 which corresponds well with the +4 charge of the $[Co^{II}(PTZ\text{-}tpy)_2]^{2+}$ moieties. Thus, three different types of TCNQ triads observed in the solid-state structure of **6** can be described as a pentamer $\{ABCBA\}^{4-}$ and two dimers, $\{D_2\}^{2-}$ and $\{E_2\}^{2-}$. Interestingly, the estimated charges of TCNQ moieties in **7** reveal a different distribution. The charge on D (-1.06) remains almost unchanged and the charges on A (-0.96), B (-1.27) and C (-0.40) indicate that the pentamer $\{ABCBA\}^{5-}$ has a total of -5 charges instead of -4. The charge on E (-0.55) also suggests a different oxidation state for $\{E_2\}^{-}$, namely that the isolated $[TCNQ_2]^{-\cdot}$ dimer shares only one negative charge. Although the unit cell

parameters and packing styles are very similar to each other, the charge state of TCNQ triads are clearly different.

In order to investigate the SCO behavior of $[Co^{II}(PTZ\text{-}tpy)_2]^{2+}$ moieties in **6**, temperature-dependent single-crystal X-ray diffraction studies were performed with a synchrotron radiation source from 100-300 K. The Co1-N bond lengths (Figure III-4 (a)) exhibit moderate temperature dependence for all six bonds from 100-300 K which is an indication that the Co1 center remains in the high-spin state over this temperature range. On the contrary, two axial (Co2-N7, from 1.93 to 2.02 Å, and Co2-N10, from 1.98 to 2.03 Å) and two equatorial (Co2-N8, from 2.05 to 2.10 Å, and Co2-N9, from 2.05 to 2.13 Å) Co2-N bonds gradually increase as the temperature increases and approach the value of the Co1-N bond distances, (Figure III-4 (b), Table III-7) which reveals spin-crossover behavior for the Co2 moiety. No significant temperature dependence for $[Zn^{II}(PTZ\text{-}tpy)_2]^{2+}$ moieties in **7** are observed for the Zn1-N and Zn2-N bonds. (Figure III-4 (c) and (d)).

The temperature-dependent charge distributions were evaluated by using the empirical Kistenmatcher formula. (Figure III-5) For compound **6** ($M = Co^{II}$), significant trends in temperature dependence were observed. The negative charge on type A increases from -0.8 to -1.3 whereas the negative charge on type E decreases from -0.95 to -0.60, which becomes closer to the charge on E in the case of **7** at 110 K. In contrast, the charge on type D decreases only slightly from -1.02 to -1.11 as the temperature increases and the charge on B varies from -1.18 ± 0.13 with no significant temperature dependence. The evaluated charge on type C (Table III-8 and III-9) is less reliable due to

the low precision of C-C bond lengths induced by the disorder of TCNQ which resides on an inversion center. Therefore, it is not valid to evaluate the charge on type C directly from the empirical formula. Nevertheless, information about the charge state of type C moieties can be ascertained from the known charges on the $[Co^{II}(PTZ\text{-}tpy)_2]^{2+}$ moieties and the stoichiometry of the unit cell contents. The sum of negative charges on A, B, D and E have a variation of -4.06 ± 0.25 which corresponds well with the total charge (+4) for two cationic $[Co^{II}(PTZ\text{-}tpy)_2]^{2+}$ moieties in a crystallographic asymmetric unit; this assessment indicates that type C TCNQ remains essentially neutral over the temperature range of 100-300 K.

The evaluation of TCNQ charges for compound **7** ($M = Zn^{II}$) are relatively less accurate as the precision of C-C bond lengths (~0.02 Å) are less than those for **6** (~0.01 Å). Nevertheless, several conclusions of temperature dependence can be extracted from a charge state analysis. The total charges on A, B, D and E are approximately -4.15 ± 0.36 which agrees well with the total charge on the cationic counterions but with larger variations and overestimations compared to **6**, an indication that the type C TCNQ is in its neutral form as in the case of **6**. Charges on B (-1.29 ± 0.16) and D (-1.15 ± 0.29) in **7** are also close but larger than the ones in **6**. The most significant difference between **6** and **7** is the temperature dependence of charges on TCNQ type A and E. No significant increase/decrease trends of negative charges on type A and E were observed in compound **7** compared to the ones in **6**. The negative charge on A varies over the range of -1.10 ± 0.17 and is -0.60 ± 0.25 for type E.

From the TCNQ charge state analysis described above, the temperature dependence of **6** and **7** can be summarized as follow:

(1) The summation of charges on all TCNQ units in the asymmetric units are all approximately -4, which indicates that the type C TCNQ is in its neutral form ($TCNQ^0$) for both **6** and **7**.

(2) Type B TCNQ is in the anionic radical form for both **6** and **7** over the temperature range of 100-300 K.

(3) Type A TCNQ remains in its $TCNQ^{\cdot -}$ form over the investigated temperature range for **7** whereas an increase of negative charge (-0.8 to -1.3) for **6** is observed with increasing temperature. Thus, the pentamer {ABCBA} changes from $\{ABCBA\}^{4-}$ to $\{ABCBA\}^{5-}$ in **6** as the temperature increases, whereas it remains in $\{ABCBA\}^{5-}$ form for the compound **7** case. (Figure III-6)

(4) Type D TCNQ is in its $\{D_2\}^{2-}$ form and does not exhibit significant temperature dependence in the cases of **6** and **7**.

(5) The charge on the type E TCNQ decreases from -0.95 to -0.60 for **6** as the temperature increases, which indicates a transition of the TCNQ charge state from $TCNQ^{\cdot -}$ to $TCNQ^{-0.5}$ (from $\{E_2\}^{2-}$ to $\{E_2\}^{\cdot -}$) whereas the TCNQ dimer is most likely in the $\{E_2\}^{\cdot -}$ form in compound **7**. This evidence supports the conclusion that a temperature-dependent electron transfer occurs from the $\{E_2\}$ dimer to the {ABCBA} pentamer as the temperature increases for **6** while no significant changes of the TCNQ charge states occur for **7**.

The temperature-dependent intermolecular TCNQ-TCNQ and TCNQ-PTZ distances were also investigated for **6** and **7** (Figure III-7, Table III-10, III-11), and were found to be similar. The spacing between A-B, D-D and E-E pairs (Figure III-8 (a), (c) and (d) respectively) and the negatively charged $(TCNQ)_2^{\delta-}$ dimers exhibit temperature-related trends over the temperature range of 100-300 K. The thermal expansion of the interplanar spacing can be rationalized by the thermally activated inter-layer vibrational modes of pancake bonding.[203-205] On the contrary, the B-C spacing, which is larger than other interplanar distances between TCNQ units, exhibits less temperature dependence (Figure III-8 (b)). Such differences are related to the weaker intermolecular interactions between negatively charged type B TCNQ units and the neutral type C TCNQ.

In considering the TCNQ-PTZ distances, different trends are observed for **6** and **7** (Figure III-9). For the packing $\{\ldots P_3DDP_3\ldots\}$ only involves the phenothiazinyl groups from Co1/Zn1 units and the D-P_3 spacing increases as the temperature increases for both **6** (3.388 to 3.446 Å) and **7** (3.418 to 3.502 Å) (Figure III-9 (b)). The distances between type A(E) TCNQ and the PTZ groups (Figure III-9 (a) and (c)) increase from 3.482 to 3.561 Å (3.280 to 3.332 Å) as the temperature is raised for **6** but there is no significant temperature-dependent trend for **7**. In terms of the two types of packing cases observed for **6**, $\{\ldots P_2P_1ABCBAP_1P_2\ldots\}$ and $\{P_4EEP_4\}$, both involve the phenothiazinyl groups, P_2 and P_4, on the spin-crossover Co2 moiety. The spin-crossover behavior of Co2 corresponds to the temperature dependence of the TCNQ-PTZ intermolecular spacing, as less temperature dependence is observed for **7** with the Zn^{II} ions.

Table III-12 EPR fitting parameters: *g* values, ^{59}Co hyperfine coupling parameters (*A*) and line width (lw) of compound 4 in solid state.

T/K	g_x	g_y	g_z	g_{aver}	A_x/ 10^{-4} cm^{-1}	A_y/ 10^{-4} cm^{-}	A_z/ 10^{-4} cm^{-}	lw/ mT
4	1.99	2.09	2.32	2.14	1.6	28.9	35.7	18.5
25	2.00	2.08	2.31	2.13	1.6	28.9	35.7	15.0
50	2.02	2.07	2.31	2.14	1.5	21.4	48.2	16.1
75	2.02	2.07	2.31	2.14	1.5	21.4	48.2	14.0

Table III-13 EPR fitting parameters: *g* values, ^{59}Co hyperfine coupling parameters (*A*) and line width (lw) of compound 6 in solid state.

T/K	g_x	g_y	g_z	g_{aver}	A_x/ 10^{-4} cm^{-1}	A_y/ 10^{-4} cm^{-1}	A_z/ 10^{-4} cm^{-1}	lw/ mT
4	2.02	2.04	2.35	2.14	6.3	3.7	22.6	36.6
25	2.03	2.03	2.35	2.14	4.2	4.9	24.9	34.1
50	2.03	2.02	2.35	2.14	2.9	3.0	23.9	34.1
75	2.02	2.03	2.33	2.13	3.9	4.1	34.1	26.1
RT	N.A.							

T/K	g_{rad}	lw/ mT	percentage
4	N.A.		
25	N.A.		
50	2.00	6.8	0.51%
75	2.00	6.8	0.50%
RT	2.00	6.8	N.A.

Table III-14 EPR fitting parameters: *g* values and line width of compound 7 in solid state.

T/K	g_{iso}	lw/ mT
4	2.000	1.97
25	2.000	1.62
50	2.000	1.91
75	2.000	1.58
RT	2.000	2.00

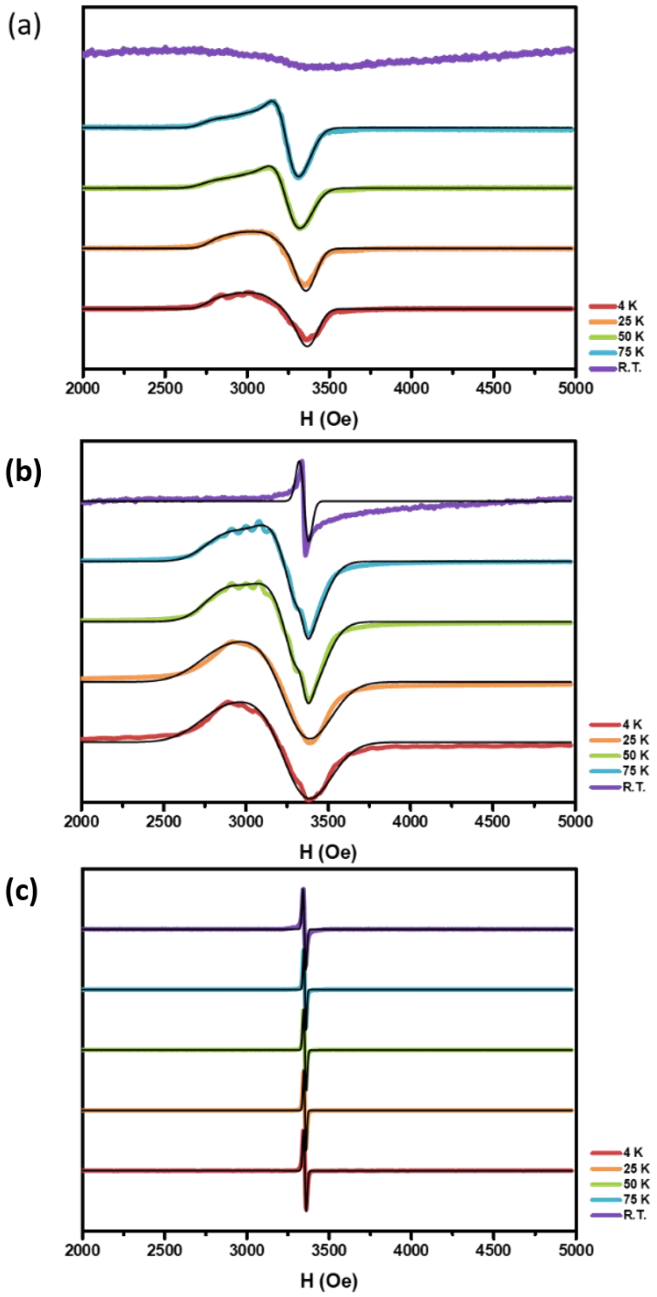

Figure III-10 Temperature-dependent X-band EPR spectra of (a) 4, (b) 5 and (c) 6. The black solid lines represent the best fit with the parameters in table III-12, III-13 and III-14. The resonance intensities were all scaled by the maximum intensity.

Electron Paramagnetic Resonance (EPR) Studies

EPR is a powerful tool for determining g factors for paramagnetic species in the solid state. Temperature-dependent X-band EPR measurements were conducted on crystalline powders of **4**, **6** and **7** from 4–75 K and at room temperature (Figure III-10). Compound **4** (Figure III-10 (a)) exhibits typical resonance patterns for L.S. Co^{II} (S = 1/2) at 4 K with rhombic g tensors under cryogenic temperatures whereas only a weak broad background is observed at room temperature due to the transition of Co^{II} centers from L.S. (S = 1/2) to H.S. (S = 3/2) and rapid spin relaxation at room temperature. The resonance of H.S. Co^{II} is not visible due to its extremely short relaxation time.[206-207] Fittings of the EPR spectra were performed with the EasySpin 5.2.28 package.[208] The parameters from the best fits are summarized in Table III-12. The g_x, g_y and g_z values for **4** at 4 K are 1.99, 2.09 and 2.32 respectively with ^{59}Co (I = 7/2) hyperfine coupling constants (A_x, A_y and A_z) being 1.6, 28.9 and 35.7 × 10^{-4} cm^{-1}. The estimated hyperfine coupling constants are qualitative values as the coupling patterns are not fully resolved with X-band EPR data on crystalline powder samples. Nevertheless, the magnitudes of g_i and A_i (i = x, y, z) values are similar to the reported ones for Co^{II}(bis-terpy) compounds in the literature.[209] No significant temperature dependence of the g_i values were observed from 4-75 K.

.

Similar EPR patterns were observed for **6** with evaluated g_i and A_i (i = x, y, z) values of (2.02, 2.04, 2.35) and (6.3, 3.7, 22.6) × 10^{-4} cm^{-1} respectively at 4 K. No contribution from free radicals was observed at 4 K. The g_i values also exhibit little variation up to 75 K (Table III-13). Additional shoulder peaks appeared at ~ 3300 Oe at 50 and 75 K which are attributed to the contribution from trace radical species (~0.5 %, g_{iso} = 2.00) of TCNQ (Figure III-10 (b)). In contrast to the EPR spectra collected on **4**, a sharp resonance for a free radical was observed for **6** at room temperature. In the case of compound **7**, a resonance from an organic radical with g_{iso} = 2.000 is observed at all temperatures that were investigated (Figure III-10 (c), Table III-14). The results of EPR measurements correspond well with the temperature-dependent charge distribution on the TCNQ units in **6** and **7** estimated from single-crystal XRD structures.

Table III-15 Fitting parameters of χT vs T plots for 4 and 6 found via the least-squares method.

Compound	**4**	**6**
ΔH (kJ mol^{-1})	3.91	5.12
ΔS (J K^{-1} mol^{-1})	9.83	21.6
χ_{TIP} (emu mol^{-1})	0.0029	0.0019
$T_{1/2}$(K)	397	237

Table III-16 Evaluated temperature-dependent $(TCNQ)_2^{\cdot -}$ radical fraction from charges on type E TCNQ and the reaction constants K.

T/K	charge on E	n_{rad}	K
100	-0.95	0.10	0.01
110	-0.89	0.22	0.06
120	-0.90	0.20	0.05
140	-0.85	0.30	0.13
160	-0.82	0.36	0.20
180	-0.85	0.30	0.13
200	-0.85	0.30	0.13
220	-0.83	0.34	0.18
240	-0.71	0.58	0.80
260	-0.73	0.54	0.63
280	-0.69	0.62	1.01
300	-0.60	0.80	3.20

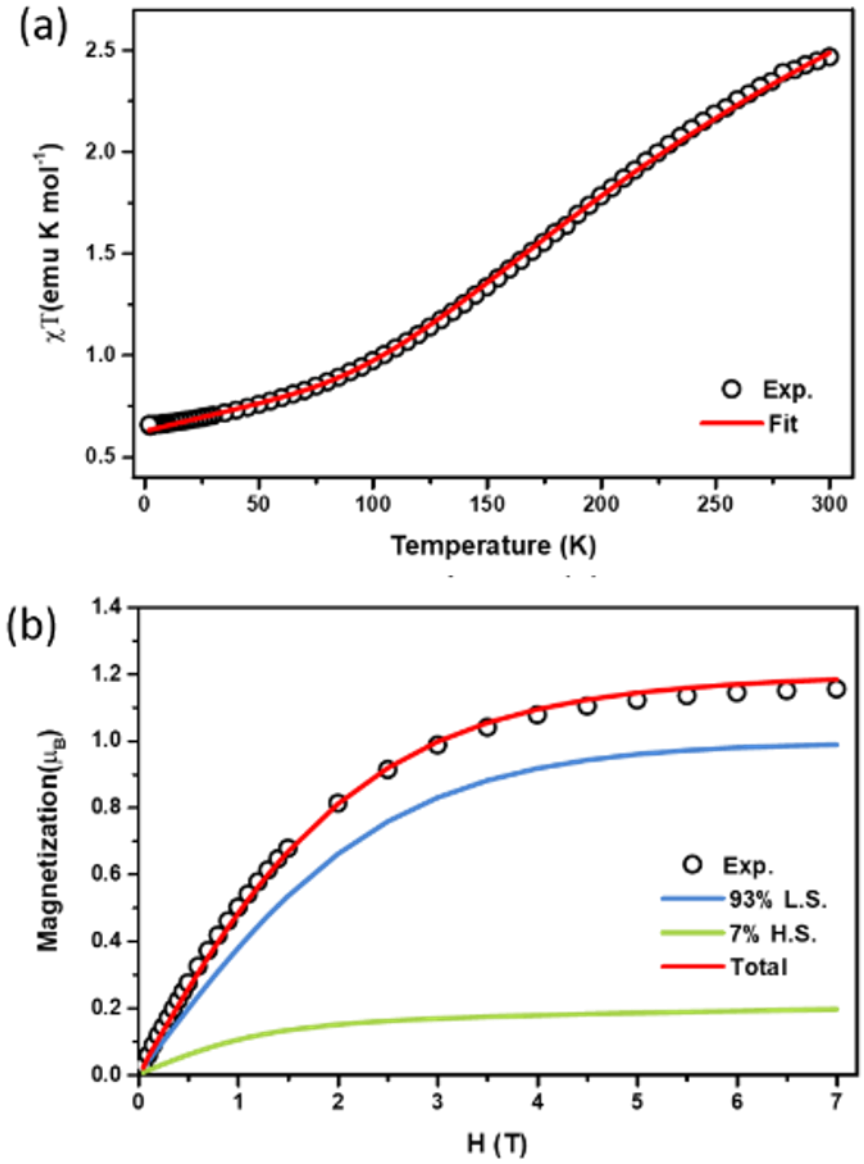

Figure III-11 The χT vs T plots, (a), (c), (e), and the Magnetization vs H plots, (b), (d), (e), for compound 4, 6 and 7 respectively. The open circles represent the experimental data points. The solid lines indicate the theoretical fittings.

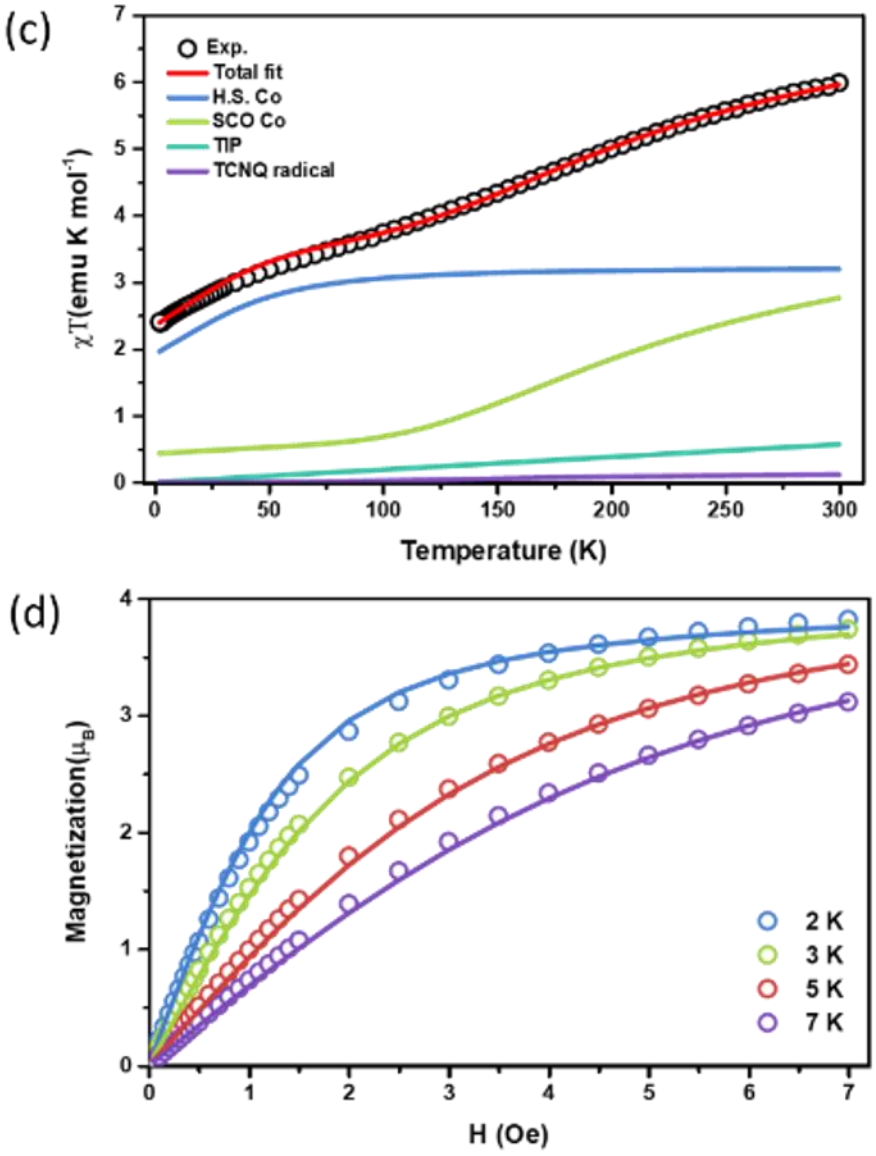

Figure III-11 Continued

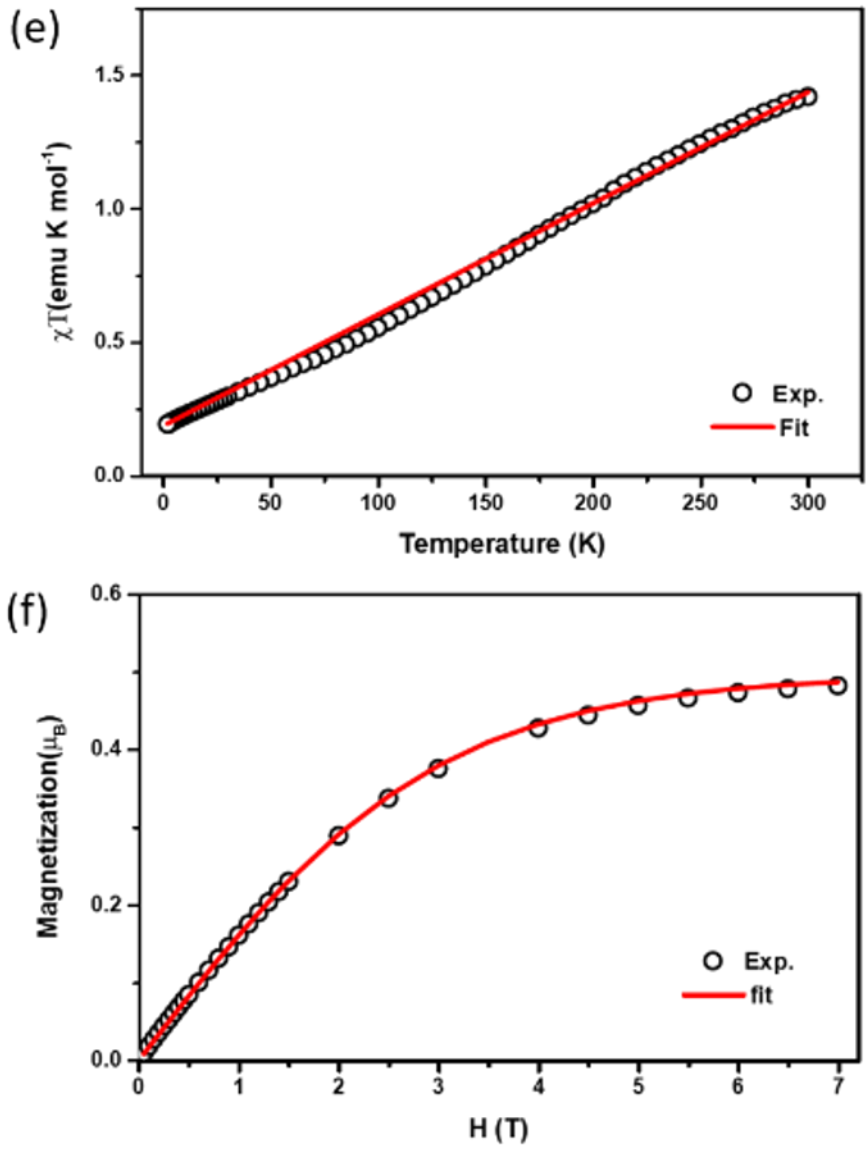

Figure III-11 Continued

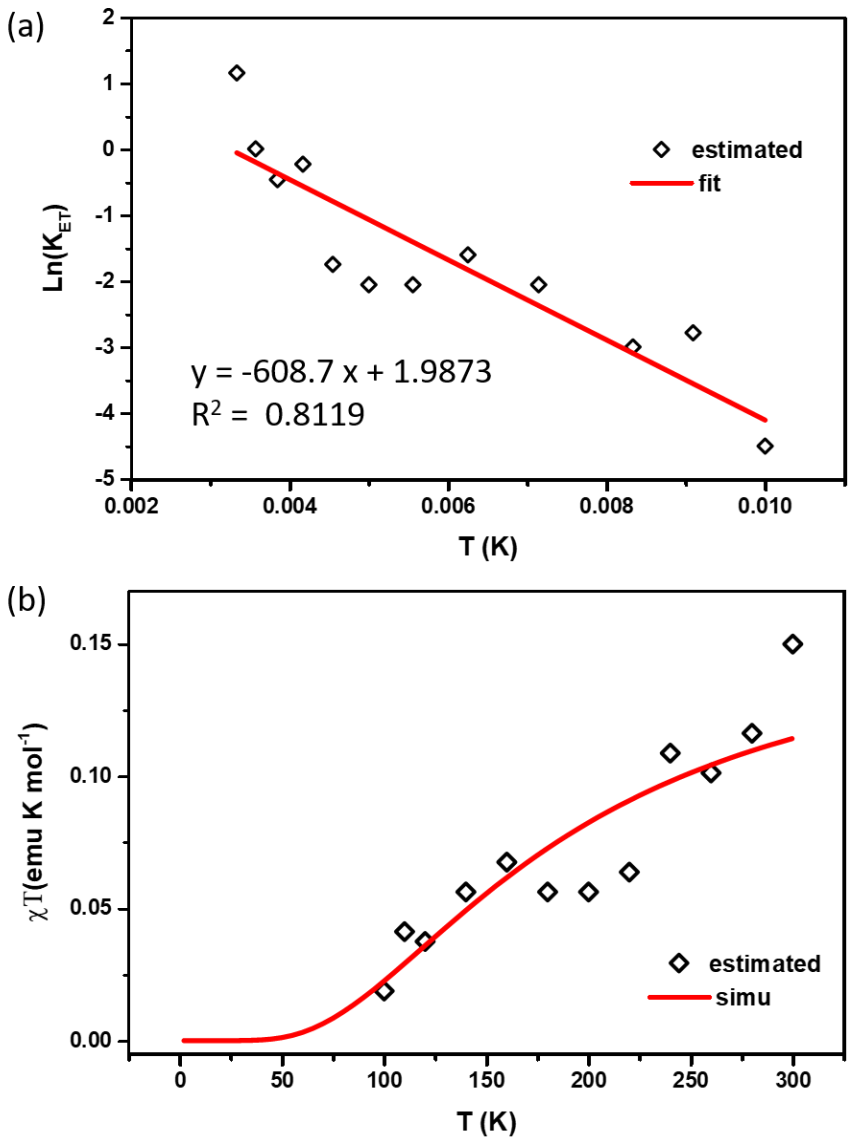

Figure III-12 (a) ln $\left[\frac{n_{rad}^2}{(1-n_{rad})}\right]$ vs 1/*T* plot and (b) the localized radical contribution to χT.

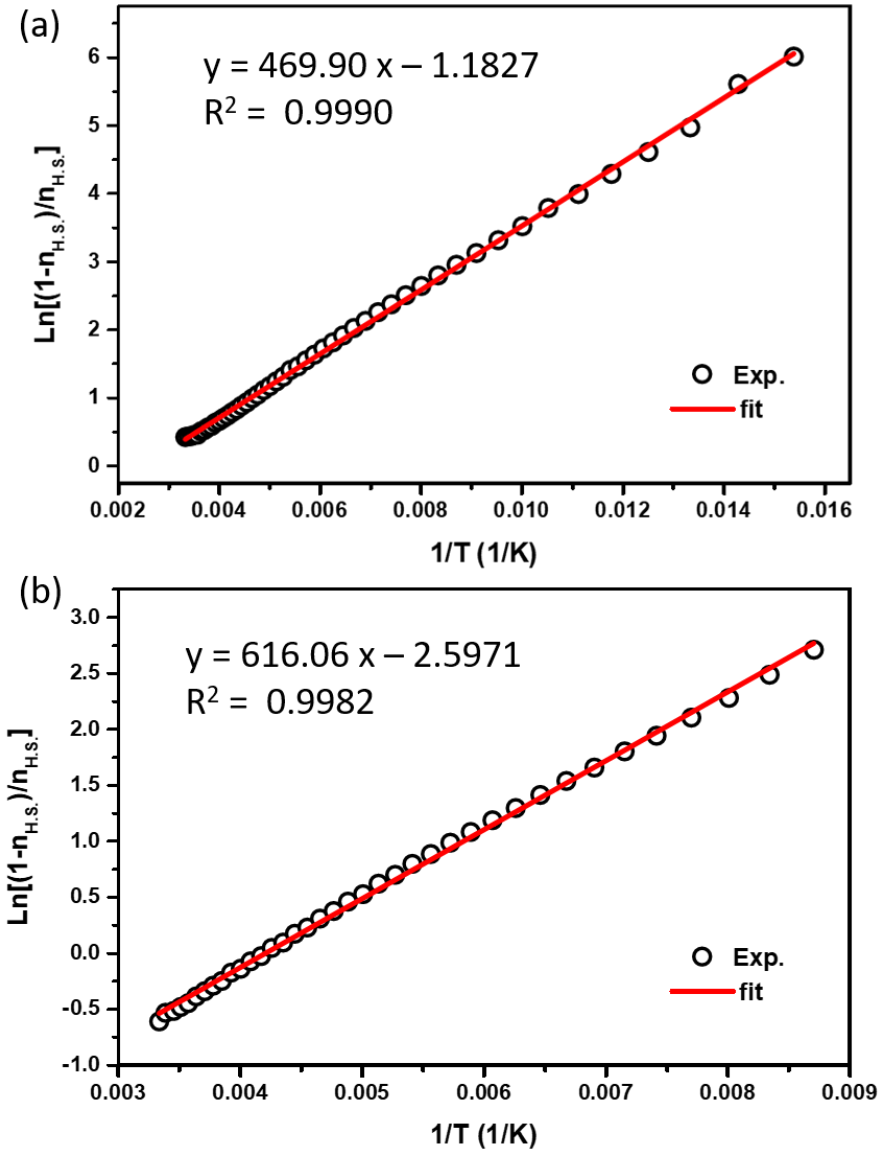

Figure III-13 ln $\left[\frac{1-n_{HS}}{n_{HS}}\right]$ vs 1/*T* plots of (a) 4 and (b) 6 for fitting the SCO thermodynamic parameters.

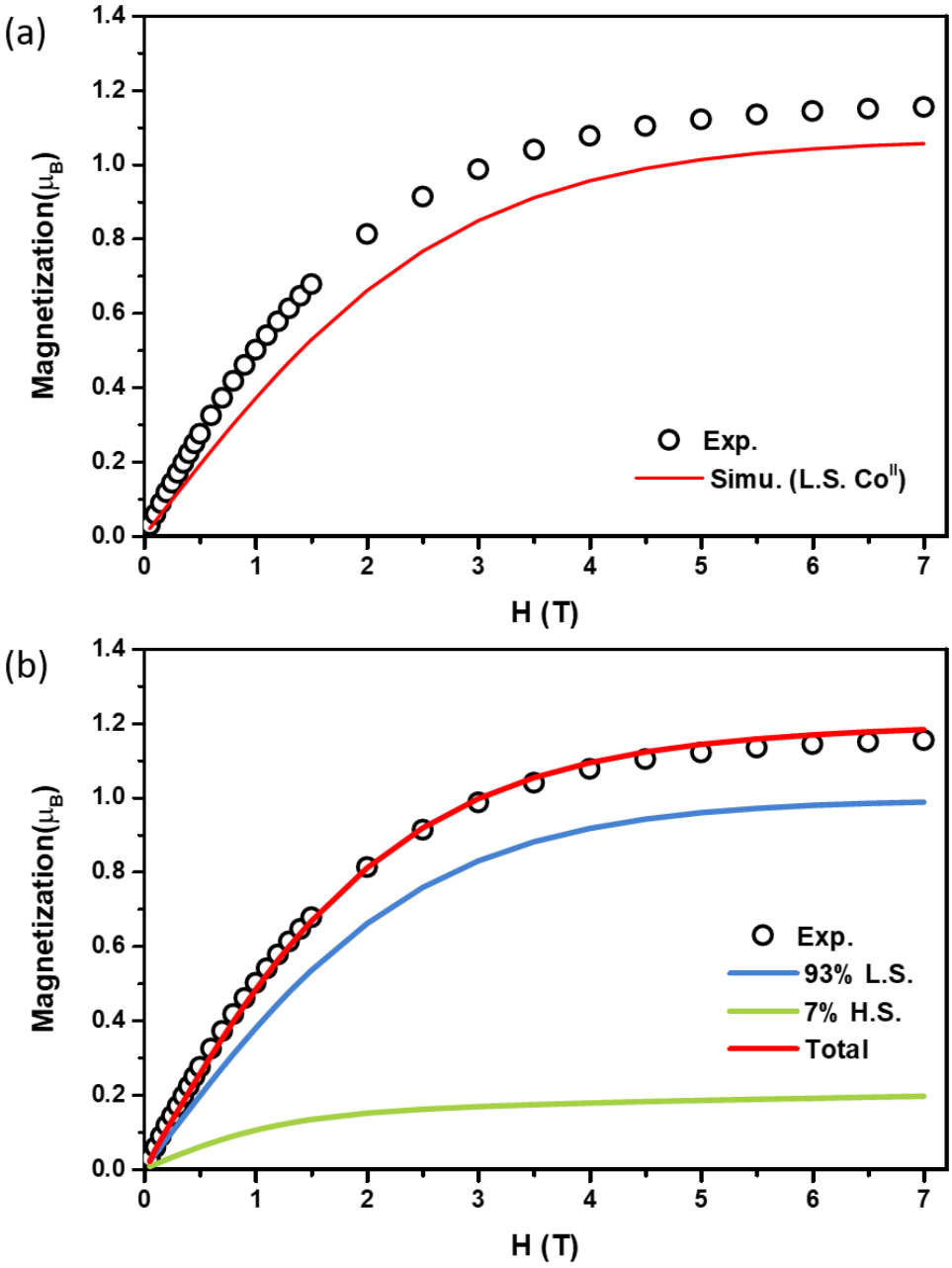

Figure III-14 Magnetization vs magnetic field (H) at 1.8 K of 1 (open circle) and simulation (solid lines) with (a) L.S. Co^{II} (S = 1/2, g_{aver} = 2.14) and (b) 93% L.S. Co^{II} (S = 1/2, g_{aver} = 2.14) and 7% H.S. Co^{II} (S = 3/2, g_{iso} = 2.62 and D = + 44.9 cm^{-1}).

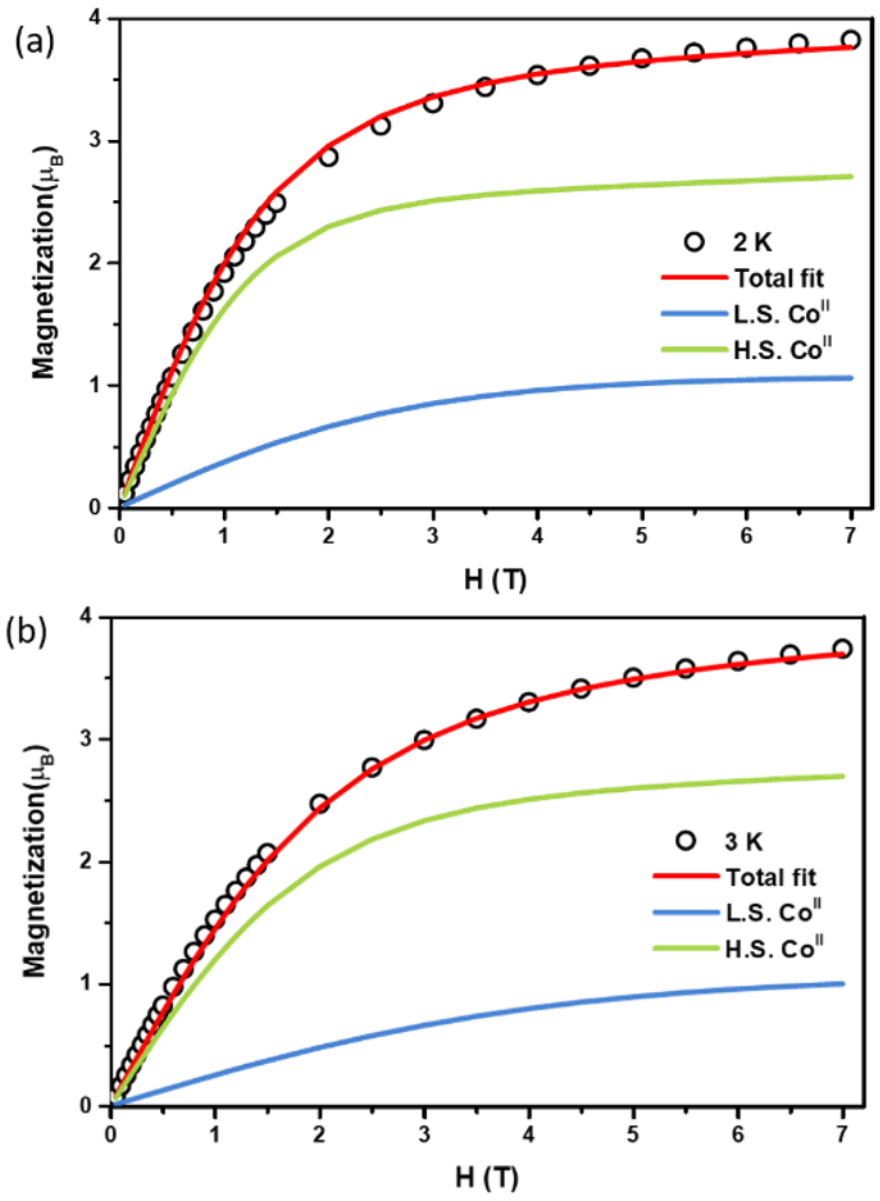

Figure III-15 . Magnetization vs magnetic field (H) at 1.8 K of 6 (open circle) and simulation (solid lines) with L.S. Co^{II} (S = 1/2, g_{aver} = 2.14) and H.S. Co^{II} (S = 3/2, g_{iso} = 2.62 and D = + 44.9 cm^{-1}) at (a) 2 K, (b) 3 K, (c) 5 K and (d) 7 K.

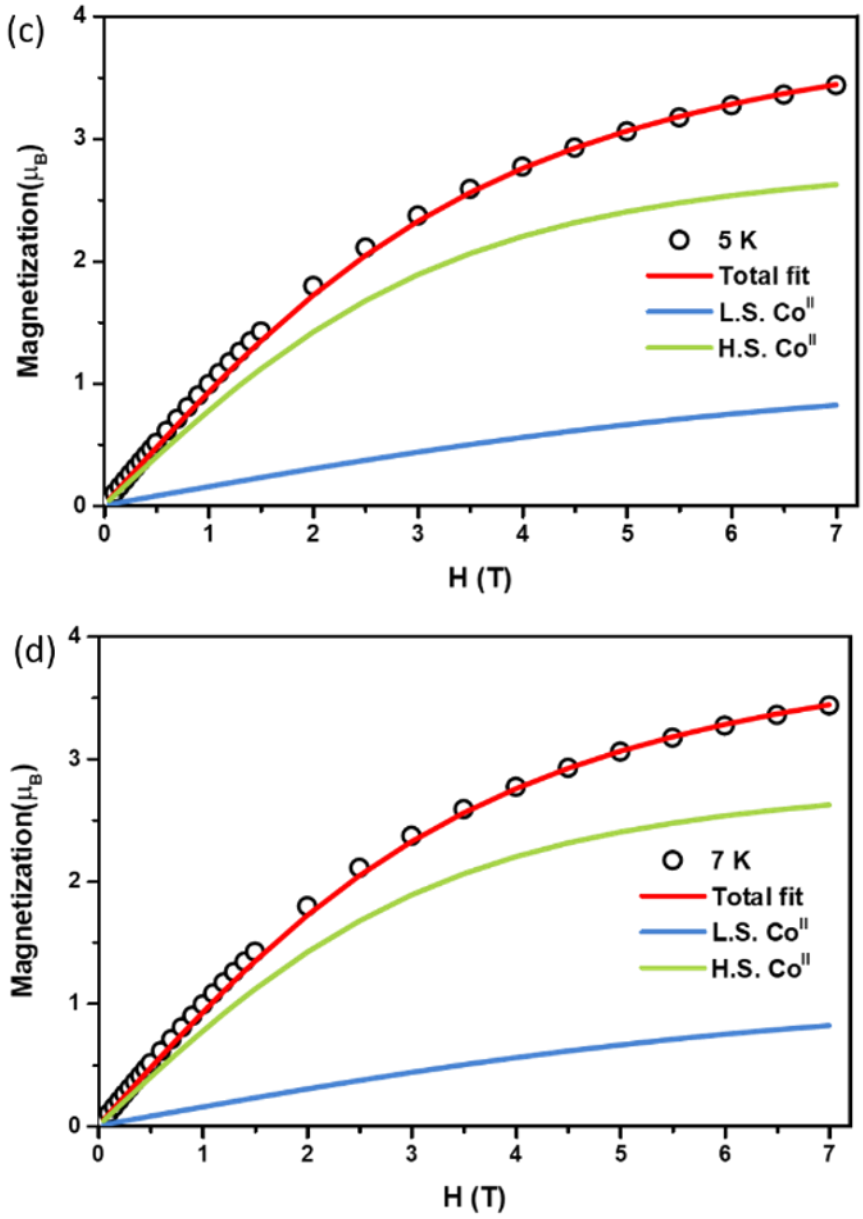

Figure III-15 Continued

Magnetic Properties

Direct current magnetic susceptibility studies of compounds **4**, **6** and **7** were performed with a SQUID magnetometer. A typical spin-crossover behavior for Co^{II} was observed in the case of **4** with χT values increasing from 0.657 to 2.467 emu K mol^{-1} as the temperature is raised from 2 to 300 K (Figure III-11 (a)). The χT value at 2 K is higher than 0.430 emu K mol^{-1} (with g_{ave} = 2.14, from EPR spectra), which suggests an incomplete SCO transition at 2 K which is attributed to defects and/or constraints of the crystal lattice.[18, 167, 172-173] Based on the experimental χT value at 2K, the magnetization curve at 1.8 K (Figure III-11 (b), III-14) can be fit well with 93% L.S. Co^{II} (g_{aver} = 2.14) and 7% H.S. Co^{II} (g_{iso} = 2.62 and D = +44.9 cm^{-1}). The thermodynamic equation, Equation 1.13 was applied for fitting the thermodynamic parameters of the SCO behavior of compound **4**.[210-211] For compound **4**, n_{HS} values at certain temperatures were determined from the equation as follow:

$$n_{HS}(T) = [\chi T - (\chi T)_{LS} - (\chi T)_{TIP}]/[(\chi T)_{HS} - (\chi T)_{LS}] \qquad \textbf{Equation 3.1}$$

Note that the χT value in Equation 3.1 was rescaled by $\chi T' = [\chi T - x(\chi T)_{HS}]/(1-x)$, where x, determined as 7%, is the H.S. Co^{II} fraction that undergoes the incomplete SCO behavior. The χT value of **4** at a certain temperature can be expressed as:

$$\chi T = (1-x)[n_{HS}(\chi T)_{HS} + (1-n_{HS})(\chi T)_{LS} + \chi_{TIP}T] + x(\chi T)_{HS} \qquad \textbf{Equation 3.2}$$

The linear relationships are shown on plots Figure III-13. The slope and the intersection with the y-axis of $\ln\left[\frac{1-n_{HS}}{n_{HS}}\right]$ vs $1/T$ plot are $\Delta H/R$ and $-\Delta S/R$ respectively. A reasonable fit of the SCO behavior of compound **4** can be obtained with

the thermodynamic parameters ΔH = 3.91 kJ mol^{-1} and ΔS = 9.83 J K^{-1} mol^{-1} and $T_{1/2}$ = 397 K (Table III-15). The ΔS is larger than the contribution from a solely electronic spin state transition, ΔS_{el} = 5.8 J K^{-1} mol^{-1} the difference is attributed to contributions from molecular and lattice vibrations.[175, 189, 210-211]

The magnetic behavior of **6** is more complicated, as four paramagnetic spices (H.S. Co^{II}, SCO Co^{II}, localized and delocalized spin centers on TCNQ) coexist in the same crystal lattice. Based on the EPR spectral analysis of compound **6**, the magnetic species that contribute to the magnetization at low temperature are H.S. and L.S. Co^{II} centers. The magnetization vs H curves from 2 to 7 K (Figure III-11 (d) and Figure III-15) can be simulated well with one L.S. Co^{II} (S = 1/2, g_{aver} = 2.14, from EPR) and one H.S. Co^{II} (S = 3/2, g_{iso} = 2.62 and D = +44.9 cm^{-1}) per asymmetric unit. For temperature dependence of the χT curve, the contributions from different magnetic components are described with the equation as follows:

$$\chi T = n_{HS}(\chi T)_{HS} + (1 - n_{HS})(\chi T)_{LS} + n_{HS}(\chi T)_{HS} + (\chi T)_{rad} + \chi_{TIP} T \quad \textbf{Equation 3.3}$$

where $(\chi T)_{HS}$, $(\chi T)_{LS}$, $(\chi T)_{rad}$ and $(\chi T)_{TIP}$ are the χT values for high-spin Co(II), low-spin Co(II), localized TCNQ based radical and temperature-independent paramagnetism. The $(\chi T)_{LS}$ value was fixed as $(\chi T)_{LS}$ = 0.430 emu K mol^{-1} (S = 1/2, g_{aver} = 2.14, from EPR). The $(\chi T)_{HS}$ value is simulated with S = 3/2, g_{iso} = 2.62 and D = 44.9 cm^{-1}. $(\chi T)_{rad}$ was estimated from the charge on type E TCNQ and the relationship between the Gibbs free energy (ΔG) and the equilibrium constant (K). A qualitative thermodynamic model was applied to estimate the contribution of localized TCNQ based radicals to χT values by considering the electron transfer process:

$$(TCNQ)_2^{2-} \rightleftharpoons (TCNQ)_2^{\cdot -} + \{e^{\cdot -}\}_{delocalized}$$ **Equation 3.4**

The reaction constant can be expressed as:

$$K = \frac{n_{rad}^2}{(1-n_{rad})}$$ **Equation 3.5**

where n_{rad} is the fraction of localized radical spices.

The reaction constant can be related to the molar Gibbs free energy (ΔG) and thus the molar enthalpy (ΔH) and molar entropy (ΔS) as follow:

$$\ln K = -\frac{\Delta G}{RT} = -\frac{\Delta H}{RT} + \frac{\Delta S}{R}$$ **Equation 3.6**

A linear regression was used to extract the thermodynamic parameters (Figure III-12 (a)). The slope and the intersection with the y-axis of $\ln\left[\frac{n_{rad}^2}{(1-n_{rad})}\right]$ vs $1/T$ plot are $-\Delta H/R$ and $\Delta S/R$ respectively. The best fit yielded ΔH = 5.06 kJ mol^{-1} and ΔS = 16.5 J K^{-1} mol^{-1} (Table III-16). Thus, the n_{rad} value can be solved by integrating Equitation 3.5 and 3.6 at certain temperatures. The localized radical contribution to χT can be calculated by the following equation:

$$(\chi T)_{rad} = 0.375 \times \frac{n_{rad}}{2}\ emu\ K\ mol^{-1}$$ **Equation 3.7**

The result is shown in Figure III-12 (b). The χT contribution from the localized radical is insignificant (<0.001 emu K mol^{-1}) below 50 K and gradually increases to ~0.11 emu K mol^{-1} (0.18 emu K mol^{-1} for full conversion) at 300K (Figure III-12).

The thermodynamic equation, Equation 1.13 was also applied for the thermodynamic parameters of the SCO behavior of compound **6**.The temperature dependence of n_{HS} values were determined from the equation as follow:

$n_{HS}(T) = [\chi T - (\chi T)_{LS} - (\chi T)_{HS} - (\chi T)_{rad} - (\chi T)_{TIP}]/[(\chi T)_{HS} - (\chi T)_{LS}]$ **Equation 3.8**

The linear relationships shown in the plots Figure. III-13 (b) indicate that the Γ terms are negligible for **6** such that Equation 1.13 can be rewritten as Equation 1.14. The slope and the intersection with the y-axis of $\ln\left[\frac{1-n_{HS}}{n_{HS}}\right]$ vs $1/T$ plot are $\Delta H/R$ and $-\Delta S/R$ respectively. With the fitting parameters of L.S. and H.S. Co^{II} centers and the estimated temperature-dependent localized TCNQ radical contributions obtained above, the SCO behavior and the contributions from a delocalized radical (χ_{TIP}) were fit with ΔH = 5.12 kJ mol^{-1} and ΔS = 21.6 J K^{-1} mol^{-1} with $T_{1/2}$ = 237 K and $\chi_{TIP} = 1.90 \times 10^{-3}$ emu mol^{-1} (Table III-15). The enthalpy (ΔH) and entropy (ΔS) changes for **6** are larger than for **4**. As **4** and **6** have the same SCO moiety, $[Co^{II}(PTZ\text{-}tpy)_2]^{2+}$, these differences can be attributed to additional intermolecular interactions, lattice constraints and available vibration modes present in **6**.

In the case of **7**, the magnetization curve at 2 K can be fit well with one-half of a localized radical spin center (S = 1/2, g = 2.00) (Figure III-11 (f)) per asymmetric unit, but the χT vs T curve has a significant deviation from the Curie law for 0.5 radical centers with S = 1/2, g = 2.00. The strong deviation of the room temperature χT value (1.43 emu K mol^{-1}) from the expected value (0.188 emu K mol^{-1}) and the linear relationship between χT and T indicates a large temperature-independent susceptibility. There are two possible origins of temperature-independent susceptibility (TIP). One is the contribution from the magnetic moments of delocalized electron spins (Pauli paramagnetism) and the other one is the van Vleck TIP caused by state mixing with low

lying magnetic excited states. The latter one is usually observed in the system with heavy elements but not significant for first-row transition metals and organic compounds. Thus, it is more appropriate to attribute the χ_{TIP} value as Pauli paramagnetism (χ_{Pauli}) and, indeed, this phenomenon has been reported in acceptor-doped polymers with electron donors.[212-214] The fitting of magnetic susceptibilities with the equation: $\chi T = C + \chi_{Pauli} T$ yields C = 0.186 emu K mol^{-1} and $\chi_{Pauli} = 4.17\times10^{-3}$ emu mol^{-1} (Figure III-11 (e)). The Curie constant is very close to the expected value (0.188 emu K mol^{-1}) for one-half of a localized radical, which is in accord with the fitting of magnetization curve at 2 K, the charge states of TCNQ estimated from the solid state structure, as well as the EPR spectra for **7**. The relatively large χ_{Pauli} value is indicative of delocalized radical spins and the magnitude is directly related to the density of states near the Fermi level by the relationship of $\chi_{Pauli} = \mu_B^2 \rho(E_F)$ where μ_B is the Bohr magneton and $\rho(E_F)$ is the density of states at the Fermi level. The calculated $\rho(E_F) = 3.7\times10^{22}$ eV^{-1} cm^{-3} is larger than the reported value of 5.7×10^{21} eV^{-1} cm^{-3} in a 2-D system with $TCNQF_4$ doped polythiophene.[212]

Table III-17 Redox potential and current intensities of cyclic voltammetry measurements of 4, 5 and TCNQ.

Redox Events	$[Co(PTZ\text{-}tpy)_2]^{3+}/[Co(PTZ\text{-}tpy)_2]^{5+}$	$[Co(PTZ\text{-}tpy)_2]^{2+}/[Co(PTZ\text{-}tpy)_2]^{3+}$	$[Co(PTZ\text{-}tpy)_2]^{+}/[Co(PTZ\text{-}tpy)_2]^{2+}$
E_c/V	+0.406	-0.212	-1.198
E_a/V	+0.478	-0.146	-1.138
$E_{1/2}$/V	+0.442	-0.179	-1.168
ΔE/mV	72	66	60
i_c/μA	3.58	2.30	2.33
i_a/μA	4.09	2.38	2.10
i_c/ i_a	0.87	0.97	1.10

Redox Events	$[Zn(PTZ\text{-}tpy)_2]^{2+}/[Zn(PTZ\text{-}tpy)_2]^{4+}$	$[Zn(PTZ\text{-}tpy)_2]^{+}/[Zn(PTZ\text{-}tpy)_2]^{2+}$	$[Zn(PTZ\text{-}tpy)_2]^{0}/[Zn(PTZ\text{-}tpy)_2]^{+}$
E_c/V	+0.382	-1.658	-1.799
E_a/V	+0.443	-1.613	-1.737
$E_{1/2}$/V	+0.413	-1.636	-1.768
ΔE/mV	61	45	62
i_c/μA	6.05	3.19	2.33
i_a/μA	5.74	2.87	2.16
i_c/ i_a	1.05	1.11	1.07

Redox Events	$TCNQ^0/TCNQ^-$	$TCNQ^-/TCNQ^{2-}$
E_c/V	-0.252	-0.784
E_a/V	-0.184	-0.734
$E_{1/2}$/V	-0.218	-0.759
ΔE/mV	68	50
i_c/μA	4.00	4.16
i_a/μA	3.80	4.13
i_c/ i_a	1.05	1.00

Table III-18 Potential, current intensities and full width of half maximum (FWHM) of differential pulse voltammetry peaks of compound 4 and 6.

4	E/ V	A/ μA	FWHM/ V	**6**	E/ V	A/ μA	FWHM/ V
	0.507	12.5	0.106		0.390	3.46	0.108
	0.452	12.5	0.118		0.359	3.46	0.108
	-0.130	13.1	0.113		-1.885	2.04	0.136
	-1.133	12.5	0.106		-1.967	2.10	0.128

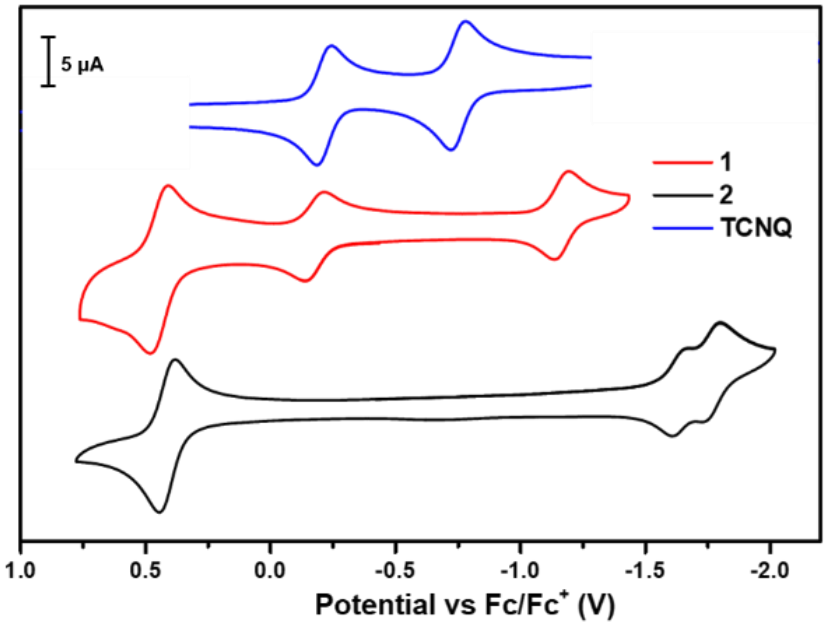

Figure III-16 cyclic voltammetry diagram of compound 4, 5 and TCNQ in acetonitrile (vs Fc/Fc+) with 2 M NBu_4PF_6 as electrolyte.

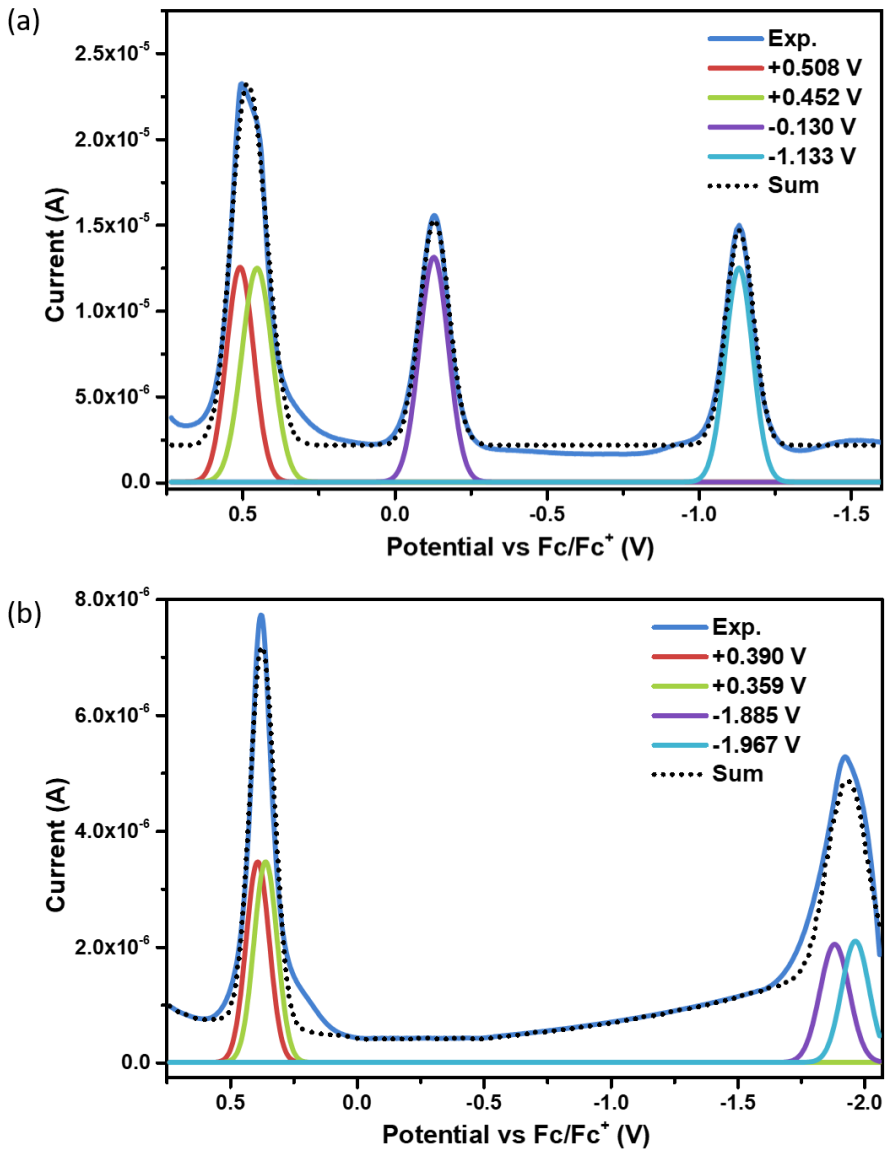

Figure III-17 Differential pulse voltammetry plots of (a) 4 and (b) 5 and the fitting of peaks with Gaussian function.

Cyclic Voltammetry Measurements

The cyclic voltammograms of **4** and **5** in acetonitrile (vs Fc/Fc+) also reveal the redox activities of the $[M(PTZ\text{-}tpy)_2]^{2+}$ moieties (Figure III-16, Table III-17). The first redox couples are related to PTZ based events with $E_{1/2}$ = +0.442 V for Co^{II} and $E_{1/2}$ = +0.413 V for Zn^{II}. The redox couple at $E_{1/2}$ = -179 mV only appears in the M = Co case which corresponds to the Co^{II}/ Co^{III} redox couple. The features at the negative potentials of $E_{1/2}$ = -1.168 V for **4** and $E_{1/2}$ = -1.636 V/ -1.768 V for **5** are terpy-based reductions. The current intensities of the PTZ redox events for **4** and **5** are approximately twice the magnitude than other redox events, which indicates a coupled two-electron redox process. The differential pulse voltammetry measurements for **4** and **5** (Figure III-17) have also been performed to confirm the number of electrons involved in the redox events. The peaks that correspond to the PTZ group can be fitted with two Gaussian functions with similar peak currents and FWHM (full width at half maximum) as other redox events (Table III-18). The redox couples of $TCNQ^0/TCNQ^-$ and $TCNQ^-/TCNQ^{2-}$ occur at -0.218 V and -0.759 V. The $TCNQ^0/TCNQ^-$ couple is very close to the $[Co(PTZ\text{-}tpy)_2]^{2+}/[Co(PTZ\text{-}tpy)_2]^{3+}$ one with only a 0.039 V difference and is 0.660 V and 0.631 V from the PTZ based $[Co(PTZ\text{-}tpy)_2]^{3+}/[Co(PTZ\text{-}tpy)_2]^{5+}$ and $[Zn(PTZ\text{-}tpy)_2]^{2+}/[Zn(PTZ\text{-}tpy)_2]^{4+}$ couples. The $TCNQ^-/TCNQ^{2-}$ couple is close to the terpyridine based redox events (ΔE = 0.409 V for $[Co(PTZ\text{-}tpy)_2]^{+}/[Co(PTZ\text{-}tpy)_2]^{2+}$ and 0.877 mV for $[Zn(PTZ\text{-}tpy)_2]^{+}/[Zn(PTZ\text{-}tpy)_2]^{2+}$). From these data, it can be concluded that the $TCNQ^0$ species could be an electron acceptor in **5** and **7** and undergo charge-transfer

interactions with PTZ groups and/or Co^{II} centers whereas the $TCNQ^{2-}$ species can act as an electron donor in interactions with the terpyridine ligand moieties.

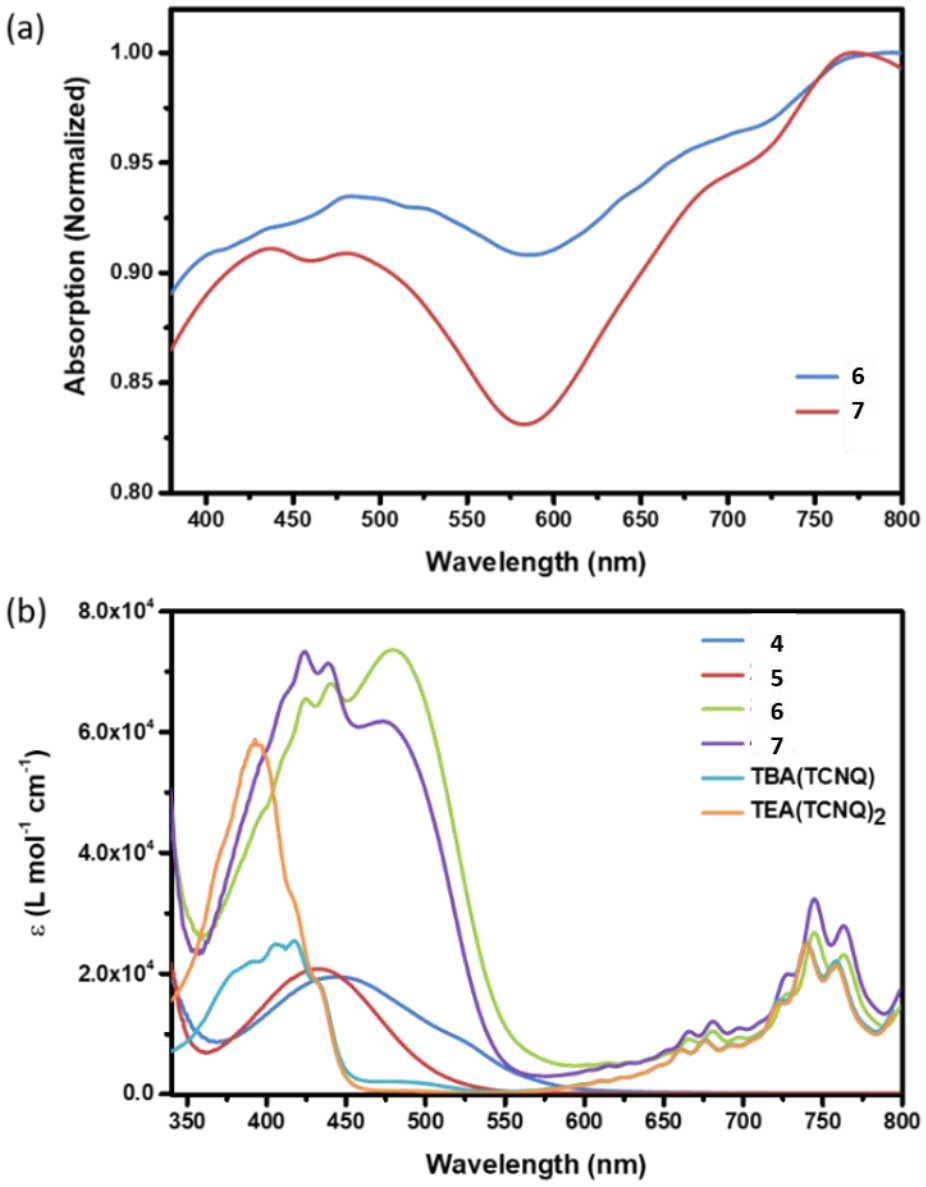

Figure III-18 (a) Solid state UV-vis absorption spectra of 6 and 7. The intensities were scaled by the absorption of maximum peaks. (b) UV-vis spectra of of compound 4-7, TBA(TCNQ) and $TEA(TCNQ)_2$ in acetone solution.

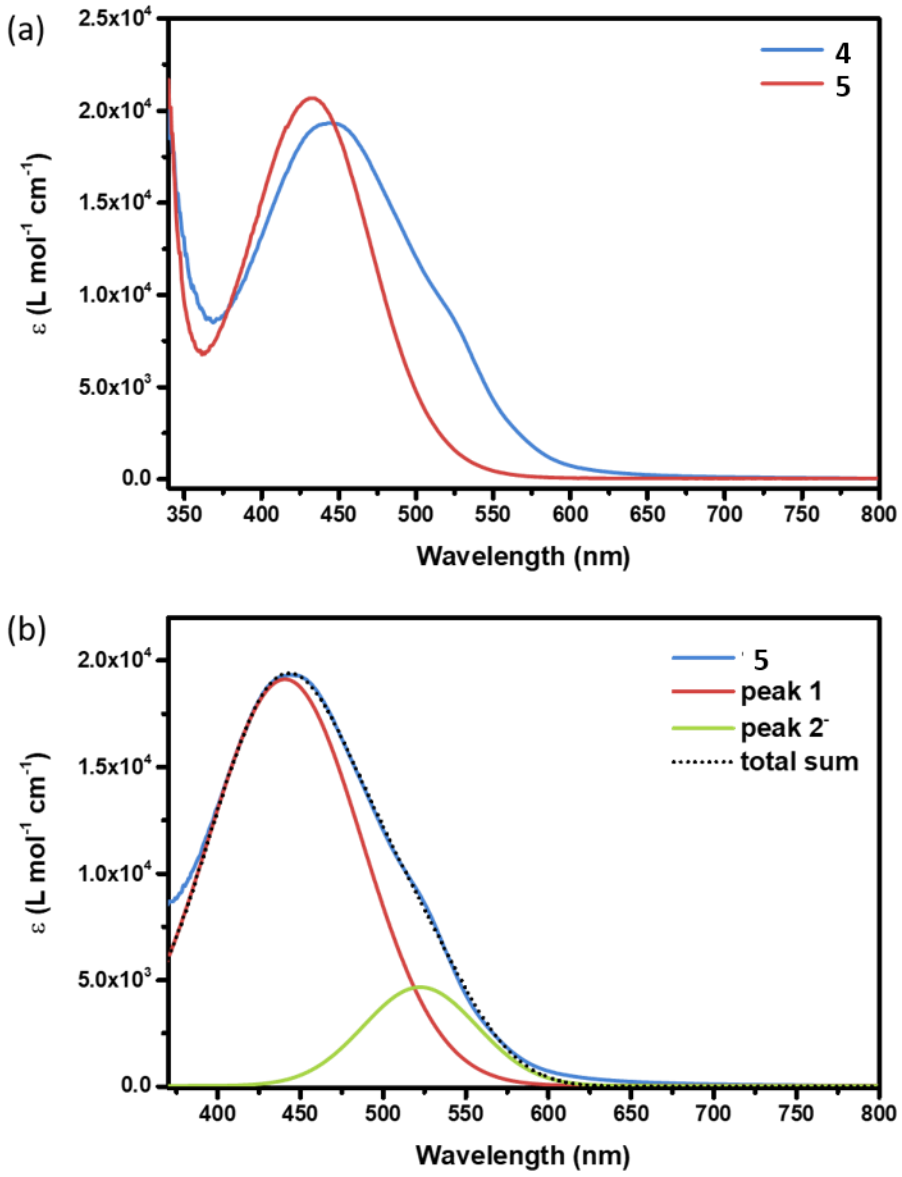

Figure III-19 (a) UV-vis absorption spectra of 4 and 5. (b) Gaussian decomposition of 1 with two different components.

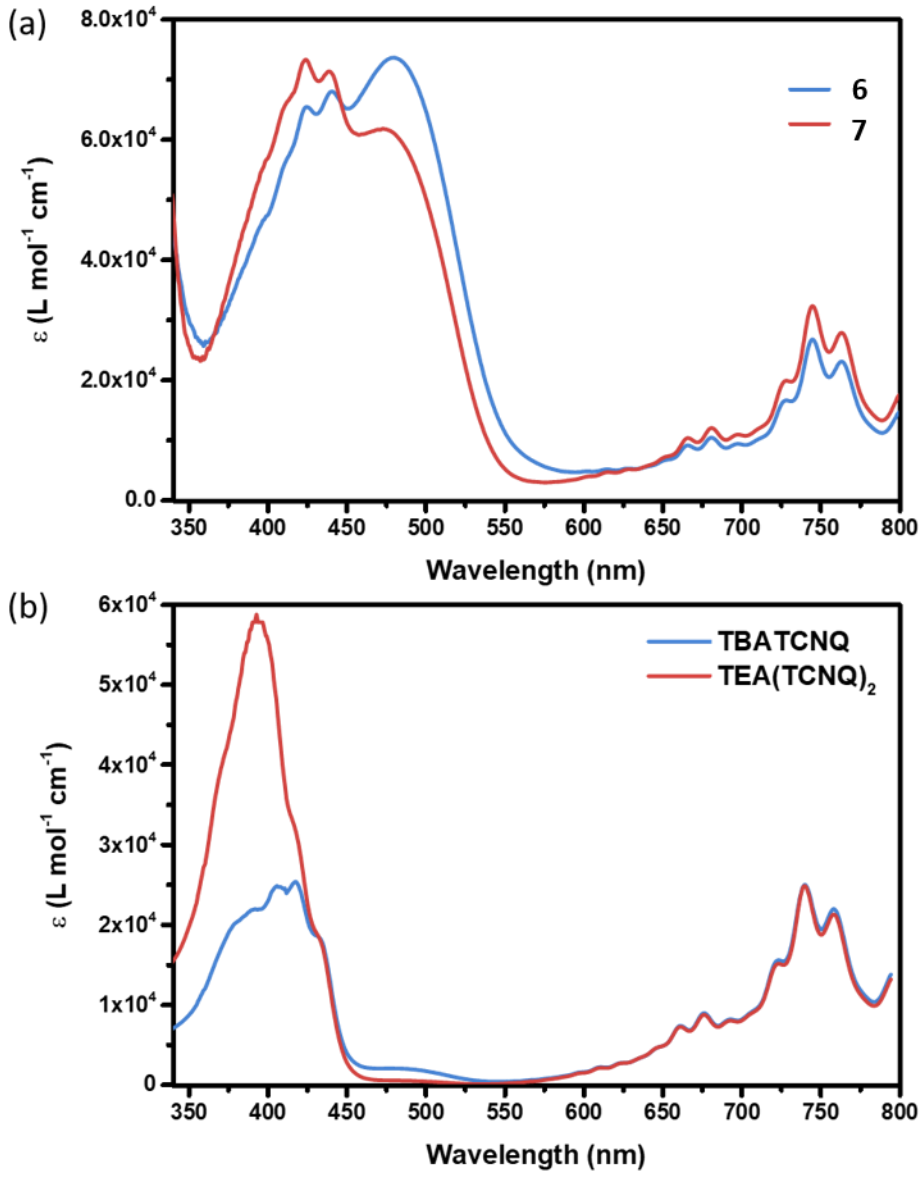

Figure III-20 (a) UV-vis absorption spectra of 6 and 7. (b) UV-vis absorption spectra of TCNQ starting material TBA(TCNQ) and TEA(TCNQ)$_2$.

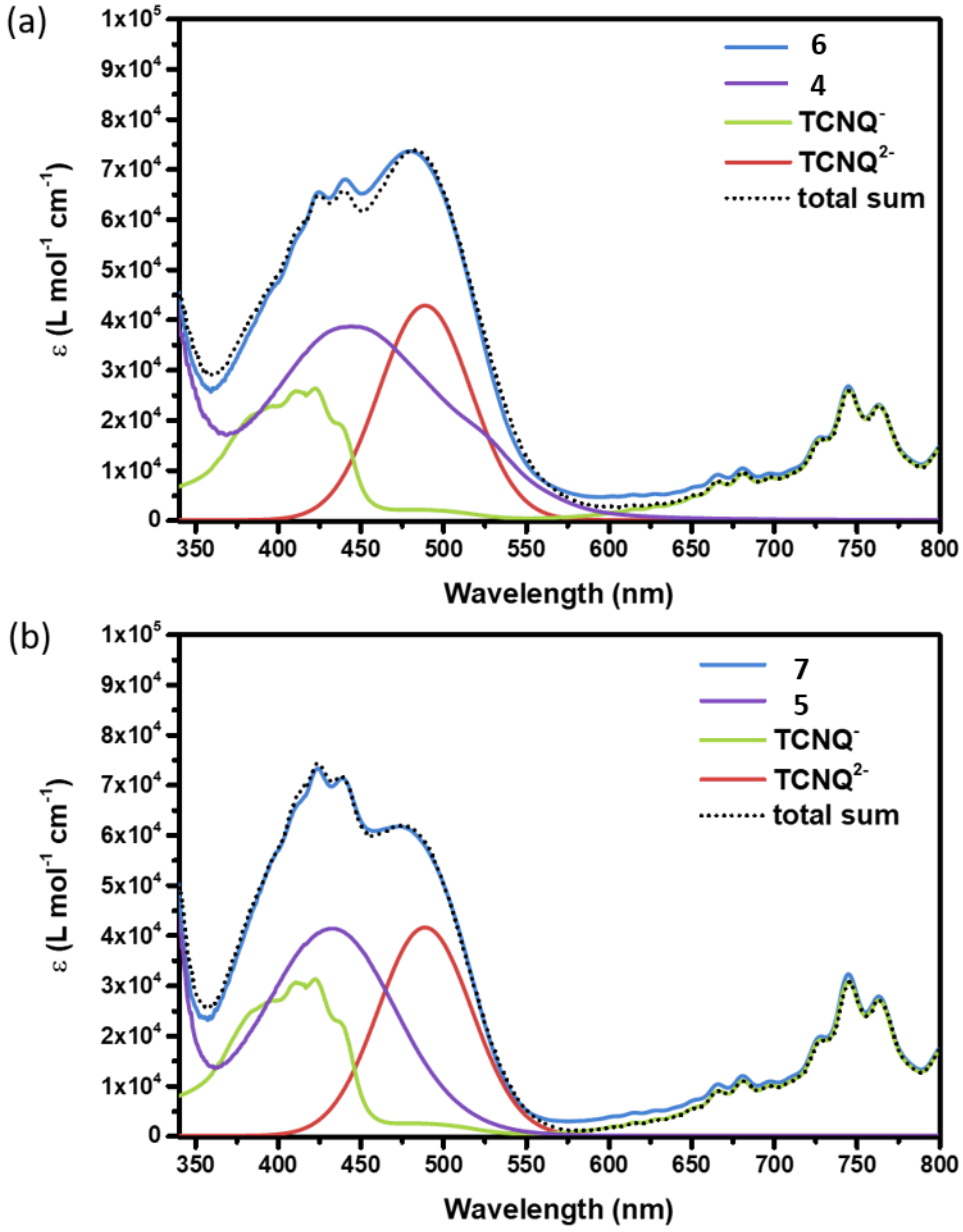

Figure III-21 . UV-vis absorption spectra of (a) 6; and (b) 7 and the contributions from deferent components.

UV-vis Spectra

The solid state UV-vis spectra were measured for compounds **6** and **7**. Significant absorption maxima at ~695 nm and ~772 nm were observed for both compounds in the range of 600-800 nm and in the range of 380-600 nm, two absorption peaks at ~437 nm and ~484 nm were observed for both **6** and **7** while there were two additional peaks observed at 404 nm and 526 nm for compound **3**. In order to decipher the electronic transitions in the solid state, the UV-vis spectra (Figure III-18) of compounds **4**-**7** as well as the TCNQ salts TBA(TCNQ) and $TEA(TCNQ)_2$ in acetone solution were measured. The spectra of the tetraflouroborate salts (Figure III-19 (a)) **4** and **5** reveals the absorption properties of $[M(PTZ\text{-}tpy)]^{2+}$ (M = Co, Zn). The lowest absorption band for compound **5** is at 431 nm ($\varepsilon = 2.0 \times 10^4$ L mol^{-1} cm^{-1}) which corresponds to the intra-ligand charge transfer (ILCT) from the PTZ to the terpyridine group. In contrast, the spectrum of **4** has an absorption at 441 nm with a shoulder at 523 nm (Figure III-19 (b)). The presence of two features can be attributed to the coexistence of H.S. and L.S. $[Co(PTZ\text{-}tpy)]^{2+}$ species with the same type of ILCT transitions. The spectra for compound **6** and **7** (Figure III-20) are relatively complicated as the $[M(PTZ\text{-}tpy)]^{2+}$ cation and TCNQ with different oxidation states coexist in the solution. By comparing with the UV-vis spectra of TCNQ starting materials, TBA(TCNQ) and $TEA(TCNQ)_2$ (Figure III-20 (b)), the peaks in the 400-450 nm and 650-800 nm ranges, which were also observed in the solid state, correspond to the absorptions of the $TCNQ^{\cdot-}$ radical anion. The additional absorption features at ~486 nm that appear in the solution phase spectra of **6** and **7** as well as in the solid state, can be attributed to the contribution

of the $TCNQ^{2-}$ dianion[215-217] which corresponds well with the estimated negative charge on type A TCNQ, which is higher than -1 on the average (the mixture of $TCNQ^{\cdot-}$ and $TCNQ^{2-}$), at room temperature in compound **6** and **7.** The total extinction coefficient curves of **6** and **7** are nicely simulated by considering the contributions from $[M(PTZ\text{-}tpy)]^{2+}$, the $TCNQ^{\cdot-}$ radical and the $TCNQ^{2-}$ dianion (Figure III-21). Although the $TCNQ^{2-}$ species exists in solid state, there are other possible sources of the $TCNQ^{2-}$ dianion in solution, such as the disproportion of the $TCNQ^{\cdot-}$ radical anion and/or charge transfer between the redox-active PTZ moiety and TCNQ moiety .[215-217] The charge transfer hypothesis is supported by the fact that no absorption features for neutral TCNQ spices were observed in spectra of **6** and **7** as it is likely converted to $TCNQ^{\cdot-}$/ $TCNQ^{2-}$ by the charge transfer mechanism. The additional two peaks (404 nm and 526 nm) for **6** in the solid state are attributed to the contribution of the L.S. $[Co(PTZ\text{-}tpy)]^{2+}$ component.

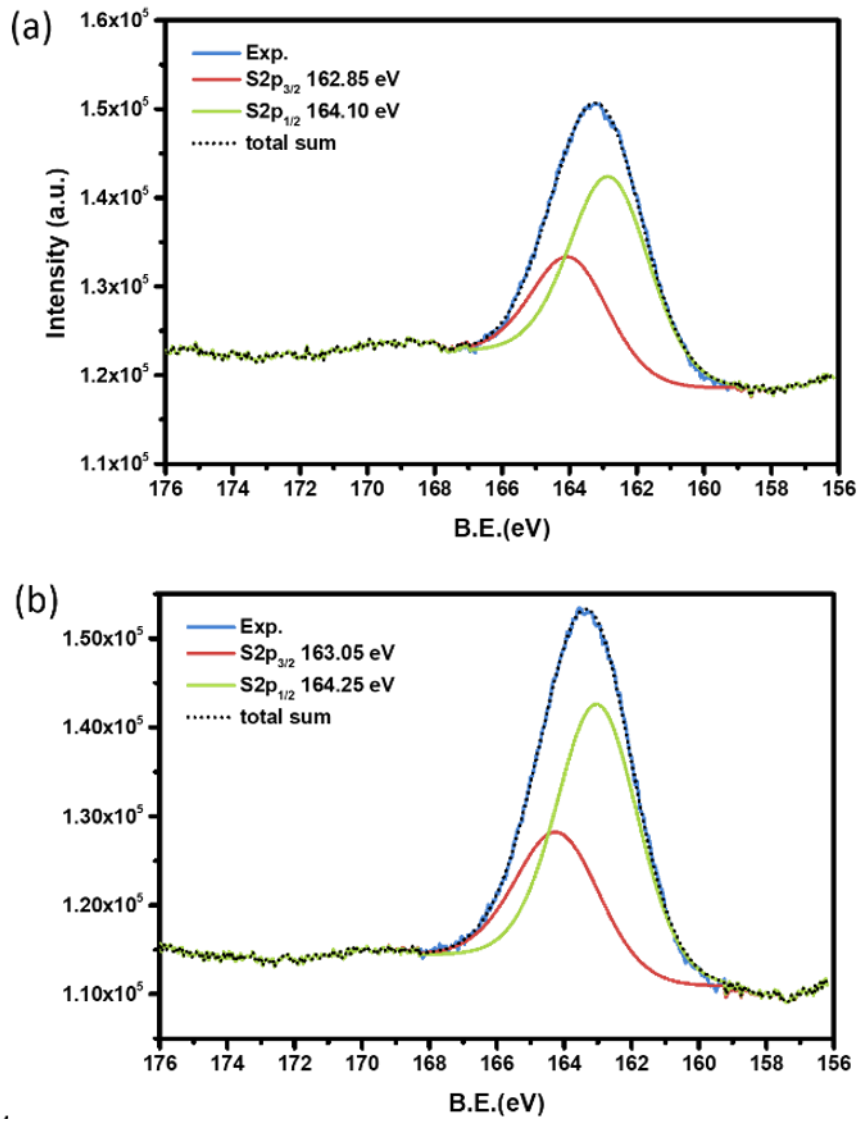

Figure III-22 XPS spectra for S2p of compound (a) 4, (b) 5, (c) 6 and (d) 7. The blue, green and red lines represent the experimental data, fits of $S2p_{3/2}$ and $S2p_{1/2}$ respectively. The short dots represents for the sum of total fits.

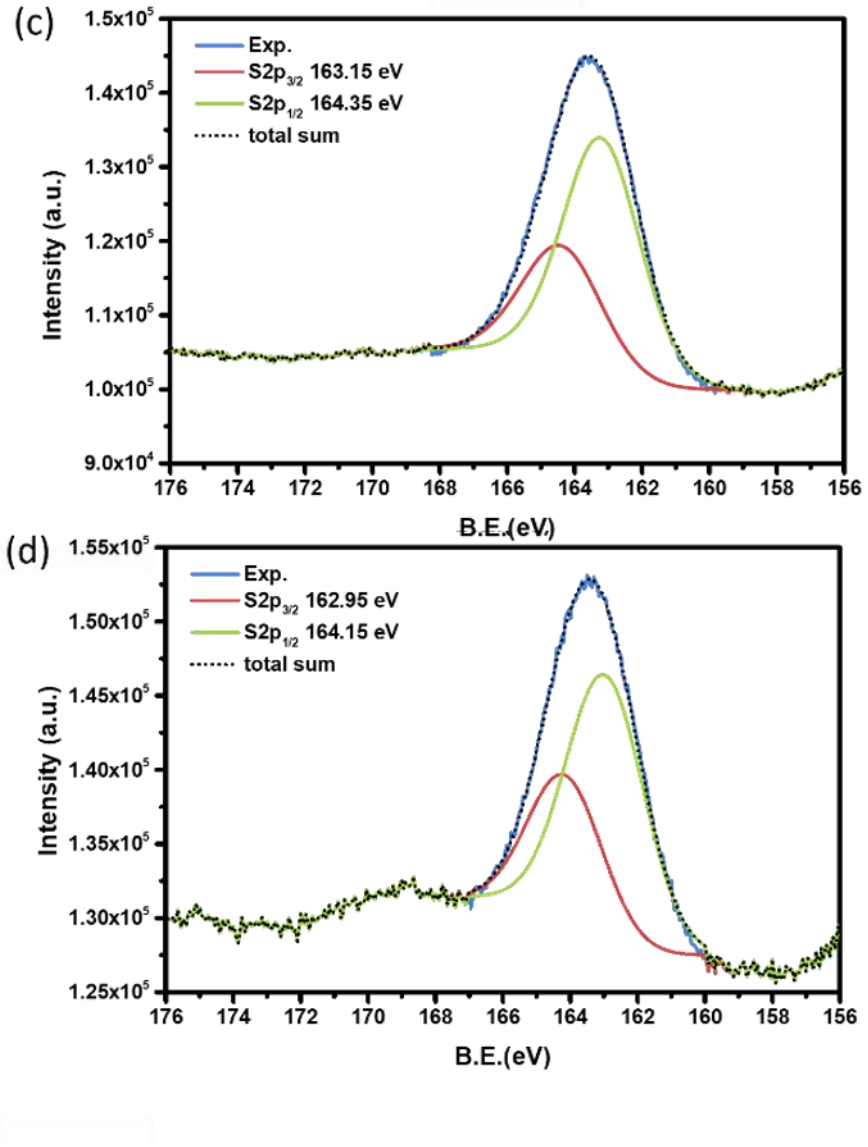

Figure III-22 Continued

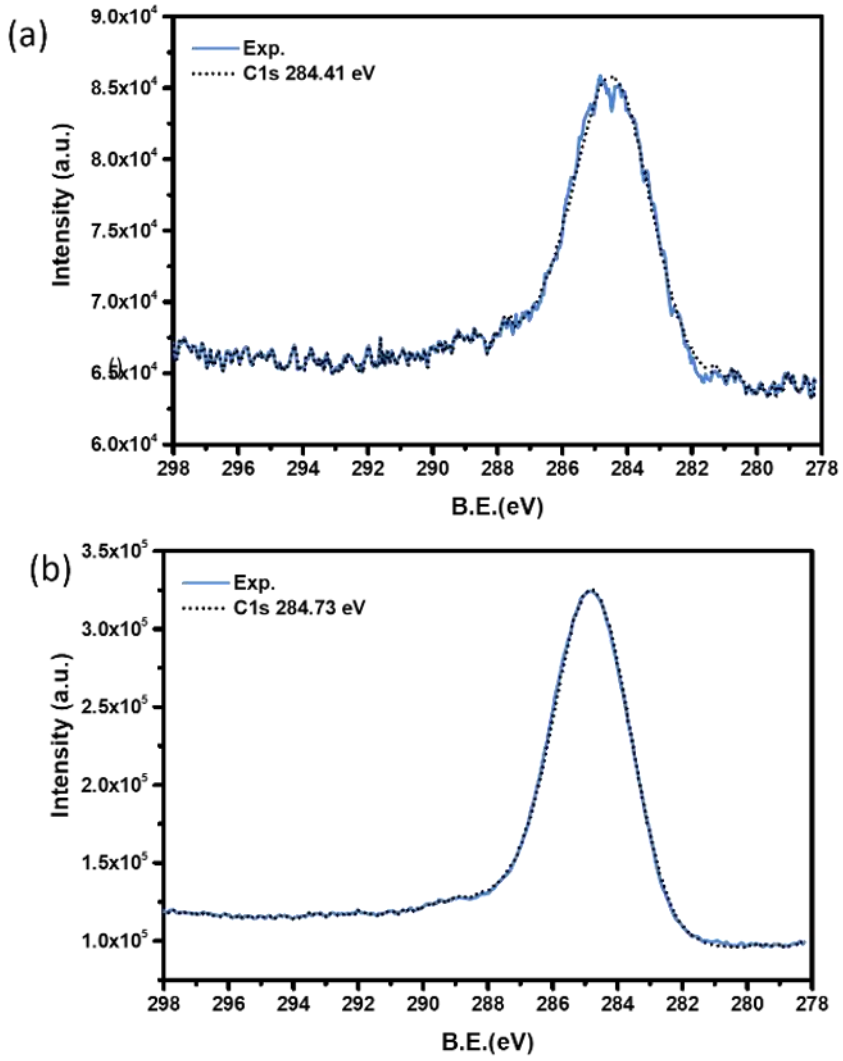

Figure III-23 . XPS spectra for C1s of compound (a) 4, (b) 5, (c) 6 and (d) 7. The blue represents the experimental data. The short dots represent the full fitting. The red and green lines represent for the different C1s components in compound 6 and 7.

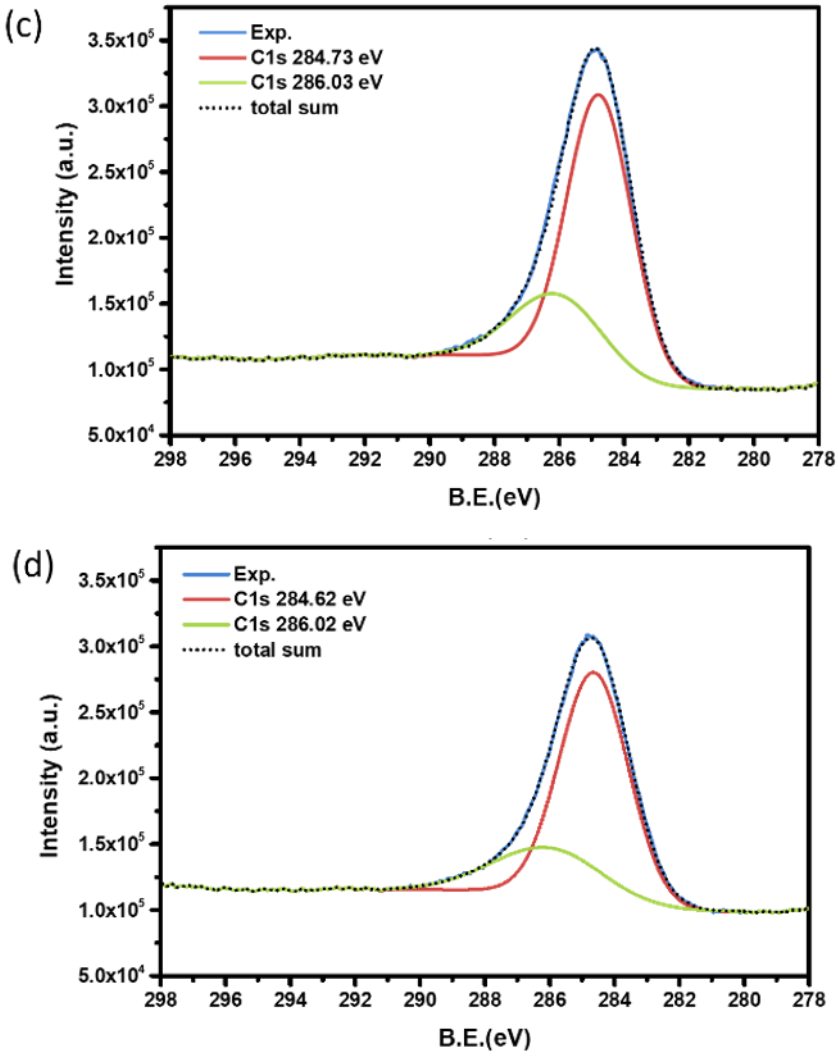

Figure III-23 Continued

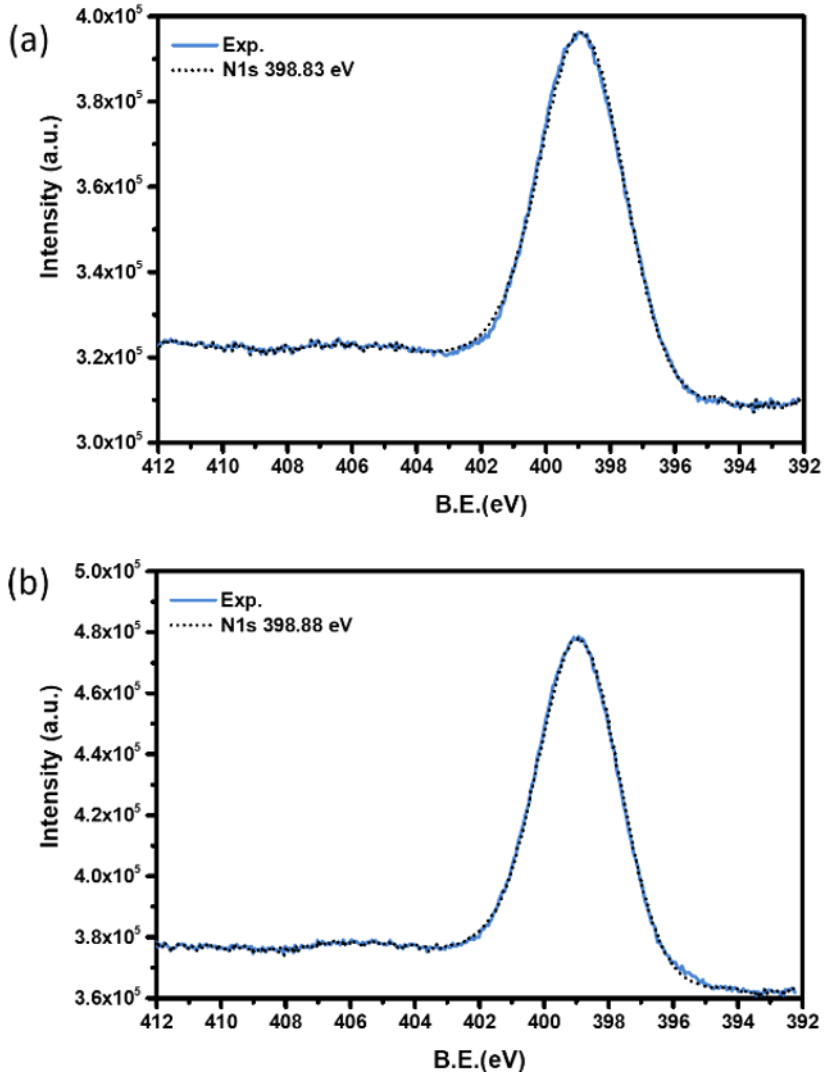

Figure III-24 XPS spectra for N1s of compound (a) 4, (b) 5, (c) 6 and (d) 7. The blue represents the experimental data. The short dots represent the full fitting.

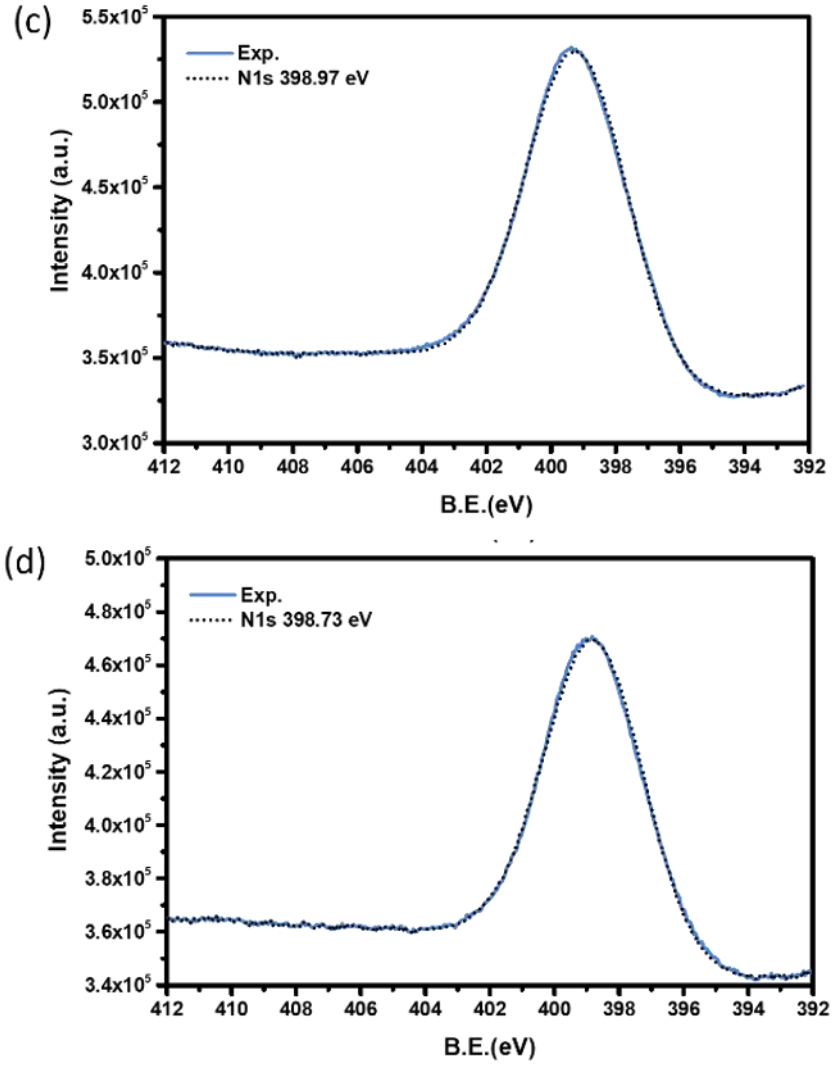

Figure III-24 Continued

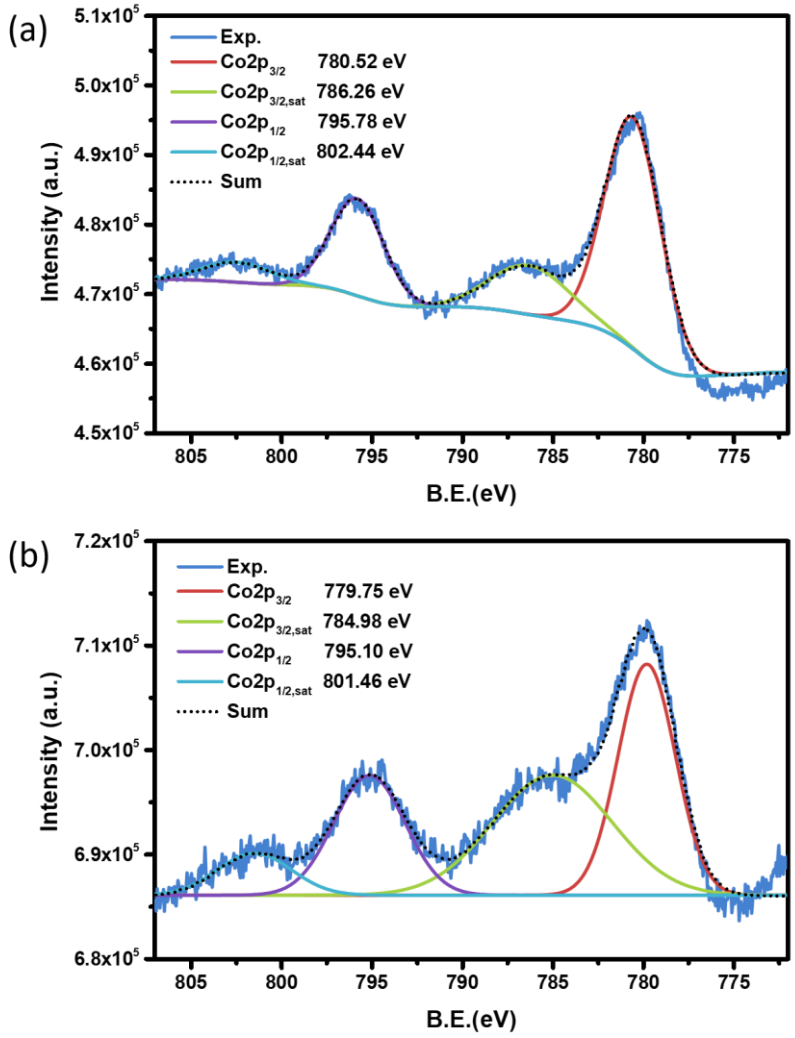

Figure III-25 XPS spectra for Co2p of compound (a) 4 and (b) 7. The blue represents the experimental data. The short dots represent the full fitting. The red and purple lines represent the fitting for $Co2p_{3/2}$ and $Co2p_{1/2}$ while green and azure lines represent for the fitting of their satellite peaks.

X-ray Photoelectron Spectroscopy (XPS)

The X-ray photoelectron spectroscopy measurements of compounds **4**-**7** were performed to investigate the oxidation states of sulfur on the phenothiazinyl groups. The typical S2p peaks at ~163 eV which can be deconvoluted into two spin-orbit splitting components, $S2p_{3/2}$ and $S2p_{1/2}$ were observed for all compounds (Figure III-22). The energy separations and peak area ratio of $S2p_{3/2}$ and $S2p_{1/2}$ were set to 1.2 eV and 2:1 for the peak deconvolution.[218-219] The positions of $S2p_{3/2}$ peaks for compounds **4**-**7**,162.85, 163.05, 163.15 and 162.95 eV respectively, are very close to each other and correspond well with reported values for C-S-C bonding.[219] The reported binding energy for $C\text{-}S^{+}\text{-}C$, ~167.5 eV, [218-219] is significantly higher than the values observed here. Therefore, a conclusion can be drawn that no significant changes of sulfur oxidation were observed for the phenothiazinyl group when the $[M(PTZ\text{-}tpy)_2]^{2+}$ cations are co-crystallized with TCNQ species in compounds **6** and **7** which rules out a paramagnetic contribution from $PTZ^{+\bullet}$ radical.

Other than the peaks for sulfur, peaks of C1s (Figure III-23), N1s (Figure III-24) for **4**-**7** and Co2p (Figure III-25) for **4**-**7** were observed. The C1s peak at ~284.6 eV, which corresponds to CH_x species, was observed in all four compounds while an additional peak, at ~286.0 eV, for carbons on TCNQ cyano groups was observed for compounds **6** and **7**.[220] For the N1s case, only one peak at ~398.8 eV was observed for all four compounds as the N1s binding energy values for pyridinic-N[219, 221-222] and cyano-N[220] are very close to each other in the range of 398.4-398.6 eV. The XPS spectra for Co2p for **4** and **6** exhibit similar patterns with $Co2p_{3/2}$ peaks at 780.52 eV and 779.75

eV as well as Co $2p_{1/2}$ peaks at 795.78 eV and 795.10 eV along with smaller satellite peaks. The peak positions match well with the expected values for a terpyridine ligand coordinated Co^{II} species.[221, 223]

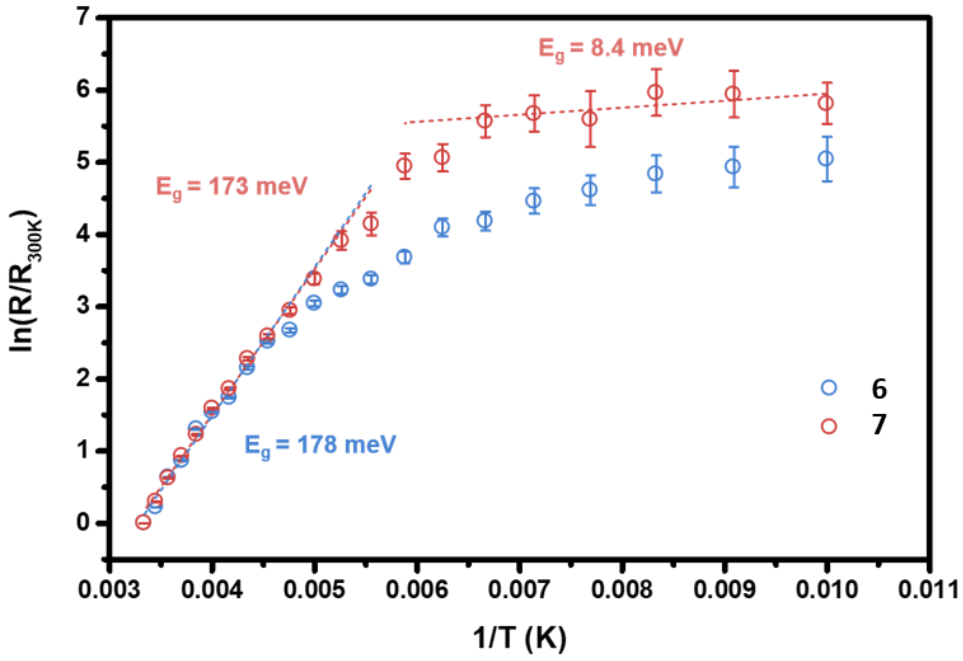

Figure III-26 Ln of relative resistance vs inverse temperature plots of 6 (blue open circle) and 7 (red open circle) with the linear fits (dash lines) in the range of 100-300 K.

Conducting Properties

Due to the small size of the crystals, the temperature-dependent resistivity measurements were performed on pressed pellets of **6** and **7** over the temperature range of 100-300 K. The room temperature resistivities are $\rho = 4.0\times10^{6}$ Ω·cm ($\sigma = 2.5\times10^{-7}$ S

cm^{-1}) for **6** and $\rho = 9.3\times10^{6}$ Ω·cm ($\sigma = 9.3 \times10^{-7}$ S cm^{-1}) for **7**. These values are relatively higher than the previously reported values for partially charged semiconducting complexes which can be due to contact resistivity and anisotropic conducting behavior along different crystal axis.[224] To investigate the temperature dependence of resistivities, the ln of relative resistance versus inverse temperature plots were evaluated and are depicted in Figure 10. The resistances of both **6** and **7** increase as the temperature decreases which is typical of semiconducting behavior. The relative resistance values of **6** and **7** are very close to each other and range from 3.3×10^{-3} to 4.5×10^{-3} K^{-1} (over the range 300 to 220 K) and exhibit linear trends with similar values for the thermal activation band gap (E_g), namely 178 meV for **6** and 173 meV for **7** by applying the Arrhenius equation, $R = R_0 \exp(E_g/k_BT)$ (Figure III-26). The activation energy values are similar to reported TCNQ compounds with fractional charge states. [109, 111, 113, 224-228] The similarities of the activation energies and relative resistance values are attributed to the similar structures and charge distributions on the TCNQ stacks between **6** and **7** in the high-temperature region. The temperature dependence of **7** follows the linear trend to ~160 K and then transitions to a plateau in the range of 160–100 K with a lower energy gap of ~8 meV. Such changes are likely due to the transition from intrinsic semiconducting behavior to the extrinsic semiconducting region of **7**.[229] In contrast, the temperature-dependent relative resistance of **6** deviates from the Arrhenius equation and behaves differently from **7** below 200 K**.** The gradual changes of $\ln(R/R_{300K})$ values for **6** can be attributed to the changes in the charge states of TCNQ stacks in synergy with the SCO behavior of the $[Co(PTZ\text{-}tpy)_2]^{2+}$ moiety.

Conclusions

In this work, Co^{II} based spin-crossover charge transfer complex with redox-active partially charged TCNQ counter anions, namely $[Co(PTZ\text{-}tpy)_2]_2(TCNQ)_{4.5}\cdot 2.5MeCN$(**3**)**,** as well as the Zn^{II} analog, $[Zn(PTZ\text{-}tpy)_2]_2(TCNQ)_{4.5}\cdot 2.5MeCN$(**7**) have been synthesized. Temperature-dependent single-crystal X-ray studies revealed an electron transfer behavior between different TCNQ stacks in the solid state which accompanies spin-crossover behavior of the Co^{II} ions in **6**. In contrast, compound **7** exhibits less temperature-dependent structural changes. Magnetic measurements as well as the EPR spectra support synergistic SCO and electron transfer. The temperature-dependent resistivity measurements indicate that both compounds **6** and **7** exhibit semiconducting behavior in the temperature range of 100-300 K. The differences in $\ln(R/R_{300K})$ vs 1/T curves of **6** and **7** in the SCO temperature range suggests that the conducting behavior in **6** is affected by the SCO induced electron transfer. These results demonstrate that introducing the PTZ pendant group to the SCO system which has strong charge-transfer interactions with TCNQ moieties, $[Co(PTZ\text{-}tpy)_2]^{2+}$, not only results in interesting packing patterns in the solid state, but also induces synergistic effects between magnetic bistability and electrical transport properties.

CHAPTER IV

MAGNETIC CHARACTERIZATION OF METAL-ORGANIC FRAMEWORKS FUNCTIONALIZED WITH SINGLE MOLECULE MAGNETS

Introduction

Metal-organic frameworks (MOFs) are a category of crystalline materials that consist of metal ions or molecular building blocks connected by organic linkers. Enormous achievements have been made in the structural manipulation, functionalization and practical applications of MOFs over the past two decades.[230] The structural and functional flexibilities of MOFs are enabled by the powerful organic synthesis tools used for bridging ligand design and the variations in coordination modes of metal ions/clusters nodes. The highly crystalline nature of MOFs enables the investigation of structure-function relationships via single-crystal X-ray diffraction. Apart from the traditional applications of MOFs in gas absorption, storage and separation and catalysis, the integration of optical, electrical and magnetic properties into the highly ordered porous structure has been a forefront topic in recent years. The first example of a multifunctional material with cooperative magnetic ordering and metallic conductivity is the combination of the magnetic $[Mn^{II}Cr^{III}(C_2O_4)_3]^-_\infty$ anionic MOF skeleton with stacked bis(ethylenedithio)tetrathiafulvalene (BEDT-TTF) moieties.[231] In order to introduce magnetic ordering in MOFs, short linkers such as oxalate, formate and cyanide ligands, are required to allow for an appreciable superexchange interaction between spin centers.[232] Another strategy in this vein is the introduction of paramagnetic

bridging ligands, such as semiquinoid, tetracyanoethene (TNCE) and TCNQ radicals. Instead of diamagnetic ligands which mediate superexchange, the radical bridging ligands engage in magnetic coupling between spin centers via strong direct exchange interactions. [233-235]

Introducing molecular magnetic bistability into MOFs, such as the properties exhibited by single molecule magnets is an interesting possibility. [232, 236-248] Specifically, MOFs are an ideal platform to minimize the spin relaxation in molecules contained either as a unit in their architecture or in their pores. There are several positions that can be capitalized upon to install the SMM moieties including the metal nodes, bridging linkers and the porous cavities (Figure IV-1).

Collaborative research between the Dunbar group and Dr. Mario Wriedt's group at Clarkson University have demonstrated that the long-range nanostructuring of SMM moieties, such as Mn_{12} and its derivatives, can be achieved by using mesoporous MOFs as temperates.[236, 243, 247] Thermal stabilities of SMMs are enhanced by their incorporation into pores of MOFs with the preservation of magnetic properties. An excellent example of this point is the work of Zhou and co-workers who demonstrated that post-synthetic modification methods can be used to replace the diamagnetic carboxylate ligands with $Co^{II}(Py)_nCl_2$ moieties (n = 2 or 4) which led to the observation of SMM behavior.[245] Other reports of cooperating metal clusters based SMMs,[237, 240, 242] transition metals,[244] and lanthanides[232, 238-239, 246] single-ion magnets into the metal nodes have also been published. The most well-known transition metal based SMM moieties are Co^{II} SMMs with octahedral geometry as metal nodes for MOFs[244, 249-254] as the d^7 electronic

configuration in an octahedral coordination sphere due to the prediction of large magnetic anisotropy. The synthetic methods of the reported MOFs with SMMs as nodes are mainly based on the direct reaction between the bridging ligands and simple cobalt metal salts such as $CoCl_2$ and $Co(NO_3)_2$. The topologies of these MOFs are typically interpenetrating networks such that the distances between metal centers are less than the span of the bridging ligands which causes a larger dipolar interaction between magnetic centers.

In the current studies, we used post-synthetic methods to incorporate the Co^{II} based SMM moiety into the Zn_4O nodes of the well-known MOF, UMCM-1. The reasons for selecting UMCM-1 are: (1) the mechanism of metal ion exchange between Zn_4O nodes and Co^{2+} have been reported by Dinca and the coworkers who determined that the Co^{II} ion can be incorporated as a $CoZn_3O$ metal node (Figure IV-2).[255] (2) The mesoporous structure of UMCM-1 ensures the efficient exchange of the metal ions and (3) the shortest distance between metal nodes is ~12.9 Å which is sufficiently large to suppress dipolar interactions between magnetic centers. Given that the direct synthesis of the UMCM-1 structure with Co^{II} substituted M_4O metal nodes is unknown, the post-synthetic ion-exchange chemistry is critical for the installation of Co^{II} ions into the metal nodes.

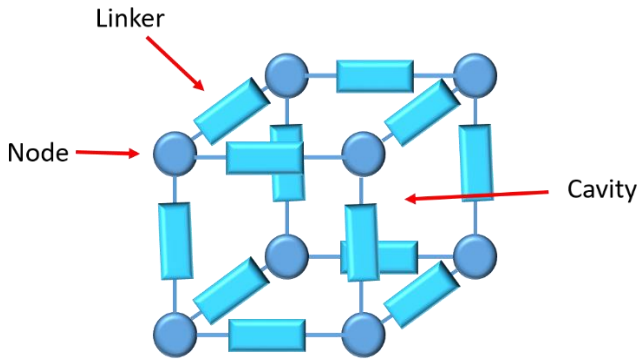

Figure IV-1 Structural positions of MOFs that can be used to install SMMs

In this chapter, the magnetic characterization and analysis of a Co^{II} SMM incorporated into the UMCM-1 metal-organic framework (MOF) is described. The project is a collaboration between the Dunbar group at Texas A&M University and the Wriedt group at Clarkson University. The samples were prepared by Dr. Darpandeep Aulakh in the Wriedt group and the solid state UV, magnetic measurements and analyses were performed by Haomiao Xie, the author of this dissertation, in the Dunbar laboratories.

Experimental Section

Sample Preparation

UMCM-1-pink

The pristine MOF UMCM-1, which was prepared according to the reported procedure in the literature,[256] was soaked in a 10 mL acetonitrile solution of $CoCl_2$ (0.03 M) for 12 hours. The color of the crystalline sample turned pink during the soaking period. The prepared sample, UMCM-1-pink (**8**), was washed with acetonitrile followed

by diethyl ether under a nitrogen atmosphere. The solid sample was sealed in a quartz NMR tube for magnetic characterization.

UMCM-1-blue

The pristine MOF UMCM-1 was soaked in10 mL of an acetonitrile solution of $CoCl_2$ (0.03 M) for one week. The color of the sample turned to pink first and then turned an intense blue color as the time of soaking increased. The prepared sample, UMCM-1-blue (**9**), was washed with acetonitrile followed by diethyl ether under a nitrogen atmosphere. The solid sample was sealed in a quartz NMR tube for magnetic characterization.

Neutron Activation Analysis(NAA)

The neuron activation analyses were performed by the Elemental Analysis Lab at Texas A&M University. The samples of **8** and **9** were pre-dried under a nitrogen atmosphere. Aliquots of 0.5 mL each of the Co (SCP Science Plasma CAL, Cat. No. 140-051-271) and Zn (Alfa Aesar Specpure, Stock No. 13835) calibrator solutions (nominally 1000 g/mL) were accurately transferred by pipet and heat-sealed in acid-washed 2/5-dram polyethylene irradiation vials. The MOF samples of approximately 7 mg each were transferred into pre-weighed, acid-washed irradiation vials inside of a dry-nitrogen glove box. The sample masses were determined with a calibrated analytical balance with readability of 0.01 mg. The closed sample vials were weighed in ambient atmosphere and heat-sealed prior to irradiation. The neutron irradiations were performed sequentially in the pneumatic-tube facility of the TEES Nuclear Science Center 1 MW TRIGA reactor. The subsequent gamma-ray spectrometry was performed using a high-

purity Ge (HPGe) gamma-ray detector (from Ortec), and the data reduction was performed using NAA software from Canberra Industries.

Solid State UV-vis Spectra

Solid state UV-visible spectra were measured on a Shimadzu UV-2450 with a diffuse reflectance accessory. $BaSO_4$ was used as the blank substrate and reference to correct the baseline. The ground samples were directly pressed onto the $BaSO_4$ substrate for measurements.

Magnetic Measurements

A Quantum Design MPMS-XL SQUID instrument was used for magnetic measurements over the temperature range of 1.8-300 K. Samples were sealed in quartz tubes under nitrogen. The diamagnetic contributions of sample holders and diamagnetic contributions of atoms were corrected by using an empty sample holder as a blank and Pascal's constants[257], respectively. The program PHI v3.1.1 was used for the fitting of dc magnetic susceptibilities. [258]

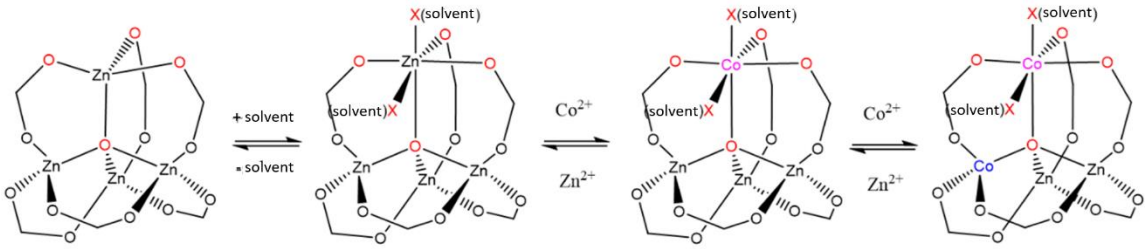

Figure IV-2 Exchange mechanism of the Co^{2+} metal ion with the Zn_4O nodes.

Results and Discussion

Elemental Analysis and Solid State UV-vis Spectra

The Co^{2+} ion exchange with the Zn_4O nodes in UMCM-1 resulted in two different products, **8** and **9**, with significantly different colors. The one from the shorter reaction time (12 hours), **8,** is pink color while the longer one (1 week), **9**, is an intense blue color. The color changes of the samples correspond well with the reported phenomenon.[255] The pink color is from a Co^{II} center in an octahedral geometry whereas the blue color is from Co^{II} centers in a tetrahedral coordination environment. The substitution of Co^{II} centers occurs at the solvated octahedral environment first and the additional substitution of Co^{II} ions results in the presence of Co^{II} centers in the tetrahedral sites. (Figure IV-2) The elemental analysis results from neutron activation (Table IV-1) suggest that sample **8** has 0.2 Co^{II} substitution per M_4O cluster and sample **9** has 1.3 Co^{II} substitutions per M_4O cluster. The substitution values are close to the reported ones, 0.5 per M_4O and 1.5 per M_4O, respectively, in the literature.[255]

Table IV-1Elemental analysis results from NAA experiment

Sample	Zn [wt%]	± u (2s)	Co [wt%]	± u (2s)	Zn:Co (molar)	Co per node
8	22.3	0.5	1.2	0.1	17:1	0.2
9	11.4	0.3	4.8	0.2	2.2:1	1.3

The solid state UV-vis spectra of **8** and **9** were also collected to investigate the Co^{II} coordination environments. (Figure IV-3) For **8**, only one absorption peak was observed at 504 nm which corresponds to the Co^{II} centers in an octahedral environment.

In the spectrum of **9**, apart from the peak at 504 nm, an additional feature at 623 nm and a shoulder at 583 nm was observed. The additional peaks correspond to the Co^{II} centers in a tetrahedral geometry. The absence of Co^{II} (T_d) in sample **8** suggests that only the mono-substituted cluster $CoZn_3O$ exists in the product due to the low loading of Co^{II} centers per M_4O node. The coexistence of Co^{II} species in both O_h and T_d environments indicate the existence of Co_2Zn_2O and/or $CoZn_3O$ node types.

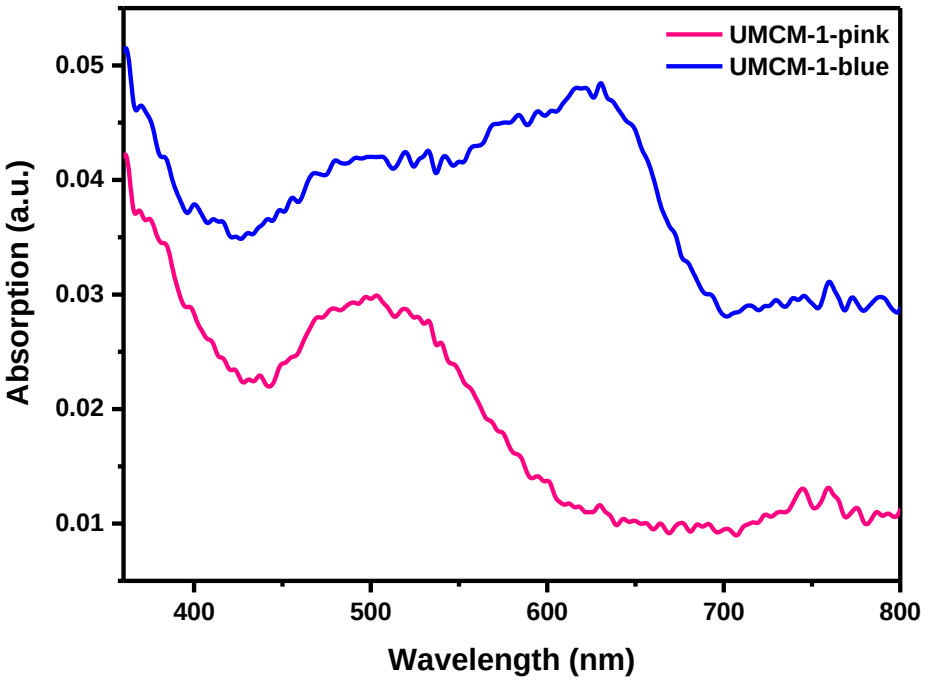

Figure IV-3. Solid state UV-visible spectra of 8 (pink) and 9 (blue).

Magnetic Properties

Magnetic measurements of **8** and **9** were performed on freshly prepared samples sealed in quartz tubes. Temperature-dependent direct current (dc) susceptibility

measurements were carried out under a 1000 Oe dc field over the temperature range of 1.8-300 K. All molar magnetic susceptibility values were calculated based per molar Co^{II} centers. The χT value of **1** at 300 K is 3.61 emu K mol^{-1} which is higher than the expected spin-only value for $S = 3/2$ of 1.88 emu K mol^{-1} due to spin-orbit coupling magnetic anisotropy. [259] The χT value drops as the temperature decreases as shown in Figure IV-4 which is likely due to the zero-field splitting rather than the antiferromagnetic coupling since the solid state UV-vis spectrum of **8** suggests only mono-substituted $CoZn_3O$ in the sample and the M_4O nodes are well separated from each other by the ligands. A fit of the static magnetic susceptibility was performed based on the Hamiltonian in Equation 4-1:

$$\hat{\mathrm{H}} = g_{iso}\beta H\widehat{\boldsymbol{S}} + D\left[\widehat{\boldsymbol{S}}_z^2 - 3\widehat{\boldsymbol{S}}\left(\widehat{\boldsymbol{S}}+1\right)\right] + E(\widehat{\boldsymbol{S}}_x^2 - \widehat{\boldsymbol{S}}_y^2) \qquad \textbf{Equation 4.1}$$

where g, H, β, D and E represent the g factor, the magnetic field strength, the Bohr magneton and the axial and rhombic magnetic anisotropy, respectively. The best fit of magnetic susceptibility gives $g = 2.82$, $D = +68.0$ cm^{-1} and $E = -0.004$ cm^{-1}. These values are comparable to the previously reported examples of pseudo-octahedral Co^{II} SMMs. [176, 244, 254, 260-269] On the contrary, the χT value for **9** (Figure IV-5) is 1.88 emu K mol^{-1} at 300 K, which is close to the anticipated spin-only value. The 1/χ vs T curve from 150 K to 300 K was fit to the Curie-Weiss law and yielded $C = 2.90$ emu K mol^{-1} and $\theta = -164$ K. The large negative Weiss constant is a further indication of the presence of antiferromagnetic coupling between Co^{II} centers within the M_4O nodes. [259, 270]

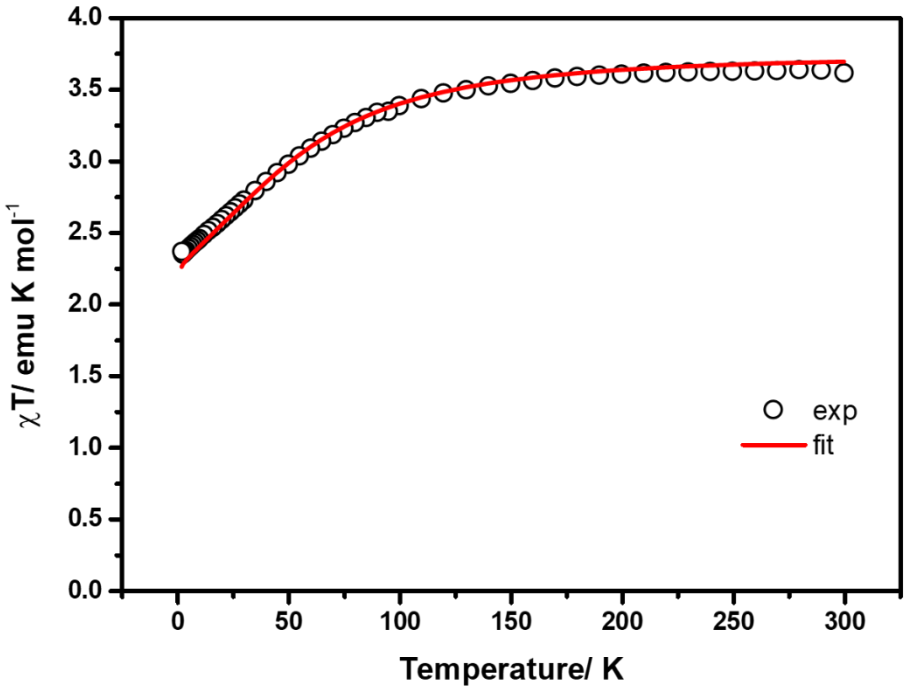

Figure IV-4 . Temperature-dependent magnetic susceptibility data for 8 (open circles) measured under a field of H = 1000 Oe. The solid line represents the best fit with the Hamiltonian shown in Equation 4.1.

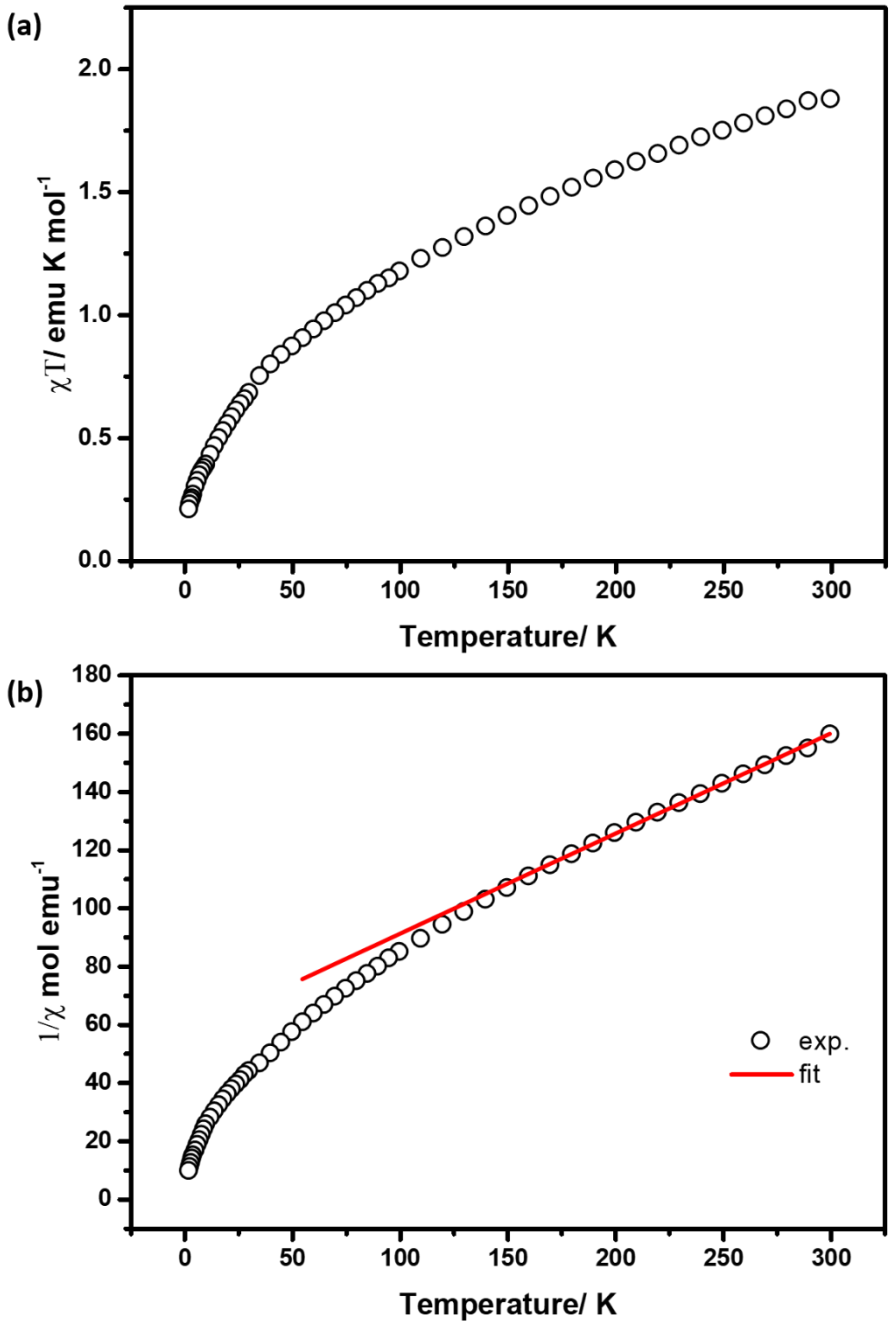

Figure IV-5 Temperature dependence of (a) χT (black circles) and (b) $1/\chi$ (open circle) of 9 with Curie-Weiss law: $1/\chi = T/C - \theta$, where C is Curie constant and θ is Weiss constant. The best fit yield C = 2.90 emu K mol^{-1} and θ = -164 K.

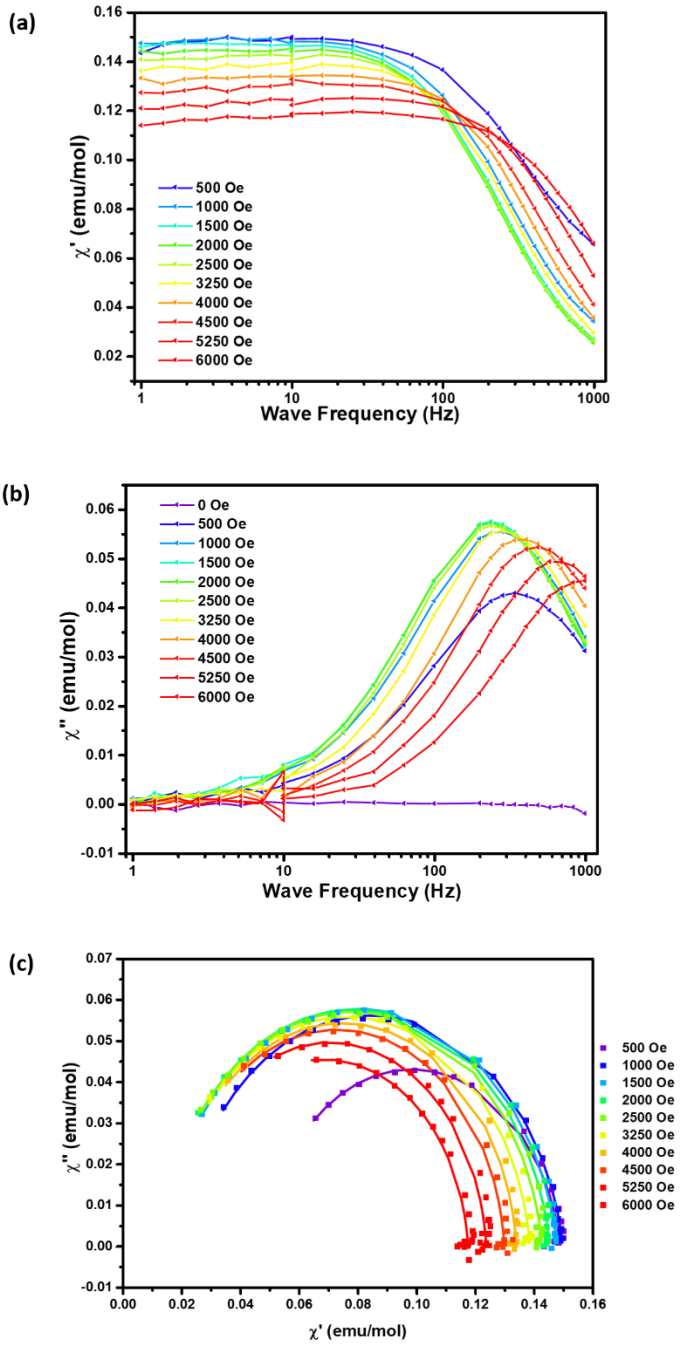

Figure IV-6 Frequency dependence of (a) in-phase and (b) out-of-phase ac susceptibility data from 1 Hz to 1000 Hz under a dc field ranging from 0 Oe to 6000 Oe at T = 2.5 K and (c) Cole-Cole plots with best fit (solid lines) for 8.

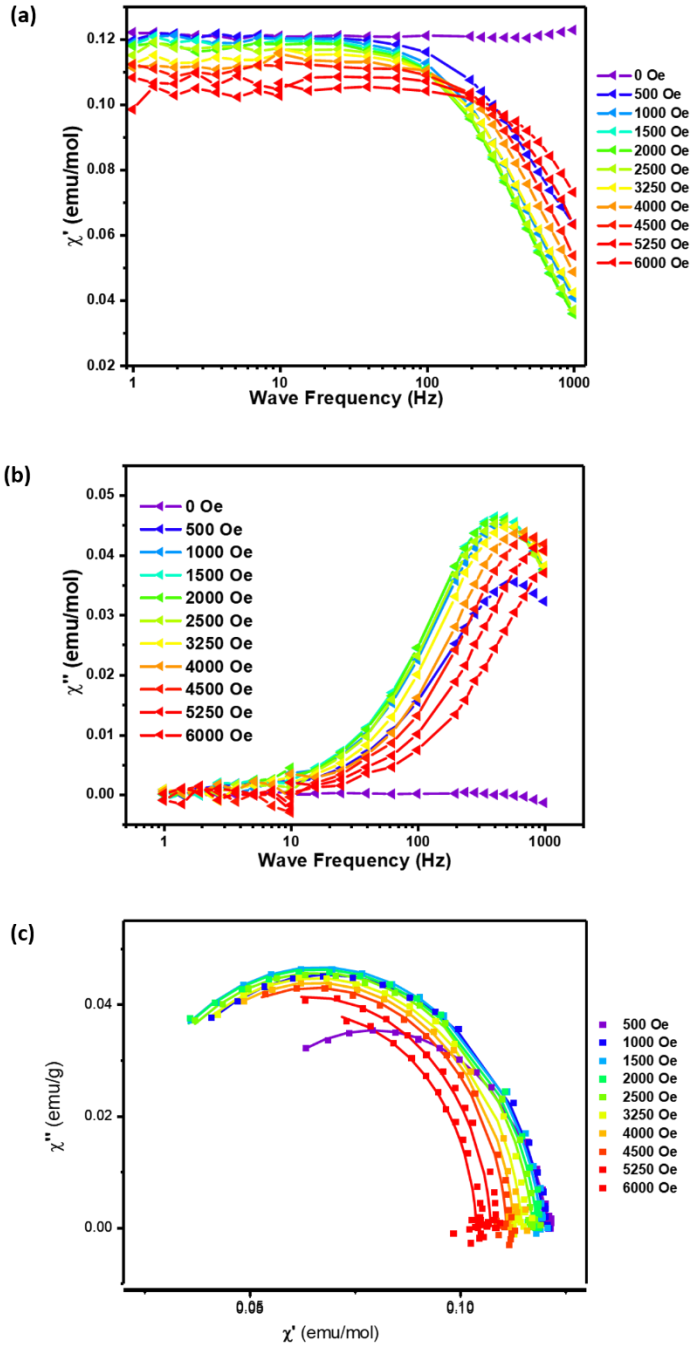

Figure IV-7 Frequency dependence of (a) in-phase and (b) out-of-phase ac susceptibility data from 1 Hz to 1000 Hz under dc fields ranging from 0 Oe to 6000 Oe at T = 3.0 K and (c) Cole-Cole plots with best fit (solid lines) for 8

Table IV-2 . Fitting parameters of the Cole-Cole plots of variable-field AC magnetic susceptibilities of 8 at T = 2.5 K

H/Oe	χ_s / emu mol^{-1}	χ_T / emu mol^{-1}	τ / s	α
500	0.048025	0.149116	0.000453	0.101837
1000	0.019116	0.149921	0.000598	0.095763
1500	0.013057	0.148033	0.000642	0.098210
2000	0.012442	0.145572	0.000649	0.091232
2500	0.01295	0.142927	0.00062	0.081471
3250	0.014057	0.138781	0.000524	0.069251
4000	0.015453	0.134167	0.000408	0.055973
4500	0.016126	0.130005	0.000335	0.048595
5250	0.017487	0.123825	0.000243	0.044222
6000	0.019698	0.11763	0.000176	0.047376

Table IV-3 Fitting parameters of the Cole-Cole plots of variable-field AC magnetic susceptibilities of 8 at T = 3.0 K.

H/Oe	χ_s / emu mol^{-1}	χ_T / emu mol^{-1}	τ / s	α
500	0.038249	0.121041	0.000277	0.100956
1000	0.016958	0.120311	0.000336	0.083543
1500	0.013802	0.119564	0.000363	0.079775
2000	0.01372	0.118601	0.000362	0.079460
2500	0.01527	0.117519	0.000351	0.072274
3250	0.017	0.114912	0.000306	0.057845
4000	0.018489	0.112992	0.000253	0.047448
4500	0.019691	0.111256	0.000217	0.040481
5250	0.020549	0.107505	0.000166	0.032391
6000	0.023681	0.104054	0.000128	0.026309

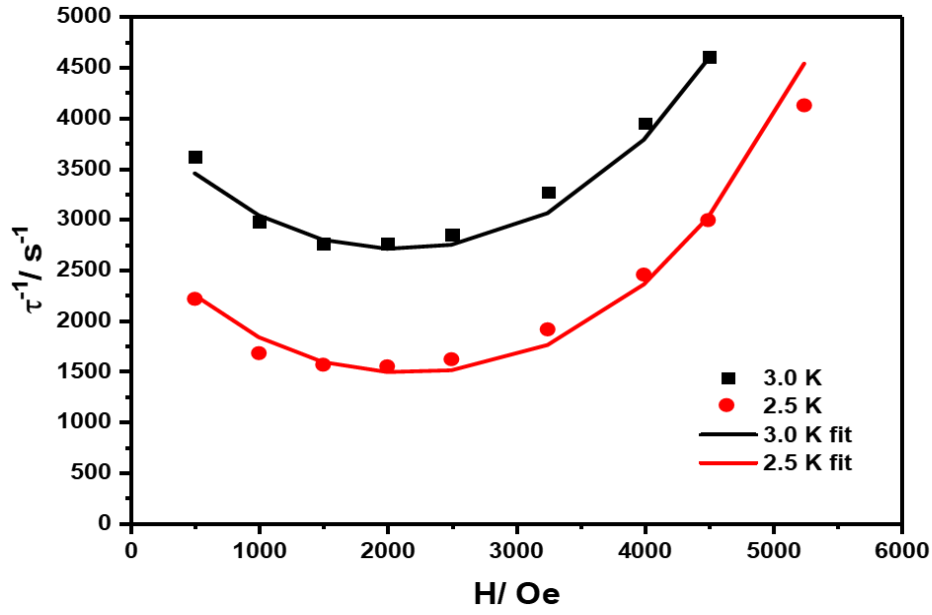

Figure IV-8 Field dependence of the inverse of relaxation time τ^{-1} of 8 at 2.5 K (red circle) and 3.0 K (black square). The solid lines show the best fit to the data with Equation 1.12.

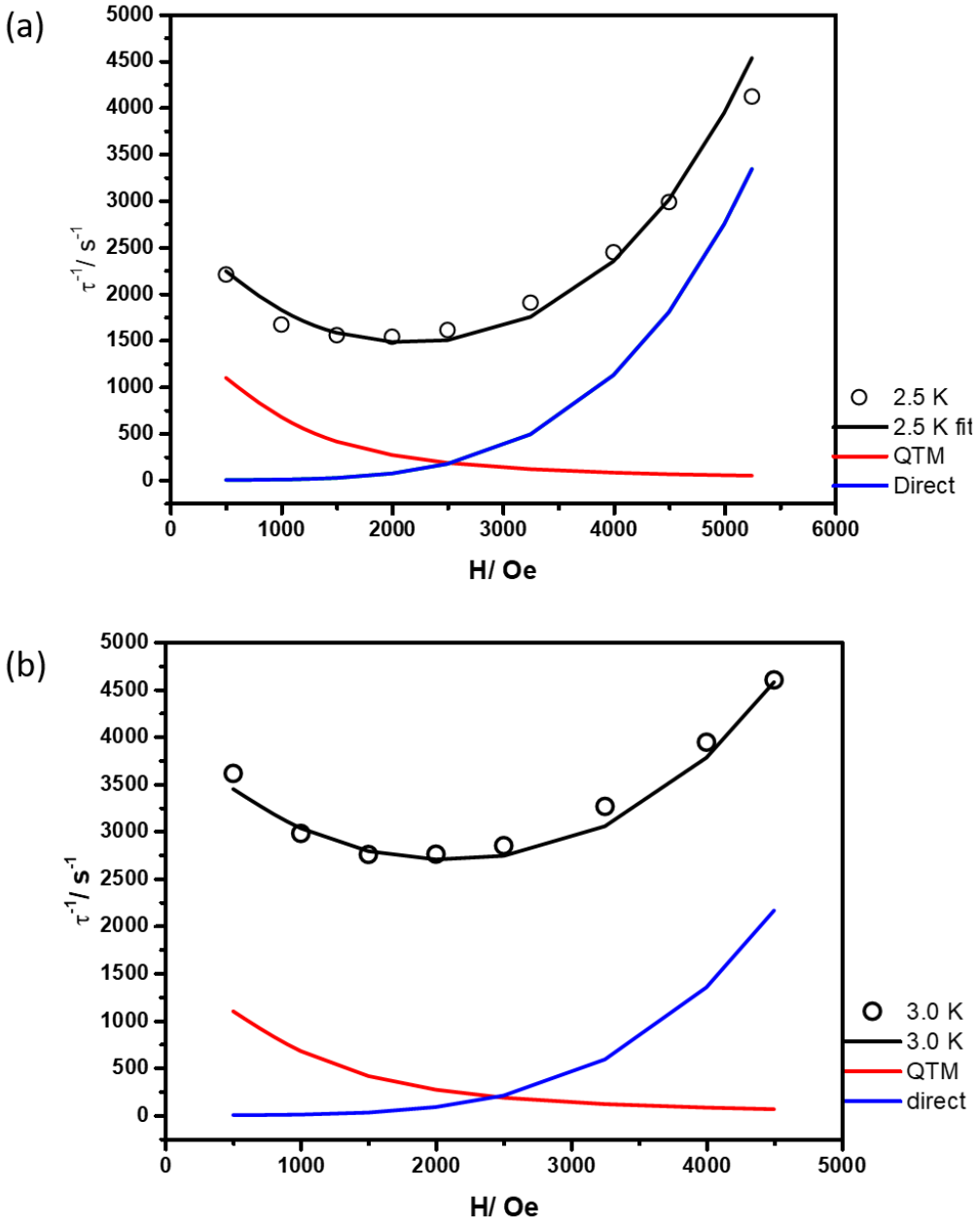

Figure IV-9 Field dependence of the inverse relaxation time τ^{-1} at (a) 2.5 K and (b) 3.0 K. Red lines show best fits to data with Equation 1.12. The red and blue lines show relative contributions from QTM and direct spin-phonon relaxation processes.

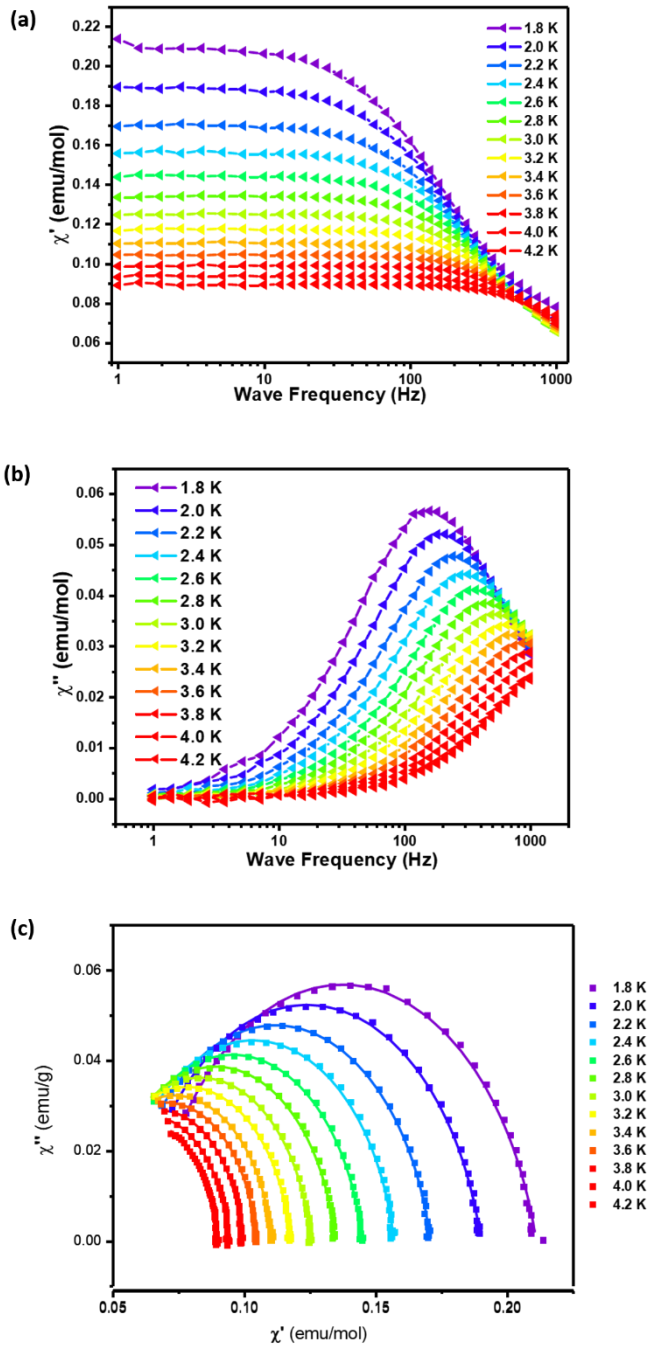

Figure IV-10 Frequency dependence of (a) in-phase and (b) out-of-phase ac susceptibility data from 1 Hz to 1000 Hz under H_{DC} = 500 Oe and (c) Cole-Cole plots with best fits (solid lines) for 8.

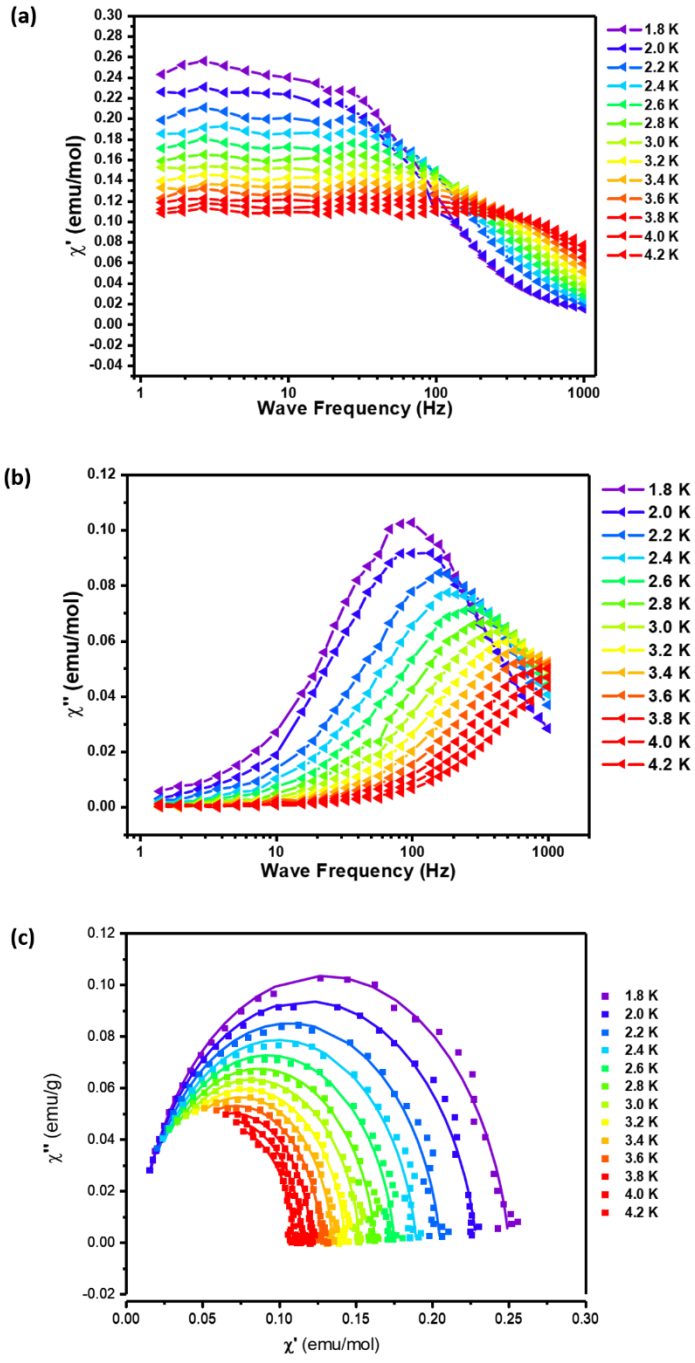

Figure IV-11 Frequency dependence of (a) in-phase and (b) out-of-phase ac susceptibility data from 1 Hz to 1000 Hz under H_{DC} = 1500 Oe and (c) Cole-Cole plots with best fits (solid lines) for 8.

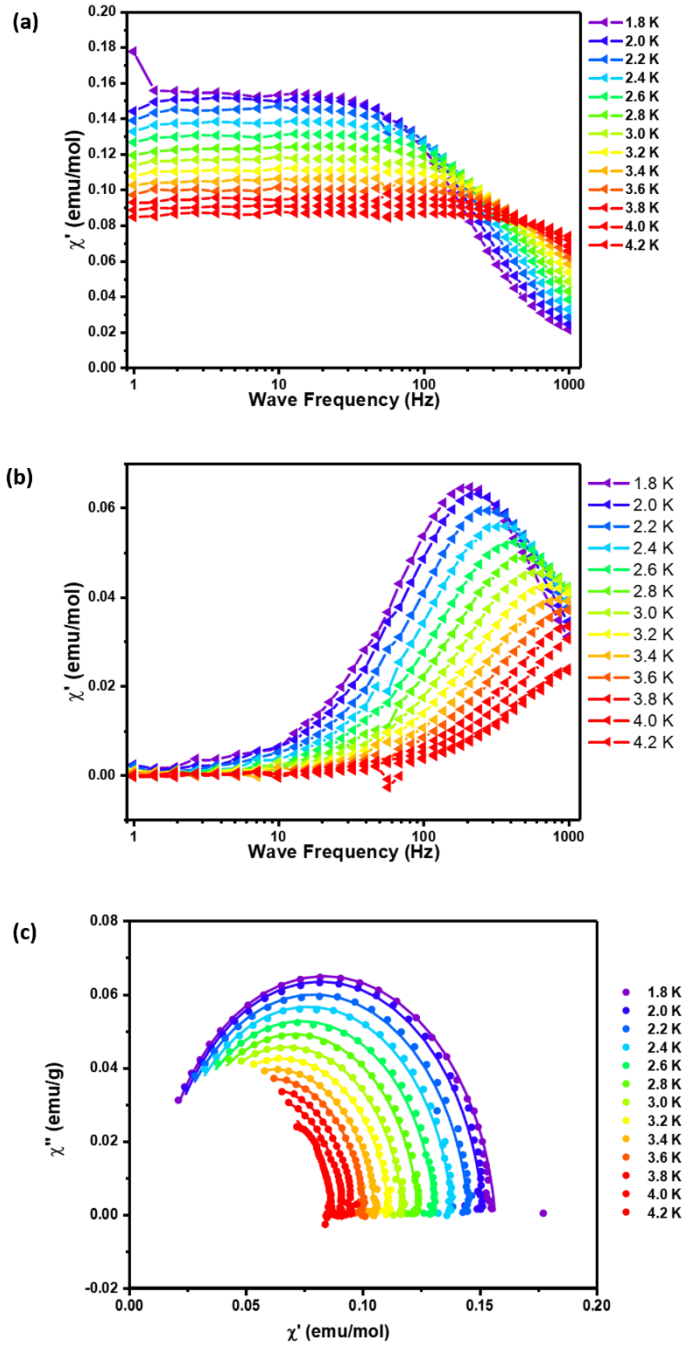

Figure IV-12 Frequency dependence of (a) in-phase and (b) out-of-phase ac susceptibility data from 1 Hz to 1000 Hz under H_{DC} = 4000 Oe and (c) Cole-Cole plots with best fits (solid lines) for 8.

Table IV-4 Fitting parameters of the Cole-Cole plots of variable-temperature AC magnetic susceptibilities for 8 under H_{DC} = 500 Oe.

T/K	χ_S / emu mol^{-1}	χ_T / emu mol^{-1}	τ / s	α
1.8	0.064046	0.211021	0.00094	0.162058
2	0.057975	0.190165	0.000758	0.147664
2.2	0.053046	0.170924	0.000609	0.132715
2.4	0.049716	0.157085	0.0005	0.119836
2.6	0.046502	0.144957	0.000418	0.112276
2.8	0.04396	0.134642	0.000348	0.102194
3	0.041556	0.125355	0.000293	0.093808
3.2	0.039334	0.117642	0.000246	0.088404
3.4	0.036259	0.110526	0.000202	0.090973
3.6	0.036631	0.104504	0.000176	0.065853
3.8	0.036703	0.099049	0.000152	0.048318
4	0.034173	0.093839	0.000125	0.048676
4.2	0.033069	0.089474	0.000101	0.040764

Table IV-5 Fitting parameters of the Cole-Cole plots of variable-temperature AC magnetic susceptibilities for 8 under H_{DC} = 1500 Oe.

T/K	χ_S / emu mol^{-1}	χ_T / emu mol^{-1}	τ / s	α
1.8	0.008383	0.250611	0.001629	0.100128
2	0.007218	0.229349	0.001486	0.108827
2.2	0.008756	0.20564	0.000932	0.093082
2.4	0.009875	0.190006	0.000739	0.087286
2.6	0.010123	0.175769	0.000584	0.084064
2.8	0.011128	0.16305	0.000467	0.076611
3	0.012277	0.152981	0.000381	0.068837
3.2	0.013571	0.143471	0.000312	0.057156
3.4	0.015231	0.134947	0.000256	0.039969
3.6	0.016499	0.127684	0.000211	0.031635
3.8	0.01774	0.120898	0.000176	0.019100
4	0.018963	0.114812	0.000146	0.008477
4.2	0.019083	0.109408	0.000121	0.000000

Table IV-6 Fitting parameters of the Cole-Cole plots of variable-temperature AC magnetic susceptibilities for 8 under H_{DC} = 4000 Oe.

T/K	χ_S / emu mol^{-1}	χ_T / emu mol^{-1}	τ / s	α
1.8	0.010746	0.156897	0.000767	0.074839
2	0.012656	0.151721	0.000654	0.058220
2.2	0.012969	0.14565	0.00054	0.064376
2.4	0.015281	0.138374	0.000456	0.053306
2.6	0.016593	0.13105	0.00038	0.052720
2.8	0.017946	0.123869	0.000319	0.047807
3	0.018195	0.117405	0.000264	0.053103
3.2	0.019689	0.111282	0.000223	0.048557
3.4	0.019945	0.105381	0.000184	0.049549
3.6	0.022735	0.10008	0.00016	0.029844
3.8	0.024945	0.095025	0.000137	0.015786
4	0.025873	0.090805	0.000117	0.009896
4.2	0.021201	0.086562	0.000080	0.034069

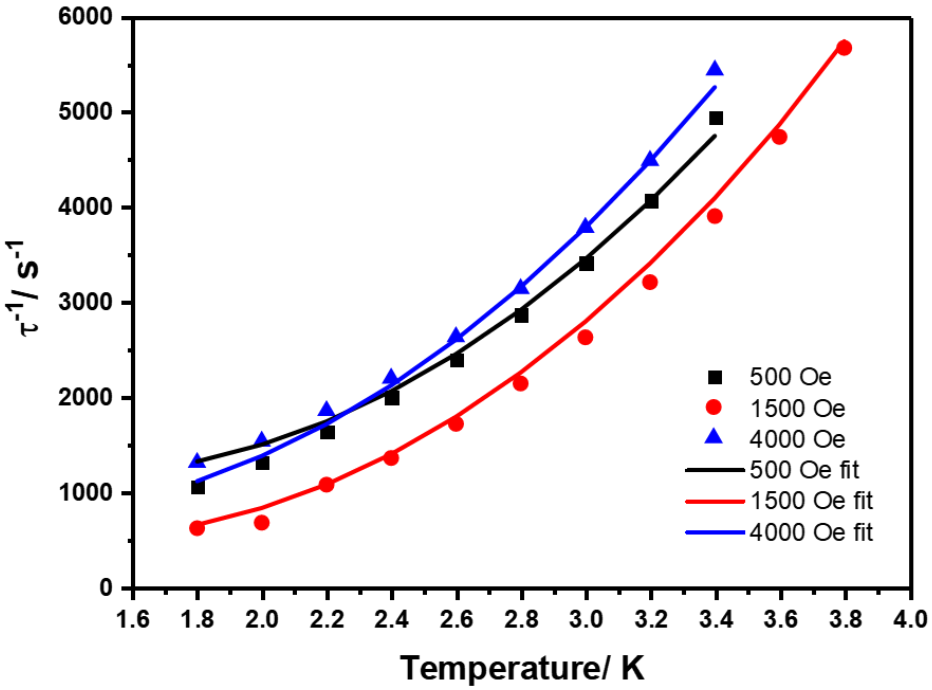

Figure IV-13 Temperature dependence of the inverse of relaxation time τ-1 of 1 under H_{DC} = 500 (black squares), 1500 (red circle) and 4000 Oe (blue triangles). The solid lines show the best fits to the data with Equation 1.11.

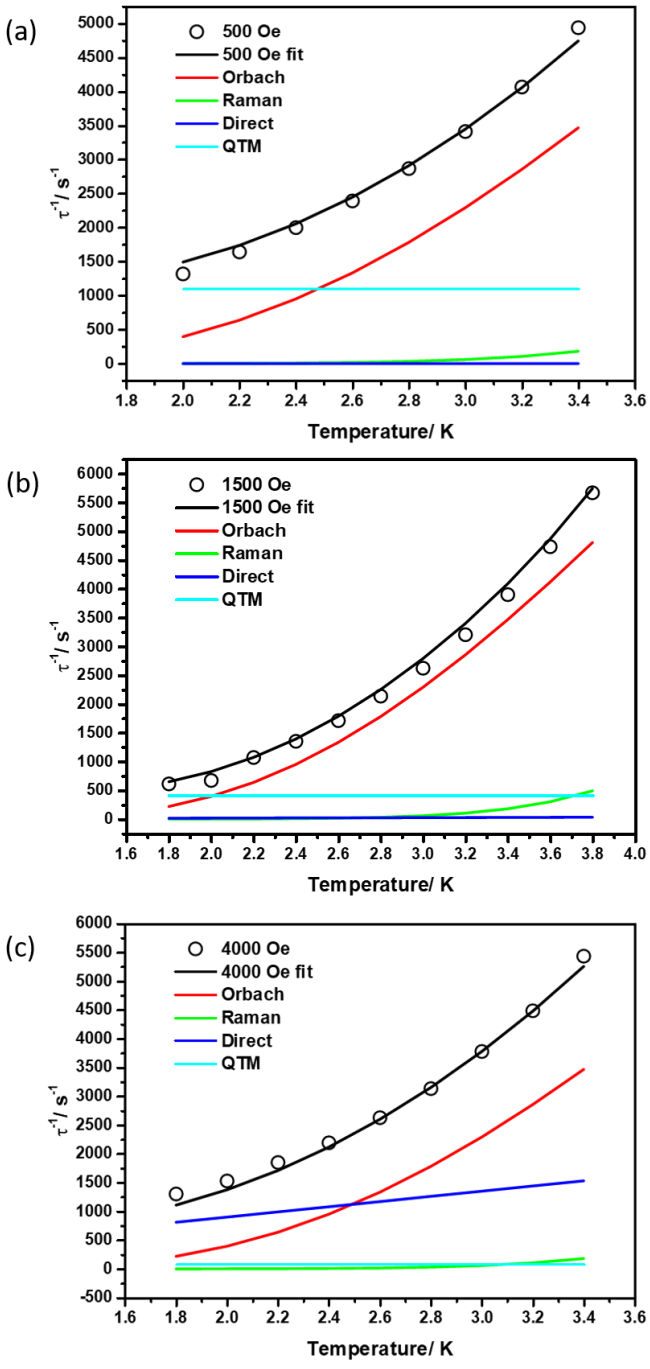

Figure IV-14 Temperature dependence of the inverse relaxation time τ^{-1} under (a) 500 Oe and (b) 1500 Oe and (c) 4000 Oe. Black lines show fits to data with Equation 1.11. The red, blue, green and teal lines show relative contributions from Orbach, direct, Raman relaxation and QTM processes.

To study the magnetic relaxation dynamics, alternating-current (ac) magnetic susceptibility studies of **8** were performed under different static fields in the range of 0 – 6000 Oe. No significant out-of-phase magnetic susceptibilities (χ'') signals were observed under zero static field, which is attributed to fast quantum tunneling of the ground states due to the positive D value with $m_s = \pm 1/2$ as ground states. Out-of-phase signals appeared when a small static field (≥500 Oe) was applied. In order to investigate the field dependence of the dynamic magnetic susceptibility in detail, variable-frequency ac data were collected in the range of 0 – 6000 Oe at two different temperatures, 2.5 K and 3.0 K (Figure IV-6 and IV-7). The fitting of the Cole-Cole plot (χ'' vs χ') gives the field dependence of relaxation times τ (Table IV-2 and IV-3). Two relaxation mechanisms, quantum tunneling and direct spin-phonon relaxation processes, respectively, are considered for the magnetic field dependence of τ^{-1} at constant temperature in Equation 1.12. The power of the magnetic field for the direct relaxation term is 4 for a Kramers doublet.[14] The field dependence of τ^{-1} (Figure IV-8) follows the same trend at both temperatures in that the value decreases when the field increases from 500 Oe to 1500 Oe, which indicates the existence of direct quantum tunneling in the ground state. The value of τ^{-1} then increases as the field increases up to 6000 Oe, which is caused by the direct spin-phonon relaxation process. The least-square fitting yields $A = 17.6(7) \times 10^3\ T^{-4}\ K^{-1}s^{-1}$, $B_1 = 1.4(2) \times 10^3\ s^{-1}$ and $B_2 = 1.0(4) \times 10^2\ T^{-2}$. The contributions of the quantum tunneling mechanism (QTM) and the direct spin-phonon relaxation are shown in Figure IV-9. The contribution of QTM dominates at low fields and then is

quenched as the field strength increases. On the contrary, the contribution of the direct spin-phonon process is insignificant at low fields but increases rapidly at higher fields.

The temperature dependence of the relaxation time was also studied under three different static fields (500, 1500 and 4000 Oe, shown in Figure IV-10, IV-11, IV-12). The relaxation time values, τ, fitted with a generalized Debye mode are given in Table IV-4, IV-5, IV-6. Four terms were included to fit the τ^{-1} values including the field-dependent terms, QTM and direct spin-phonon relaxation processes, and temperature-dependent terms which are Orbach and Raman processes (Equation 1.11). Parameters for the field-dependent terms that were determined above were used here to prevent over-parameterization. The n value is fixed as 9 for the Kramers doublet.[14, 244] The best fit (Figure IV-13) yields the following set of parameters: U_{eff} = 10.6(9) K, $\tau_0 = 1.3(5) \times 10^{-5}$ s, $C = 0.003(4)$ K^{-9} s^{-1} with $n = 9$. The relative contributions of four relaxation processes are shown in Figure IV-14. The main trend of the temperature dependence of τ^{-1} results from an Orbach process. The contribution from a Raman process is insignificant over the temperature range of 1.8-3.8 K. Compared to the previously reported example of a 3D MOF that built from Co^{II} SMM with a pseudo-octahedral geometry[244] (Table IV-7), the coefficients for the direct and Raman relaxation processes, A and C, of **8** are much lower. Although the nearest distance between Co^{II} centers in different nodes is 12.92 Å which is smaller than that in previously reported work (13.39 Å), the highly dilute nature of **8** significantly inhibits the direct and Raman relaxation processes, which is a desirable feature for practical application. Whereas, for **9**, no signal for χ'' was observed even under applied static fields up to 6000 Oe as a result of a non-magnetic ground state from

antiferromagnetic coupling. The absence of an AC signal also suggests the majority of M_4O nodes are in the Co_2Zn_2O form, despite the loading rate is 1.3 Co per node, as the $CoZn_3O$ node would exhibit some slow relaxation if it existed in sample **9**.

Table IV-7. Fitting parameters of relaxation processes of 8 and reported example of $\{[(Co(NCS)_2)_3(k^3\text{-}TPT)_4]\cdot a(H2O)\cdot b(MeOH)\}_n$

	8	$\{[(Co(NCS)_2)_3(k^3\text{-}TPT)_4]\cdot a(H_2O)\cdot b(MeOH)\}_n$
A/ T^{-4} $K^{-1}s^{-1}$	$1.76(7)\times10^4$	1.43×10^8
C/ K^{-n} s^{-1}	0.003(4)	0.94
n	9	8.97

Conclusions

The successful functionalization of UMCM-1 with octahedral a Co^{II} SMM has been realized by post-synthetic ion exchange between the Zn^{2+} ions in the Zn_4O metal nodes and Co^{2+} ions in solution. Different ion exchange times result in two distinct products, **8** (12 hours, pink) and **9** (1 week, blue). The loading rates and composites of **8** and **9** were confirmed by elemental analyses, solid state UV-vis spectroscopy and magnetic studies. Sample **8** exhibits a typical field-induced SMM behavior with U_{eff} = 10.6(9) K. On the other hand, **9** exhibits antiferromagnetically coupled behavior with C = 2.90 emu K mol^{-1} and θ = - 164 K. The contributions of different relaxation processes to the relaxation time were analyzed in detail. The direct relaxation and QTM processes can be suppressed by applying an optimized field (1500 Oe). The major relaxation process is an Orbach one while the contribution from a Raman process is insignificant. Compared to the reported SMMs with Co^{II} in an octahedral environment, the direct and Raman relaxation processes are significantly suppressed. These results demonstrate the

feasibility of installing the Co^{II} SMM moiety into a mesoporous MOFs via post-synthetic ion exchange methods. The analysis of relaxation time contributions from different mechanisms suggests that the direct and Raman process can be suppressed via installing the SMM moiety to the mesoporous MOF, UMCM-1.

CHAPTER V

SUMMARY AND FUTURE OUTLOOK

In order to reach the demand of miniaturization and new functionalities for future generations of electronic devices, materials with multiple functionalities, such as electrical, magnetic, optical properties etc., are of high interest. Molecule-based materials have advantages in tackling these goals under nanoscale conditions, as their properties can be preserved and manipulated at the molecular level. Key tools for realizing the synthesis, assembly and property tuning of molecular materials are supramolecular interactions, such as $\pi^{\cdots}\pi$ stacking, electrostatic and charge-transfer interactions. They are not only critical in determining the solid state assembly of these molecular building blocks, but also essential in achieving tunability and synergistic interactions between different functionalities. The work presented in this dissertation are mainly focused on using TCNQ and its derivatives along with structurally functionalized molecular magnetic moieties as building blocks to introduce supramolecular interactions in order to probe their effect on synergistic interactions of functionalities. In an unrelated effort, the installation of SMM units into a mesoporous MOF to reduce undesirable relaxation processes were demonstrated.

In Chapter II, TCNQ anion-radical derivatives were used to fine tune the magnetic properties of the $[Co^{II}(Fctp)_2]^{2+}$ cation in the solid state. The co-crystallization of $[Co^{II}(Fctp)_2]^{2+}$ and TCNQ results in two pseudo-polymorphic products, namely $[Co^{II}(Fctp)_2]$ $(TCNQ)_2$ (**1**) and $[Co^{II}(Fctp)_2]$ $(TCNQ)_2 \cdot MeCN$ (**2**). It was also found that the reaction with $TCNQF^{\cdot-}$ yields only $[Co^{II}(Fctp)_2]$ $(TCNQF)_2 \cdot MeCN$ (**3**). Compound **1**

exhibits field-induced SMM properties SMMs property with U_{eff} = 19.1 K and τ_0 = 9.8 × 10^{-6} s. The studies of magnetic relaxation mechanisms for **1** revealed that the main contributions are from Orbach and Raman processes in the optimal field of 1750 Oe. Compounds **2** and **3** are isostructural and exhibit spin-crossover behavior with different transition temperatures of $T_{1/2}$ = 336 K and 226 K, respectively. Close inspection of solid state structure along with theoretical DFT calculations reveal that the differences in the magnetic properties of $[Co^{II}(Fctp)_2]^{2+}$ originate from supramolecular interactions between $[Co^{II}(Fctp)_2]^{2+}$ and tunable $TCNQ^{\cdot-}$/$TCNQF^{\cdot-}$ anion-radical derivatives. The substitution of the fluorine substituent on the TCNQ radical anion introduces more repulsion between the ferrocenyl group on $[Co^{II}(Fctp)_2]^{2+}$ and the electrons on fluorine compared to the hydrogen atom on original TCNQ. The $\pi\cdots\pi$ interactions between $TCNQF^{\cdot-}$ and the ferrocenyl group in the phase-I structure are also weakened by the larger energy gap between the LUMO on the ferrocenyl group and the HOMO on the $(TCNQF)_2^{2-}$ dimer. These differences result in the phase-I product being unfavored in the reaction with $TCNQF^{\cdot-}$. The difference in SCO transition temperatures of the isostructural products, **2** and **3**, are likely caused by electric dipole interactions between the $[Co^{II}(Fctp)_2]^{2+}$ moiety and $TCNQ^{\cdot-}$ (zero net dipole)/ $TCNQF^{\cdot-}$ (non-zero dipole). The work presented here demonstrates that supramolecular interactions can be used to tune molecular magnetic properties, but the results are limited to the existence of two kinds of molecular magnetic bistability in two distinct crystal structures. It will be more promising if the switches can be enabled by external stimuli, such as irradiation, in the same crystal structure. Embedding photoswitchable building blocks, such as

diarylethenes and azobenzenes,[248] into the SCO moieties with co-crystallized[248] into the SCO moieties and cocrystallize with TCNQ radical anions could be a promising strategy for this purpose.

Chapter III describes the synthesis and characterizations of conducting SCO compounds with synergistic interactions between the magnetic and semiconducting properties. The SCO moiety, $[Co^{II}(PTZ\text{-}tpy)_2]^{2+}$ and its diamagnetic analog, $[Zn^{II}(PTZ\text{-}tpy)_2]^{2+}$, were synthesized and co-crystallized with partially charged TCNQ moieties to give $[Co(PTZ\text{-}tpy)_2]_2(TCNQ)_{4.5}\cdot 2.5MeCN$ (**6**) and $[Zn(PTZ\text{-}tpy)_2]_2(TCNQ)_{4.5}\cdot 2.5MeCN$ (**7**). The mixed-stacking patterns of the TCNQ and PTZ groups on the SCO moieties were achieved in compounds **6** and **7** as TCNQ has strong charge-transfer interactions with the PTZ group. Compounds **6** and **7** are isostructural and exhibit different magnetic and semiconducting behavior. Temperature-dependent single-crystal X-ray structures were collected with synchrotron irradiation at the Advanced Photon Source facility located in Argonne National Laboratories. Detailed analysis of the temperature-dependent M-N coordination bond distances and the charge states of different TCNQ moieties reveals that the synergy between the SCO behavior and electron transfer between different TCNQ moieties was found for compound **6** whereas the diamagnetic zinc analog, compound **7**, did not exhibit any significant changes in bond distances and TCNQ charge states. Magnetic susceptibility measurements revealed that one of the Co^{II} centers preserves SCO properties in compound **6** but only the contributions of localized and delocalized radical species from TCNQ moieties were observed in compound **7**. The EPR spectra of **6** and **7** further confirm the identities of the paramagnetic species in

compound **4**, **6** and **7**. The temperature-dependent conductivity measurements of **6** and **7** indicate that the semiconducting properties of **6** and **7** are similar at room temperature while differences are observed at low temperature which is attributed to the SCO induced charge transfer in **6**. The results obtained thus far demonstrate that introducing supramolecular interactions, such as charge transfer interactions between conducting and SCO moieties, can be used to modify the solid state structures as well as realize synergism between SCO and semiconducting behavior. There are still several aspects that can be further investigated in such systems: (1) the PTZ group on $[Co^{II}(PTZ\text{-}tpy)_2]^{2+}$ is not planar as the sulfur is in sp^3 hybridization. Planar electron donor moieties such as the phenazine radical and tetrathiafulvalene would be good choices to achieve better overlap between electron donor moieties and the electron acceptor TCNQ, (2) replacing TCNQ with other TCNQ derivatives as electron acceptors in such system would be useful for investigating how the redox potential of TCNQ moieties can affect the synergistic interactions between SCO and semiconducting behavior and (3) Other spin-crossover moieties, such as those based on Fe^{II} that undergo abrupt transitions may lead to more pronounced synergistic interactions between SCO and semiconducting behavior.

Other than enhancing the intermolecular interactions, minimizing the spin-spin and spin-phonon relaxations are critical for high-performance SMMs. Chapter IV describes a method of installing octahedral Co^{II} based SMM intoSMMs to the metal nodes of the mesoporous MOF, UMCM-1, via ion exchange. Two samples with different Co^{II} loading percentages, **8** and **9** were synthesized and characterized. The direct current and alternating current magnetic characterizations indicate that sample **8** with a 0.3 Co

per M_4O node loading shows typical octahedral Co^{II} SMM behavior under applied fields, while sample **9**, with a higher loading percentage, exhibits antiferromagnetic coupling between the Co^{II} centers. A detailed investigation of the relaxation processes indicates that the Raman and direct relaxation processes can be suppressed by loading the SMM moiety into the mesoporous MOF. This work is an excellent proof-of-concept to demonstrate a method for introducing SMM moieties into mesoporous MOFs to minimize undesired relaxation processes. Thus, incorporating SMMs with high energy barriers, such as lanthanide SMMs, into mesoporous MOFs is expected to be very promising for practical applications. The way in which the topology of MOFs, such as connectivity, symmetry and distance between metal nodes, will affect the relaxation mechanism is also worth being investigated using different types of MOFs.

REFERENCES

1. Vela, S.; Mota, F.; Deumal, M.; Suizu, R.; Shuku, Y.; Mizuno, A.; Awaga, K.; Shiga, M.; Novoa, J. J.; Ribas-Arino, J., The Key Role of Vibrational Entropy in the Phase Transitions of Dithiazolyl-Based Bistable Magnetic Materials. *Nat. Commun.* **2014,** *5* (1), 4411.

2. Fujita, W.; Awaga, K., Room-Temperature Magnetic Bistability in Organic Crystals: A Comparison with Spin Crossover Transitions. *J. Solid State Chem.* **2001,** *159* (2), 451-454.

3. Caneschi, A.; Gatteschi, D.; Sessoli, R.; Barra, A. L.; Brunel, L. C.; Guillot, M., Alternating Current Susceptibility, High Field Magnetization, and Millimeter Band Epr Evidence for a Ground S = 10 State in $[Mn_{12}O_{12}(CH_3COO)_{16}(H_2O)_4].2CH_3COOH.4H_2O$. *J. Am. Chem. Soc.* **1991,** *113* (15), 5873-5874.

4. Sessoli, R.; Tsai, H. L.; Schake, A. R.; Wang, S.; Vincent, J. B.; Folting, K.; Gatteschi, D.; Christou, G.; Hendrickson, D. N., High-Spin Molecules: $[Mn_{12}O_{12}(O_2CR)_{16}(H_2O)_4]$. *J. Am. Chem. Soc.* **1993,** *115* (5), 1804-1816.

5. Sessoli, R.; Gatteschi, D.; Caneschi, A.; Novak, M. A., Magnetic Bistability in a Metal-Ion Cluster. *Nature* **1993,** *365* (6442), 141-143.

6. Ako, A. M.; Hewitt, I. J.; Mereacre, V.; Clérac, R.; Wernsdorfer, W.; Anson, C. E.; Powell, A. K., A Ferromagnetically Coupled Mn19 Aggregate with a Record S=83/2 Ground Spin State. *Angew. Chem. Int. Ed.* **2006,** *45* (30), 4926-4929.

7. Stamatatos, T. C.; Abboud, K. A.; Wernsdorfer, W.; Christou, G., "Spin Tweaking" of a High-Spin Molecule: An Mn_{25} Single-Molecule Magnet with an S=61/2 Ground State. *Angew. Chem. Int. Ed.* **2007,** *46* (6), 884-888.

8. Wang, X.-Y.; Prosvirin, A. V.; Dunbar, K. R., A Docosanuclear {Mo8mn14} Cluster Based on $[Mo(CN)_7]^{4-}$. *Angew. Chem. Int. Ed.* **2010,** *49* (30), 5081-5084.

9. Guo, F.-S.; Day, B. M.; Chen, Y.-C.; Tong, M.-L.; Mansikkamäki, A.; Layfield, R. A., Magnetic Hysteresis up to 80 Kelvin in a Dysprosium Metallocene Single-Molecule Magnet. *Science* **2018,** *362* (6421), 1400.

10. Yao, X.-N.; Du, J.-Z.; Zhang, Y.-Q.; Leng, X.-B.; Yang, M.-W.; Jiang, S.-D.; Wang, Z.-X.; Ouyang, Z.-W.; Deng, L.; Wang, B.-W.; Gao, S., Two-Coordinate Co(Ii) Imido Complexes as Outstanding Single-Molecule Magnets. *J. Am. Chem. Soc.* **2017,** *139* (1), 373-380.

11. Caneschi, A.; Ohm, T.; Paulsen, C.; Royal, D.; Sangregorio, C.; Sessolia, R., Quantum Tunneling of the Magnetic Moment in Manganese and Iron Molecular Clusters. *J. Magn. Magn. Mater.* **1998,** *177-181*, 1330-1336.

12. Gatteschi, D.; Sessoli, R., Quantum Tunneling of Magnetization and Related Phenomena in Molecular Materials. *Angew. Chem. Int. Ed.* **2003,** *42* (3), 268-297.

13. Lindgard, P.-A., Tables of Products of Tensor Operators and Stevens Operators. *J. Phys. C* **1975,** *8* (20), 3401-3407.

14. Abragam, A.; Bleaney, B., *Electron Paramagnetic Resonance of Transition Ions*. Clarendon P.: Oxford, 1970.

15. Woodruff, D. N.; Winpenny, R. E. P.; Layfield, R. A., Lanthanide Single-Molecule Magnets. *Chem. Rev.* **2013,** *113* (7), 5110-5148.

16. Craig, G. A.; Murrie, M., 3d Single-Ion Magnets. *Chem. Soc. Rev.* **2015,** *44* (8), 2135-2147.

17. Zhang, P.; Zhang, L.; Tang, J., Lanthanide Single Molecule Magnets: Progress and Perspective. *Dalton Trans.* **2015,** *44* (9), 3923-3929.

18. Frost, J. M.; Harriman, K. L. M.; Murugesu, M., The Rise of 3-D Single-Ion Magnets in Molecular Magnetism: Towards Materials from Molecules? *Chem Sci* **2016,** *7* (4), 2470-2491.

19. Feng, M.; Tong, M.-L., Single Ion Magnets from 3d to 5f: Developments and Strategies. *Chem. Eur. J.* **2018,** *24* (30), 7574-7594.

20. Zhu, Z.; Guo, M.; Li, X.-L.; Tang, J., Molecular Magnetism of Lanthanide: Advances and Perspectives. *Coord. Chem. Rev.* **2019,** *378*, 350-364.

21. Cole, K. S.; Cole, R. H., Dispersion and Absorption in Dielectrics I. Alternating Current Characteristics. *J. Chem. Phys.* **1941,** *9* (4), 341-351.

22. Coffey, W. T. In *Theory of Anomalous Dielectric Relaxation*, Nonlinear Dielectric Phenomena in Complex Liquids, Dordrecht, 2005//; Rzoska, S. J.; Zhelezny, V. P., Eds. Springer Netherlands: Dordrecht, 2005; pp 19-29.

23. Liddle, S. T.; van Slageren, J., Improving F-Element Single Molecule Magnets. *Chem. Soc. Rev.* **2015,** *44* (19), 6655-6669.

24. Ding, Y.-S.; Yu, K.-X.; Reta, D.; Ortu, F.; Winpenny, R. E. P.; Zheng, Y.-Z.; Chilton, N. F., Field- and Temperature-Dependent Quantum Tunnelling of the

Magnetisation in a Large Barrier Single-Molecule Magnet. *Nat. Commun.* **2018,** *9* (1), 3134.

25. Inoshita, T.; Sakaki, H., Electron-Phonon Interaction and the So-Called Phonon Bottleneck Effect in Semiconductor Quantum Dots. *Physica B Condens. Matter* **1996,** *227* (1), 373-377.

26. Shrivastava, K. N., Theory of Spin–Lattice Relaxation. *physica status solidi (b)* **1983,** *117* (2), 437-458.

27. Cambi, L.; Szegö, L., Über Die Magnetische Susceptibilität Der Komplexen Verbindungen. *Ber. Dtsch. Chem. Ges.* **1931,** *64* (10), 2591-2598.

28. Pauling, L.; Coryell, C. D., The Magnetic Properties and Structure of Hemoglobin, Oxyhemoglobin and Carbonmonoxyhemoglobin. *Proc. Natl. Acad. Sci. U.S.A.* **1936,** *22* (4), 210.

29. Halcrow, M. A., *Spin-Crossover Materials : Properties and Applications*. Wiley: Chichester, West Sussex, 2013.

30. Achey, D.; Meyer, G. J., Ligand Coordination and Spin Crossover in a Nickel Porphyrin Anchored to Mesoporous Tio2 Thin Films. *Inorg. Chem.* **2013,** *52* (16), 9574-9582.

31. Ma, H.; Petersen, J. L.; Young, V. G.; Yee, G. T.; Jensen, M. P., Solid-State Spin Crossover of Ni(Ii) in a Bioinspired N3s2 Ligand Field. *J. Am. Chem. Soc.* **2011,** *133* (15), 5644-5647.

32. Lancashire, R. J. Tanabe-Sugano Diagrams Via Spreadsheets. http://wwwchem.uwimona.edu.jm/courses/Tanabe-Sugano/TSspread.html (accessed 14 Oct.).

33. Real, J. A.; Gaspar, A. B.; Muñoz, M. C., Thermal, Pressure and Light Switchable Spin-Crossover Materials. *Dalton Trans.* **2005,** (12), 2062-2079.

34. Köppel, H.; Yarkony, D. R.; Barentzen, H., *The Jahn-Teller Effect: Fundamentals and Implications for Physics and Chemistry*. Springer Berlin Heidelberg: 2009.

35. Ohkoshi, S.-i.; Takano, S.; Imoto, K.; Yoshikiyo, M.; Namai, A.; Tokoro, H., 90-Degree Optical Switching of Output Second-Harmonic Light in Chiral Photomagnet. *Nat. Photonics* **2014,** *8* (1), 65-71.

36. Wang, C.-F.; Li, R.-F.; Chen, X.-Y.; Wei, R.-J.; Zheng, L.-S.; Tao, J., Synergetic Spin Crossover and Fluorescence in One-Dimensional Hybrid Complexes. *Angew. Chem. Int. Ed.* **2015,** *54* (5), 1574-1577.

37. Slichter, C. P.; Drickamer, H. G., Pressure-Induced Electronic Changes in Compounds of Iron. *J. Chem. Phys.* **1972,** *56* (5), 2142.

38. Tanabe, Y.; Sugano, S., On the Absorption Spectra of Complex Ions. I. *J. Phys. Soc. Jpn.* **1954,** *9* (5), 753-766.

39. Muñoz Lara, F. J.; Gaspar, A. B.; Aravena, D.; Ruiz, E.; Muñoz, M. C.; Ohba, M.; Ohtani, R.; Kitagawa, S.; Real, J. A., Enhanced Bistability by Guest Inclusion in Fe(II) Spin Crossover Porous Coordination Polymers. *Chem. Commun.* **2012,** *48* (39), 4686-4688.

40. Brooker, S., Spin Crossover with Thermal Hysteresis: Practicalities and Lessons Learnt. *Chem. Soc. Rev.* **2015,** *44* (10), 2880-2892.

41. Gu, Y.; Hu, Y.; Huang, J.; Li, Q.; Yang, J., Spin-Crossover and Coherent Transport Behaviors of a Six-Coordinate Iron(II) Complex with a N4o2 Donor Set. *J. Phys. Chem. C* **2019,** *123* (26), 16366-16372.

42. Li, F.; Huang, J.; Hu, Y.; Li, Q., Transport Property of Ligand-Driven Light-Induced Spin-Change Fe-Based Spin Crossover Complexes. *RSC Advances* **2019,** *9* (22), 12339-12345.

43. Harzmann, G. D.; Frisenda, R.; van der Zant, H. S. J.; Mayor, M., Single-Molecule Spin Switch Based on Voltage-Triggered Distortion of the Coordination Sphere. *Angew. Chem. Int. Ed.* **2015,** *54* (45), 13425-13430.

44. Calbo, J.; Golomb, M. J.; Walsh, A., Redox-Active Metal–Organic Frameworks for Energy Conversion and Storage. *J. Mater. Chem. A* **2019,** *7* (28), 16571-16597.

45. Kreuer, K.-D., Proton Conductivity: Materials and Applications. *Chem. Mater.* **1996,** *8* (3), 610-641.

46. Zhang, Z.; Zhao, H.; Kojima, H.; Mori, T.; Dunbar, K. R., Conducting Organic Frameworks Based on a Main-Group Metal and Organocyanide Radicals. *Chem. Eur. J.* **2013,** *19* (10), 3348-3357.

47. Kojima, H.; Zhang, Z.; Dunbar, K. R.; Mori, T., Energy Band Structure and Metal‐Organic Interactions in Tetracyanoquinodimethane (Tcnq) and N,N′-Dicyanoquinonediimine (Dcnqi) Materials. *J. Mater. Chem. C* **2013,** *1* (9), 1781-1790.

48. Guan, Y.-S.; Hu, Y.; Zhang, H.; Wu, G.; Yan, H.; Ren, S., A Highly Conductive, Transparent Molecular Charge-Transfer Salt with Reversible Lithiation. *Chem. Commun.* **2019,** *55* (50), 7179-7182.

49. Akutagawa, T.; Hasegawa, T.; Nakamura, T.; Inabe, T.; Saito, G., Coupled Protonic and Electronic Conduction in the Molecular Conductor 2-(2-1h-Benzimidazolyl) 1h-Benzimidazolium -Tcnq. *Chem. Eur. J.* **2002,** *8* (19), 4402-4411.

50. Akutagawa, T.; Hasegawa, T.; Nakamura, T.; Saito, G., Hydrogen-Bonded Supramolecular (2,2 '-Bi-1h-Benzimidazole)(2-(2-1h-Benzimidazolyl)-1h-Benzimidazolium(+))(2) (Cl^-) as an Electron Donor in a Tcnq Complex. *CrystEngComm* **2003**, 54-57.

51. Akutagawa, T.; Takeda, S.; Hasegawa, T.; Nakamura, T., Proton Transfer and a Dielectric Phase Transition in the Molecular Conductor (Hdabco(+))(2)(TCNQ)(3). *J. Am. Chem. Soc.* **2004,** *126* (1), 291-294.

52. Morita, Y.; Murata, T.; Fukui, K.; Yamada, S.; Sato, K.; Shiomi, D.; Takui, T.; Kitagawa, H.; Yamochi, H.; Saito, G.; Nakasuji, K., Hydrogen-Bonded Networks in Organic Conductors: Crystal Structures and Electronic Properties of Charge-Transfer Salts of Tetracyanoquinodimethane with 4,4 '-Biimidazolium Having Multiprotonated States. *J. Org. Chem.* **2005,** *70* (7), 2739-2744.

53. Murata, T.; Morita, Y.; Nakasuji, K., Pluri-Dimensional Hydrogen-Bonded Networks of Novel Thiophene-Introduced Oligo(Imidazole)S and Physical Properties of Their Charge-Transfer Complexes with TCNQ. *Tetrahedron* **2005,** *61* (25), 6056-6063.

54. Murata, T.; Morita, Y.; Yakiyama, Y.; Yamamoto, Y.; Yamada, S.; Nishimura, Y.; Nakasuji, K., Hydrogen-Bond Architectures of Protonated 4,4 '-Biimidazolium Derivatives and Oligo(Imidazolium)S in Charge-Transfer Salts with Tetracyanoquinodimethane. *Cryst. Growth Des.* **2008,** *8* (8), 3058-3065.

55. Kistenmacher, T. J.; Emge, T. J.; Bloch, A. N.; Cowan, D. O., Structure of the Red, Semiconducting Form of 4,4',5,5'-Tetramethyl-Δ2,2'-Bi-1,3-Diselenole-7,7,8,8-Tetracyano-P-Quinodimethane, TMTSF–TCNQ. *Acta Crystallographica Section B* **1982,** *38* (4), 1193-1199.

56. Chappell, J. S.; Bloch, A. N.; Bryden, W. A.; Maxfield, M.; Poehler, T. O.; Cowan, D. O., Degree of Charge Transfer in Organic Conductors by Infrared Absorption Spectroscopy. *J. Am. Chem. Soc.* **1981,** *103* (9), 2442-2443.

57. Cohen, M. J.; Coleman, L. B.; Garito, A. F.; Heeger, A. J., Electrical Conductivity of Tetrathiofulvalinium Tetracyanoquinodimethan (TTF) (TCNQ). *Physical Review B* **1974,** *10* (4), 1298-1307.

58. Jiang, H.; Hu, P.; Ye, J.; Zhang, K. K.; Long, Y.; Hu, W.; Kloc, C., Tuning of the Degree of Charge Transfer and the Electronic Properties in Organic Binary Compounds by Crystal Engineering: A Perspective. *J. Mater. Chem. C* **2018,** *6* (8), 1884-1902.

59. Goetz, K. P.; Vermeulen, D.; Payne, M. E.; Kloc, C.; McNeil, L. E.; Jurchescu, O. D., Charge-Transfer Complexes: New Perspectives on an Old Class of Compounds. *J. Mater. Chem. C* **2014,** *2* (17), 3065-3076.

60. Melby, L. R.; Harder, R. J.; Hertler, W. R.; Mahler, W.; Benson, R. E.; Mochel, W. E., Substituted Quinodimethans. Ii. Anion-Radical Derivatives and Complexes of 7,7,8,8-Tetracyanoquinodimethan. *J. Am. Chem. Soc.* **1962,** *84* (17), 3374-3387.

61. Wang, J. W.; Ji, Z. Y.; Yang, G. H.; Chuai, X. C.; Liu, F. J.; Zhou, Z.; Lu, C. Y.; Wei, W.; Shi, X. W.; Niu, J. B.; Wang, L.; Wang, H.; Chen, J. Z.; Lu, N. D.; Jiang, C.; Li, L.; Liu, M., Charge Transfer within the F(4)Tcnq-Mos2 Van Der Waals Interface: Toward Electrical Properties Tuning and Gas Sensing Application. *Adv. Funct. Mater.* **2018,** *28* (51).

62. Shafiei, M.; Hoshyargar, F.; Lipton-Duffin, J.; Piloto, C.; Motta, N.; O'Mullane, A. P., Conversion of N-Type Cutcnq into P-Type Nitrogen-Doped Cuo and the Implication for Room-Temperature Gas Sensing. *J. Phys. Chem. C* **2015,** *119* (38), 22208-22216.

63. Ramanathan, R.; Kandjani, A. E.; Walia, S.; Balendhran, S.; Bhargava, S. K.; Kalantar-zadeh, K.; Bansal, V., 3-D Nanorod Arrays of Metal-Organic Ktcnq Semiconductor on Textiles for Flexible Organic Electronics. *Rsc Advances* **2013,** *3* (39), 17654-17658.

64. Fang, C.; Ye, Z.; Wang, Y.; Zhao, X.; Huang, Y.; Zhao, R.; Liu, J.; Han, J.; Huang, Y., Immobilizing an Organic Electrode Material through Π–Π Interaction for High-Performance Li-Organic Batteries. *J. Mater. Chem. A* **2019,** *7* (39), 22398-22404.

65. Huang, Y.; Fang, C.; Zhang, W.; Liu, Q.; Huang, Y., Sustainable Cycling Enabled by a High-Concentration Electrolyte for Lithium-Organic Batteries. *Chem. Commun.* **2019,** *55* (5), 608-611.

66. Ma, J.; Zhou, E.; Fan, C.; Wu, B.; Li, C.; Lu, Z. H.; Li, J. Z., Endowing Cutcnq with a New Role: A High-Capacity Cathode for K-Ion Batteries. *Chem. Commun.* **2018,** *54* (44), 5578-5581.

67. Kanzaki, Y.; Mitani, S.; Shiomi, D.; Morita, Y.; Takui, T.; Sato, K., Microscopic Behavior of Active Materials inside a Tcnq-Based Lithium-Ion Rechargeable Battery by in Situ 2d Esr Measurements. *ACS Appl. Mater. Interfaces* **2018,** *10* (50), 43631-43640.

68. Liu, J. H.; Yang, L. M.; Ganz, E., Electrochemical Reduction of Co2 by Single Atom Catalyst Tm-Tcnq Monolayers. *J. Mater. Chem. A* **2019,** *7* (8), 3805-3814.

69. Mohammadtaheri, M.; Ramanathan, R.; Walia, S.; Ahmed, T.; Weerathunge, P.; Anderson, S. R.; Field, M. R.; Dekiwadia, C. D.; O'Mullane, A. P.; Della Gaspera, E.; Bhaskaran, M.; Sriram, S.; Bansal, V., Broadband Light Active Mtcnq-Based Metal-Organic Semiconducting Hybrids for Enhanced Redox Catalysis. *Applied Materials Today* **2018,** *13*, 107-115.

70. Deng, Q. M.; Wu, T. T.; Chen, G. B.; Hansen, H. A.; Vegge, T., Combinatorial Selection of a Two-Dimensional 3d-Tm-Tetracyanoquinodimethane (Tm-TCNQ) Monolayer as a High-Activity Nanocatalyst for Co Oxidation. *PCCP* **2018,** *20* (7), 5173-5179.

71. Siu, M. C.; Anderson, S. R.; Mohammadtaheri, M.; Ahmed, T.; Walia, S.; Ramanathan, R.; Bansal, V., Role of Water in the Dynamic Crystallization of CuTCNQ for Enhanced Redox Catalysis (TCNQ = Tetracyanoquinodimethane). *Advanced Materials Interfaces* **2017,** *4* (15).

72. Xue, D.; Lv, Q. Y.; Lin, C. N.; Zhan, S. Z., Function of 7,7,8,8-Tetracyanoquinodimethane (Tcnq) on Electrocatalytic Hydrogen Generation Catalyzed by N,N '-Benzene Bis (Salicylideniminato)Nickel(II). *Polyhedron* **2016,** *117*, 300-308.

73. Ungor, O.; Shatruk, M., Transition Metal Complexes with Fractionally Charged Tcnq Radical Anions as Structural Templates for Multifunctional Molecular Conductors. *Polyhedron* **2020,** *177*.

74. Nafady, A.; Sabri, Y. M.; Kandjani, A. E.; Alsalme, A. M.; Bond, A. M.; Bhargava, S., Preferential Synthesis of Highly Conducting Tl(TCNQ) Phase II Nanorod Networks Via Electrochemically Driven TCNQ/Tl(TCNQ) Solid-Solid Phase Transformation. *J. Solid State Electrochem.* **2016,** *20* (12), 3303-3314.

75. Berlie, A.; Terry, I.; Szablewski, M.; Giblin, S. R., Separating the Ferromagnetic and Glassy Behavior within the Metal-Organic Magnet $Ni(TCNQ)_2$. *Physical Review B* **2015,** *92* (18).

76. Shimomura, S.; Yanai, N.; Matsuda, R.; Kitagawa, S., Impact of Metal-Ion Dependence on the Porous and Electronic Properties of TCNQ-Dianion-Based Porous Coordination Polymers. *Inorg. Chem.* **2011,** *50* (1), 172-177.

77. Abrahams, B. F.; Elliott, R. W.; Hudson, T. A.; Robson, R.; Sutton, A. L., X_4TCNQ^{2-} Dianions: Versatile Building Blocks for Supramolecular Systems. *CrystEngComm* **2018,** *20* (23), 3131-3152.

78. Zhang, X.; Saber, M. R.; Prosvirin, A. P.; Reibenspies, J. H.; Sun, L.; Ballesteros-Rivas, M.; Zhao, H. H.; Dunbar, K. R., Magnetic Ordering in Tcnq-Based Metal-Organic Frameworks with Host-Guest Interactions. *Inorganic Chemistry Frontiers* **2015,** *2* (10), 904-911.

79. Saber, M. R.; Prosvirin, A. V.; Abrahams, B. F.; Elliott, R. W.; Robson, R.; Dunbar, K. R., Magnetic Coupling between Metal Spins through the 7,7,8,8-Tetracyanoquinodimethane (TCNQ) Dianion. *Chem. Eur. J.* **2014,** *20* (25), 7593-7597.

80. Kosaka, W.; Morita, T.; Yokoyama, T.; Zhang, J.; Miyasaka, H., Fully Electron-Transferred Donor/Acceptor Layered Frameworks with $TCNQ^{2-}$. *Inorg. Chem.* **2015,** *54* (4), 1518-1527.

81. Shimomura, S.; Matsuda, R.; Tsujino, T.; Kawamura, T.; Kitagawa, S., Tcnq Dianion-Based Coordination Polymer Whose Open Framework Shows Charge-Transfer Type Guest Inclusion. *J. Am. Chem. Soc.* **2006,** *128* (51), 16416-16417.

82. Shimomura, S.; Yanai, N.; Matsuda, R.; Kitagawa, S., Impact of Metal Ion Dependence on the Porous and Electronic Properties of Tcnq-Dianion-Based Porous Coordination Polymers. *Inorg. Chem.* **2011,** *50* (1), 172-177.

83. Zhang, J.; Kosaka, W.; Kitagawa, Y.; Miyasaka, H., Host-Guest Hydrogen Bonding Varies the Charge-State Behavior of Magnetic Sponges. *Angewandte Chemie-International Edition* **2019,** *58* (22), 7351-7356.

84. Taniguchi, K.; Shito, N.; Fukunaga, H.; Miyasaka, H., Charge-Transfer Layered Assembly of a Trans-Heteroleptic Paddlewheel-Type Diruthenium(II, II) Complex with a TCNQ Derivative: Electrochemical Tuning of the Magnetism. *Chem. Lett.* **2018,** *47* (5), 664-667.

85. Sekine, Y.; Shimada, T.; Miyasaka, H., Ionic Donor-Acceptor Chain Derived from an Electron-Transfer Reaction of a Paddlewheel-Type Diruthenium(Ii, Ii) Complex and N,N '-Dicyanoquinonediimine. *Chem. Eur. J.* **2018,** *24* (50), 13093-13097.

86. Sekine, Y.; Aliyah, K. H.; Shimada, T.; Zhang, J.; Kosaka, W.; Miyasaka, H., Hammett-Law Correlation in the Electron-Donation Ability of Trans-Heteroleptic Benzoate-Bridged Paddlewheel-Type Diruthenium(II,II) Complexes. *Chem. Lett.* **2018,** *47* (5), 693-696.

87. Kosaka, W.; Takahashi, Y.; Nishio, M.; Narushima, K.; Fukunaga, H.; Miyasaka, H., Magnetic Sponge with Neutral-Ionic Phase Transitions. *Advanced Science* **2018,** *5* (2), 1700526.

88. Kosaka, W.; Liu, Z. Y.; Zhang, J.; Sato, Y.; Hori, A.; Matsuda, R.; Kitagawa, S.; Miyasaka, H., Gas-Responsive Porous Magnet Distinguishes the Electron Spin of Molecular Oxygen. *Nat. Commun.* **2018,** *9*, 5420.

89. Kosaka, W.; Itoh, M.; Miyasaka, H., Metamagnetism with T_N=97 K in a Layered Assembly of Paddlewheel Ru-2 Units and Tcnq: An Empirical Rule for Interlayer Distances Determining the Magnetic Ground State. *Mater. Chem. Front.* **2018,** *2* (3), 497-504.

90. Taniguchi, K.; Narushima, K.; Sagayama, H.; Kosaka, W.; Shito, N.; Miyasaka, H., In Situ Reversible Ionic Control for Nonvolatile Magnetic Phases in a Donor/Acceptor Metal-Organic Framework. *Adv. Funct. Mater.* **2017,** *27* (5), 1604990.

91. Taniguchi, K.; Narushima, K.; Mahin, J.; Kosaka, W.; Miyasaka, H., Construction of an Artificial Ferrimagnetic Lattice by Lithium Ion Insertion into a Neutral Donor/Acceptor Metal-Organic Framework. *Angew. Chem. Int. Ed.* **2016,** *55* (17), 5238-5242.

92. Miyasaka, H., Functional Mofs toward the Synergistic Control of Electrons, Spins, Structures, and Chemical Interactions. *Abstr. Pap. Am. Chem. Soc.* **2015,** *249*.

93. Kosaka, W.; Morita, T.; Yokoyama, T.; Zhang, J.; Miyasaka, H., Fully Electron-Transferred Donor/Acceptor Layered Frameworks with $TCNQ^{2-}$. *Inorg. Chem.* **2015,** *54* (4), 1518-1527.

94. Kosaka, W.; Fukunaga, H.; Miyasaka, H., Electron-Transferred Donor/Acceptor Ferrimag Net with T_C=91 K in a Layered Assembly of Paddlewheel Ru-2 Units and TCNQ. *Inorg. Chem.* **2015,** *54* (20), 10001-10006.

95. Fukunaga, H.; Miyasaka, H., Magnet Design by Integration of Layer and Chain Magnetic Systems in a Pi-Stacked Pillared Layer Framework. *Angew. Chem. Int. Ed.* **2015,** *54* (2), 569-573.

96. Miyasaka, H., Control of Charge Transfer in Donor/Acceptor Metal-Organic Frameworks. *Acc. Chem. Res.* **2013,** *46* (2), 248-257.

97. Motokawa, N.; Matsunaga, S.; Takaishi, S.; Miyasaka, H.; Yamashita, M.; Dunbar, K. R., Reversible Magnetism between an Antiferromagnet and a Ferromagnet Related to Solvation/Desolvation in a Robust Layered [Ru-2](2)TCNQ Charge-Transfer System. *J. Am. Chem. Soc.* **2010,** *132* (34), 11943-11951.

98. Heintz, R. A.; Zhao, H. H.; Xiang, O. Y.; Grandinetti, G.; Cowen, J.; Dunbar, K. R., New Insight into the Nature of Cu(TCNQ): Solution Routes to Two Distinct Polymorphs and Their Relationship to Crystalline Films That Display Bistable Switching Behavior. *Inorg. Chem.* **1999,** *38* (1), 144-156.

99. Avendano, C.; Zhang, Z. Y.; Ota, A.; Zhao, H. H.; Dunbar, K. R., Dramatically Different Conductivity Properties of Metal-Organic Framework Polymorphs of Tl(Tcnq): An Unexpected Room-Temperature Crystal-to-Crystal Phase Transition. *Angewandte Chemie-International Edition* **2011,** *50* (29), 6543-6547.

100. Clerac, R.; O'Kane, S.; Cowen, J.; Ouyang, X.; Heintz, R.; Zhao, H. H.; Bazile, M. J.; Dunbar, K. R., Glassy Magnets Composed of Metals Coordinated to 7,7,8,8-Tetracyanoquinodimethane: M(TCNQ)(2) (M = Mn, Fe, Co, Ni). *Chem. Mater.* **2003,** *15* (9), 1840-1850.

101. Ballesteros-Rivas, M.; Ota, A.; Reinheimer, E.; Prosvirin, A.; Valdes-Martinez, J.; Dunbar, K. R., Highly Conducting Coordination Polymers Based on Infinite M(4,4'-Bpy) Chains Flanked by Regular Stacks of Non-Integer TCNQ Radicals. *Angew. Chem. Int. Ed. Engl.* **2011,** *50* (41), 9703-7.

102. Wang, Z. X.; Zhang, X.; Zhang, Y. Z.; Li, M. X.; Zhao, H.; Andruh, M.; Dunbar, K. R., Single-Chain Magnetic Behavior in a Hetero-Tri-Spin Complex Mediated by Supramolecular Interactions with $TCNQF^-$ Radicals. *Angew. Chem. Int. Ed. Engl.* **2014,** *53* (43), 11567-70.

103. Bagai, R.; Christou, G., The Drosophila of Single-Molecule Magnetism: $[Mn_{12}O_{12}(O2CR)_{16}(H2O)_4]$. *Chem. Soc. Rev.* **2009,** *38* (4), 1011-1026.

104. Gatteschi, D.; Sessoli, R.; Villain, J., Molecular Nanomagnets. *Molecular Nanomagnets* **2006**, 1-395.

105. Zhang, X.; Xie, H.; Ballesteros-Rivas, M.; Woods, T. J.; Dunbar, K. R., Conducting Molecular Nanomagnet of Dy^{III} with Partially Charged TCNQ Radicals. *Chem. Eur. J.* **2017,** *23*, 7448.

106. Zhang, X.; Wang, Z.-X.; Xie, H.; Li, M.-X.; Woods, T. J.; Dunbar, K. R., A Cobalt(Ii) Spin-Crossover Compound with Partially Charged TCNQ Radicals and an Anomalous Conducting Behavior. *Chem. Sci.* **2016,** *7* (2), 1569-1574.

107. Phan, H.; Benjamin, S. M.; Steven, E.; Brooks, J. S.; Shatruk, M., Photomagnetic Response in Highly Conductive Iron(Ii) Spin-Crossover Complexes with TCNQ Radicals. *Angew. Chem. Int. Ed.* **2015,** *54* (3), 823-827.

108. Zhang, X.; Wang, Z. X.; Xie, H. M.; Li, M. X.; Woods, T. J.; Dunbar, K. R., A Cobalt(Ii) Spin-Crossover Compound with Partially Charged Tcnq Radicals and an Anomalous Conducting Behavior. *Chem. Sci.* **2016,** *7* (2), 1569-1574.

109. Shvachko, Y. N.; Starichenko, D. V.; Korolyov, A. V.; Yagubskii, E. B.; Kotov, A. I.; Buravov, L. I.; Lyssenko, K. A.; Zverev, V. N.; Simonov, S. V.; Zorina, L. V.; Shakirova, O. G.; Lavrenova, L. G., The Conducting Spin-Crossover Compound

Combining Fe(II) Cation Complex with Tcnq in a Fractional Reduction State. *Inorganic Chemistry* **2016,** *55* (17), 9121-9130.

110. Zhang, J. Y.; Su, L. J.; Guo, Q. J.; Tao, J., Semiconducting Spin-Crossover Cobalt (II) Compound with Non-Integer Charge Distribution among Tcnq Radicals. *Inorg. Chem. Commun.* **2017,** *82*, 39-43.

111. Shvachko, Y. N.; Starichenko, D. V.; Korolyov, A. V.; Kotov, A. I.; Buravov, L. I.; Zverev, V. N.; Simonov, S. V.; Zorina, L. V.; Yagubskii, E. B., The Highly Conducting Spin-Crossover Compound Combining Fe(III) Cation Complex with Tcnq in a Fractional Reduction State. Synthesis, Structure, Electric and Magnetic Properties. *Magnetochemistry* **2017,** *3* (1), 9.

112. Kazakova, A. V.; Tiunova, A. V.; Korchagin, D. V.; Shilov, G. V.; Yagubskii, E. B.; Zverev, V. N.; Yang, S. C.; Lin, J. Y.; Lee, J. F.; Maximova, O. V.; Vasiliev, A. N., The First Conducting Spin-Crossover Compound Combining a Mn-Iii Cation Complex with Electroactive Tcnq Demonstrating an Abrupt Spin Transition with a Hysteresis of 50 K. *Chem. Eur. J.* **2019,** *25* (43), 10204-10213.

113. Ishikawa, R.; Ueno, S.; Nifuku, S.; Horii, Y.; Iguchi, H.; Miyazaki, Y.; Nakano, M.; Hayami, S.; Kumagai, S.; Katoh, K.; Li, Z.-Y.; Yamashita, M.; Kawata, S., Simultaneous Spin-Crossover Transition and Conductivity Switching in a Dinuclear Iron(Ii) Coordination Compound Based on 7,7′,8,8′-Tetracyano-P-Quinodimethane. *Chem. Eur. J.* **2020,** *26* (6), 1278-1285.

114. Lehn, J. M., Supramolecular Chemistry. *Science* **1993,** *260* (5115), 1762-1763.

115. Amabilino, D. B.; Smith, D. K.; Steed, J. W., Supramolecular Materials. *Chem. Soc. Rev.* **2017,** *46* (9), 2404-2420.

116. Kuhlman, B.; Bradley, P., Advances in Protein Structure Prediction and Design. *Nat. Rev. Mol. Cell Biol.* **2019,** *20* (11), 681-697.

117. Belmont, P.; Constant, J.-F.; Demeunynck, M., Nucleic Acid Conformation Diversity: From Structure to Function and Regulation. *Chem. Soc. Rev.* **2001,** *30* (1), 70-81.

118. Erbas-Cakmak, S.; Leigh, D. A.; McTernan, C. T.; Nussbaumer, A. L., Artificial Molecular Machines. *Chem. Rev.* **2015,** *115* (18), 10081-10206.

119. Hosseini, M. W., Reflexion on Molecular Tectonics. *CrystEngComm* **2004,** *6*, 318-322.

120. Kahn, O.; Martinez, C. J., Spin-Transition Polymers: From Molecular Materials toward Memory Devices. *Science* **1998,** *279* (5347), 44-48.

121. Kumar, K. S.; Ruben, M., Emerging Trends in Spin Crossover (Sco) Based Functional Materials and Devices. *Coord. Chem. Rev.* **2017,** *346*, 176-205.

122. Molnar, G.; Rat, S.; Salmon, L.; Nicolazzi, W.; Bousseksou, A., Spin Crossover Nanomaterials: From Fundamental Concepts to Devices. *Adv. Mater.* **2018,** *30* (5).

123. Moreno-Pineda, E.; Godfrin, C.; Balestro, F.; Wernsdorfer, W.; Ruben, M., Molecular Spin Qudits for Quantum Algorithms. *Chem. Soc. Rev.* **2018,** *47* (2), 501-513.

124. Bogani, L.; Wernsdorfer, W., Molecular Spintronics Using Single-Molecule Magnets. *Nat. Mater.* **2008,** *7* (3), 179-86.

125. Thiele, S.; Balestro, F.; Ballou, R.; Klyatskaya, S.; Ruben, M.; Wernsdorfer, W., Electrically Driven Nuclear Spin Resonance in Single-Molecule Magnets. *Science* **2014,** *344* (6188), 1135-8.

126. Gaita-Arino, A.; Luis, F.; Hill, S.; Coronado, E., Molecular Spins for Quantum Computation. *Nat. Chem.* **2019,** *11* (4), 301-309.

127. Tao, J.; Wei, R. J.; Huang, R. B.; Zheng, L. S., Polymorphism in Spin-Crossover Systems. *Chem. Soc. Rev.* **2012,** *41* (2), 703-37.

128. Takahashi, K.; Sakurai, T.; Zhang, W. M.; Okubo, S.; Ohta, H.; Yamamoto, T.; Einaga, Y.; Mori, H., Spin-Singlet Transition in the Magnetic Hybrid Compound from a Spin-Crossover Fe(Iii) Cation and Pi-Radical Anion. *Inorganics* **2017,** *5* (3), 54.

129. Tsukiashi, A.; Nakaya, M.; Kobayashi, F.; Ohtani, R.; Nakamura, M.; Harrowfield, J. M.; Kim, Y.; Hayami, S., Intermolecular Interaction Tuning of Spin-Crossover Iron(Iii) Complexes with Aromatic Counteranions. *Inorg. Chem.* **2018,** *57* (5), 2834-2842.

130. Wernsdorfer, W.; Aliaga-Alcalde, N.; Hendrickson, D. N.; Christou, G., Exchange-Biased Quantum Tunnelling in a Supramolecular Dimer of Single-Molecule Magnets. *Nature* **2002,** *416* (6879), 406-9.

131. Nguyen, T. N.; Wernsdorfer, W.; Abboud, K. A.; Christou, G., A Supramolecular Aggregate of Four Exchange-Biased Single-Molecule Magnets. *J. Am. Chem. Soc.* **2011,** *133* (51), 20688-91.

132. Mowson, A. M.; Nguyen, T. N.; Abboud, K. A.; Christou, G., Dimeric and Tetrameric Supramolecular Aggregates of Single-Molecule Magnets Via Carboxylate Substitution. *Inorg. Chem.* **2013,** *52* (21), 12320-2.

133. Nguyen, T. N.; Wernsdorfer, W.; Shiddiq, M.; Abboud, K. A.; Hill, S.; Christou, G., Supramolecular Aggregates of Single-Molecule Magnets: Exchange-Biased

Quantum Tunneling of Magnetization in a Rectangular [Mn3]4 Tetramer. *Chem. Sci.* **2016,** *7* (2), 1156-1173.

134. Alexandropoulos, D. I.; Dolinar, B. S.; Vignesh, K. R.; Dunbar, K. R., Putting a New Spin on Supramolecular Metallacycles: Co3 Triangle and Co4 Square Bearing Tetrazine-Based Radicals as Bridges. *J. Am. Chem. Soc.* **2017,** *139* (32), 11040-11043.

135. Dolinar, B. S.; Alexandropoulos, D. I.; Vignesh, K. R.; James, T.; Dunbar, K. R., Lanthanide Triangles Supported by Radical Bridging Ligands. *J. Am. Chem. Soc.* **2018,** *140* (3), 908-911.

136. Zhang, X.; Wang, Z. X.; Xie, H.; Li, M. X.; Woods, T. J.; Dunbar, K. R., A Cobalt(Ii) Spin-Crossover Compound with Partially Charged Tcnq Radicals and an Anomalous Conducting Behavior. *Chem. Sci.* **2016,** *7* (2), 1569-1574.

137. Scott, H. S.; Gartshore, C. J.; Guo, S. X.; Moubaraki, B.; Bond, A. M.; Batten, S. R.; Murray, K. S., Ferrocene-Appended Ligands for Use in Spin Crossover-Redox "Hybrid" Complexes of Iron(Ii) and Cobalt(Ii). *Dalton Trans.* **2014,** *43* (40), 15212-20.

138. Takami, K.; Ohtani, R.; Nakamura, M.; Kurogi, T.; Sugimoto, M.; Lindoy, L. F.; Hayami, S., Redox Induced Colour Changes between Red-Violet and Blue in Hetero-Metal Complexes of the Type [Co-II(4 '-Ferrocenyl-2,2 ';6 ' 2 "-Terpyridine)(2)]X-2 (X = Counter Anion). *Dalton Trans.* **2015,** *44* (42), 18354-18359.

139. Hayami, S.; Komatsu, Y.; Shimizu, T.; Kamihata, H.; Lee, Y. N., Spin-Crossover in Cobalt(Ii) Compounds Containing Terpyridine and Its Derivatives. *Coord. Chem. Rev.* **2011,** *255* (17-18), 1981-1990.

140. Mossin, S.; Tran, B. L.; Adhikari, D.; Pink, M.; Heinemann, F. W.; Sutter, J.; Szilagyi, R. K.; Meyer, K.; Mindiola, D. J., A Mononuclear Fe(III) Single Molecule Magnet with a 3/2<-->5/2 Spin Crossover. *J. Am. Chem. Soc.* **2012,** *134* (33), 13651-61.

141. Ababei, R.; Pichon, C.; Roubeau, O.; Li, Y. G.; Brefuel, N.; Buisson, L.; Guionneau, P.; Mathoniere, C.; Clerac, R., Rational Design of a Photomagnetic Chain: Bridging Single-Molecule Magnets with a Spin-Crossover Complex. *J. Am. Chem. Soc.* **2013,** *135* (39), 14840-53.

142. Feng, X.; Mathoniere, C.; Jeon Ie, R.; Rouzieres, M.; Ozarowski, A.; Aubrey, M. L.; Gonzalez, M. I.; Clerac, R.; Long, J. R., Tristability in a Light-Actuated Single-Molecule Magnet. *J. Am. Chem. Soc.* **2013,** *135* (42), 15880-4.

143. Gass, I. A.; Tewary, S.; Nafady, A.; Chilton, N. F.; Gartshore, C. J.; Asadi, M.; Lupton, D. W.; Moubaraki, B.; Bond, A. M.; Boas, J. F.; Guo, S. X.; Rajaraman, G.; Murray, K. S., Observation of Ferromagnetic Exchange, Spin Crossover, Reductively

Induced Oxidation, and Field-Induced Slow Magnetic Relaxation in Monomeric Cobalt Nitroxides. *Inorg. Chem.* **2013,** *52* (13), 7557-72.

144. Cui, H. H.; Wang, J.; Chen, X. T.; Xue, Z. L., Slow Magnetic Relaxation in Five-Coordinate Spin-Crossover Cobalt(II) Complexes. *Chem. Commun. (Camb.)* **2017,** *53* (67), 9304-9307.

145. Shao, D.; Deng, L. D.; Shi, L.; Wu, D. Q.; Wei, X. Q.; Yang, S. R.; Wang, X. Y., Slow Magnetic Relaxation and Spin-Crossover Behavior in a Bicomponent Ion-Pair Cobalt(Ii) Complex. *Eur. J. Inorg. Chem.* **2017,** *2017* (33), 3862-3867.

146. Chen, L.; Song, J.; Zhao, W.; Yi, G.; Zhou, Z.; Yuan, A.; Song, Y.; Wang, Z.; Ouyang, Z. W., A Mononuclear Five-Coordinate Co(II) Single Molecule Magnet with a Spin Crossover between the S = 1/2 and 3/2 States. *Dalton Trans.* **2018,** *47* (46), 16596-16602.

147. Shao, D.; Shi, L.; Yin, L.; Wang, B. L.; Wang, Z. X.; Zhang, Y. Q.; Wang, X. Y., Reversible on-Off Switching of Both Spin Crossover and Single-Molecule Magnet Behaviours Via a Crystal-to-Crystal Transformation. *Chem. Sci.* **2018,** *9* (41), 7986-7991.

148. Shah, P.; Westwell, A. D., The Role of Fluorine in Medicinal Chemistry. *J. Enzyme Inhib. Med. Chem.* **2007,** *22* (5), 527-40.

149. Gillis, E. P.; Eastman, K. J.; Hill, M. D.; Donnelly, D. J.; Meanwell, N. A., Applications of Fluorine in Medicinal Chemistry. *J. Med. Chem.* **2015,** *58* (21), 8315-59.

150. Meanwell, N. A., Fluorine and Fluorinated Motifs in the Design and Application of Bioisosteres for Drug Design. *J. Med. Chem.* **2018,** *61* (14), 5822-5880.

151. Melby, L. R.; Mahler, W.; Mochel, W. E.; Harder, R. J.; Hertler, W. R.; Benson, R. E., Substituted Quinodimethans .2. Anion-Radical Derivatives and Complexes of 7,7,8,8-Tetracyanoquinodimethan. *J. Am. Chem. Soc.* **1962,** *84* (17), 3374-&.

152. Hasegawa, T.; Inukai, K.; Kagoshima, S.; Sugawara, T.; Mochida, T.; Sugiura, S.; Iwasa, Y., Synthesis, Structure, and Electronic Properties of (BEDT-TTF)(F_NTCNQ) (N=0,1,2,4). *Synth. Met.* **1997,** *86* (1-3), 1801-1802.

153. O'Kane, S. A.; Clerac, R.; Zhao, H. H.; Xiang, O. Y.; Galan-Mascaros, J. R.; Heintz, R.; Dunbar, K. R., New Crystalline Polymers of Ag(TCNQ) and Ag($TCNQF_4$): Structures and Magnetic Properties. *J. Solid State Chem.* **2000,** *152* (1), 159-173.

154. Constable, E. C.; Edwards, A. J.; Martinezmanez, R.; Raithby, P. R.; Thompson, A. M. W. C., Complexes Containing Ferrocenyl Groups as Redox Spectators -

Synthesis, Molecular-Structure and Coordination Behavior of 4'-Ferrocenyl-2,2'/6',2"-Terpyridine. *Dalton Trans.* **1994,** *0* (5), 645-650.

155. Winter, A.; van den Berg, A. M. J.; Hoogenboom, R.; Kickelbick, G.; Schubert, U. S., A Green and Straightforward Synthesis of 4 '-Substituted Terpyridines. *Synthesis-Stuttgart* **2006,** (17), 2873-2878.

156. Sheldrick, G. M., Shelxt - Integrated Space-Group and Crystal-Structure Determination. *Acta Crystallogr. A Found Adv.* **2015,** *71* (Pt 1), 3-8.

157. Sheldrick, G. M., Crystal Structure Refinement with Shelxl. *Acta Crystallogr C Struct. Chem.* **2015,** *71* (Pt 1), 3-8.

158. Dolomanov, O. V.; Bourhis, L. J.; Gildea, R. J.; Howard, J. A. K.; Puschmann, H., Olex2: A Complete Structure Solution, Refinement and Analysis Program. *J. Appl. Crystallogr.* **2009,** *42*, 339-341.

159. Neese, F., The Orca Program System. *Wiley Interdiscip. Rev. Comput.* **2012,** *2* (1), 73-78.

160. Weigend, F.; Ahlrichs, R., Balanced Basis Sets of Split Valence, Triple Zeta Valence and Quadruple Zeta Valence Quality for H to Rn: Design and Assessment of Accuracy. *Phys. Chem. Chem. Phys.* **2005,** *7* (18), 3297-305.

161. Tao, J. M.; Perdew, J. P.; Staroverov, V. N.; Scuseria, G. E., Climbing the Density Functional Ladder: Nonempirical Meta-Generalized Gradient Approximation Designed for Molecules and Solids. *Phys. Rev. Lett.* **2003,** *91* (14).

162. Staroverov, V. N.; Scuseria, G. E.; Tao, J. M.; Perdew, J. P., Comparative Assessment of a New Nonempirical Density Functional: Molecules and Hydrogen-Bonded Complexes. *J. Chem. Phys.* **2003,** *119* (23), 12129-12137.

163. Schafer, A.; Horn, H.; Ahlrichs, R., Fully Optimized Contracted Gaussian-Basis Sets for Atoms Li to Kr. *J. Chem. Phys.* **1992,** *97* (4), 2571-2577.

164. Schafer, A.; Huber, C.; Ahlrichs, R., Fully Optimized Contracted Gaussian-Basis Sets of Triple Zeta Valence Quality for Atoms Li to Kr. *J. Chem. Phys.* **1994,** *100* (8), 5829-5835.

165. Frisch, M. J.; Trucks, G. W.; Schlegel, H. B.; Scuseria, G. E.; Robb, M. A.; Cheeseman, J. R.; Scalmani, G.; Barone, V.; Mennucci, B.; Petersson, G. A.; Nakatsuji, H.; Caricato, M.; Li, X.; Hratchian, H. P.; Izmaylov, A. F.; Bloino, J.; Zheng, G.; Sonnenberg, J. L.; Hada, M.; Ehara, M.; Toyota, K.; Fukuda, R.; Hasegawa, J.; Ishida, M.; Nakajima, T.; Honda, Y.; Kitao, O.; Nakai, H.; Vreven, T.; Montgomery Jr, J. A.; Peralta, J. E.; Ogliaro, F.; Bearpark, M. J.; Heyd, J.; Brothers, E. N.; Kudin, K. N.;

Staroverov, V. N.; Kobayashi, R.; Normand, J.; Raghavachari, K.; Rendell, A. P.; Burant, J. C.; Iyengar, S. S.; Tomasi, J.; Cossi, M.; Rega, N.; Millam, N. J.; Klene, M.; Knox, J. E.; Cross, J. B.; Bakken, V.; Adamo, C.; Jaramillo, J.; Gomperts, R.; Stratmann, R. E.; Yazyev, O.; Austin, A. J.; Cammi, R.; Pomelli, C.; Ochterski, J. W.; Martin, R. L.; Morokuma, K.; Zakrzewski, V. G.; Voth, G. A.; Salvador, P.; Dannenberg, J. J.; Dapprich, S.; Daniels, A. D.; Farkas, O.; Foresman, J. B.; Ortiz, J. V.; Cioslowski, J.; Fox, D. J. *Gaussian 09 Rev. D.01*, Wallingford, CT, 2013.

166. Chai, J. D.; Head-Gordon, M., Long-Range Corrected Hybrid Density Functionals with Damped Atom-Atom Dispersion Corrections. *Phys. Chem. Chem. Phys.* **2008,** *10* (44), 6615-20.

167. Zhang, X.; Xie, H.; Ballesteros-Rivas, M.; Wang, Z.-X.; Dunbar, K. R., Structural Distortions of the Spin-Crossover Material $[Co(Pyterpy)_2](TCNQ)_2$ Mediated by Supramolecular Interactions. *J. Mater. Chem. C* **2015,** *3* (36), 9292-9298.

168. Llunell, M.; Casanova, D.; Cirera, J.; Alemany, P.; Alvarez, S., Shape, Version 2.1. *Universitat de Barcelona, Barcelona, Spain* **2013,** *2103*.

169. Garcia-Yoldi, I.; Miller, J. S.; Novoa, J. J., Theoretical Study of the Electronic Structure of $[TCNQ]_2^{2-}$ (TCNQ =7,7,8,8-Tetracyano-P-Quinodimethane) Dimers and Their Intradimer, Long, Multicenter Bond in Solution and the Solid State. *J. Phys. Chem. A* **2009,** *113* (25), 7124-7132.

170. Starodub, T. N.; Cizmar, E.; Kliuikov, A.; Starodub, V. A.; Feher, A.; Kozlowska, M., Stabilization of Pancake Bonding in $(TCNQ)_2^{\cdot-}$ Dimers in the Radical-Anionic Salt $(N\text{-}CH_3\text{-}2\text{-}NH_2\text{-}5Cl\text{-}Py)(TCNQ)(CH_3CN)$ Solvate and Antiferromagnetism Induction. *ChemistryOpen* **2019,** *8* (7), 984-988.

171. Shrivastava, K. N., Theory of Spin-Lattice Relaxation. *Physica Status Solidi B-Basic Research* **1983,** *117* (2), 437-458.

172. Klug, C. M.; McDaniel, A. M.; Fiedler, S. R.; Schulte, K. A.; Newell, B. S.; Shores, M. P., Anion Dependence in the Spin-Crossover Properties of a Fe(II) Podand Complex. *Dalton Trans.* **2012,** *41* (40), 12577-85.

173. Park, J. G.; Jeon, I. R.; Harris, T. D., Electronic Effects of Ligand Substitution on Spin Crossover in a Series of Diiminoquinonoid-Bridged Fe_2(II) Complexes. *Inorg. Chem.* **2015,** *54* (1), 359-369.

174. Hogue, R. W.; Singh, S.; Brooker, S., Spin Crossover in Discrete Polynuclear Iron(II) Complexes. *Chem. Soc. Rev.* **2018,** *47* (19), 7303-7338.

175. Gaspar, A. B.; Munoz, M. C.; Niel, V.; Real, J. A., [Co-II(4-Terpyridone)$_2$]X_2: A Novel Cobalt(II) Spin Crossover System [4-Terpyridone=2,6-Bis(2-Pyridyl)-4(1H)-Pyridone]. *Inorg. Chem.* **2001,** *40* (1), 9.

176. Gomez-Coca, S.; Cremades, E.; Aliaga-Alcalde, N.; Ruiz, E., Mononuclear Single-Molecule Magnets: Tailoring the Magnetic Anisotropy of First-Row Transition-Metal Complexes. *J. Am. Chem. Soc.* **2013,** *135* (18), 7010-8.

177. Schulte, K. A.; Vignesh, K. R.; Dunbar, K. R., Effects of Coordination Sphere on Unusually Large Zero Field Splitting and Slow Magnetic Relaxation in Trigonally Symmetric Molecules. *Chem. Sci.* **2018,** *9* (48), 9018-9026.

178. Cirera, J.; Ruiz, E., Computational Modeling of Transition Temperatures in Spin-Crossover Systems. *Comments Inorg. Chem.* **2019,** *39* (4), 216-241.

179. Ye, S. F.; Neese, F., Accurate Modeling of Spin-State Energetics in Spin-Crossover Systems with Modern Density Functional Theory. *Inorg. Chem.* **2010,** *49* (3), 772-774.

180. Schmidt, M.; Wiedemann, D.; Moubaraki, B.; Chilton, N. F.; Murray, K. S.; Vignesh, K. R.; Rajaraman, G.; Grohmann, A., Iron(II) Complexes of Two Amine/Imine N-5 Chelate Ligands Containing a 1,4-Diazepane Core - to Crossover or Not to Crossover. *Eur. J. Inorg. Chem.* **2013,** (5-6), 958-967.

181. Kobayashi, F.; Ohtani, R.; Nakamura, M.; Lindoy, L. F.; Hayami, S., Slow Magnetic Relaxation Triggered by a Structural Phase Transition in Long-Chain-Alkylated Cobalt(II) Single-Ion Magnets. *Inorg. Chem.* **2019,** *58* (11), 7409-7415.

182. Higgins, R. F.; Livesay, B. N.; Ozumerzifon, T. J.; Joyce, J. P.; Rappe, A. K.; Shores, M. P., A Family of Related Co(II) Terpyridine Compounds Exhibiting Field Induced Single-Molecule Magnet Properties. *Polyhedron* **2018,** *143*, 193-200.

183. Janiak, C., A Critical Account on Pi-Pi Stacking in Metal Complexes with Aromatic Nitrogen-Containing Ligands. *Dalton Trans.* **2000,** (21), 3885-3896.

184. Anzellotti, A. I.; Bayse, C. A.; Farrell, N. P., Effects of Nucleobase Metalation on Frontier Molecular Orbitals: Potential Implications for Pi-Stacking Interactions with Tryptophan. *Inorg. Chem.* **2008,** *47* (22), 10425-31.

185. Wang, H. J.; Xu, H. Y.; Jia, W. H.; Liu, J.; Ren, S. L., Revealing the Intermolecular Interactions of Asphaltene Dimers by Quantum Chemical Calculations. *Energy Fuels* **2017,** *31* (3), 2488-2495.

186. Rodriguez-Jimenez, S.; Barltrop, A. S.; White, N. G.; Feltham, H. L. C.; Brooker, S., Solvent Polarity Predictably Tunes Spin Crossover $T_{1/2}$ in Isomeric Iron(Ii) Pyrimidine Triazoles. *Inorg. Chem.* **2018,** *57* (11), 6266-6282.

187. Gaspar, A. B.; Munoz, M. C.; Niel, V.; Real, J. A., [Co-II(4-Terpyridone)(2)]X-2: A Novel Cobalt(II) Spin Crossover System [4-Terpyridone=2,6-Bis(2-Pyridyl)-4(1H)-Pyridone]. *Inorg. Chem.* **2001,** *40* (1), 9-10.

188. Bousseksou, A.; McGarvey, J. J.; Varret, F.; Real, J. A.; Tuchagues, J. P.; Dennis, A. C.; Boillot, M. L., Raman Spectroscopy of the High- and Low-Spin States of the Spin Crossover Complex $Fe(Phen)_2(NCS)_2$: An Initial Approach to Estimation of Vibrational Contributions to the Associated Entropy Change. *Chem. Phys. Lett.* **2000,** *318* (4-5), 409-416.

189. Brehm, G.; Reiher, M.; Schneider, S., Estimation of the Vibrational Contribution to the Entropy Change Associated with the Low- to High-Spin Transition in $Fe(Phen)_2(NCS)_2$ Complexes: Results Obtained by Ir and Raman Spectroscopy and Dft Calculations. *J. Phys. Chem. A* **2002,** *106* (50), 12024-12034.

190. Molnar, G.; Niel, V.; Gaspar, A. B.; Real, J. A.; Zwick, A.; Bousseksou, A.; McGarvey, J. J., Vibrational Spectroscopy of Cyanide-Bridged, Iron(II) Spin-Crossover Coordination Polymers: Estimation of Vibrational Contributions to the Entropy Change Associated with the Spin Transition. *J. Phys. Chem. B* **2002,** *106* (38), 9701-9707.

191. Garcia, Y.; Paulsen, H.; Schunemann, V.; Trautwein, A. X.; Wolny, J. A., Estimate of the Vibrational Contribution to the Entropy Change Associated with the Spin Transition in the D4 Systems $[Mn^{III}(Pyrol)_3Tren]$ and $[Cr^{II}(DEPE)])_2I_2]$. *Phys. Chem. Chem. Phys.* **2007,** *9* (10), 1194-201.

192. Klokishner, S. I.; Roman, M. A.; Reu, O. S., A Model of Spin Crossover in Manganese(III) Compounds: Effects of Intra- and Intercenter Interactions. *Inorg. Chem.* **2011,** *50* (22), 11394-402.

193. Bowman, D. N.; Jakubikova, E., Low-Spin Versus High-Spin Ground State in Pseudo-Octahedral Iron Complexes. *Inorg. Chem.* **2012,** *51* (11), 6011-9.

194. Mebs, S.; Braun, B.; Kositzki, R.; Limberg, C.; Haumann, M., Abrupt Versus Gradual Spin-Crossover in $Fe\text{-}Ll(Phen)_2(NCS)_2$ and $Fe(III)(DEDTC)_3$ Compared by X-Ray Absorption and Emission Spectroscopy and Quantum-Chemical Calculations. *Inorg. Chem.* **2015,** *54* (24), 11606-11624.

195. Coronado, E.; Day, P., Magnetic Molecular Conductors. *Chem. Rev.* **2004,** *104* (11), 5419-48.

196. Coronado, E.; Day, P., Magnetic Molecular Conductors. *Chem Rev* **2004,** *104* (11), 5419-5448.

197. Enoki, T.; Miyazaki, A., Magnetic Ttf-Based Charge-Transfer Complexes. *Chem. Rev.* **2004,** *104* (11), 5449-5477.

198. Coronado, E.; Galan-Mascaros, J. R., Hybrid Molecular Conductors. *J. Mater. Chem.* **2005,** *15* (1), 66-74.

199. Miyasaka, H., Control of Charge Transfer in Donor/Acceptor Metal–Organic Frameworks. *Acc. Chem. Res.* **2013,** *46* (2), 248-257.

200. Geng, H.; Zheng, X.; Shuai, Z.; Zhu, L.; Yi, Y., Understanding the Charge Transport and Polarities in Organic Donor–Acceptor Mixed-Stack Crystals: Molecular Insights from the Super-Exchange Couplings. *Adv. Mater.* **2015,** *27* (8), 1443-1449.

201. Zhu, L.; Yi, Y.; Fonari, A.; Corbin, N. S.; Coropceanu, V.; Brédas, J.-L., Electronic Properties of Mixed-Stack Organic Charge-Transfer Crystals. *J. Phys. Chem. C* **2014,** *118* (26), 14150-14156.

202. Barthelmes, K.; Winter, A.; Schubert, U. S., Dyads and Triads Based on Phenothiazine, Bis(Terpyridine)Ruthenium(II) Complexes, and Fullerene. *Eur. J. Inorg. Chem.* **2016,** (32), 5132-5142.

203. Kertesz, M., Pancake Bonding: An Unusual Pi-Stacking Interaction. *Chem. Eur. J.* **2019,** *25* (2), 400-416.

204. Casado, J.; Burrezo, P. M.; Ramírez, F. J.; Navarrete, J. T. L.; Lapidus, S. H.; Stephens, P. W.; Vo, H.-L.; Miller, J. S.; Mota, F.; Novoa, J. J., Evidence for Multicenter Bonding in Dianionic Tetracyanoethylene Dimers by Raman Spectroscopy. *Angew. Chem. Int. Ed.* **2013,** *52* (25), 6421-6425.

205. Starodub, T. N.; Čižmár, E.; Kliuikov, A.; Starodub, V. A.; Feher, A.; Kozlowska, M., Stabilization of Pancake Bonding in $(TCNQ)_2^{\cdot -}$ Dimers in the Radical-Anionic Salt $(N{-}CH_3{-}2\text{-}NH_2{-}5Cl{-}Py)(TCNQ)(CH_3CN)$ Solvate and Antiferromagnetism Induction. *ChemistryOpen* **2019,** *8* (7), 984-988.

206. Kennedy, F. S.; Hill, H. A. O.; Kaden, T. A.; Vallee, B. L., Electron Paramagnetic Resonance Spectra of Some Active Cobalt(II) Substituted Metalloenzymes and Other Cobalt(II) Complexes. *Biochem. Biophys. Res. Commun.* **1972,** *48* (6), 1533-1539.

207. Bell-Taylor, A.; Gorden, J. D.; Hardy, E. E.; Goldsmith, C. R., A Spin-Crossover Co(II) Complex Catalyzes the Activation of Sp3 C–H Bonds by Two-Electron Oxidants. *Inorg. Chim. Acta* **2018,** *482*, 206-212.

208. Stoll, S.; Schweiger, A., Easyspin, a Comprehensive Software Package for Spectral Simulation and Analysis in Epr. *J. Magn. Reson.* **2006,** *178* (1), 42-55.

209. Nielsen, P.; Toftlund, H.; Bond, A. D.; Boas, J. F.; Pilbrow, J. R.; Hanson, G. R.; Noble, C.; Riley, M. J.; Neville, S. M.; Moubaraki, B.; Murray, K. S., Systematic Study of Spin Crossover and Structure in $[Co(Terpyrx)_2](Y)_2$ Systems (Terpyrx = 4′ -Alkoxy-2,2′ :6′ ,2′ ′ -Terpyridine, X = 4, 8, 12, Y = Bf4−, Clo4−, Pf6−, Bph4−). *Inorg. Chem.* **2009,** *48* (15), 7033-7047.

210. Nicolazzi, W.; Bousseksou, A., Thermodynamical Aspects of the Spin Crossover Phenomenon. *C. R. Chim.* **2018,** *21* (12), 1060-1074.

211. Molnár, G.; Mikolasek, M.; Ridier, K.; Fahs, A.; Nicolazzi, W.; Bousseksou, A., Molecular Spin Crossover Materials: Review of the Lattice Dynamical Properties. *Annalen der Physik* **2019,** *531* (10), 1900076.

212. Kang, K.; Watanabe, S.; Broch, K.; Sepe, A.; Brown, A.; Nasrallah, I.; Nikolka, M.; Fei, Z.; Heeney, M.; Matsumoto, D.; Marumoto, K.; Tanaka, H.; Kuroda, S.; Sirringhaus, H., 2d Coherent Charge Transport in Highly Ordered Conducting Polymers Doped by Solid State Diffusion. *Nat. Mater.* **2016,** *15* (8), 896-902.

213. Tanaka, H.; Hirate, M.; Watanabe, S.; Kuroda, S., Microscopic Signature of Metallic State in Semicrystalline Conjugated Polymers Doped with Fluoroalkylsilane Molecules. *Adv. Mater.* **2014,** *26* (15), 2376-83.

214. Chen, J.; Heeger, A. J., In Situ Electron Spin Resonance Experiments on Polyacetylene During Electrochemical Doping. *Synth. Met.* **1988,** *24* (4), 311-327.

215. Panja, S.; Kadhane, U.; Andersen, J. U.; Holm, A. I. S.; Hvelplund, P.; Kirketerp, M.-B. S.; Nielsen, S. B.; Støchkel, K.; Compton, R. N.; Forster, J. S.; Kilså, K.; Nielsen, M. B., Dianions of 7,7,8,8-Tetracyano-P-Quinodimethane and Perfluorinated Tetracyanoquinodimethane: Information on Excited States from Lifetime Measurements in an Electrostatic Storage Ring and Optical Absorption Spectroscopy. *J. Chem. Phys.* **2007,** *127* (12), 124301.

216. Kim, Y. H.; Jung, S. D.; Chung, M. A.; Song, K. D.; Cho, D. W., Photoinduced Charge-Transfer Association of Tetracyanoquinodimethane with Aminobiphenyls. *Bull. Korean Chem. Soc.* **2008,** *29* (5), 948-952.

217. Ma, L.; Hu, P.; Jiang, H.; Kloc, C.; Sun, H.; Soci, C.; Voityuk, A. A.; Michel-Beyerle, M. E.; Gurzadyan, G. G., Single Photon Triggered Dianion Formation in TCNQ and F4tcnq Crystals. *Sci. Rep.* **2016,** *6* (1), 28510.

218. Gui, A. L.; Liu, G.; Chockalingam, M.; Le Saux, G.; Harper, J. B.; Gooding, J. J., A Comparative Study of Modifying Gold and Carbon Electrode with 4-Sulfophenyl Diazonium Salt. *Electroanalysis* **2010,** *22* (12), 1283-1289.

219. Blacha-Grzechnik, A.; Piwowar, K.; Koscielniak, P.; Kwoka, M.; Szuber, J.; Zak, J., Phenothiazines Grafted on the Electrode Surface from Diazonium Salts as Molecular Layers for Photochemical Generation of Singlet Oxygen. *Electrochim. Acta* **2015,** *182*, 1085-1092.

220. Xie, M.; Xiong, X.; Yang, L.; Shi, X.; Asiri, A. M.; Sun, X., An $Fe(TCNQ)_2$ Nanowire Array on Fe Foil: An Efficient Non-Noble-Metal Catalyst for the Oxygen Evolution Reaction in Alkaline Media. *Chem. Commun.* **2018,** *54* (18), 2300-2303.

221. Lee, M. S.; Yang, M. H.; Park, J. S.; Chang, D. W., Terpyridine-Containing Imine-Rich Graphene for the Oxygen Reduction Reaction. *Catalysts* **2017,** *7* (11), 338.

222. Huo, Z.; Zang, D.; Yang, S.; Farha, R.; Goldmann, M.; Hasenknopf, B.; Xu, H.; Ruhlmann, L., Synthesis and Characterization of Lindqvist-Type Polyoxometalate–Porphyrin Copolymers. *Electrochim. Acta* **2015,** *179*, 326-335.

223. Lin, Z.; Thacker, N. C.; Sawano, T.; Drake, T.; Ji, P.; Lan, G.; Cao, L.; Liu, S.; Wang, C.; Lin, W., Metal–Organic Layers Stabilize Earth-Abundant Metal–Terpyridine Diradical Complexes for Catalytic C–H Activation. *Chemical Science* **2018,** *9* (1), 143-151.

224. Üngör, Ö.; Shatruk, M., Transition Metal Complexes with Fractionally Charged Tcnq Radical Anions as Structural Templates for Multifunctional Molecular Conductors. *Polyhedron* **2020,** *177*, 114254.

225. Phan, H.; Benjamin, S. M.; Steven, E.; Brooks, J. S.; Shatruk, M., Photomagnetic Response in Highly Conductive Iron(II) Spin-Crossover Complexes with Tcnq Radicals. *Angewandte Chemie International Edition* **2015,** *54* (3), 823-827.

226. Zhang, X.; Wang, Z.-X.; Xie, H.; Li, M.-X.; Woods, T. J.; Dunbar, K. R., A Cobalt(II) Spin-Crossover Compound with Partially Charged Tcnq Radicals and an Anomalous Conducting Behavior. *Chem. Sci.* **2016,** *7* (2), 1569-1574.

227. Zhang, X.; Xie, H.; Ballesteros-Rivas, M.; Woods, T. J.; Dunbar, K. R., Conducting Molecular Nanomagnet of Dy^{III} with Partially Charged TCNQ Radicals. *Chem. Eur. J* **2017,** *23* (31), 7448-7452.

228. Kazakova, A. V.; Tiunova, A. V.; Korchagin, D. V.; Shilov, G. V.; Yagubskii, E. B.; Zverev, V. N.; Yang, S. C.; Lin, J.-Y.; Lee, J.-F.; Maximova, O. V.; Vasiliev, A. N., The First Conducting Spin-Crossover Compound Combining a Mn^{III} Cation Complex

with Electroactive Tcnq Demonstrating an Abrupt Spin Transition with a Hysteresis of 50 K. *Chem. Eur. J.* **2019,** *25* (43), 10204-10213.

229. Hummel, R. E., *Electronic Properties of Materials, Fourth Edition*. Springer: New York, 2011; p 1-488.

230. Zhou, H.-C. J.; Kitagawa, S., Metal–Organic Frameworks (MOFs). *Chem. Soc. Rev.* **2014,** *43* (16), 5415-5418.

231. Coronado, E.; Galan-Mascaros, J. R.; Gomez-Garcia, C. J.; Laukhin, V., Coexistence of Ferromagnetism and Metallic Conductivity in a Molecule-Based Layered Compound. *Nature* **2000,** *408* (6811), 447-9.

232. Baldovi, J. J.; Coronado, E.; Gaita-Arino, A.; Gamer, C.; Gimenez-Marques, M.; Espallargas, G. M., A Sim-Mof: Three-Dimensional Organisation of Single-Ion Magnets with Anion-Exchange Capabilities. *Chem. Eur. J.* **2014,** *20* (34), 10695-10702.

233. D'Alessandro, D. M., Exploiting Redox Activity in Metal–Organic Frameworks: Concepts, Trends and Perspectives. *Chem. Commun.* **2016,** *52* (58), 8957-8971.

234. Murase, R.; Abrahams, B. F.; D'Alessandro, D. M.; Davies, C. G.; Hudson, T. A.; Jameson, G. N. L.; Moubaraki, B.; Murray, K. S.; Robson, R.; Sutton, A. L., Mixed Valency in a 3d Semiconducting Iron–Fluoranilate Coordination Polymer. *Inorg. Chem.* **2017,** *56* (15), 9025-9035.

235. Atzori, M.; Benmansour, S.; Mínguez Espallargas, G.; Clemente-León, M.; Abhervé, A.; Gómez-Claramunt, P.; Coronado, E.; Artizzu, F.; Sessini, E.; Deplano, P.; Serpe, A.; Mercuri, M. L.; Gómez García, C. J., A Family of Layered Chiral Porous Magnets Exhibiting Tunable Ordering Temperatures. *Inorg. Chem.* **2013,** *52* (17), 10031-10040.

236. Aulakh, D.; Pyser, J. B.; Zhang, X.; Yakovenko, A. A.; Dunbar, K. R.; Wriedt, M., Metal-Organic Frameworks as Platforms for the Controlled Nanostructuring of Single-Molecule Magnets. *J. Am. Chem. Soc.* **2015,** *137* (29), 9254-9257.

237. Chen, D. M.; Ma, X. Z.; Zhang, X. J.; Xu, N.; Cheng, P., Switching a 2d Co(II) Layer to a 3d Co-7-Cluster-Based Metal-Organic Framework: Syntheses, Crystal Structures, and Magnetic Properties. *Inorg. Chem.* **2015,** *54* (6), 2976-2982.

238. Liu, K.; Li, H. H.; Zhang, X. J.; Shi, W.; Cheng, P., Constraining and Tuning the Coordination Geometry of a Lanthanide Ion in Metal-Organic Frameworks: Approach toward a Single-Molecule Magnet. *Inorg. Chem.* **2015,** *54* (21), 10224-10231.

239. Zhang, X.; Vieru, V.; Feng, X.; Liu, J.-L.; Zhang, Z.; Na, B.; Shi, W.; Wang, B.-W.; Powell, A. K.; Chibotaru, L. F.; Gao, S.; Cheng, P.; Long, J. R., Influence of Guest

Exchange on the Magnetization Dynamics of Dilanthanide Single-Molecule-Magnet Nodes within a Metal–Organic Framework. *Angew. Chem. Int. Ed.* **2015,** *54* (34), 9861-9865.

240. Campo, J.; Falvello, L. R.; Forcen-Vazquez, E.; de Pipaon, C. S.; Palacio, F.; Tomas, M., A Symmetric, Triply Interlaced 3-D Anionic Mof That Exhibits Both Magnetic Order and Smm Behaviour. *Dalton Trans.* **2016,** *45* (42), 16764-16768.

241. Nguyen, T. N.; Abboud, K. A.; Christou, G., Mof-Like Supramolecular Network of Mn-3 Single-Molecule Magnets Formed by Extensive Pi-Pi Stacking. *Polyhedron* **2016,** *103*, 150-156.

242. Rigamonti, L.; Cotton, C.; Nava, A.; Lang, H.; Ruffer, T.; Perfetti, M.; Sorace, L.; Barra, A. L.; Lan, Y. H.; Wernsdorfer, W.; Sessoli, R.; Cornia, A., Diamondoid Structure in a Metal-Organic Framework of Fe-4 Single-Molecule Magnets. *Chem. Eur. J.* **2016,** *22* (38), 13705-13714.

243. Aulakh, D.; Xie, H. M.; Shen, Z.; Harley, A.; Zhang, X.; Yakovenko, A. A.; Dunbar, K. R.; Wriedt, M., Systematic Investigation of Controlled Nanostructuring of Mn-12 Single-Molecule Magnets Templated by Metal-Organic Frameworks. *Inorg. Chem.* **2017,** *56* (12), 6965-6972.

244. Brunet, G.; Safin, D. A.; Jover, J.; Ruiz, E.; Murugesu, M., Single-Molecule Magnetism Arising from Cobalt(II) Nodes of a Crystalline Sponge. *J. Mater. Chem. C* **2017,** *5* (4), 835-841.

245. Yuan, S.; Qin, J.-S.; Su, J.; Li, B.; Li, J.; Chen, W.; Drake, H. F.; Zhang, P.; Yuan, D.; Zuo, J.; Zhou, H.-C., Sequential Transformation of Zirconium(Iv)-Mofs into Heterobimetallic Mofs Bearing Magnetic Anisotropic Cobalt(II) Centers. *Angew. Chem. Int. Ed.* **2018,** *57* (38), 12578-12583.

246. Zhao, F.; Guo, X. Y.; Dong, Z. P.; Liu, Z. L.; Wang, Y. Q., 3d Ln(III)-MOFs: Slow Magnetic Relaxation and Highly Sensitive Luminescence Detection of Fe^{3+} and Ketones. *Dalton Trans.* **2018,** *47* (27), 8972-8982.

247. Aulakh, D.; Liu, L.; Varghese, J. R.; Xie, H.; Islamoglu, T.; Duell, K.; Kung, C.-W.; Hsiung, C.-E.; Zhang, Y.; Drout, R. J.; Farha, O. K.; Dunbar, K. R.; Han, Y.; Wriedt, M., Direct Imaging of Isolated Single-Molecule Magnets in Metal–Organic Frameworks. *J. Am. Chem. Soc.* **2019,** *141* (7), 2997-3005.

248. Grosjean, S.; Hodapp, P.; Hassan, Z.; Wöll, C.; Nieger, M.; Bräse, S., Synthesis of Functionalized Azobiphenyl- and Azoterphenyl- Ditopic Linkers: Modular Building Blocks for Photoresponsive Smart Materials. *ChemistryOpen* **2019,** *8* (6), 743-759.

249. Shi, L.; Shen, F. X.; Shao, D.; Zhang, Y. Q.; Wang, X. Y., Syntheses, Structures, and Magnetic Properties of Three Two-Dimensional Cobalt(II) Single-Ion Magnets with a (CoN_4X_2)-N-II Octahedral Geometry. *CrystEngComm* **2019,** *21* (20), 3176-3185.

250. Ma, D. Y.; Peng, G.; Zhang, Y. Y.; Li, B., Field-Induced Slow Magnetic Relaxation in Two-Dimensional and Three-Dimensional Co(II) Coordination Polymers. *Dalton Trans.* **2019,** *48* (41), 15529-15536.

251. Kong, J. J.; Shao, D.; Zhang, J. C.; Jiang, Y. X.; Ji, C. L.; Huang, X. C., From Mononuclear to Two-Dimensional Cobalt(II) Complexes Based on a Mixed Benzimidazole-Dicarboxylate Strategy: Syntheses, Structures, and Magnetic Properties. *CrystEngComm* **2019,** *21* (4), 749-757.

252. Shi, L.; Shao, D.; Wei, H. Y.; Wang, X. Y., Two Interpenetrated Cobalt(Ii) Metal-Organic Frameworks with Guest-Dependent Structures and Field-Induced Single-Ion Magnet Behaviors. *Cryst. Growth Des.* **2018,** *18* (9), 5270-5278.

253. Mondal, P.; Dey, B.; Roy, S.; Bera, S. P.; Nasani, R.; Santra, A.; Konar, S., Field-Induced Slow Magnetic Relaxation and Anion/Solvent Dependent Proton Conduction in Cobalt(II) Coordination Polymers. *Cryst. Growth Des.* **2018,** *18* (10), 6211-6220.

254. Shao, D.; Shi, L.; Wei, H. Y.; Wang, X. Y., Field-Induced Single-Ion Magnet Behaviour in Two New Cobalt(II) Coordination Polymers with 2,4,6-Tris(4-Pyridyl)-1,3,5-Triazine. *Inorganics* **2017,** *5* (4), 90.

255. Brozek, C. K.; Michaelis, V. K.; Ong, T.-C.; Bellarosa, L.; López, N.; Griffin, R. G.; Dincă, M., Dynamic Dmf Binding in Mof-5 Enables the Formation of Metastable Cobalt-Substituted Mof-5 Analogues. *ACS Central Science* **2015,** *1* (5), 252-260.

256. Koh, K.; Wong-Foy, A. G.; Matzger, A. J., A Crystalline Mesoporous Coordination Copolymer with High Microporosity. *Angew. Chem. Int. Ed.* **2008,** *47* (4), 677-680.

257. Bain, G. A.; Berry, J. F., Diamagnetic Corrections and Pascal's Constants. *J. Chem. Educ.* **2008,** *85* (4), 532-536.

258. Chilton, N. F.; Anderson, R. P.; Turner, L. D.; Soncini, A.; Murray, K. S., Phi: A Powerful New Program for the Analysis of Anisotropic Monomeric and Exchange-Coupled Polynuclear D- and F-Block Complexes. *J. Comput. Chem.* **2013,** *34* (13), 1164-75.

259. Kurmoo, M., Magnetic Metal-Organic Frameworks. *Chem. Soc. Rev.* **2009,** *38* (5), 1353-79.

260. Zhang, Y. Z.; Gomez-Coca, S.; Brown, A. J.; Saber, M. R.; Zhang, X.; Dunbar, K. R., Trigonal Antiprismatic Co(II) Single Molecule Magnets with Large Uniaxial Anisotropies: Importance of Raman and Tunneling Mechanisms. *Chem. Sci.* **2016,** *7* (10), 6519-6527.

261. Wang, Y. L.; Chen, L.; Liu, C. M.; Du, Z. Y.; Chen, L. L.; Liu, Q. Y., 3d Chiral and 2d Achiral Cobalt(II) Compounds Constructed from a 4-(Benzimidazole-1-Yl)Benzoic Ligand Exhibiting Field-Induced Single-Ion-Magnet-Type Slow Magnetic Relaxation. *Dalton Trans.* **2016,** *45* (18), 7768-75.

262. Vallejo, J.; Fortea-Perez, F. R.; Pardo, E.; Benmansour, S.; Castro, I.; Krzystek, J.; Armentano, D.; Cano, J., Guest-Dependent Single-Ion Magnet Behaviour in a Cobalt(II) Metal-Organic Framework. *Chem. Sci.* **2016,** *7* (3), 2286-2293.

263. Switlicka-Olszewska, A.; Palion-Gazda, J.; Klemens, T.; Machura, B.; Vallejo, J.; Cano, J.; Lloret, F.; Julve, M., Single-Ion Magnet Behaviour in Mononuclear and Two-Dimensional Dicyanamide-Containing Cobalt(II) Complexes. *Dalton Trans.* **2016,** *45* (25), 10181-93.

264. Sun, L.; Zhang, S.; Chen, S. P.; Yin, B.; Sun, Y. C.; Wang, Z. X.; Ouyang, Z. W.; Ren, J. L.; Wang, W. Y.; Wei, Q.; Xie, G.; Gao, S. L., A Two-Dimensional Cobalt(II) Network with a Remarkable Positive Axial Anisotropy Parameter Exhibiting Field-Induced Single-Ion Magnet Behavior. *J. Mater. Chem. C* **2016,** *4* (33), 7798-7808.

265. Mondal, A. K.; Khatua, S.; Tomar, K.; Konar, S., Field-Induced Single-Ion-Magnetic Behavior of Octahedral Co-II in a Two-Dimensional Coordination Polymer. *Eur. J. Inorg. Chem.* **2016,** (22), 3545-3552.

266. Polunin, R. A.; Burkovskaya, N. P.; Satska, J. A.; Kolotilov, S. V.; Kiskin, M. A.; Aleksandrov, G. G.; Cador, O.; Ouahab, L.; Eremenko, I. L.; Pavlishchuk, V. V., Solvent-Induced Change of Electronic Spectra and Magnetic Susceptibility of Co(II) Coordination Polymer with 2,4,6-Tris(4-Pyridyl)-1,3,5-Triazine. *Inorg. Chem.* **2015,** *54* (11), 5232-8.

267. Novikov, V. V.; Pavlov, A. A.; Nelyubina, Y. V.; Boulon, M. E.; Varzatskii, O. A.; Voloshin, Y. Z.; Winpenny, R. E., A Trigonal Prismatic Mononuclear Cobalt(II) Complex Showing Single-Molecule Magnet Behavior. *J. Am. Chem. Soc.* **2015,** *137* (31), 9792-5.

268. Liu, X.; Sun, L.; Zhou, H.; Cen, P.; Jin, X.; Xie, G.; Chen, S.; Hu, Q., Single-Ion-Magnet Behavior in a Two-Dimensional Coordination Polymer Constructed from Co(II) Nodes and a Pyridylhydrazone Derivative. *Inorg. Chem.* **2015,** *54* (18), 8884-6.

269. Herchel, R.; Vahovska, L.; Potocnak, I.; Travnicek, Z., Slow Magnetic Relaxation in Octahedral Cobalt(II) Field-Induced Single-Ion Magnet with Positive Axial and Large Rhombic Anisotropy. *Inorg. Chem.* **2014,** *53* (12), 5896-8.

270. Heering, C.; Boldog, I.; Vasylyeva, V.; Sanchiz, J.; Janiak, C., Bifunctional Pyrazolate-Carboxylate Ligands for Isoreticular Cobalt and Zinc MOF-5 Analogs with Magnetic Analysis of the {Co_4(μ4-O)} Node. *CrystEngComm* **2013,** *15* (45), 9757-9768.